DROP-ON-DEMAND PRINTING OF LIQUID CRYSTALS AND COMPOSITES

Waqas Kamal

Exeter College

University of Oxford

A thesis presented for the degree of

Doctor of Philosophy in Engineering Science

Trinity Term 2022

DECLARATION

This thesis entitled "DROP-ON-DEMAND PRINTING OF LIQUID CRYSTALS AND COMPOSITES" is supervised by:

1) Stephen Morris – Professor of Engineering Science
2) Alfonso A Castrejón-Pita – Professor of Engineering Science
2) Steve Elston – Professor of Engineering Science

I hereby declare that this submission is my own work and to the best of my knowledge it contains no materials previously published or written by another person, other than me. The only material taken for this thesis is from my first-authors published work that are listed below:

1) Electrically Tunable Printed Bifocal Liquid Crystal Microlens Arrays. Advanced Materials Interfaces (7, 2000578, 2020)

2) Spatially Patterned Polymer Dispersed Liquid Crystals for Image–Integrated Smart Windows Advanced Optical Materials Journal (10, 2101748, 2022).

Name: ***Waqas Kamal*** *Date:* ***01-07-2022***

Abstract

DROP-ON-DEMAND PRINTING OF LIQUID CRYSTALS AND COMPOSITES

By Waqas Kamal

This thesis focuses on the development and investigation of drop-on-demand (DoD) printing of liquid crystal (LC) and polymer composites with a focus on the manufacture of new photonics technologies that encompass a range of length scales. Both inkjet and electrohydrodynamic printing are employed as advanced material deposition tools with the end goal of forming droplets on both the micro-and nano-scale. The benefits of using these two forms of printing lie in their ability to deposit viscous and complex fluids in a non-contact, maskless, scalable and additive manner. These advantages have led both techniques to be considered for the manufacture of a range of different applications including printed electronics, printed photonics, displays and biotechnology.

The first part of the thesis investigates the droplet generation process of a nematic liquid crystal (LC) when ejected from a piezoelectric-driven inkjet nozzle. For this study, high speed shadowgraphy imaging technique is used to visualise the droplet formation process and to determine the range of experimental conditions (e.g., temperature, voltage waveform applied to the piezoelectric transducer) where stable and reproducible inkjet printing of a nematic LC can be performed. These findings are then explained in terms of the fluid dimensionless numbers. Using the experimental conditions identified in the first part of the study, the thesis then demonstrates the precision offered by printing nematic LC microlens arrays for potential micro-optics applications.

With the accuracy afforded by DoD inkjet printing, microlenses with a variety of different diameters and focal lengths in the range of 120 – 255 μm and 220 – 463 μm, respectively, are deposited precisely between in-plane electrodes. These microlenses are then subjected to an in-plane electric field and their resulting behaviour characterised with the aid of polarising optical microscopy and measurements of the focal length. The LC

director is observed to align with the electric field direction leading to tuning of the focal length. Moreover, a bifocal behaviour is observed due to the formation of two separate domains with different alignments of the LC director over a range of electric field amplitudes. Subsequently, these two different LC domains gives rise to different refractive index profiles. These experimental findings are supported by finite element modelling of the LC director for different electric field amplitudes.

Following the successful demonstration of electrically tunable microlenses, this thesis then employs DoD inkjet printing to manufacture large-area printed photonic devices. This is achieved by printing a polymer dispersed liquid crystal (PDLC) mixture to form arrays of droplets that make up emblems/logos that can be made to disappear with the application of a voltage. After device assembly and subsequent illumination with ultraviolet light, the PDLC droplets are shown to scatter the incident light in much the same way as that observed for conventional PDLC thin films. By applying an electric field across the device, the printed droplets become transparent and the scattering disappears. The thesis investigates the electro-optic properties of a single printed PDLC droplet and through the formation of arrays a smart window prototype with a switchable embedded image is then demonstrated.

The final part of the thesis introduces the electrohydrodynamic (EHD) printing of liquid crystalline materials, which unlocks the possibility of forming nanoscale droplets for nanophotonic technologies including diffractive optic elements and optical circuits. To demonstrate EHD printing, a custom-built printing system is presented that is capable of depositing a nematic LC at room temperature. The response of the LC meniscus to an applied electric field is investigated using shadowgraphy imaging and the drop generation process is discussed in the context of the formation of a Taylor cone. By adjusting the input waveform and using different diameter nozzles, nematic LC droplets with droplet footprint diameters ranging from 2 – 8 μm are printed. EHD printing is then employed to form arrays of droplets that result in the appearance of shapes and alphanumeric characters at the microscale.

Acknowledgements

I would like to express my deepest gratitude and appreciation to my incredible research supervisors, Stephen Morris, Steve Elston, and Alfonso Castrejón-Pita for their continuous support during my DPhil. Thank you, Steve M, for the unconditional support and for providing me research facilities that made me capable of producing a comprehensive thesis and publishing research articles. Steve E, I am genuinely grateful to you. Thank you for helping me understand liquid crystals science. Before coming to Oxford, I had never imagined that a research supervisor would help me in understanding science as well as speaking over various different sort of topics over a cup of coffee. Your excitement about the experimental results and your saying, "Look at That". I cannot forget that. I really enjoyed working with you in the labs. Thank you for your time, patience, teaching, and supervision. Thank you Alfonso, for your enthusiasm, guidance and friendly supervision. You have always been motivating me, and especially during the national lockdown, you showed extra care towards my mental health.Thanks for the incredible support and supervision. Thank you to the whole Fluid Dynamics Group for enjoyable chats and socialisation at The Royal Oak.

I am incredibly thankful to all members of Soft Matter Photonics Group. I feel fortunate to have had the opportunity to work with such a unique and talented bunch of individuals who will continue to inspire me. I am particularly thankful to Ellis, David, Lake and Julian, who made me feel so welcome when I started my DPhil. Thanks to John, who was always there for help and support. To my dear friend Taimoor, a very humble, kind, and a helping person who trained me on various experimental tools. I am thankful to Andrew for his fruitful advice on developing an experimental setup. Thanks to Yihan for being so friendly and lively. To Jia-De, thank you for your incredible support. Your stay in the SMP was advantageous. Thanks to Zimo, Bohan, Guanxiong, Linpei, Peng, Camron, Nathan, Mengmeng, Yunuen, Bradley, and Xuke, although we never had much get-together but you guys are very energetic. I wish you all the very best in your PhDs and life beyond. I thank Mengmeng for working with me so diligently on the EHD printing project over the past few months. Thanks to Nathan for always saying yes whenever I insisted you to play squash.

I am thankful to my Oxford friends, including Mohsin, Talha Pirzada, Mehroz, Ghani Bhai, Taimoor, Naeem, Saed, Arun, and Abhijeet. To Usama, thank you for your incredible warmth and kindness. I am glad we met just before the pandemic and spent complete lockdown with a lot of fun. Thank you for encouraging and showing me the joys of a balanced approach to DPhil life. Thanks to Abdullah Azzam for being a knowledgeable and thought-provoking person. My deepest gratitude to you and best wishes to you. A special thanks to my friend Malik Arslan for being a moral and emotional support.

To one of the most important person in my life, my beloved wife, Nimra. Thank you for the support, love, encouragement and unwavering faith in me when I have none. Thank you for making stressful days of my thesis writing full of fun.

Thanks to the Punjab Educational Endowment fund (PEEF) for sponsoring my DPhil and providing me a scholarship to study at the University of Oxford. A special thanks to Steve M for providing me financial support during the COVID-19 pandemic when I faced financial difficulties. Similarly, a bundle of thanks to Alfonso for financially supporting me through various routes. Thanks to the Rank Prize for providing me with a one-time research grant.

Finally, I extend my love and gratitude to my dear mother, who could never get higher education, and despite having financial difficulties after my father's demise, she has given me endless encouragement, unfaltering confidence, and never-ending moral and emotional support. Thanks to my brothers and sister, who always supported me during difficult times. Lastly, I dedicate this thesis to my late father, who died at the age of 41.

Publications

1. **Waqas Kamal**, Mengmeng Li, Andrew Orr, Steve J Elston, Alfonso A Castrejón-Pita, Stephen M Morris, "Electrohydrodynamic printing of Nematic Liquid Crystals." [*in preparation*].

2. **Waqas Kamal**, Ellis Parry, Steve J Elston, Alfonso A Castrejón-Pita, Stephen M Morris, "Inkjet printing nematic liquid crystals for photonics technologies." [*in submission at Nano.Micro Small journal*].

3. **Waqas Kamal**, Jia-De Lin, Steve J Elston, Taimoor Ali, Alfonso A Castrejón-Pita, Stephen M Morris, "Electrically tunable printed bifocal liquid crystal microlens arrays." *Advanced Materials Interfaces*, (7, 2000578, 2020).

4. **Waqas Kamal**, Mengmeng Li, Jia-De Lin, Ellis Parry, Yihan Jin, Steve J Elston, Alfonso A Castrejón-Pita, Stephen M Morris, "Spatially Patterned Polymer Dispersed Liquid Crystals for Image-Integrated Smart Windows." *Advanced Optical Materials*, (10, 2101748, 2022).

5. Mengmeng Li, **Waqas Kamal**, Andrew Orr, Steve J Elston, Alfonso A Castrejón-Pita, Stephen M Morris, "Printed Polymer-stabilized Chiral Nematic Liquid Crystal Privacy Windows." *Macromolecular Chemistry and Physics*, (2200154, 2022).

6. Arun Babal, Samraj Mollick, **Waqas Kamal**, Steve J Elston, Alfonso A Castrejón-Pita, Stephen M Morris, Jin-Chong Tan "Nano-Trap Engineering in MOF Microenvironment for Ultratrace Iodine Sensors." *materialstoday*, (2022).

7. Yihan Jin, Steve J Elston, Bohan Chen, Mengmeng Li, **Waqas Kamal**, Zimo Zhao and Stephen M Morris, "Backflow-assisted time-resolved phase modulation in nematic liquid crystal Pi-Cells." *Optics & Laser Technology*, (156, 108596, 2022).

8. Microlenses: Electrically Tunable Printed Bifocal Liquid Crystal Microlens Arrays (Adv. Mater. Interfaces 16/2020) [Front Cover of the Journal issue]

Note: Articles 5-7 are not related to this Thesis but are based on the collaborative work. Therefore no content from these articles is added to this Thesis.

Conferences

IOP PGS Printing for the Future
London, United Kingdom – 28^{th} June 2022 (Invited Oral)
"Printing of Polymer Dispersed Liquid Crystals for Smart Windows."

28^{th} International Liquid Crystal Conference
Lisbon, Portugal – July 2020 (Oral)
"Printed Nematic Liquid Crystal Droplets for Thin-Film Optical Elements."
(Cancelled due to COVID-19 pandemic)

Materials Research Society
Arizona, United States – April 2020 (Poster)
"Printed Electrically tunable Bifocal Liquid Crystal Microlenses."
(Cancelled due to COVID-19 pandemic)

University of Oxford Photonics Day
Oxford – April 2019 (Poster)
"Printed Liquid Crystal Microlens Arrays."

TABLE OF CONTENTS

LIST OF ABBREVIATIONS

DoD ..... Drop-on-demand

CIJ ..... Continuous Inkjet

EHD ..... Electrohydrodynamic

LC ..... Liquid Crystal

CLC ..... Chiral Liquid Crystal

PDLC ..... Polymer Dispersed Liquid Crystal

PCC ..... Phantom Camera Control

PVA ..... Polyvinyl alcohol

PI ..... Polyimide

UV ..... Ultraviolet

ITO ..... Indium Tin Oxide

POM ..... Polarised Optical Microscopy

CCD ..... Charge Coupled Device

PIPS ..... Photopolymerisation Induced Phase Separation

TIPS ..... Temperature Induced Phase Separation

SIPS ..... Solvent Induced Phase Separation

LED . . . . . Light Emitting Diode

EC . . . . . Electrochromic

dpi . . . . . dots per inch

ID . . . . . Inner Diameter

OD . . . . . Outer Diameter

CRT . . . . . Cathode Ray Tube

NaNs . . . . . Not available Numbers

CHAPTER 1

INTRODUCTION

This chapter describes the motivation for the research presented in the thesis and how it relates to the current state-of-the-art of drop-on-demand printing of advanced functional materials. The chapter concludes with a description of the layout of the thesis and the key objectives presented in each chapter.

1.1 Introduction

Since its conception in 1980, piezoelectric Drop-on-Demand (DoD) inkjet printing has emerged as a powerful material deposition technique that enables picolitre volumes of a functional ink to be deposited precisely on a variety of different substrates. Today, it is considered to be an essential part of the field of additive manufacturing. Briefly, the technique incorporates a piezoelectric printhead that ejects a droplet of ink from a nozzle when a voltage is applied to the piezoelectric membrane, which contracts and expands generating a pressure pulse inside the fluid-filled chamber. The versatile nature of this method of manufacturing has meant that it has become recognised as a scalable technique that allows for a range of functional inks to be delivered to a substrate at high speeds and with a high degree of accuracy. Because of its benefits in terms of ease of processing, inkjet printing is now employed in a wide range of industries including displays, pharmaceuticals, bioengineering and printed electronics [1–4].

Despite the wide range of printable inks that are now available, inkjet printing is still limited in terms of printing resolution (i.e., droplet size). The printing resolution in inkjet printing is mostly determined by the orifice size of the printing nozzle and is typically limited to about 30 μm. To overcome the limitation in terms of resolution, Electrohydrodynamic (EHD) printing offers greater freedom in terms of printing functional inks at smaller feature sizes. In EHD printing, the droplet is formed by the electric field at the cone tip, and can be significantly smaller than the nozzle orifice size, which results in the ability to print nanoscale features.

Liquid crystals (LCs) are a class of material that exhibit properties that are between the conventional solid and liquid states of matter. Their chemical structure and partially crystalline-like nature results in anisotropy in the physical properties. For example, calamitic LC molecules have a rod-like shape leading to uniaxial optical anisotropy. This optical anisotropy, referred to as birefringence, makes these materials ideally suited for optoelectronic applications. Also, LC molecules have the ability to adopt a preferential macroscopic orientation in the presence of a stimulus, whilst at the same time being able

to flow like a fluid. A macroscopic uniform orientation of the LC molecules can be imposed by using alignment layers i.e., at the interface between the LC layer and the device substrate. Therefore, due to the anisotropic physical properties coupled with the fluidity, the orientation of the LC molecules in the bulk can be controlled with the application of external stimuli such as variations in the temperature and electric or magnetic fields.

The work presented in this thesis focuses on developing new printed photonics technologies that combine soft matter in the form of LC and polymers with DoD printing technologies in the form of inkjet and EHD printing. The previous research in this area has been relatively limited and has primarily focused on the continuous printing of LCs with drop feature sizes greater than 120 μm in order to manufacture passive optical devices such as temperature and humidity sensors and thermally tunable microlenses. Additionally, except for the printing of polyimides (PI) as an alignment layer, there has been no work so far on the EHD printing of LCs. Therefore, the work presented in this thesis demonstrates the manufacture and characterisation of new printed LC photonics devices (in the form of smart windows and electrically tuneable micro-lenses) and progresses the understanding of the deposition process of these materials. Furthermore, for the first time, EHD printing of LCs is demonstrated. The following section outlines the structure of this thesis and provides a brief description of the content and subject of each chapter.

1.2 Thesis outline

Chapter 2 provides a general introduction to the macroscopic properties of LC materials. This chapter provides the necessary background needed to understand and interpret the experimental results presented later in the thesis. The second half of the chapter goes on to describe the imaging techniques that were used to characterise the LC droplet formation process and the droplet morphology when printed on glass substrates treated with different surfactants.

Chapter 3 introduces inkjet printing and reviews the previous research carried out on the drop-on-demand inkjet printing of LCs. This chapter also describes the experimental procedures used to print nematic LC droplets and LC-polymer composites from a

piezoelectrically driven inkjet printing nozzle. The chapter uses a nematic LC as a case study to investigate the effect of different printing parameters, such as printhead temperature and voltage waveform, on the deposition of the LC. These results are then discussed in the context of fluid-dimensionless numbers. The results from this study have been written up and are ready to submit to a peer-reviewed journal for publication.

After investigating the printing conditions for nematic LCs, this thesis then considers the deposition of nematic LC droplets onto glass substrates with in-plane electrodes so as to fabricate tuneable microlenses. **Chapter 4** demonstrates that the printed droplets can form plano-convex microlenses with diameters ranging from 120 to 255 μm and that the focal length can be tuned with an applied voltage. An interesting feature of these microlenses is that bifocal tuning is observed over a range of voltage amplitudes. To understand the behaviour that is observed, the chapter then presents finite element modelling simulations of the LC director reorientation in the microlenses when subjected to an electric field. Some of the results presented in this chapter have already been published in the paper *"Electrically Tunable Printed Bifocal Liquid Crystal Microlens Arrays." Advanced Materials Interfaces (7, 2000578, 2020).*

Chapter 5 continues the work on DoD inkjet printing by using an LC and prepolymer ink formulation to form printed polymer dispersed liquid crystal (PDLC) films with features that can be made to disappear with the application of an electric field. The potential of these printed PDLCs is demonstrated by the fabrication of privacy windows that consist of intricate patterns/logos. The approach described in this chapter would allow for artistic designs, motifs, and additional information, such as dynamic company logos or advertisements to be displayed in smart windows that could be removed with an applied voltage. Results from this chapter have been published in the paper *"Spatially Patterned Polymer Dispersed Liquid Crystals for Image–Integrated Smart Windows." Advanced Optical Materials Journal (10, 2101748, 2022).*

Having demonstrated printing of nematic LC droplets to form microlenses and tuneable light scattering elements, the primary objective of **Chapter 6** is to demonstrate the

formation of nematic LC droplets with much smaller footprints using EHD printing. Results are presented that demonstrate that feature sizes that are less than 10 μm can be obtained. The chapter introduces the physics behind the EHD phenomenon and discusses the effect of system parameters on the droplet's formation process. This is then followed by a presentation of the development of a bespoke EHD printing setup that is used to deposit nematic LC droplets. The unique capabilities of the assembled printing setup are exploited and droplets with sizes in the range of 3 – 8 μm are printed. Furthermore, the chapter presents results of the behaviour of the LC meniscus in the form of dynamic shadowgraph images when subjected to high amplitude electric fields. The flexibility of the printing system is demonstrated by assembling LC droplets through a DoD approach to form arrays and patterns. The results presented in this chapter represent, to the best of author's knowledge, the first demonstration of EHD printing of liquid crystalline materials. This work is being prepared for publication in a peer-reviewed journal.

To conclude the thesis, **Chapter 7** provides an overall summary and concluding remarks for the studies carried out in this thesis that relate to the DoD printing of LC and polymer composites for the development of printed photonic devices. The final part of the chapter describes possible future work for each of the studies presented in this thesis as well as new avenues that could be explored.

CHAPTER 2

BACKGROUND AND EXPERIMENTAL TECHNIQUES

This chapter provides a general introduction and background to liquid crystals (LC) and discusses the technological achievements of these materials. A brief review of the different liquid crystal phases is followed by a detailed discussion of the dielectric and optical properties of nematic liquid crystal. LC continuum theory in terms of the Frank-Oseen free energy density equation is then introduced, and equations are derived that are used to simulate the liquid crystal director in the finite element modelling software package COMSOL multiphysics. Lastly, the chapter discusses the experimental techniques used to study and characterise the LC droplets and devices fabricated in this thesis.

2.1 Introduction

Liquid Crystals (LCs) are an optically active state of matter which is intermediate between the crystalline solid and isotropic fluid states. The LC molecules can flow like a fluid and, depending upon the mesophase, have the ability to self-organise into complex periodic structures on the molecular scale. The interesting properties of LCs are a result of their anisotropic molecular structure, which leads to anisotropy in many other physical properties such as refractive index and dielectric permitivity. Due to such properties LCs has been important for a range of opto-electronic devices including flat panel displays [5].

The liquid crystalline state was first discovered by an Austrian botanist named Friederich Reinitzer in the year 1888 while studying the melting point of cholesteryl benzoate where he observed an unusual colour change upon heating and cooling. In collaboration with the German physicist Otto Lehman, who was studying the crystallization properties of different substances using polarised light microscopy, they observed distinct optical properties and confirmed the discovery of a new thermodynamic state of matter [6]. Despite the discovery of a new state of matter, the field received relatively little attention from the scientific community for about 80 years. However, since the 1960s, LCs have become an important field of research, giving rise to a technological revolution in the information-display industry by replacing cathode ray tube (CRT) television sets with flat-panel Liquid Crystal Displays (LCD). In 1991, the significance of the field was further acknowledged by the award of the Noble Prize in Physics to the French scientist Pierre–Gilles de Gennes for his work on order and disorder in LCs and related complex soft matter.

Before 2007 the LCD was the dominant flat panel display technology but this is now being challenged by other advanced display technologies such as organic light-emitting (LED/OLED) diode displays. This shift in flat panel display technology has led the research community to explore other potential avenues for LCs, such as the use of additive manufacturing technologies in the form of inkjet printing and direct laser writing to engineer next-generation photonic devices [7, 8]. More recently, the Meta (previously known as Facebook) reality lab has started investing in LC technology to develop advanced LC

optics to integrate with existing and emerging augmented reality and virtual reality display solutions [9]. Additionally, recent discoveries have shown that LCs combined with materials such as polymers, glues, chiral dopants, and dyes open up new doors for advanced technological applications such as lasers, lenses, micro-robotics, chemical sensors and even biomedical devices [10–15].

2.2 Liquid Crystal Phases

The molecules that form a LC phase do not have rigid positional order like solids and are free to flow past each other as they would in a liquid. However, they possess a degree of orientational and sometimes positional ordering that an isotropic fluid does not have. This is why a LC phase is classed as a mesophase (meaning an intermediate phase) and the LC molecules themselves are referred to as mesogens. The transitions to the mesophases can be achieved using two different classes of materials: 1) Thermotropic and 2) Lyotropic. For thermotropic LCs, the mesophase appears by either heating from the crystalline solid phase or cooling from the isotropic fluid phase. In contrast, lyotropic LC exhibit phase transitions as a function of the concentration of the LC molecules in a solvent [6].

2.2.1 Nematic Liquid Crystals

Depending upon the geometrical structure of the mesogens, various types of thermotropic LCs can be formed. The most common type is a rod-shaped molecule as shown in Figure 2.1, in which one axis is larger than the other. This is a calamitic LC. A typical structure of a nematic LC molecule consists of two or more phenyl rings linked together via rigid linking groups and a flexible hydrocarbon chain at one end. Figure 2.1 shows an example illustration of the molecular structure superimposed over a rod shape LC molecule. The Smectic phase is another mesophase observed for calamitic LCs where the rod-like molecules self-organise to form a layer-like structure. Apart from the nematic phase, no other LC is used in this thesis and not discussed further.

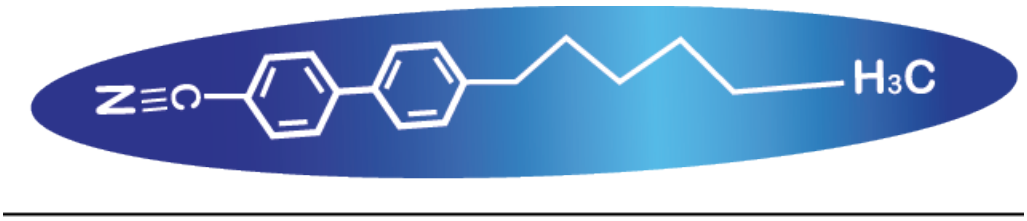

Figure 2.1: A basic illustration of a nematic liquid crystal molecule and the molecular structure.

In the nematic phase, the LC molecules have no positional order but they exhibit long range orientational order with their long axes oriented roughly parallel to each other. The average preferred orientation can be represented by a unit vector $\boldsymbol{n}$, known as the director, as illustrated in Figure 2.2(a). The degree of orientational order in the LC phase is represented by the order parameter, S which is an average of the second Legendre polynomial and can be expressed mathematically (Equation 2.1) [16].

$$S = \frac{1}{2}\langle 3cos^2\theta - 1\rangle \tag{2.1}$$

where θ is the angle between the long axis of a molecule and the director $\boldsymbol{n}$, and the average is taken over a large number of molecules. For a perfectly ordered LC phase with all the molecules aligned in the same direction $S = 1$, whereas for an isotropic liquid with the molecular axis pointing in all directions randomly $S = 0$. A nematic LC usually exhibits an order parameter in the range of $0.3 < S < 0.8$ [17]. The orientational order decreases with increasing temperature as the isotropic phase is approached. At the clearing temperature, the transition temperature at which the isotropic liquid phase appears, the LC molecules cease to have any orientational order as shown in Figure 2.2(b).

2.3 LC Director Alignment

LC molecules have the ability to exhibit long range orientational order when they interact with a chemically modified surface or interface with a fluid such as gas/air [18]. The mechanism of the alignment of the director at the interface is usually a balance of forces/energies associated with the elastic energy of the director. The surface induced alignment of rod-shaped nematic LC can result in orientations both parallel and perpendicular to the substrate. In the case of planar alignment, the director $\boldsymbol{n}$ is parallel to the

plane of the interface and in the case of homeotropic alignment

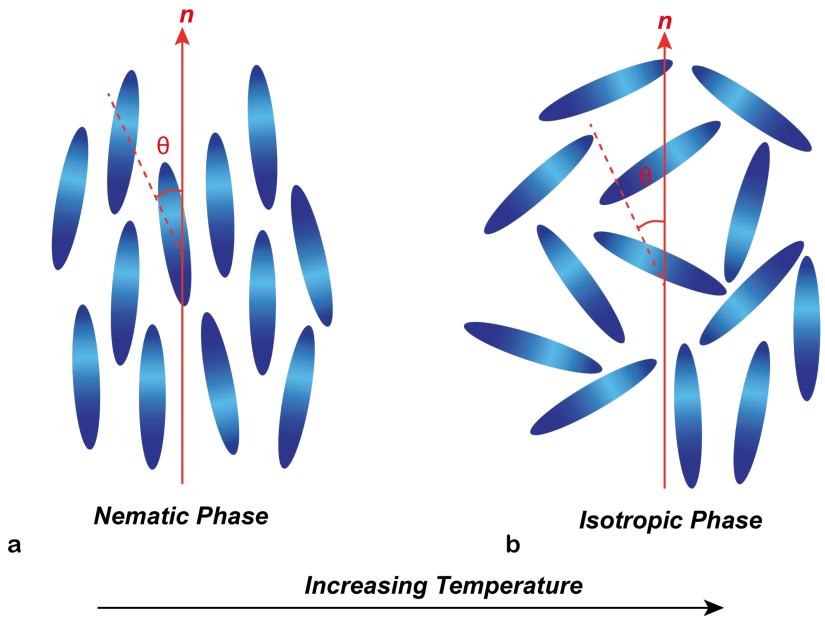

Figure 2.2: **a)** An illustration of a thermotropic nematic LC showing the average pointing direction of the molecules (referred to as the director, $\boldsymbol{n}$. **b)** The influence of temperature on order parameter, S, in a thermotropic nematic LC. As the temperature is increased, the order decreases and a phase transition from the nematic LC phase to an isotropic fluid occurs.

it is perpendicular to the interface. Figure 2.3(a, b) shows schematic illustrations of planar and homeotropic alignment of a nematic LC. The planar alignment can be achieved by coating the substrate with polyimide layers and rubbing them in a particular direction. This kind of planar alignment where the director $\boldsymbol{n}$ is mostly parallel to the interface this is known as planar homogeneous alignment. However, when the director $\boldsymbol{n}$ is parallel to substrate but with many in-plane orientations is known as planar degenerate alignment. [19] Unlike planar alignment, homeotropic alignment causes the LC director to align perpendicular to the substrate and it can be achieved by coating a thin surfactant layer on the substrate to promote a vertical alignment of the director [20].

In this thesis, homeotropic alignment layers on glass slides are frequently used for the printing substrate. Lecithin coating is considered to provide homeotropic alignment with a polar anchoring strength of 4.6 $\times 10^{-4}$ Jm $^{-2}$ [21]. To promote such alignment a lecithin solution mixed in isopropanol alcohol (IPA) was used. Solution composition and substrate preparation procedures are discussed in more detail in Section 4.2.1 of Chapter 4.

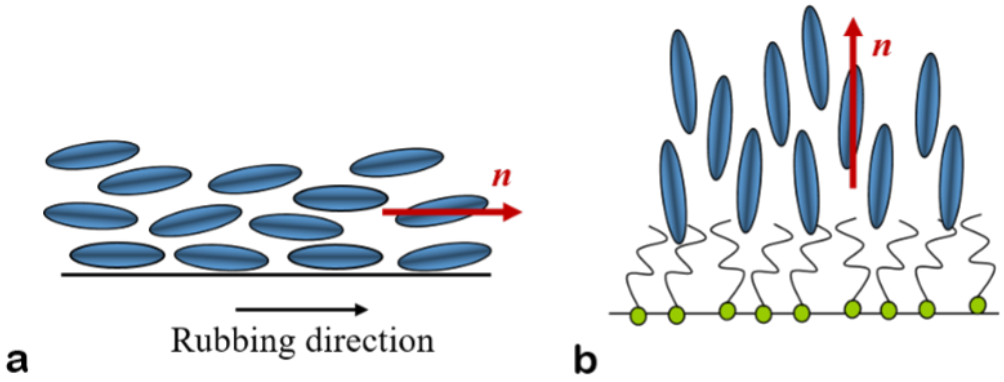

Figure 2.3: Schematic representation of a nematic LC on **a)** a planar alignment layer and **b)** a homeotropic alignment layer, where ***n*** corresponds to average molecular orientation. The threads with green head corresponds to surfactant which chemically attaches to the substrate, and the hydrocarbon tail points out, perpendicular to its surface. (The solid aligned rubbed polymer in (a) is not shown.)

2.4 Response to Electric Fields

Liquid crystal materials are considered to be non-conductive as the conductivity is typically found to be in the range of $10^{-12} < \sigma < 10^{-8}$ Sm^{-1}. In addition, they possess dielectric properties, which means that the application of an electric field rearranges the free charges inside the molecules and creates a net polarisation which contributes to the dielectric permittivity ε_r of the LC material. The dielectric permittivity has different values depending upon whether it is measured parallel $\varepsilon_\parallel$ or $\varepsilon_\perp$ to the LC director. The difference between the permittivities is known as the dielectric anisotropy, $\Delta\varepsilon = \varepsilon_\parallel - \varepsilon_\perp$. Nematic liquid crystal mixtures are typically available with dielectric anisotropies in the range -6 to 30. [22]

This dielectric interaction between the LC director and an applied electric field $\boldsymbol{E}$ contributes to the free energy density of the system and takes the form. [23]

$$f_e = -\frac{1}{2}\varepsilon_0 \Delta\varepsilon (\boldsymbol{n} \cdot \boldsymbol{E})^2 \tag{2.2}$$

where ε_0 = 8.85 $\times$ 10^{-12} C^2/Nm^2 is the permittivity of free space. In an applied electric field, the director favours the lowest energy configuration, and the dipoles align parallel to the field. The dielectric anisotropy can be either positive or negative, depending upon

the permanent dipole orientation of the LC molecules. For a positive dielectric anisotropy $\Delta\varepsilon > 0$, the director tends to align parallel to the electric field and for negative dielectric anisotropy $\Delta\varepsilon < 0$, the director tends to orient perpendicular to the electric field.

The dielectric anisotropy usually exhibits a dependence on the frequency of the applied electric field. A permanent dipole tends to provide greater polarisation than an induced one and hence this contribution to the dielectric anisotropy dominates at lower frequencies. Higher frequency fields (such as optical frequencies) oscillate too quickly such that the permanent dipoles are unable to follow the field. Therefore, the dielectric anisotropy decreases at higher frequencies. In addition, the dielectric anisotropy also depends upon temperature, which decreases with increasing temperature due to changes in the order parameter. [6]

As discussed, a positive dielectric anisotropy nematic LC ($\Delta\varepsilon > 0$) reorients in the direction of an applied electric field. However, the elasticity of the LC system tends to oppose the response to the electric field when the applied field is below a critical value, which is known as the Fréedericksz threshold. Above the threshold voltage, the LC director reorients in the direction of the field. When the field strength is reduced, the director then returns back to the original state due to the elastic restoring force. The threshold transition voltage (V_{th}) is given as: [16]

$$V_{th} = \pi \times \sqrt{\frac{K}{\varepsilon_0 \Delta\varepsilon}} \tag{2.3}$$

where ε_0 = 8.85 $\times$ 10^{-12} C^2/Nm^2 is the permittivity of free space and K is the elastic constant which depending upon type of elastic distortion can be splay, twist and bend. These elastic distortions are discussed in the section 2.6.

2.5 Optical Properties

Light is an electromagnetic wave with electric and magnetic fields that oscillate in space and time perpendicular to the direction of propagation. The direction of oscillation of

the electric field in a light wave dictates its polarisation state. The refractive index n of a material dictates the speed c/n that light propagates through it. For an isotropic material, the refractive index is constant in all directions and therefore light entering from any direction would experience the same change in speed and wavelength. However, for anisotropic materials such as LCs the refractive index is not constant in all directions. A uniaxial nematic LC has two principal refractive indices, the ordinary refractive index (n_o) and the extraordinary refractive index (n_e). Figure 2.4 illustrates the optical refractive indices for a uniaxial nematic LC. When the electric field vector of the incident plane polarised light enters an LC medium, it can experience two different refractive indices depending upon the orientation of the polarisation relative to the director. Light polarised along the director 'sees' the extraordinary refractive index, n_e and it is termed the extraordinary ray (E-ray), and when it is polarised perpendicular to the director it 'sees' the ordinary refractive index, n_o and it is termed the ordinary ray (O-ray).

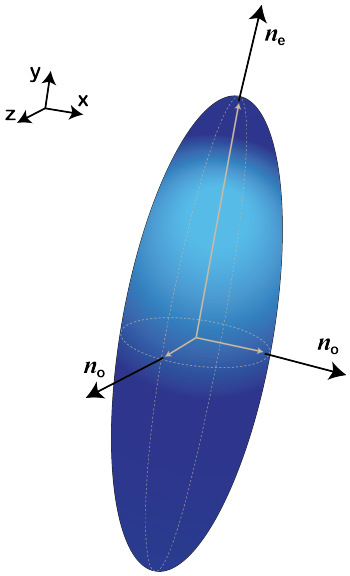

Figure 2.4: Refractive indices of a uniaxial nematic LC with $n_e > n_o$.

The optical anisotropy is referred to as the birefringence (Δn) and is defined in Equation 2.4. Most nematic LCs have positive birefringence ($\Delta n > 0$), meaning that the E-ray is delayed with respect to the O-ray on passage through the material.

$$\Delta n = n_e - n_o \tag{2.4}$$

In some cases, when incident light strikes the LC at an angle θ, with respect to the director it sees an effective refractive index (n_{eff}), which can be expressed as (Equation 2.5). [16]

$$n_{eff} = \frac{n_e n_o}{\sqrt{n_e^2\, cos^2\theta + n_o^2\, sin^2\theta}} \tag{2.5}$$

Birefringence is also responsible for the appearance of the interference colours observed when LC devices are viewed between crossed polarisers. When plane polarised light traverses through a birefringent film the ordinary and extraordinary rays propagate at different velocities which results in a phase difference between them. This phase difference/retardation, δ is given by (Equation 2.6):

$$\delta = \frac{2\pi\, \Delta n\, d}{\lambda} \tag{2.6}$$

where d is the LC layer thickness and λ is the wavelength of light. The indices of refraction have a strong temperature dependence. As discussed in Section 2.2.1 the increase in temperature reduces the order parameter which consequently affects both n_e and n_o, and their difference Δn. Above the isotropic temperature, Δn reduces to zero [24].

2.6 Elastic Properties

The director ***n*** of an undeformed LC that is free from any boundary conditions and external forces does not vary in space. However, a small distortion to the LC system in the form of anchoring conditions/external forces changes the director orientation from point to point and results in curvature strains of the director field. In the 1950s, Sir Charles Frank [25] formulated a mathematical description of these curvature strains in terms of three possible fundamental deformations of a LC, as shown in Figure 2.5. Frank's work was built on the earlier work of Oseen [26] and Zocher [27].

According to the Frank-Oseen theory, a LC can be thought of as an elastic medium in which the LC director can undergo a combination of splay, twist and bend deformities by storing elastic energy for each type of curvature strain. The distorted structure would

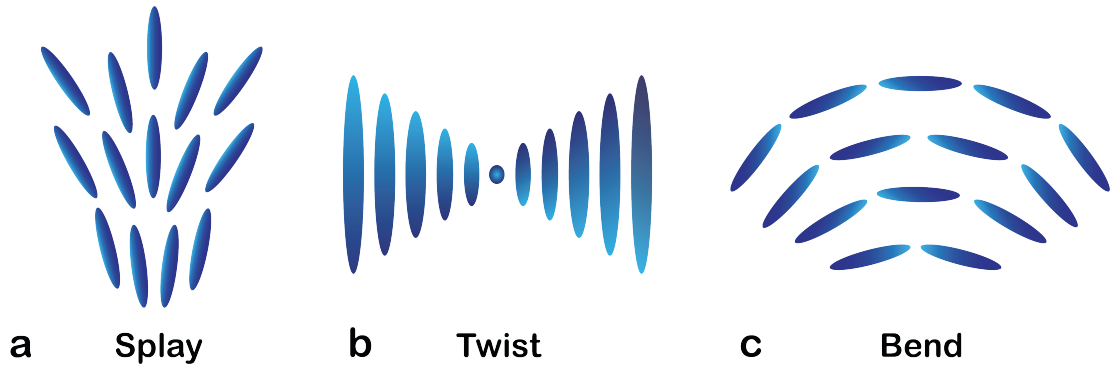

Figure 2.5: Schematic illustrations of the three fundamental distortions of a nematic LC: **a)** Splay, **b)** Twist, and **c)** Bend.

return to the equilibrium state when the external force is then removed. The following Frank-Oseen free-energy equation (Equation 2.7) represents the elastic free-energy density.

$$f_d = \frac{1}{2}K_{11}(\nabla \cdot \boldsymbol{n})^2 + \frac{1}{2}K_{22}[\boldsymbol{n} \cdot (\nabla \times \boldsymbol{n})]^2 + \frac{1}{2}K_{33}\left|\boldsymbol{n} \times (\nabla \times \boldsymbol{n})\right|^2 \tag{2.7}$$

where $\boldsymbol{n} = (n_x, n_y, n_z)$ is the unit vector (director) parallel to the local optic axis, and K_{11}, K_{22}, K_{33} are the splay, twist and bend coefficients, respectively, which vary depending on the temperature and LC, and are typically in the range of 1 – 20 pN. Each of these terms represents an energy penalty for the presence of splay, twist and bend, and in most LCs the relative magnitudes of the elastic coefficients is observed to be $K_{33} > K_{11} > K_{22}$. The elastic constants co-determine the spatial and temporal response of the director to an applied external electric field. The single elastic constant approximation of the form $K_{11} = K_{22} = K_{33} = K$ is often used to describe the free energy due to elastic deformation in the simulations of nematic LC droplets. Equation 2.7 can be simplified by using one constant approximation. [28] [29] The elastic free energy density equation then becomes (Equation 2.8):

$$f_d = \frac{1}{2}K[(\nabla \cdot \boldsymbol{n})^2 + \left|(\nabla \times \boldsymbol{n})\right|^2] \tag{2.8}$$

As discussed in Section 2.4, a LC in the presence of an external electric field behaves in such a way so as to minimise the free energy by aligning relative to the direction of the electric field, depending upon the sign of the dielectric anisotropy. Equation 2.9 describes the overall free energy density taking into account an elastic deformation (in the one-constant approximation) and the presence of an electric field, and can be written as:

$$F = \frac{1}{2}K[(\nabla \cdot \boldsymbol{n})^2 + (\nabla \times \boldsymbol{n})]^2] - \frac{1}{2}\varepsilon_0 \Delta\varepsilon(\boldsymbol{n} \cdot \boldsymbol{E})^2 \tag{2.9}$$

2.7 LC Director Modelling in COMSOL

In Chapter 4, the alignment of the LC director in spherical capped droplets printed onto glass substrates with a homeotropic alignment layer is discussed. These droplets, which are later subjected to electric fields, are investigated by observing the change in the LC director orientation on a polarising optical microscope (POM). To understand the experimentally observed results, both in terms of LC director alignment and reorientation in the presence of an electric field, a commercially available finite element modelling (FEM) software package called COMSOL Multiphysics® was used to perform simulations of the LC director. The method used to perform the modelling is described in detail in Section 4.3.4. This section, however, is intended to provide an overview of how the Frank-Oseen free energy density formulation, including the external electric field coupling (Equation 2.9), is adapted so that the LC director alignment can be simulated using COMSOL. The method employed for formalising the free-energy density equation so that it could be used as an input for COMSOL where simulation approach was followed from a DPhil thesis [30].

The equilibrium configuration of the director of the nematic LC director $\boldsymbol{n}$ can be made by minimising the free energy density with n_x, n_y, and n_z components of the director $\boldsymbol{n}$ in Cartesian coordinates. This can be performed by applying the Euler-Lagrange equation, which states that a function of the form $F(y, \frac{\partial y}{\partial x_i}, \partial x_i)$, can be minimised by (Equation 2.10).

$$\frac{\partial F}{\partial y} - \frac{\partial}{\partial x_i}\left(\frac{\partial F}{\partial\left(\frac{\partial y}{\partial x_i}\right)}\right) = 0 \tag{2.10}$$

Therefore, minimisation of the free energy density is performed by substituting distortion free energy density equation 2.9 into equation 2.10. After applying the Euler-Lagrange equation, we obtain three equations one each for n_x, n_y, and n_z components of

the director. As an example, minimising for the n_x component gives (Equation 2.11):

$$\frac{\partial F}{\partial n_x} - \frac{\partial}{\partial x}\left(\frac{\partial F}{\partial\left(\frac{\partial n_x}{\partial x}\right)}\right) - \frac{\partial}{\partial y}\left(\frac{\partial F}{\partial\left(\frac{\partial n_x}{\partial y}\right)}\right) - \frac{\partial}{\partial z}\left(\frac{\partial F}{\partial\left(\frac{\partial n_x}{\partial z}\right)}\right) = 0 \tag{2.11}$$

By substituting equation 2.9 into equation 2.11 and then equating to a viscous dissipation term (where the viscous dissipation represents the rate of energy loss during LC reorientation caused by viscosity), we get (Equation 2.12):

$$K\left(-\frac{\partial n_x^2}{\partial x^2} - \frac{\partial n_x^2}{\partial y^2} - \frac{\partial n_x^2}{\partial z^2}\right) - \Delta\varepsilon\varepsilon_0 n_x E_x^2 = -\gamma\frac{\partial n_x}{\partial t} \tag{2.12}$$

where γ is the rotational viscosity of the LC. It can be seen that the equation has been converted to a time-dependent partial differential equation (PDE) for the n_x component of LC director, $\boldsymbol{n}$. By using the Laplace Operator of the form $\nabla^2 = \left(\frac{\partial^2}{\partial x^2} + \frac{\partial^2}{\partial y^2} + \frac{\partial^2}{\partial z^2}\right)$, we can then write for all three n_x, n_y, and n_z components the following:

$$K\left(-\nabla^2 n_x\right) - \underbrace{\Delta\varepsilon\varepsilon_0 n_x E_x^2}_{f_x} = -\gamma\frac{\partial n_x}{\partial t} \tag{2.13}$$

$$K\left(-\nabla^2 n_y\right) - \underbrace{\Delta\varepsilon\varepsilon_0 n_y E_y^2}_{f_y} = -\gamma\frac{\partial n_y}{\partial t} \tag{2.14}$$

$$K\left(-\nabla^2 n_z\right) - \underbrace{\Delta\varepsilon\varepsilon_0 n_z E_z^2}_{f_z} = -\gamma\frac{\partial n_z}{\partial t} \tag{2.15}$$

COMSOL software provides different modules to simulate real-world problems, and every module uses partial differential equation (PDEs) as a tool to mathematically model physical systems. COMSOL does not explicitly have any module that can directly support LC director modelling. However, the COMSOL software does provide the freedom to specify a model in the form of PDEs by using a maths module termed coefficient form PDE, which for one dependent variable $\boldsymbol{u}$ given as:

$$e_a\frac{\partial^2 \boldsymbol{u}}{\partial t^2} + d_a\frac{\partial \boldsymbol{u}}{\partial t} + \nabla\cdot(-c\nabla\boldsymbol{u} - \alpha\boldsymbol{u} + \gamma) + \beta\cdot\nabla\boldsymbol{u} + a\boldsymbol{u} = \boldsymbol{f} \tag{2.16}$$

where $\boldsymbol{u}$ can be a scalar or vector quantity that can describe a system consisting of a single PDE or a number of coupled PDEs. (Note the fonts used in equation 2.16 are consistent with those used by COMSOL.) The coefficients $e_a, d_a, c, , \gamma, \beta, a$ and $\boldsymbol{f}$ can take the form of tensors and source terms. The term $\nabla \boldsymbol{u}$ is equivalent to taking the tensor product $\nabla \times \boldsymbol{u}$. By setting the coefficients $e_a = \alpha = \gamma = \beta = 0$, and replacing $\boldsymbol{u}$ with $\boldsymbol{n}$, and c with K (one constant elastic approximation), and $d_a = \gamma$ (which is the rotational viscosity), equation 2.16 can be written as

$$\left(-K\nabla^2 \boldsymbol{n})\right) - \boldsymbol{f} + a\boldsymbol{n} = -\gamma \frac{\partial \boldsymbol{n}}{\partial t} \tag{2.17}$$

Equation 2.17 includes the n_x, n_y, and n_z components of the LC director $\boldsymbol{n}$, which are shown in equations 2.13 – 2.15. In equation 2.17, K and γ are 3×3 identity matrices, and $\boldsymbol{f}$ is the source term which describes the dielectric torque. The source terms of n_x, n_y, and n_z components for the LC director $\boldsymbol{n}$ are labelled with f_x, f_y, and f_z below the braces in equation 2.13 – 2.15. The fundamental requirement for energy minimisation is that |$\boldsymbol{n}$|=1 or in other words $({n_x}^2 + {n_y}^2 + {n_z}^2)$= 1. We therefore add another term and replace a with $100({n_x}^2 + {n_y}^2 + {n_z}^2 - 1)$, a 3 × 3 non-zero diagonal matrix, with all other elements equal to zero.

2.8 Jones Matrices

Jones matrices were separately used to model light propagation through printed nematic LC droplets, which were carried out using COMSOL simulations. The method adopted to perform this step is discussed in more detail in Section 4.3.4 of Chapter 4. This section provides a brief introduction to Jones matrices.

In 1941 R. Clark Jones developed a mathematical treatment to describe the change in the polarisation state of light caused by optical materials, which is commonly referred to as the Jones matrix method. [31] In this technique, the input light is represented by a 2×1 column matrix with two elements corresponding to the orthogonal components of the electric field of the light. This is termed as the Jones vector, which only describes the polarisation state of completely polarised light.

In the Jones method, an optical material or optical components such as polarizers and waveplates are represented as 2×2 matrices, which, when multiplied by a Jones vector, will result in an output vector that describes the polarization state of transmitted light. The Jones matrix method provides the freedom to perform a sequence of polarization transformations for more than one optical component by simply multiplying the Jones matrices together in the correct order. For example, for polarised light, $\boldsymbol{E_{in}}$, passing through four optical components in the order $\boldsymbol{M_1}$, followed by $\boldsymbol{M_2}$, $\boldsymbol{M_3}$, and $\boldsymbol{M_4}$, then the resultant Jones vector $\boldsymbol{E_{out}}$ is given by (Equation 2.18)

$$\boldsymbol{E_{out}} = \boldsymbol{M_4}\,\boldsymbol{M_3}\,\boldsymbol{M_2}\,\boldsymbol{M_1}\,\boldsymbol{E_{in}} \tag{2.18}$$

2.9 Droplet Visualisation Tools

Throughout this thesis, there is considerable use of a high-speed camera and a polarising optical microscope to visualise the in-flight dynamics of droplets and to observe the microstructure properties when printed on a substrate, respectively. The following sections provide a brief introduction to each imaging tool.

2.9.1 High-speed camera

A high-speed camera in shadowgraph configuration was used as an imaging technique to visualise droplet formation as well as droplet flight and impact, both in inkjet and electrohydrodynamic printing experiments. For this, a high-speed camera (Phantom V12.1 Vision research) with a 12× zoom lens (from NAVITAR) and a 150 W halogen light source (from Thorlabs) was used, as shown schematically in Figure 2.6. The light source was coupled to an optical fibre with a collimating lens attachment and was positioned behind the printing nozzle in a back-light configuration. The camera was connected to a desktop computer via an Ethernet cable. Parameters such as image resolution, frame rate, exposure time, and trigger settings were controlled with the Phantom Camera Control (PCC) software. The camera was able to record a dynamic event in the form of a cine file, which is a raw digital video file that can be post-processed and can be converted to a variety of standard video and image formats as required.

The cine files were calibrated using a graticule scale with which we could measure drop filament lengths and diameters. The camera can store from 6,242 to 1,000,000 frames per second with image resolutions in the range of 1280×800 – 120×8. However, a higher frame rate compromises the image resolution. In this research, most images were captured at 20,000 fps at an image resolution of 512×512 by manually triggering the

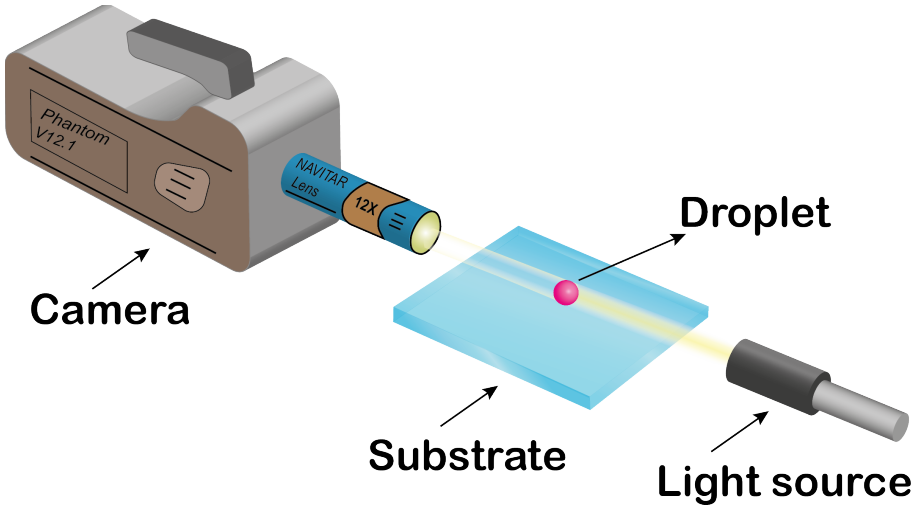

Figure 2.6: Schematic illustration showing arrange of high-speed camera and halogen light source used to capture in-flight motion of droplets in inkjet and EHD printing experiments.

camera to capture images. The high-speed camera was also used to measure the contact angles of the printed droplets. This was done by using a calibrated side profile image of the printed droplets. The side profile images were then analysed using ImageJ® software and the contact angles were calculated.

2.9.2 Polarised Optical Microscopy

Polarising optical microscopy was carried out using an Olympus BX51 microscope. The schematic illustration in Figure 2.7 shows the basic arrangement of the optical components. Microscopy was performed in a transmission mode whereby the illumination was provided by a halogen bulb. Light from the bulb first passes through a condenser lens (not shown in the diagram) and directed onto the specimen through an axially centric rotating stage. The objective lens with a certain magnification and numerical aperture collects the light and passes it to the eyepieces and/or a imaging camera. To perform polarised optical microscopy (POM), two linear polarisers were placed in such a configuration that their optical axes were orthogonal to each other. A 6.0 megapixel CCD camera (Retiga

R6) attached to the microscope was able to capture high-resolution images of the printed samples. The camera was further connected to a desktop computer via a universal serial bus cable. Parameters such as image resolution, image capturing, and exposure time were controlled by the Oculus software that was supplied with the camera.

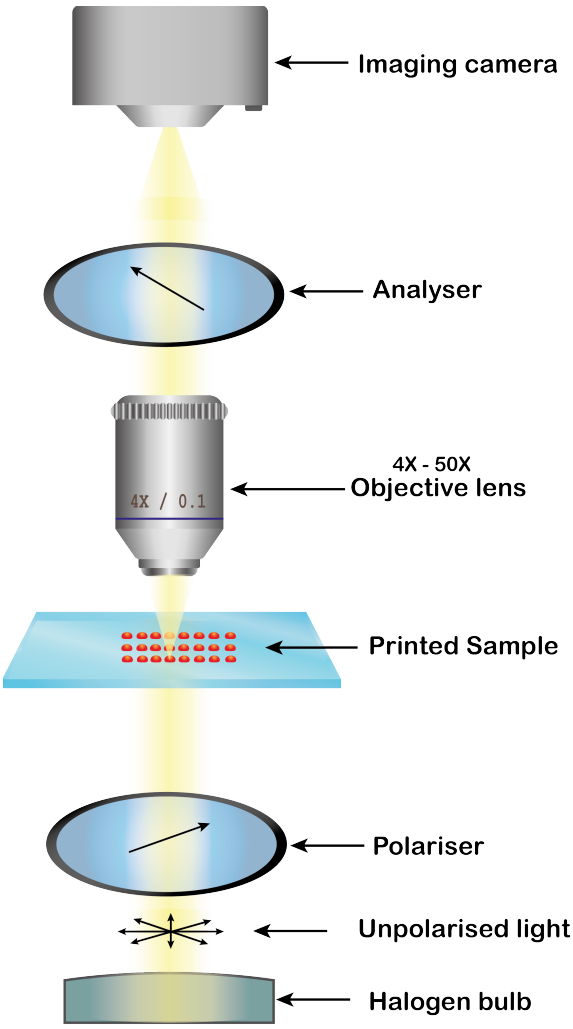

Figure 2.7: Schematic diagram of the polarising optical microscope used to image printed droplets.

In summary, this chapter provides general background on liquid crystalline materials relevant to the studies provided in this thesis. The physical properties of LC phases were briefly introduced. The chapter is followed by an introduction to the optical and electro-optic characteristics of the thermotropic nematic LC and different types of alignment, such as planar and homeotropic. The chapter then detailed how LC free energy

density equations were tailored and used to perform LC director simulation in COMSOL multiphysics software. Finally, the chapter discusses the droplet imaging tools and schematically outlines the arrangement in which they were being used.

CHAPTER 3

FUNDAMENTALS OF PRINTING NEMATIC LIQUID CRYSTALS

This chapter provides the relevant background on inkjet printing that is required to understand the work presented in this thesis. This also includes a review of the previous work on printing liquid crystals (LCs), which is then followed by a presentation of the experimental systems that have been used to obtain the experimental results contained in Chapter 3, Chapter 4, and Chapter 5. The presented systems are highly versatile, making them ideal for investigating the printing conditions of a range of LC inks. The chapter then presents an analysis of the droplet generation of the nematic LC, E7, from a piezoelectric drop-on-demand inkjet nozzle for a range of different experimental conditions. The procedures described herein serve as the basis for printing the new LC formulation that is employed in Chapter 5 of this thesis.

3.1 Introduction

Inkjet printing has been associated historically with the printing of text and graphics, but has, more recently, been viewed as an important advanced manufacturing technology. Fundamentally, it is a non-contact technique used to deposit functional fluids with precise droplet size and position control. [32] The unparalleled efficiency of the technique and the ability to accurately position pico-litre volumes of a wide range of fluids on various substrates has been of particular benefit in the manufacturing of printed ceramics, displays, printed electronics, sensors, tissue engineering and three dimensional micro optical components and thin films. [1,3,33–38] The enormous interest in this printing technique stems from the low cost, high flexibility, and scalable manufacturing.

There are two different types of inkjet printing methods depending upon the drop actuation technique, which includes continuous inkjet (CIJ) and drop-on-demand (DoD) inkjet printing. Briefly, the CIJ technique generates a continuous stream of droplets that are selectively steered and positioned onto a substrate using electrically-charged electrodes and deflection plates. The CIJ systems ejects droplets with drop generation frequencies between 20 - 60 kHz. The droplets generated are usually around twice the size in diameter of the printing orifice. [4, 39, 40]

On the contrary, the DoD technique utilises pressure impulses generated within a functional ink due to a pulse generator inside the printhead that is able to cause droplet ejection at the nozzle orifice. The drop feature size approximates the nozzle orifice diameter therefore droplets of around 30 µm diameter can be achieved. [4, 41] The pressure impulse within the functional ink can be generated using a number of techniques, each one offering distinct benefits. Among those, the piezoelectric technique is the most convenient due to the high degree of control over design of the driving waveform and thus the resulting pressure wave, which enables precise control of the droplet volume and velocity. Moreover, the piezoelectric inkjet technique covers a vast library of materials and the advancement of the piezoelectric elements to include a heating element enables the printhead temperature to be raised to reduce the viscosity of the ink. [7, 42]

3.2 Printing of Liquid Crystals for Photonic Devices

The ability of LCs to flow like a fluid makes them compatible with wet processing techniques such as inkjet printing. This physical property has motivated researchers to find ways to dispense LCs on a range of different substrates for the manufacturing of printed photonics devices. Existing reports on the subject can be divided into four main categories: (i) printing of alignment layers for LC devices; (ii) fabrication of micro-optical components; (iii) patterning of photonic structures to form optical sensors; and (iv) the rapid production of LC formulations.

It is well known that the LC director orients depending upon the boundary conditions, e.g., homeotropic or planar alignment (see Section 2.3, Chapter 2). Hwang et al. [43] reported the use of inkjet printing to generate surface alignment layers to align the LC director for the development of a large-area LC display. The authors printed a thin film of polyimide (PI) and baked it in a thermal oven. After baking, the PI film was air-buffed with an empty inkjet cartridge with a strong stream of air. The air-buffing process induced surface anisotropy in the form of nano-grooves on the printed PI film that resulted in planar alignment of the LC director.

In a different approach reported by Parry et al. [44], nematic LC droplets were printed onto partially wet films of Polyvinyl alcohol (PVA) which generated uniform LC director alignment in the LC droplet. The technique was further extended to include nematic LC printing on substrates coated with homeotropic alignment layers. The printed droplets (of variable sizes) behaved as microlenses and it was possible to tune the focal length by heating and cooling the lenses. [7] Similarly, the manufacturing of printed LC laser arrays was demonstrated by Gardiner et al. [45] at the University of Cambridge. The authors demonstrated inkjet printing of dye-doped chiral nematic LC (CLC) onto wet films of PVA to form uniform sessile droplets with the helical axis of the CLC orthogonal to the substrate. These inkjet-deposited droplets were found to exhibit laser emission when optically excited with a pulsed solid-state laser source.

Chiral nematic LCs have also been used for the printing of passive optical sensing devices. For example, the work reported by Schenning et al. [46] demonstrated a battery-free humidity sensor through inkjet printing of hydrogen-bonded chiral nematic LC polymer films to form a square pattern. The optical sensor showed red-shift in the reflection band when exposed to water vapour. In another type of sensor, printed films of a chiral nematic polymer were mechanically embossed between transparent sheets where it was demonstrated that an optically irreversible temperature sensor could be fabricated. [47]

A typical LC formulation consists of a mixture of components, and an exact composition provides the desired properties for a specific type of LC display. To circumvent the laborious material design process, Cull et al. [48] reported the use of inkjet printing to print and mix precise volumes of LC components for the development of a large library of LC formulations.

The research mentioned above on the printing of LCs has provided important demonstrations of the power of this manufacturing technique. As LCs are non-Newtonian (shearing LCs tends to align the director and can reduce the consequent viscosity), it is important to understand the processes involved in printing these materials in order to identify the optimum deposition conditions required to develop next-generation optical devices and advanced functional thin-films. In addition, a range of LC phases and composites could be considered so as to demonstrate more active and functional inkjet-printed devices instead of many of the passive devices that has tended to be the focus in the literature. This thesis further develops the understanding of the printing conditions of LC inks and presents enhanced photonic devices that have been enabled by inkjet printing. Finally, the thesis also demonstrates an alternative drop-on-demand printing that enables the deposition of even smaller LC droplet volumes.

3.3 Inkjet Printing Systems

The printing of LCs and polymer composites that is described in this thesis was conducted using two inkjet printing systems, which are termed as (i) a bespoke inkjet printing system, and (ii) a MicroFab Jetlab-II. The conditions to print a LC, as described later in

this chapter, was investigated using a DoD inkjet printing setup that was developed by a previous DPhil student. [49] This setup was purposely built to dispense LCs and has been used extensively for the printing of thermally-tunable microlens arrays [7] and the demonstration of uniform LC director alignment in a printed nematic LC droplet. [44] The work described in Chapter 4, and Chapter 5 used this system to perform preliminary printing trials of each new LC formulation so as to determine the printing conditions for these inks. Once the conditions had been established (e.g., drive waveform, temperature), these LC ink formulations were then printed using the MicroFab printer to create novel optical devices.

3.3.1 Bespoke inkjet system

A photograph of the bespoke inkjet printing setup is shown in Figure 3.1 and a schematic is presented in Figure 3.2. The setup consists of a static pressure pump to feed the print-head fitted with the MJ-ABP-01-80 dispenser (MicroFab dispenser with an 80 µm diameter nozzle), a high speed camera to capture images of droplets from the dispenser, a JetDrive-II (waveform generator) to actuate the dispenser, and a temperature controllable print-head and substrate without any feedback. The ink to the MicroFab dispenser is delivered via barb fitting and PTFE tubing. The substrate is mounted on an XY motorised stage with a bracket that supports a glass slide onto which droplets can be deposited. A National instruments DAQ card, driven by a LabVIEW program, triggers a signal to the JetDrive-II, waveform generator, the temperature unit and the stage during the printing process. The high-speed camera with a separate halogen lamp light source works in a Shadowgraphy configuration to capture droplet images (see Section 2.9.1).

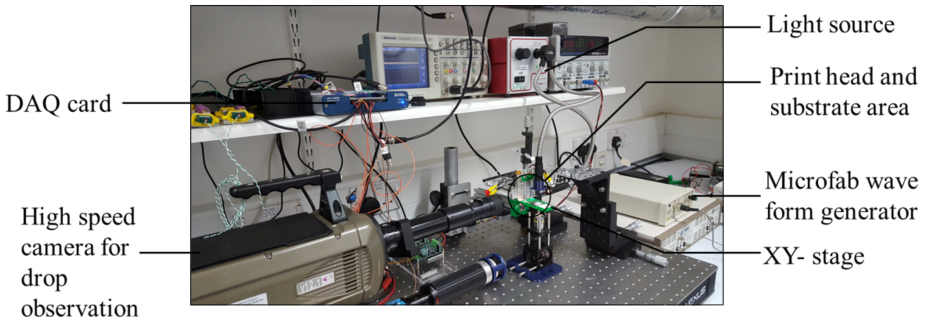

Figure 3.1: Photograph of the bespoke inkjet printing assembly used in this thesis.

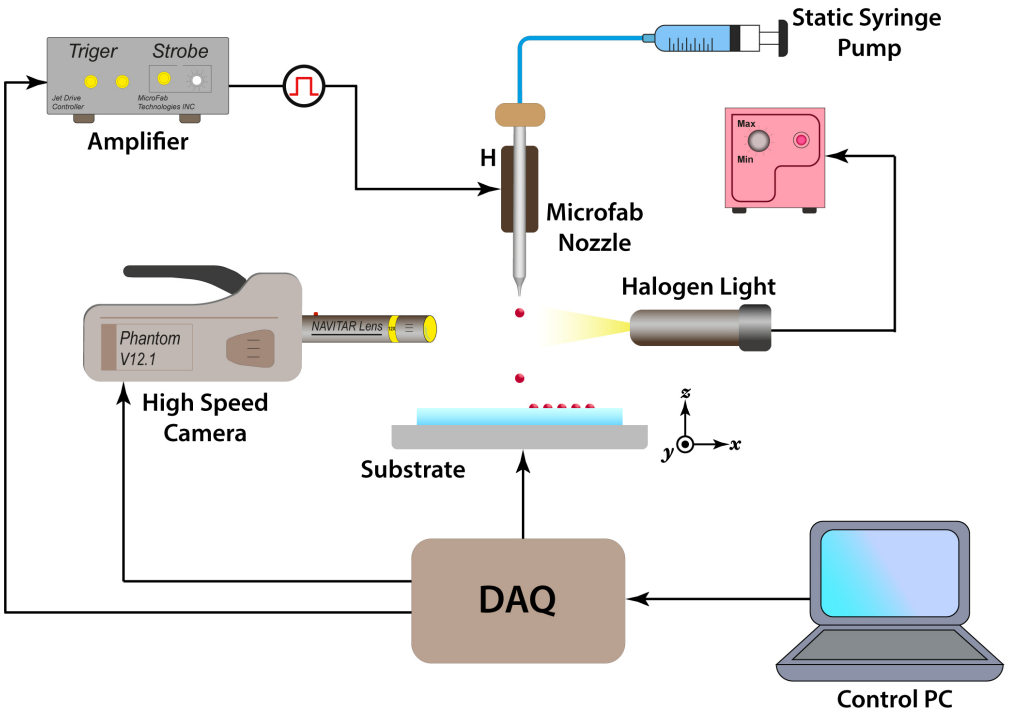

Figure 3.2: Schematic diagram of the DoD printing system used in this thesis. The amplifier corresponds to the JetDrive-II and 'H' corresponds to the heating element.

3.3.2 MicroFab Jetlab-II printer

In addition to the bespoke printing system, a commercially available bench-top printing station, Jetlab-II from MicroFab technologies-USA, was used to print arrays of LC droplets to form the basis of new optical devices. A photograph of the Jetlab-II is shown in Figure 3.3. The overall configuration and, in particular, the drop generation principle is the same for both systems used in this thesis. The fundamental difference lies in the capability of the Jetlab-II in depositing small volumes of fluids with high positional accuracy and repeatability. This entire printing system is designed to deposit multiple inks at the same time. The system can print over a 200 $\times$ 200 mm^2 area with 100 mm/s substrate speed.

The system is equipped with a PH-46 printhead that can support four independent fluid reservoirs each one can store up to ml of fluid. The printhead supports four dispensing nozzles of type MJ-ATP-01 and they are connected to a fluid reservoir through PTFE fittings and tubing. Each fluid channel has a pneumatic control that allows for positive and negative pressure to control the nozzle meniscus level for optimal jetting.

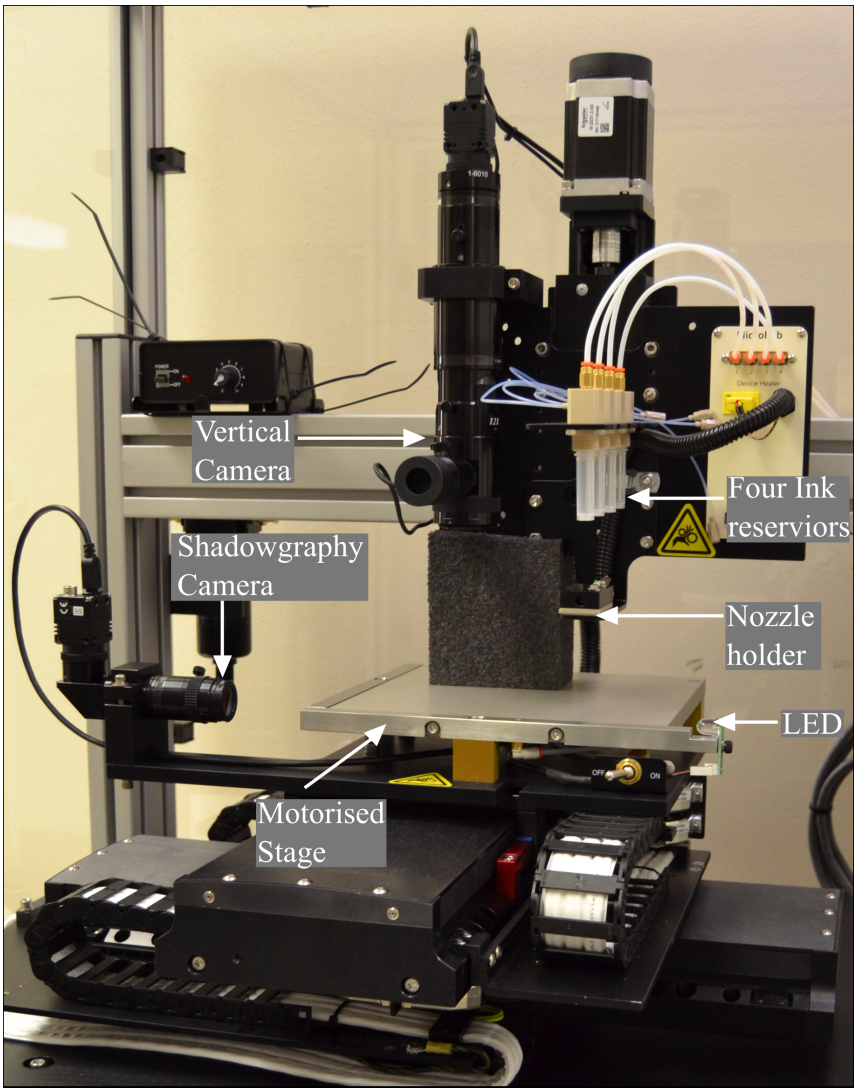

Figure 3.3: A photograph of the MicroFab Jetlab-II printer used to print liquid crystal arrays for the fabrication of optical devices in this thesis. The vertical camera is for drop inspection after the printing process whereas the shadowgraphy camera is used to monitor and adjust print parameters for printing.

Figure 3.4 shows a CAD design of the MJ-AT series MicroFab nozzle. The printhead assembly is equipped with a heater to maintain the desired temperature. The Jetlab-II is connected to a JetDrive-II to control the generation of the waveform and tailor the jetting parameters to the printhead. The Jetlab-II system also comprises a software-controlled positioning stage, drop observation and drop inspection cameras, and a computer-controlled pneumatics system.

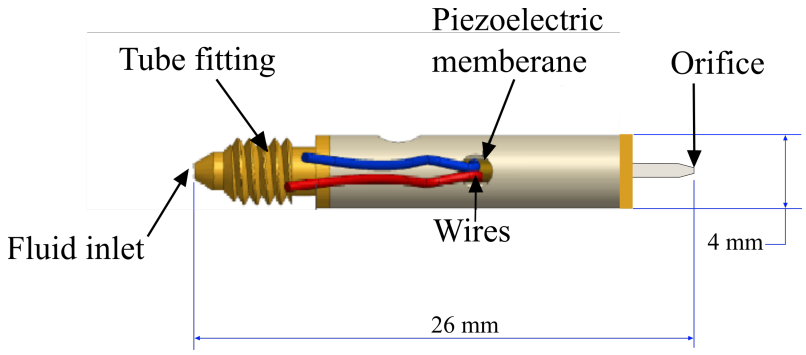

Figure 3.4: CAD design of a MJ-AT series MicroFab nozzle.

The Jetlab-II has the ability to print droplets and arrays of droplets by dispensing fluids with a 5 µm drop positional accuracy. The four separate dispensers can operate at the same time to dispense multiple inks on the substrate in a desired pattern. Patterns can be generated from a black and white bitmap image. Each pixel represents the droplet spacing, with a white pixel indicating where the printer should jet a droplet and black pixels being areas where no droplet should be deposited. Scripts can also be written to control the jetting device so as to deposited isolated droplets to form arrays or patterns.

3.4 Drop Actuation and Formation

In a typical DoD inkjet system, the drop formation depends solely upon the acoustic pressure impulses that arise in the printhead chamber due to contraction and expansion of the piezoelectric element. [50] According to acoustic pressure wave theory, the nozzle orifice of the dispenser can be considered as a closed ended boundary condition since the nozzle orifice is a small opening when compared to the cross-sectional area of the tube. [50–52] In contrast, the supply end of the dispenser is significantly large in comparison to the nozzle orifice, and therefore it can be considered as an open-ended boundary condition. [51] As a result, a pressure wave that propagates in the dispenser chamber maintains its phase when it reflects from the nozzle orifice (closed end), and the second pressure wave experiences a π-phase shift when it reflects from the supply end (open end). This process together with an example actuation waveform is illustrated in Figure 3.5. Typically, a unipolar trapezoid waveform, with a predefined amplitude, rise-time t_{rise}, dwell-time, t_{dwell}, and fall-time t_{fall}, is used to drive the piezoelectric transducer (PZT) membrane in order to generate the pressure waves as described in the literature. [53] The waveform

is schematically illustrated in Figure 3.5(b) and this kind of waveform is employed, in almost all cases, throughout this thesis.

a) Pressure wave propagation

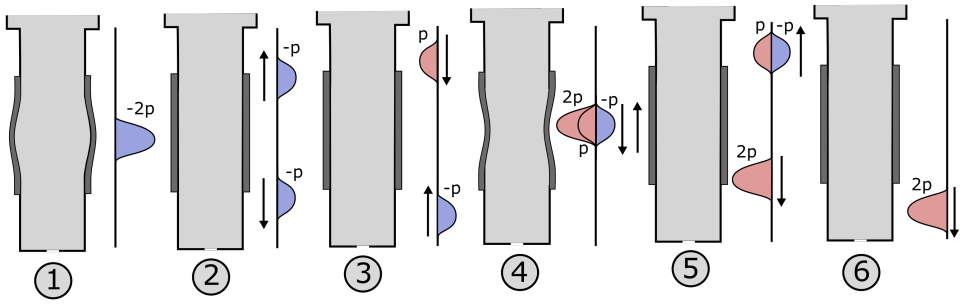

b) Actuation waveform

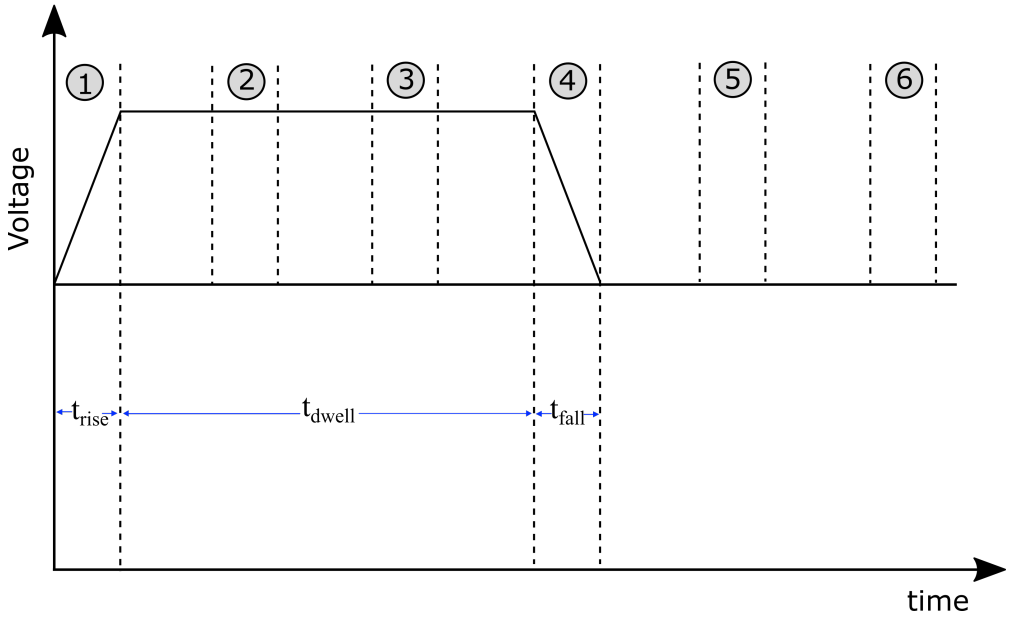

Figure 3.5: b) Illustration of both expansion and contraction of the printhead chamber (to enable the jetting of a single droplet). **b)** The diagram shows the optimum actuation waveform in relation to the associated expansion and contraction of the printhead chamber.

Figure 3.6 presents high-speed camera images of a nematic LC droplet being generated from the bespoke inkjet printing system under optimum conditions as described later in this chapter. The system was driven with a unipolar trapezoid waveform whose graphical illustration is shown in Figure 3.5(b). The waveform was held at constant rise and fall of $t_{rise} = t_{fall} = 3$ µs, and a dwell time of $t_{dwell} = 15$ µs, and with an amplitude of 53 V. The series of frames shows the fluid jet initiation.

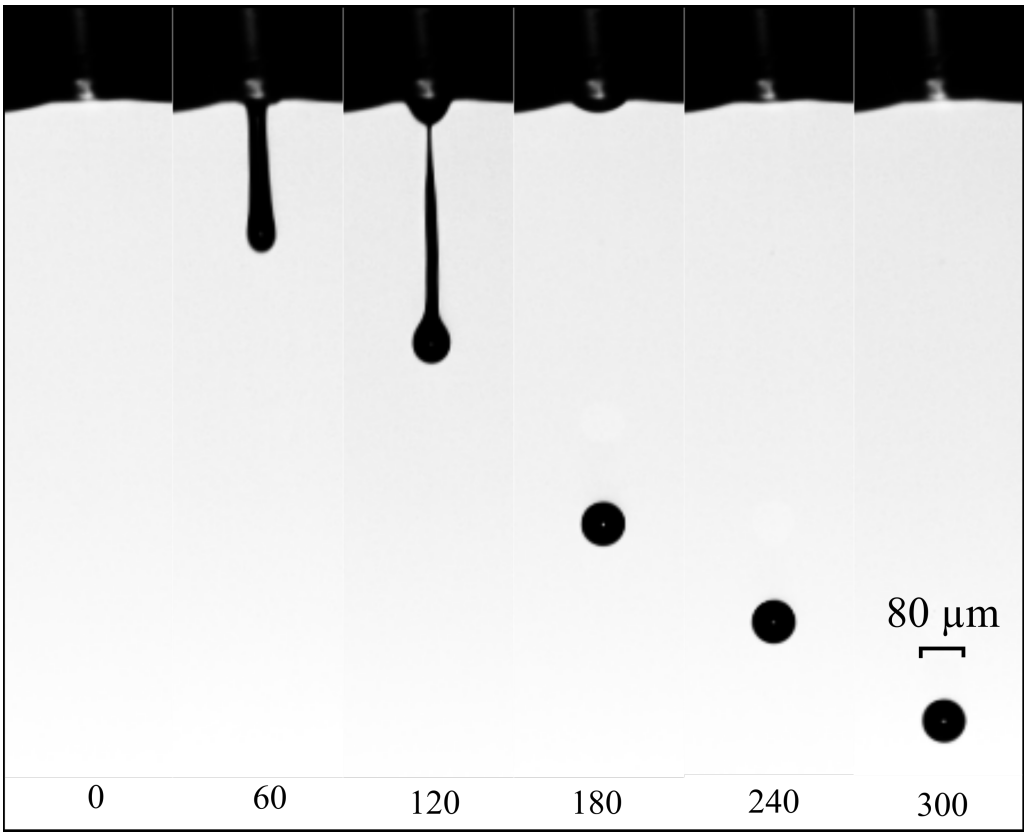

Figure 3.6: Shadowgraphy images captured of printing a nematic LC (E7) using the type of waveform shown in Figure 3.5(b). A 80 µm MicroFab nozzle was used and heated to a temperature of 60 °C. The numbers in black at the bottom of each camera frame correspond to the frame time in units of microseconds (µs).

It can be seen that the pressure pulse ejects the fluid through the nozzle orifice between the elapsed time of 0 – 60 µs. From 60 µs to 120 µs the tail of the filament near the tip continuously stretches out to form a long fluid filament with a round head and tail. The tail of the filament eventually minimizes the surface area in contact with nozzle before separating to form a single spherical droplet between 120 – 180 µs. The resultant inflight droplet is circular with a drop diameter of 80 µm.

3.5 Inkjet Printing of a Nematic LC

Fundamental to the successful development of printed LC technologies is the need to deposit the LC in a programmable and repeatable way so as to form stable and uniform droplets of different configurations and director profiles. Nematic LCs, for example, are

non-Newtonian fluids and the anisotropy in the flow properties can greatly affect the formation of stable droplets (i.e., ones without jet break-up or the formation of satellite droplets). Understanding the nature of the formation of acoustic pressure waves in the context of LC printing and how this influences the jet formation, pinch-off and break-up of the fluid is of importance in the generation of stable jetting. Therefore, the remainder of this chapter presents a detailed investigation of the printing regime for the nematic LC mixture, E7, and the conditions required to consistently dispense single droplets without the formation of satellite droplets or multiple filament break-up. Also, the procedure described in this chapter serves as an important basis for the printing of new LC and/or LC-polymer formulations, see for example Chapter 5.

3.5.1 Defining printability

Drop formation and ejection characteristics for piezoelectric-driven DoD inkjet printing systems greatly depend upon the design parameters of the inkjet dispenser (e.g., the cavity length and diameter) and the properties of the ink formulation (i.e., viscosity and surface tension). Dimensional analysis provides valuable insight in terms of understanding and predicting the fluid mechanics associated with the drop generation process. The following set of dimensionless numbers are typically employed to model an inkjet printing system: the Reynolds number, Re, which is the ratio of inertial to viscous forces; the Weber number, We, a ratio of inertial to surface tension forces; and the Ohnesorge number, Oh, the ratio between the Reynolds number and the square root of the Weber number, which describes the balance between viscous to surface tension forces. [54–56] These dimensionless numbers can be written explicitly as

$$Re = \frac{\rho U L}{\mu} \tag{3.1}$$

$$We = \frac{\rho U^2 L}{\eta} \tag{3.2}$$

$$Oh = \frac{\sqrt{We}}{Re} = \frac{\mu}{\sqrt{\eta \rho L}} \tag{3.3}$$

$$Z = Oh^{-1} = \frac{Re}{\sqrt{We}} \tag{3.4}$$

where ρ is the density of the fluid, U is the velocity, μ is the dynamic viscosity, η is the surface tension and L is a characteristic length scale, which is usually the diameter of the nozzle or the drop diameter. Based upon the work of Fromm, researchers have described the printable regimes using a dimensional analysis technique. As an example, Fromm employed the Oh parameter to characterise regimes specific to inkjet printing. In their work, the parameter $Oh = 1/Z$ was introduced whereby small values of Oh correspond to the case when the primary drop is accompanied by a number of satellite droplets whereas large values of Oh represent the case when viscous forces dominate that can lead to the prevention of drop ejection. [57] Various studies have been carried out for a range of fluids, such as ethanol, diluted polymers, and particulate suspensions, in an attempt to identify the range of Z for which stable drop formation is found to occur. [58–62] Among these studies, Derby et al. [54] have provided a range for Z of $1 < Z < 10$ ($0.1 < Oh < 1$) in the form of a printability map, which is consistent across a range of different inks, albeit with some discrepancies such as the demonstration of successful DoD inkjet printing for $Z >> 10$. [63–65]

Due to inconsistencies reported in the Z (Oh^{-1}) value (e.g., ink printability at large Z values), Liu and Derby [62] recently defined a new parameter space for Newtonian fluids using the dimensionless parameters Z and We_j, where We_j is related to the velocity of the fluid prior to drop formation (here the velocity U in equation 3.2 represents the jet velocity and We_j is therefore referred to as the fluid jet Weber number). The authors have proposed that We_j should be fall the range of $2 < We_j < 25$ for when Z is in the range of Z = 2 – 20 (or in terms of Oh, Oh = 0.5 – 0.05).

Given their non-Newtonian viscoelastic properties it is likely that the range of values for Oh (Z^{-1}) might be somewhat different for liquid crystalline materials. Therefore, in this work an attempt is made to investigate and define a printable regime for nematic LCs using the Oh number in combination with both the Reynolds number and drop Weber number, We_d.

3.5.2 LC Rheological and Physical Properties

The dynamic viscosity of the nematic LC E7 was measured using a rheometer (Anton Parr Rheometer Physica MCR301) in a cone and plate configuration. The viscosity was calculated (shear rate of 300 1/s) at a temperature sweep from 10 to 70 °C with 5 °C increments. The measurements were repeated twice. The surface tension measurement was performed by using a bubble tensiometer (SITA instruments) which measures the maximum internal pressure of a gas bubble formed in a liquid by means of a capillary. The measurements were recorded for long surface-aged droplets (1 – 2 s) in order to allow the LC director to align homeotropically on the surface of the bubble. The density of the nematic LC was taken from the literature. [66]

To investigate the influence of the fluid parameters on LC printability, measurement of the LC rheological properties was performed in both the nematic and isotropic phases, and the relevant physical parameters and dimensionless constants are presented in Table 3.1. Using equation 3.3 the Oh values at a fixed characteristic length scale L of 80 µm are extracted. The table presents the Oh values, which greatly reduce with temperature. By changing the temperature, the surface tension and viscosity can be controlled. The anisotropic viscosity components of E7 follow a typical Arrhenius relationship: that is, increasing the temperature will bring about large reductions in viscosity compared to the surface tension. As can be seen in Table 3.1, at 20 °C Oh = 1.32 remains at values >1 until 50 °C. From 50 °C to 70 °C, on the otherhand, the Oh number reduces from unity to 0.55.

3.5.3 LC droplet formation

The droplet generation was experimentally investigated for the range of values of the Oh number presented in Table 3.1. For this experiment, the waveform was set to t_{rise} = 3 µs, t_{dwell} = 15 µs, t_{fall} = 3 µs, and a voltage amplitude of 53 V was employed. From 20 °C to 50 °C (corresponding to Oh = 1.32 to Oh = 1) the inkjet dispenser did not eject droplets when using this actuation waveform, even when the driving voltage amplitude was increased to 65 V and 70 V.

Table 3.1: Relevant fluid parameters for the nematic LC mixture, E7, at a range of temperatures (°C) considered in this study. Density values are cited from the literature. [66] Surface tension (η) and viscosity (μ) were measured as described in the text. The characteristic length scale L is equal to inner nozzle diameter which is equal to 80 µm (MicroFab nozzle).

Temperature	**Density**, ρ	**Viscosity**,μ	**Surface tension**,η	***Oh***
(°C)	$(\mathrm{kg \cdot cm^{-3}})$	$(\mathrm{mPa \cdot s})$	$(\mathrm{mN \cdot m^{-1}})$	(number)
20	1010	68.8	33.6	1.32
30	1010	63.3	32.6	1.2
40	1010	58.5	31.7	1.1
50	1010	50.2	30.6	1.0
55	1010	42.5	28.2	0.9
60	1000	33.5	27.1	0.71
65	990	27.3	26.4	0.6
70	990	25.3	26	0.55

Figure 3.7 shows high-speed images of the resulting fluid jet initiation and droplet formation for different values of the Oh number. Figure 3.7(a) corresponds to the first limiting case: at 50 °C it can be seen that the fluid jet started to initiate; however, due to the viscous dissipation no droplet was formed. On the other hand, as can be seen in Figure 3.7(b), when the temperature was set to 55 °C (corresponding to Oh = 0.9) droplet generation was observed. A similar drop generation scenario was observed for Oh = 0.71 and Oh = 0.6 (corresponding to temperatures of 60 °C and 65 °C) as shown in Figure 3.7(c) and Figure 3.7(d), respectively. However, raising the temperature of the printhead further for a fixed voltage amplitude led to the formation of long fluid filaments. As can be seen in the high-speed camera frames in Figure 3.7(e), long fluid filaments started to appear at 70 °C, which is the limiting case beyond which satellite drops were generated if the voltage amplitude was further increased.

Together with the high-speed camera frames shown in Figure 3.7, an attempt was made to propose a printable regime for the nematic LC E7 in terms of the Oh and Re numbers, which is shown in the form of dashed blue and red line, and turquoise coloured region superimposed on the graph in Figure 3.8. The dashed lines in blue and red correspond to the limits of the Oh number of 0.9 and 0.55 at 55 °C and 70 °C, respectively. The four green studs corresponds to the Re number values which were obtained at the range of driving voltages and these values are displayed in Table 3.2.

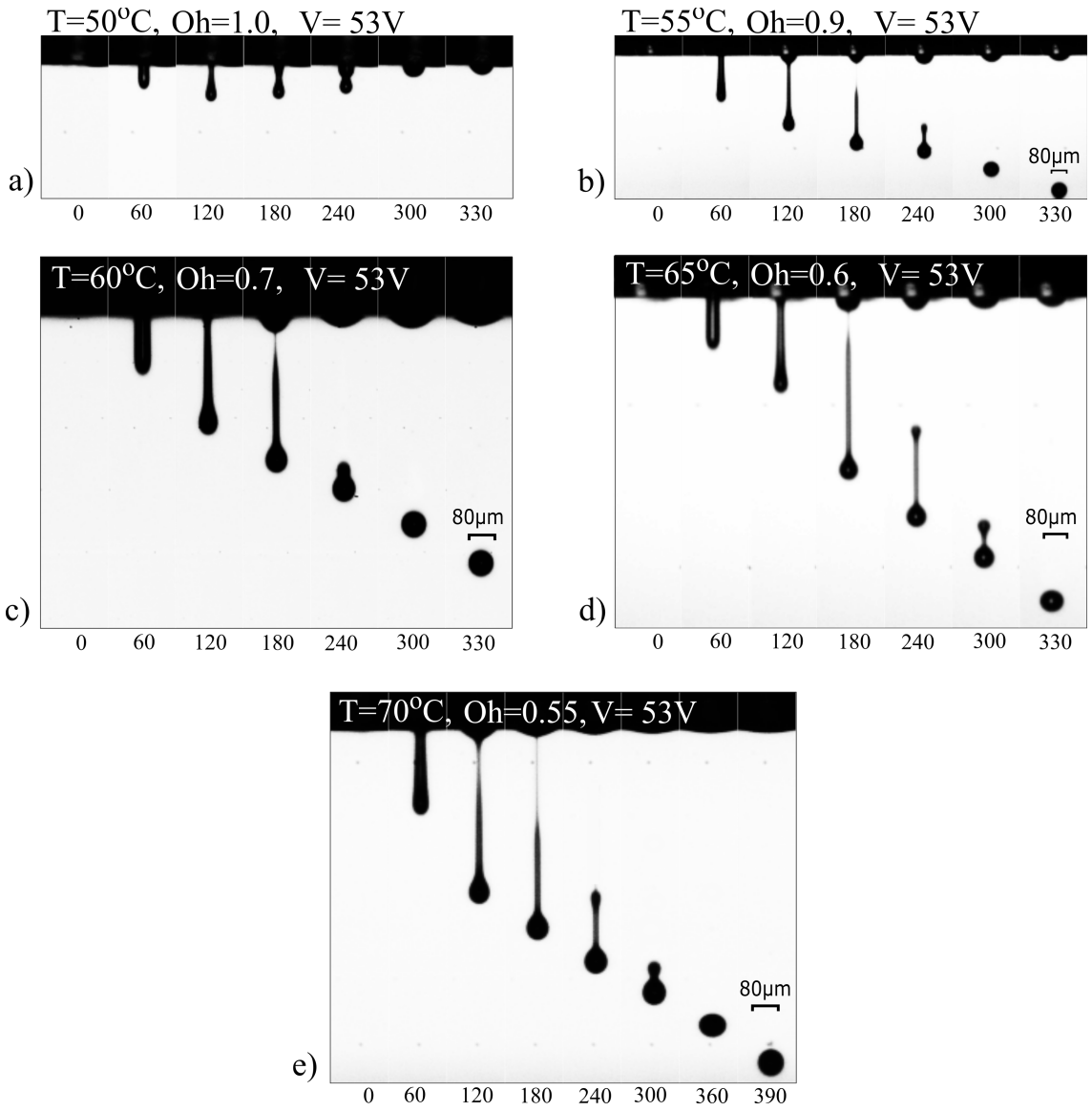

Figure 3.7: Sequence of high-speed images (captured using 16,831 fps) during the drop formation of the nematic LC E7 using a waveform with the properties t_{rise} = 3 µs, t_{dwell} = 15 µs, t_{fall} = 3 µs and dwell voltage amplitude of V = 53 V. The only parameter that was altered is the temperature, which in turn changes the Oh number. **a)** T = 50 °C **b)** T = 55 °C **c)** 60 °C **d)** 65 °C **e)** 70 °C. The numbers in black at the bottom of each camera frame corresponds to the frame time in units of microseconds (µs).

It should be made clear that the format of the graph shown in Figure 3.8 has already been reported in the literature and it is advised that the region between two diagonal lines and horizontal lines at 1 and 0.1 Oh (maximum and minimum Oh number) corresponds to a stable drop generation process. Above, below or on either side will lead to different drop generation scenarios such as insufficient energy to generate a drop, too much energy where the drop would start to splash, and the main droplet would be accompanied satellite droplets. For LC E7, I have attempted to define a printing regime in terms of dimension-

less numbers and superimposed it over the standardised printable chart as purposed by Derby et al. [54].

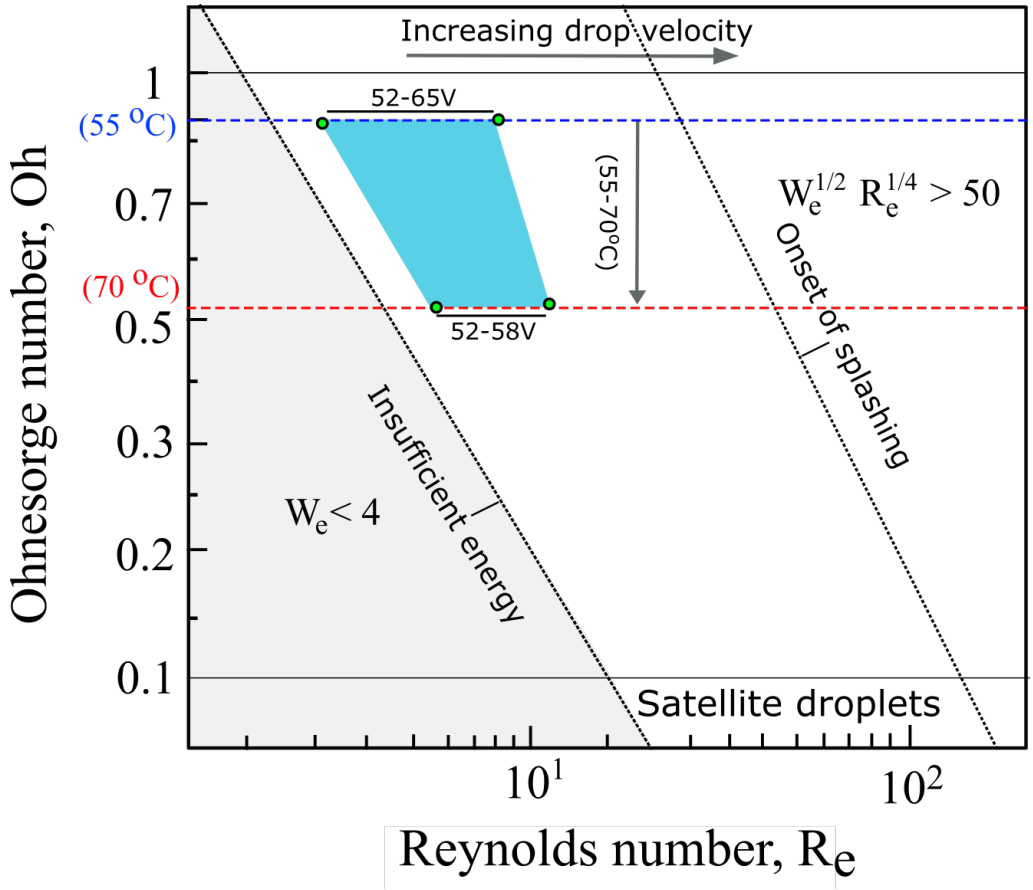

Figure 3.8: A schematic diagram showing the inkjet printing parameter space using the Ohnesorge (Oh) and Reynolds (Re) numbers. The region bounded between 1 and 0.1 with two black solid lines represents the standard printing regime range as suggested by Derby. [54] The lower and upper diagonal lines represents the kinetic energy of the droplet at which they are being ejected. The criterion for a drop to possess sufficient kinetic energy to be ejected from the nozzle is given by Derby as $We > 4$. Similarly, the criterion for onset of splashing following the impact is given as $We^{\frac{1}{2}}\ Re^{\frac{1}{4}} > 50$. The dotted lines in red and blue represents the LC Oh number of 0.9 and 0.55 at 55 °C and 70 °C temperature, respectively. The turquoise-coloured area shown in the figure represents the printable regime determined for the nematic LC E7 using an 80 µm MicroFab nozzle.

Table 3.2: Variation in the Reynolds number, Re, for changes in the dwell voltage amplitude, (V) and printhead temperature.

Temperature	**Voltage**	**Drop velocity**	**Reynolds number**
(°C)	(V)	(ms^{-1})	(Re)
55	52	1.6	3.0
55	65	4.4	8.3
70	52	2.4	7.5
70	58	3.7	11.5

The results reveal that for a fixed value of Oh of 0.9, stable droplet generation was only observed when the driving voltage amplitude was kept within the range of 52 V to 65 V. Similarly, for the minimum value of Oh = 0.55, stable droplet generation was only observed when the voltage amplitude remained within the range of 52 V to 58 V. At Oh = 0.55 above 58 V the drops formed in longer tail fluid filaments that started to form satellite droplets. It should be noted that these experimental cases were remained in the turquoise coloured region as highlighted in Figure 3.8. However a small variation in driving voltage amplitudes showed satellite droplet formation. With the aid of high-speed camera frames, the effect of varying the driving voltage amplitude at fixed Oh is further discussed in section 3.5.4.

3.5.4 Effect of Waveform Amplitude

To investigate the effect of a large driving force on the fluid jet formation and break-up when the Oh number was held constant, the following drive waveform t_{rise} = 3 µs, t_{dwell} = 15 µs and t_{fall} = 3 µs was applied to the printhead for various voltage amplitudes. Figure 3.9 shows a sequence of high-speed camera images of the fluid jet break-up when the Oh number is set to either Oh = 0.6 or Oh = 0.55. At fixed Oh = 0.6, it was observed that when the actuation voltage was smaller than 59 V the fluid jet was ejected with a smaller fluid ligament near the nozzle orifice and the resulting tail retracted itself into the main drop within 100 - 120 µs due to surface tension. Consequently, this resulted in stable droplet formation as shown previously in Figure 3.7(d). However, as shown in Figure 3.9(a–c) when the actuation voltage amplitude was varied between 60 - 65 V for a constant Oh = 0.6, longer fluid ligaments started to appear along with the main droplet. At V = 65 V, the fluid ligament pinches off from a point and separates to become another droplet, which later combines with the main droplet at t = 210 µs. When Oh = 0.55, the threshold voltage recorded for the formation of a smaller fluid ligament was 58 V. However, as shown in Figure 3.9(d), for voltage amplitudes between 59 - 61 V longer fluid ligaments were observed which retract back into the main droplet before hitting the substrate.

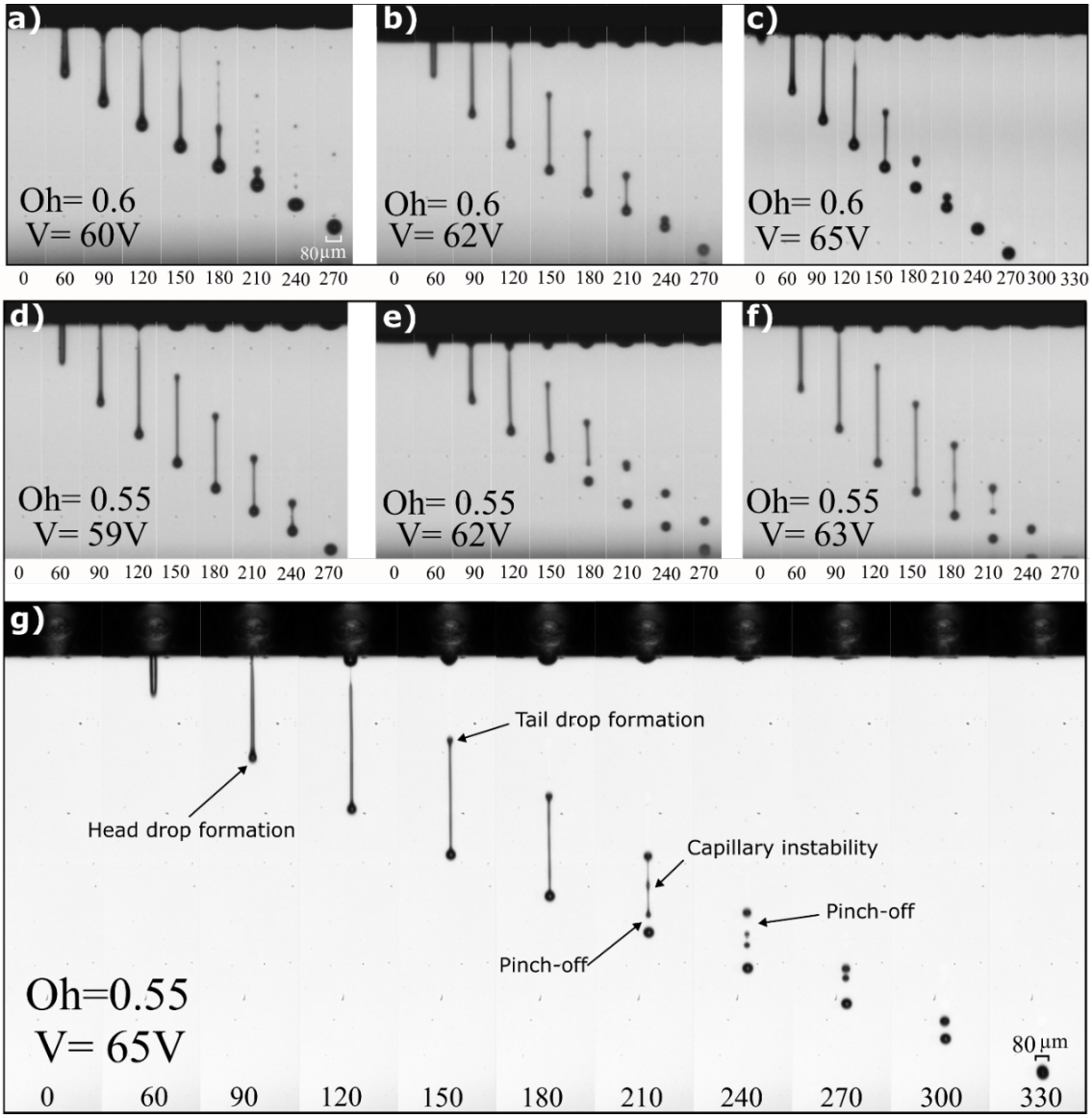

Figure 3.9: Sequence of high-speed camera images (captured using 16,831 fps) of jet formation of the nematic LC E7 at constant Oh number using the actuating waveform of t_{rise} = 3 µs, t_{dwell} = 15 µs, and t_{fall} = 3 µs. The dwell voltage amplitude was varied from 59 – 65 V. The printhead temperature was set to either 65 °C or 70 °C in order to obtain an Oh number of 0.6 or 0.55, respectively. **a)** Oh = 0.6, V = 60 V **b)** Oh = 0.6, V = 62 V **c)** Oh = 0.6, V = 65 V **d)** Oh = 0.55, V = 59 V **e)** Oh = 0.55, V = 62 V **f)** Oh = 0.55, V = 63 V **g)** Oh = 0.55, V = 65 V. The high-speed camera frames with large field of view show that at the higher temperature and voltage (70 °C and 65 V) the jet extends to form a longer fluid ligament resulting in multiple satellites droplets that eventually coalesce to form a single drop at t = 330 µs. Note: Figure (g) was obtained by Dr. Ellis Parry.

From 62 - 65 V, additional droplets were generated due to the multiple pinch-off points that form on the droplet tail, as can be seen in Figure 3.9(e - g). These are called satellite droplets. The first and largest satellite drop is produced at the tail of the jet where it is labelled 'Tail drop formation'. This type of satellite droplet is common due to the

high radius of curvature at the point where the tail meets the droplet head. Smaller satellites can also be produced when spontaneous capillary instabilities occur within the tail of the droplet, seen at t = 210 µs in Figure 3.9(g). Between 150–210 µs, the tail drop forms and grows with time where it can be seen that the tail becomes progressively thin. At higher radii of curvature, both droplets pinch-off leaving the tail to become another satellite droplet as shown in the 240 µs frame. The satellite droplets then merge with the main droplet a few frames later. However, this is not the case for every satellite droplet that is formed.

The high-speed camera frames in Figure 3.10 shows such a case. The voltage amplitude was increased to 70 V and dwell time to t_{dwell} = 17 µs. The rise and fall time were fixed to $t_{rise} = t_{fall}$ = 3 µs and the printhead temperature was 70 °C. As can be seen in the camera images, a small amount of variation in the applied waveform resulted in a larger fluid jet ligament and the capillary instability phenomenon becoming more pronounced. It can be seen that the primary droplet detaches itself from the fluid ligament around 170 µs, and between 170 – 210 µs the fluid ligament becomes thinner and breaks at multiple points into smaller droplets. These smaller droplets merge into each other to form a single secondary droplet. The primary and secondary droplets never merge into each other to form a single droplet, which was the case in Figure 3.9(g). In fact, the primary and secondary droplets reach the substrate at different times: 300 µs and 420 µs, respectively. This drop generation configuration is not desirable for practical applications as both droplets land at the substrate in different times therefore degrading the print quality in the form of non-uninform size droplets.

3.6 Defining a Regime for Printing Nematic LCs

According to the work of Derby, [54] printability requires $0.1 < Oh < 1$. However, the results presented in the previous section reveal the presence of satellite droplets at higher voltages regardless of the fixed Oh number. As Figure 3.9 shows, most of the cases exhibited the presence of satellite droplets at higher voltages even when the Oh number was inside the expected printable range of $0.1 < Oh < 1$. This would indicate that it is therefore inappropriate to define the printable limit for satellite droplets as a function of

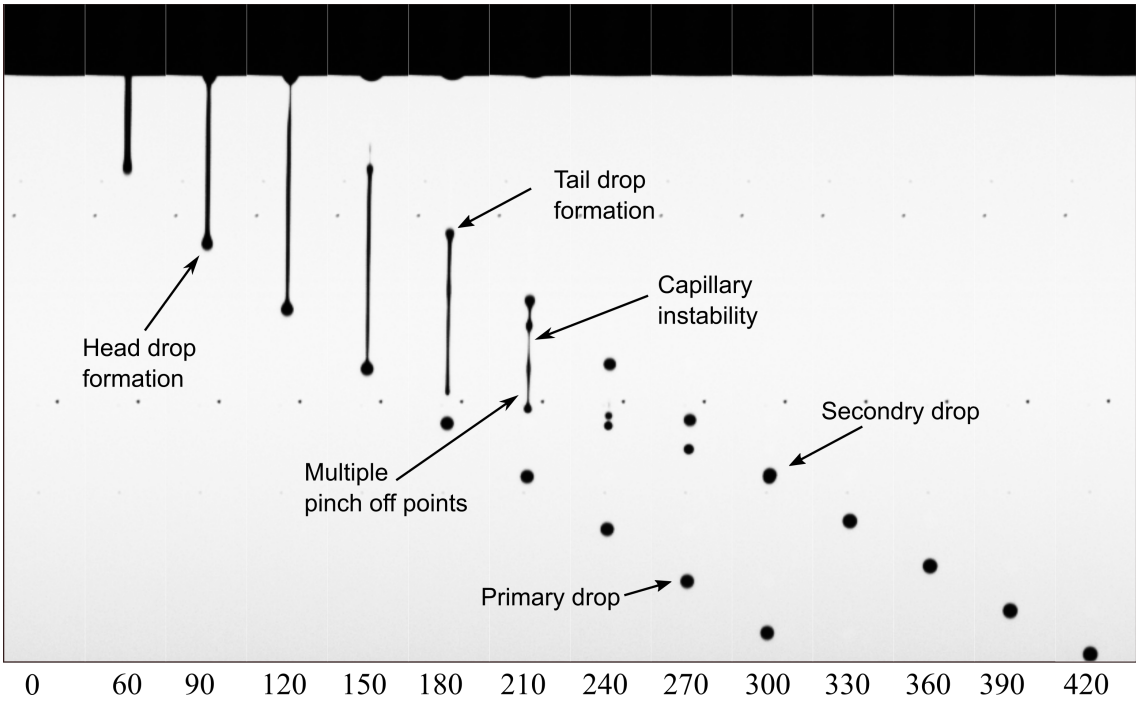

Figure 3.10: Sequence of high-speed camera images (captured using 16,831 fps) of jet formation of the nematic LC E7 with large field of view. The actuating waveform was composed of t_{rise} = 3 µs, t_{dwell} = 17 µs, and t_{fall} = 3 µs. The dwell voltage amplitude was set to 70 V and printhead temperature was set to 70 °C. The jet extends to form a longer fluid ligament resulting in multiple pinch-off points to form satellites droplets. The satellite droplets coalesce to form a single secondary drop that accompanies the primary droplet. The numbers in black at the bottom of each camera frame corresponds to the frame time in units of microseconds (µs).

Oh alone, as also seen in the plot of Oh as a function of Re shown in Figure 3.8. Instead, additional factors such as the droplet velocity, which is a function of voltage or driving force, also need to be considered. Therefore, an attempt is made to find the range of drop formation and their morphologies observed at different Oh number and pulse voltages.

Figure 3.11 shows such an attempt to account for these other parameters where the drop velocity is taken into account through the dimensionless number, We_d, which is referred to as the drop Weber number (where the velocity U in equation 3.2 represents the droplet velocity). The figure plots the values for We_d determined for the nematic LC E7 ink for four different Oh numbers. Each data point represents the droplet morphology starting from the minimum voltage required for the droplet formation at 52 V up to a voltage amplitude of 65 V. The region with the dotted red boundary corresponds to stable single droplet formation. Values above the dotted red line indicate the formation of single

or multiple satellites droplets that form from long fluid ligaments. It can be seen in the plot that at a fixed Oh number of 0.9 a variation in the voltage amplitude from 52 – 63 V leads to the formation of single drops. However, from 64 – 65 V long liquid filaments started to form along with the main droplet which recombine during flight after traveling a distance of several hundred microns i.e., before hitting the substrate. The corresponding We_d for the voltage range 52 – 65 V lies in the range We_d = 7.3 – 55.5.

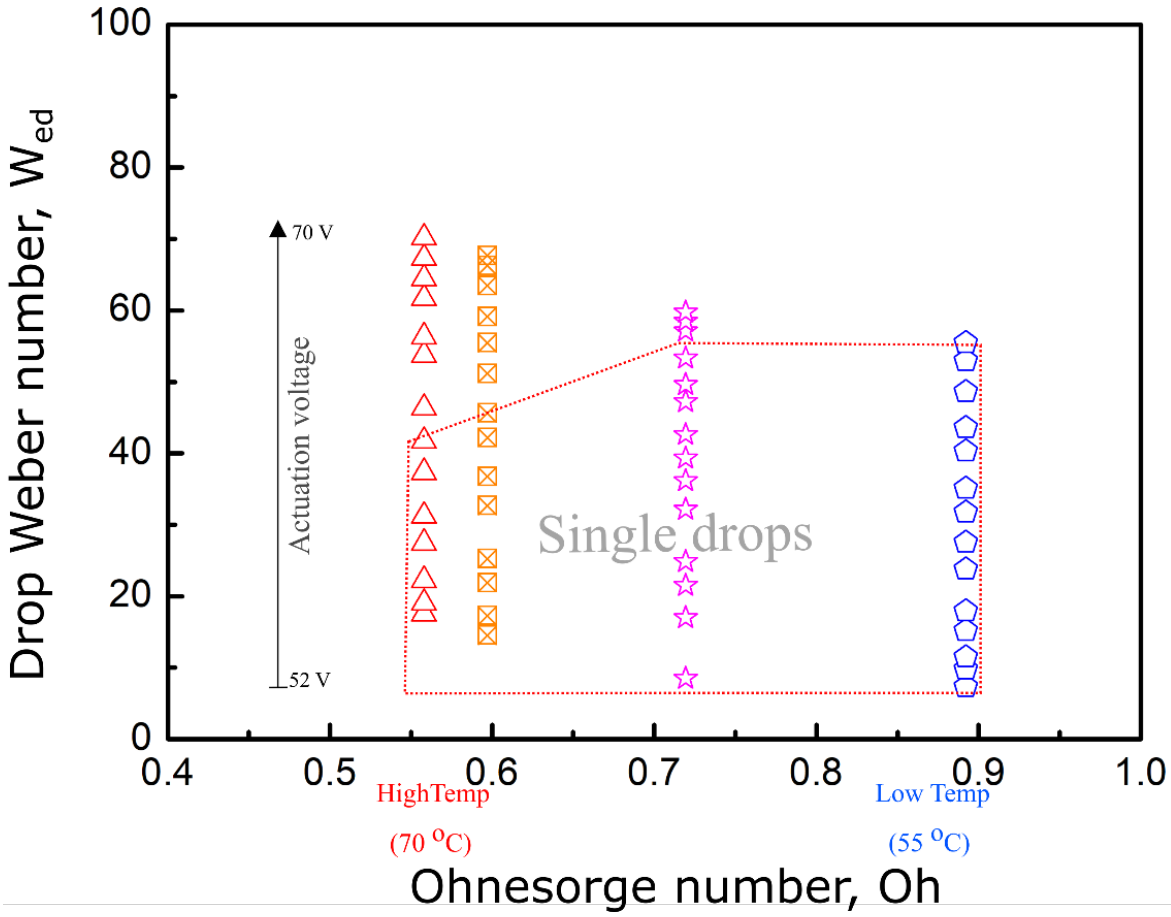

Figure 3.11: The drop Weber number (We_d) (which takes into account the droplet velocity) as a function of the Ohnesorge number (Oh). Changing the Oh number was achieved by varying the temperature whereas changing the We_d number was achieved by altering the voltage amplitude of the waveform. The data points within the red dotted line represent the case when single stable droplets are generated. The data points outside of the red dotted line represents the case when droplets with satellite droplets are generated.

Similarly, at Oh = 0.71 and from 52 – 62 V, single stable drops were produced. Between 63 V and 65 V, however, longer fluid ligaments appear, which give rise to single satellite droplets that appear with the main droplet. The corresponding We_d for voltage amplitudes from 52 V to 62 V is in the range of 8.5 to 53.3, respectively. At lower Oh

numbers of 0.6 and 0.55, stable droplet generation exists within the range of 52 - 59 V and 52 - 58 V, respectively, with the corresponding drop weber number, We_d, falling in the range of 14.5 – 45.6 and 17.5 – 41.7, respectively. Above these voltages, longer fluid ligaments resulted in satellite droplet formation. Table 3.3 presents values for We_d for each Oh number along with the drop velocities that result from the variation in the applied voltage amplitude.

Table 3.3: At each Oh number, the voltage amplitude was varied between 52 – 65 V, which led to a variation in drop velocity and, hence, the corresponding drop Weber number, We_d.

	Oh = 0.55		Oh = 0.6		Oh = 0.71		Oh = 0.9	
Voltage	Drop velocity	Drop Weber number	Drop velocity	Drop Weber number	Drop velocity	Drop Weber number	Drop velocity	Drop Weber number
(V)	(ms^{-1})	(We_d)	(ms^{-1})	(We_d)	(ms^{-1})	(We_d)	(ms^{-1})	(We_d)
52	2.4	17.5	2.2	14.5	1.7	8.5	1.6	7.3
53	2.5	19.0	2.4	17.3	2.4	17.0	1.8	9.8
54	2.7	22.2	2.7	21.9	2.7	21.5	2	11.5
55	3	27.4	2.9	25.2	2.9	24.8	2.3	15.2
56	3.2	31.2	3.3	32.7	3.3	32.1	2.5	17.9
57	3.5	37.3	3.5	36.7	3.5	36.2	2.8	23.8
58	3.7	41.7	3.7	42.2	3.6	39.3	3.1	27.5
59	3.9	46.3	3.9	45.6	3.8	42.6	3.3	31.8
60	4.2	53.7	4.1	51.2	4	47.2	3.5	35.1
61	4.3	56.3	4.3	55.5	4.1	49.6	3.7	40.3
62	4.5	61.7	4.4	59.1	4.2	53.3	3.9	43.6
63	4.6	64.5	4.6	63.5	4.4	57.2	4.1	48.6
64	4.7	67.3	4.7	66.3	4.4	58.5	4.3	53.0
65	4.8	70.2	4.7	67.7	4.5	59.8	4.4	55.5

From the above discussion and the results shown in Figures 3.9, Figure 3.10, and Figure 3.11, it can be concluded that the satellite droplet formation is not a function of Oh number alone. The satellite droplet formation appears to depend upon both the Oh number and drop Weber number, We_d, which is proportional to the drop velocity. For the nematic LC E7 and an Oh number in the range of 0.9 – 0.55, there appears to be a range of drop Weber numbers, $7 < We_d < 48$ that correspond to stable single droplet formation. The experimental observations presented in this chapter reveal that the emergence of satellite drops occurs when We_d was greater than 48.

Liu and Derby identified three separate droplet ejection regimes as the Weber number

increases. Specifically, these are: (i) the formation of an isolated stable drop; (ii) the formation of a drop accompanied by a single satellite; and (iii) the formation of a drop accompanied by multiple satellites. In their work, they suggested that the maximum and minimum values for the jet Weber number were We_j = 2 and We_j = 25, respectively, with low and high values of Z number (2 – 20). [62] The limiting values of the drop Weber number, We_d, and Oh (Z^{-1}) follow a similar trend in our findings: however, our experimental results reveal that single droplets can only be generated at higher values of the drop Weber number which may be due to the non-Newtonian properties of the nematic LC E7 ink.

3.7 Summary and Conclusion

The first part of the chapter has provided an introduction to inkjet printing and has described the printing systems that have been used in this thesis. The chapter has also described previous work on piezoelectric DoD inkjet printing of nematic LCs. It has been emphasised that the printing of these materials is a function of both the fluid and the acoustic behaviour of the fluid-filled cavity within the nozzle. Moreover, it has been shown that by carefully tailoring the shape of the actuation waveform and the printhead temperature, it is possible to dispense micron-sized LC droplets.

In addition to studying the fundamentals of pressure waveform generation and propagation inside the nozzle, this chapter has also presented results in terms of the printability of a nematic LC ink with regards to a series of dimensionless numbers. It was observed that the LC viscosity and the droplet velocity were the dominant factors in defining the LC ink printability and the suppression of the formation of satellite droplets. By increasing the printhead temperature, a significant reduction in LC viscosity was observed, which enabled the nematic LC to be printed. Similarly, the limits of stable droplet formation were determined through variations in the actuation waveform drive voltage.

Understanding the ink rheology is essential for the optimisation of the print parameters in terms of the printhead driving waveform and printhead temperature. This chapter has presented a systematic approach to the optimisation of printing nematic LCs. The

work presented in this chapter serves as a basis for Chapter 4 (Microlenses), and Chapter 5 (PDLCs).

CHAPTER 4

ELECTRICALLY TUNABLE BIFOCAL LIQUID CRYSTAL MICROLENSES

This chapter describes the fabrication of an electrically tunable bifocal microlens array using drop-on-demand inkjet printing of the nematic LC E7. Microlenses were precisely printed between in-plane indium tin oxide electrodes using the printing conditions determined in Chapter 3. It is shown that the focal length of these bespoke microlenses can be tuned with the application of a high-amplitude electric field, and it is found that there exists a range of voltages for which two distinct focal planes are observed. The COMSOL Multiphysics software was used to develop a model of the director profile of the LC microlens. Jones matrices were then used to simulate the transmission of light through the LC microlenses. Finally, the chapter documents the focal length measurements and tunability range of different diameter microlenses. Some of the results presented in this chapter formed the basis of the publication Waqas Kamal et al. 'Electrically Tunable Printed Bifocal Liquid Crystal Microlens Arrays' *Advanced Materials Interfaces* (7, 2000578, 2020), which also appeared as the front cover art of the journal's issue.

4.1 Introduction

Microlenses are of technological interest due to their small geometric profile, which has enabled arrays of these lenses to be deployed in a wide range of applications such as photovoltaics, solar concentrators, imaging, sensing, beam-steering, and optical interconnects. [67–72] In general, microlenses are manufactured with isotropic materials such as UV-curable glues, high quality glass, epoxy-based photoresists and polymers. [73–76] Fabrication processes typically employed to manufacture microlenses include thermal reflow, resist melting, hot embossing, micro-grinding, photolithography, and electric discharge machining. [72, 75–79] These methods are compatible with a range of materials and are capable of producing mechanically robust lenses. However, the fabrication/material combinations typically result in microlenses that possess a fixed focal length that cannot be altered when deployed in a device. Furthermore, these fabrication techniques consist of multiple processes, often requiring sophisticated stamps to imprint the template onto the polymer material. This in turn adds extra cost and complexity that reduces the possibility of rapid prototyping. [80]

Tunability of the focal length adds functionality to the microlenses and paves the way to an even wider range of applications. Methods developed to achieve tunability in large aperture lenses includes the fabrication of liquid-filled elastic lenses as well as gradient refractive index liquid crystal (LC) lenses, and combinations of these approaches. Liquid-filled lenses function by changing the curvature of the isotropic fluid inside the membrane using pneumatic actuation, thermal actuation or electrowetting. [81–83] LC lenses, on the other hand, utilize anisotropic materials such as nematic LCs to modulate the wave front of light. Such LC lenses are formed by spatially distributing the refractive index between homogeneously separated cell gaps either using a photopolymerisation technique or via patterned electrodes that generate a complex electric field profile, which in turn induces a gradient refractive index distribution. [84–86]

It has recently been reported that drop-on-demand (DoD) inkjet printing can be employed to fabricate thermally tunable LC microlenses. [7] Printed LC microlens arrays are

particularly appealing for the development of switchable 2D/3D autostereoscopic organic light emitting diode (OLED) displays as the printing process ensures that the lenses could be deposited directly onto the pixelated OLED layer without the need for additional glass substrates, which would increase fabrication complexity and device thickness. [87, 88]

In Ref. [7], it was demonstrated that, by either increasing or decreasing the temperature, the focal lengths of the printed lenses could be tuned due to an order parameter-induced change in the refractive indices. The reliance on thermal tuning is, however, rather limiting and would not be practical for the applications described above. While the printing process allows for the rapid fabrication of large arrays of microlenses in short timescales it needs to be combined with a voltage tunable focal length to make use of the switchable nature of the LCs and to ensure that it could be used in applications such as switchable 2D/3D autostereoscopic OLED displays.

As we have seen in Chapter 3, inkjet printing is a powerful technique for dispensing LC materials in well-defined micrometre size droplets, which can be arranged on a variety of different substrates for the development of LC-based optical components such as microlenses. This process can be used to fabricate multiple microlenses arrays over large areas with the possibility of building up large arrays of 1000s of microlenses in a matter of seconds.

In this chapter, DoD inkjet printing is used to create electrically tunable microlenses on glass substrates that include in-plane electrodes. Substrates with in-plane electrodes were prepared by etching indium tin oxide (ITO)-coated glass using a photolithography technique. An array of microlenses of different diameters was fabricated by harnessing the precision and flexibility offered by DoD inkjet printing techniques. These printed droplets were found to form plano-convex microlenses a few microseconds after deposition landing. With the application of an electric field, the LC director was aligned along the field direction leading to a reduction in the focal length. This tuning in the focal length was only observed for light polarised along the electric field direction that was generated between the in-plane electrodes.

4.2 Fabricating Electrically-Tunable Printed Microlenses

The experimental details for printing the microlenses and the processes used to fabricate the in-plane electrode substrates are discussed in this section.

4.2.1 In-plane electrode substrates

To generate an electric field in the plane of the device, in-plane electrodes were first prepared by etching a commercially available ITO-coated glass substrate to form two electrodes with a gap of 500 µm. The in-plane electrode device was prepared using a photolithography process. The schematic diagram shown in Figure 4.1 illustrates the complete procedure and is explained below.

The device preparation process begun by cleaning the surface of the ITO-coated glass substrate. To remove any dirt and impurities, the substrate was first sonicated in acetone using an ultrasonic bath. This sonication process was performed for 20 minutes at room temperature (20 °C). Furthermore, to remove any remaining residues, the surface was cleaned with an optical tissue dipped in acetone, as shown in Figure 4.1 (Steps 1 - 2). After cleaning, a positive photoresist (Microposit S9-1813) was spun-coated onto the ITO substrate at 400 rpm for 45 seconds (Step 3). After depositing the photoresist, the substrate was moved to the hot-stage where it was soft baked at 115 °C for 1 min to evaporate the excess solvent from the photoresist film (Step 4).

After baking, the photoresist was exposed to ultraviolet (UV) light that passed through a photomask. For this step, a glass-chrome mask with 500 µm spaced lines was placed above the photoresist-coated-glass substrate and illuminated with a UV light gun ($365\,\mathrm{nm}$) at 15 mW/cm^2 for 1 minute (Step 5). The exposure of the UV light caused a change in the chemical properties of the photoresist. When the substrate was immersed in a developer (Microposit MF-319) for 30 seconds, the UV exposed area resulted in the removal of the developer to form a line pattern on the photoresist (Step 6). The resulting substrate was then baked on a hot-plate at 120 °C for 5 minutes to solidify the remaining photoresist.

To perform the etching, the substrate was then immersed into a 0.1M Hydrochloric acid (HCL) solution. The solution was prepared by mixing 36.5 % HCL ACS Regent into deionised water. The substrate was left in the HCL solution for 30 minutes to etch the regions of the ITO exposed by UV light source (Step 8). The substrate was then held and dipped into an acetone solution for 30 seconds to remove the remaining photoresist and then dried with nitrogen gas (Step 9). The etched substrate was then cleaned with isopropyl alcohol (IPA) and rinsed with deionised water (Step 10). The prepared substrates were then chemically modified with a 0.02 wt.% L-phosphatidylcholine (lecithin) solution that was spin-coated onto the substrate at 1000 rpm for 30 seconds and baked at 70°C for 1 min.

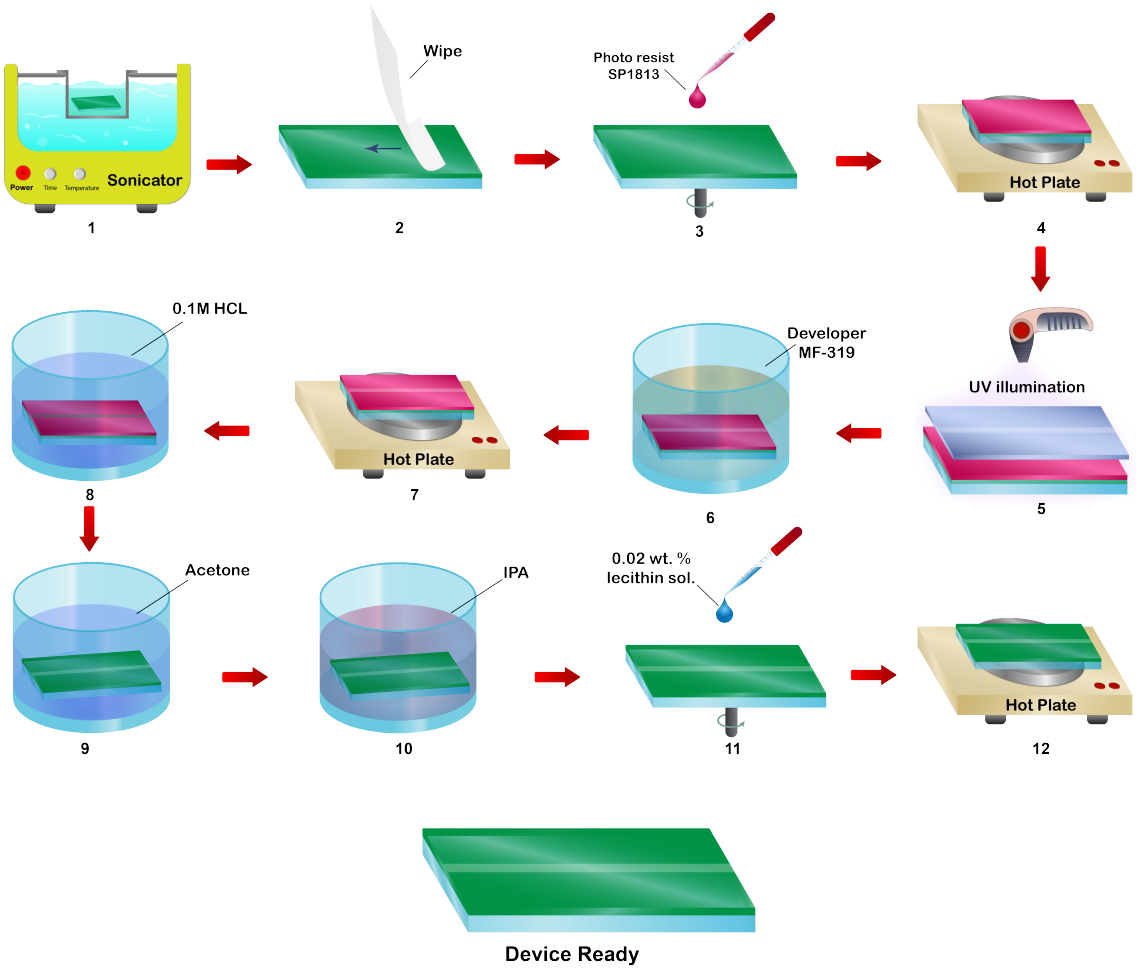

Figure 4.1: Illustration of the fabrication process for the in-plane electrode substrates using photolithography. The in-plane electrode substrate was created by patterning an ITO substrate with a photo-resist, which was followed by wet etching of the ITO before the application of lecithin to create a homeotropic alignment for the liquid crystal microlenses.

4.2.2 Printing Liquid Crystal Microlenses

The microlenses were printed using the MicroFab Jetlab-II inkjet printer as described in Section 3.3.2, Chapter 3. The printing system was chosen as it provides greater freedom to dispense droplets very precisely on a desired location on a substrate. The nematic LC, E7 (from Synthon), was used as the functional ink, which has refractive indices of n_o = 1.52 and n_e = 1.74 at 633 nm and 20 °C. [89] This LC was preferred as it is well characterised, exhibits a moderately high birefringence, and a clearing temperature which is accessible using the selected printhead.

The conditions to print a nematic LC E7 have been discussed previously in Section 3.5 of Chapter 3 where it has been concluded that the quality of the droplet formation depends upon the printhead temperature and amplitude of the actuation waveform. It has been demonstrated that the actuation waveform with a fixed rise time, dwell time, and fall time of 3 µs, 15 µs, and 3 µs, respectively, results in the ejection of stable droplets at temperatures above 55 °C and for pulse amplitudes of 55 V. As already shown, depending upon the printhead temperature there are a range of voltage amplitudes that can be used to print satellite-free nematic LC E7 droplets.

To print uniform LC droplets for the fabrication of tuneable microlenses, an 80 µm-diameter MicroFab nozzle was employed. The printhead was set to 60 °C in order to raise the nematic LC to above its clearing temperature, T_c = 58 °C. Above 60°C, the anisotropic components of the viscosity disappear leading to an increase in the homogeneity of the printed droplet properties. The printhead was actuated with a unipolar trapezoid waveform as described in Section 3.4 of Chapter 3.

Figure 4.2 shows three high-speed camera images of the nematic LC E7 being printed including an in-flight droplet image as well as images at $1\,\mathrm{ms}$ and $10\,\mathrm{ms}$ after deposition onto a lecithin-coated glass substrate. During flight, the droplet was found to have a diameter of $59\left(\pm 5\right)$ µm and a volume of $108\left(\pm 20\right)$ pl. After impact with the substrate the drop resulted in 120 µm drop diameter. The height of a drop was measured

from shadowgraph images and it was found to be around $16(\pm 2)$ µm. The contact angle measurements are discussed in section 4.3.2. It can also be seen that the droplet did not splash during the drop-surface impact process, which is due to the high viscosity of LC and an optimum droplet speed of $4.5\,\mathrm{ms}^{-1}$. The drop-splashing phenomenon becomes more obvious when printing with less viscous materials. [54]

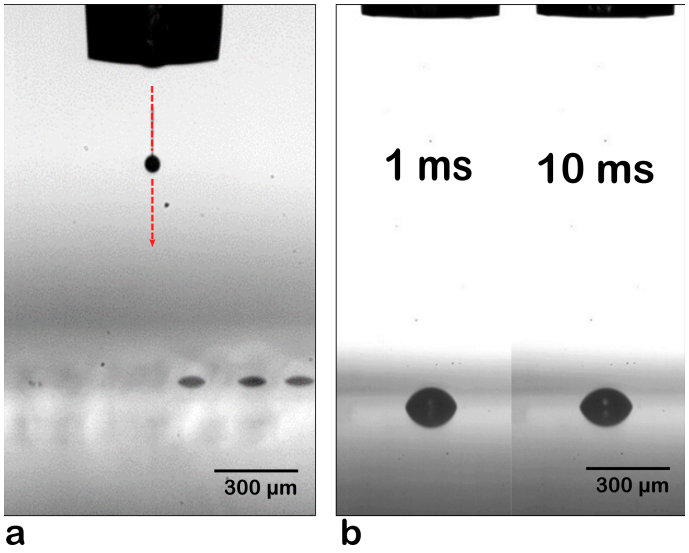

Figure 4.2: High-speed camera images showing the ejection of an LC E7 droplet **a)** during flight, and **b)** after impact with the substrate. The printing process was performed with a 80 µm MicroFab at 60°C printhead temperature and the substrate was held at room temperature.

4.3 Characterising the Printed Microlenses

4.3.1 Microlens Arrays

The shape and profile of a LC microlens depends upon the surface conditions of the printing substrate. In this chapter, a Lecithin-coated substrate was used to promote a plano-convex lens configuration with a homeotropic alignment of the LC director. It might be possible that the surface condition may vary the droplet profile in terms of drop diameter and contact angle. Therefore, before directly fabricating the variable size microlenses arrays it was deemed essential to determine repeatability of printing uniform-sized microlenses to observe any variation in the droplet diameter.

For this study, a glass substrate with a homeotropic alignment layer was held at 25 °C and was used as a printing substrate. The surface roughness of the glass substrate plays a role in terms of influencing the microlens configuration and therefore the glass substrates were thoroughly cleaned before the application of the homeotropic alignment layer to remove excess debris. The homeotropic alignment was made by spin coating of 0.02 wt.% lecithin (0.02 wt.% + 99.98 wt.% IPA) solution as shown in Steps 11 and 12 in Figure 4.1. An array of 120 E7 droplets on the lecithin-coated glass substrate were printed and microscope images of the resulting droplets were obtained. The drop diameter distribution was analysed by using the ImageJ software.

Figure 4.3 shows the resulting normal distribution of the droplet diameters. The results show that the average drop diameter was found to be 120 µm with only a small standard deviation of 0.71 µm, indicating that the repeatability of the printed droplets was very consistent. Figure 4.4 shows an example microscope image of such an array of nematic LC E7 droplets printed onto a lecithin-coated glass substrate. The droplets have shown excellent consistency, both in terms of the diameter and quality of the printed droplet shape.

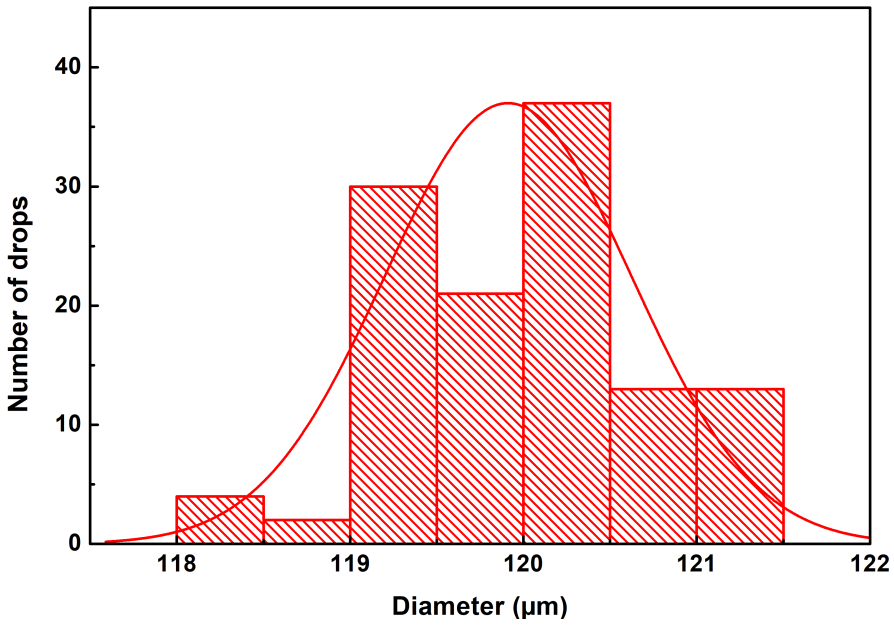

Figure 4.3: Histogram plot showing the variation of the measured droplet diameter (foot print diameter) of 120 E7 droplets printed onto a lecithin-coated substrate. The droplets were printed with an 80 µm diameter MicroFab nozzle at 60 °C printhead temperature. The substrate was held at room temperature of 25 °C. The red curve is the normal distribution fit of the experimental data.

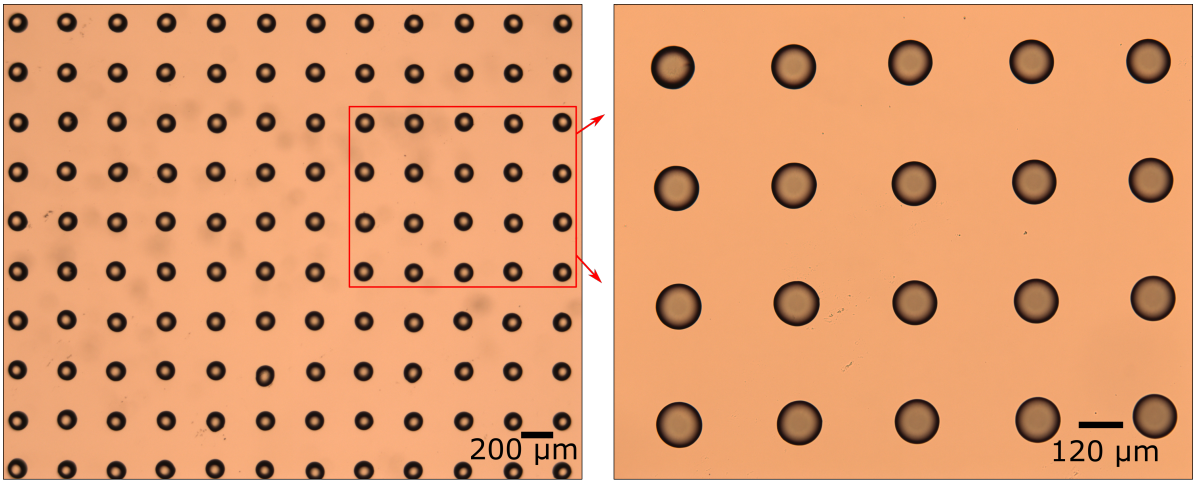

Figure 4.4: Microscope images of the printed array of nematic LC droplets with **a)** 4× microscope objective, and **b)** 10× microscope objective. The droplets were printed on a lecithin coated glass substrate and the nematic LC was E7. The droplets were printed with a 80 µm diameter MicroFab nozzle at 60 °C printhead temperature. The substrate was held at room temperature of 25 °C.

4.3.2 Printing Microlenses of Various Sizes

The printing of single droplets described in the previous section represents a useful printing trial to print uniform size microlenses arrays on a lecithin-coated glass substrate. In this section, the fabrication of microlenses arrays with different diameters between the two ITO electrodes is presented. Figure 4.5(a) shows a schematic illustration of the electrode configuration as well as the microlenses being printed within the 500 µm gap of two in-plane electrodes. Figure 4.5(b) shows a cross-sectional view of a single microlens with a homeotropic alignment of the director. The alignment of the LC director is discussed further in the section 4.3.3.

Using DoD inkjet printing, it is possible to make small changes to the droplet volume and subsequent microlens diameter by simply changing the duration and amplitude of the actuation waveform. However, as described in Section 3.5.4 of Chapter 3, this technique can lead to jet instability as well as the onset of the formation of satellite droplets that accompany the main droplet. In addition, this method does not permit a substantial increase in the microlens diameter. Therefore, to obtain large changes in the diameter of the microlenses, multiple droplets were printed onto the same location on the substrate to build up larger diameter microlenses.

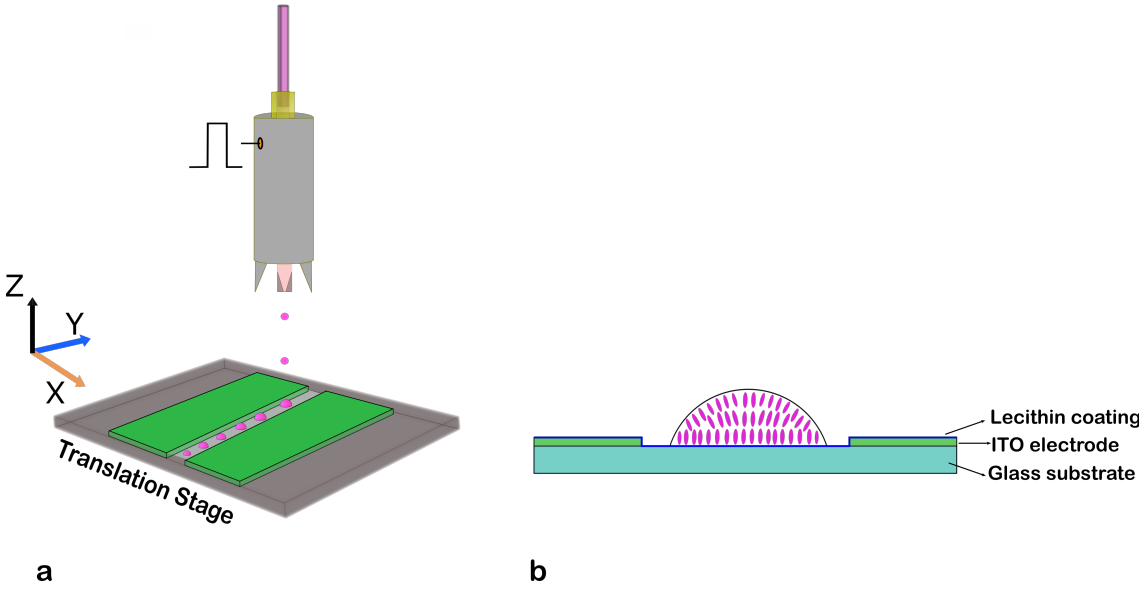

Figure 4.5: a) Illustration of the process for fabricating microlens arrays using DoD inkjet printing. **b)** Illustration of the cross-section of a glass substrate with in-plane electrodes and a single printed microlens showing the orientation of the LC director.

Figure 4.6(a) shows an example image of printed microlenses with various diameters between the in-plane ITO electrodes. The microlenses were formed using the multiple droplet deposition technique and all droplets were produced in a single printing sequence. The optical microscopy image in Figure 4.6(b) provides a closer inspection of six inkjet-printed microlenses, with a centre-to-centre distance chosen to be 1000 µm to avoid any coalescence between the droplets. The droplet diameters of the six microlenses is in the range of 120 µm to 222 µm.

Characteristics such as the microlens diameter and contact angle were determined from calibrated microscope and shadowgraph images. The magnitude of the contact angle, θ, of a printed lens is governed by the balance in the interfacial forces between the glass substrate, the nematic LC, and the surrounding environment. [90] The contact angle does not, however, depend upon the lens volume, as verified in our measurements of the inkjet-printed lenses, which were all found to be $\theta = 32^\circ \pm 1^\circ$. As an example, shadowgraphy images are presented in Figure 4.7 for five different droplet diameters ranging from 210 to 255 µm. Identical results were also found for the smaller droplet diameters considered in this study.

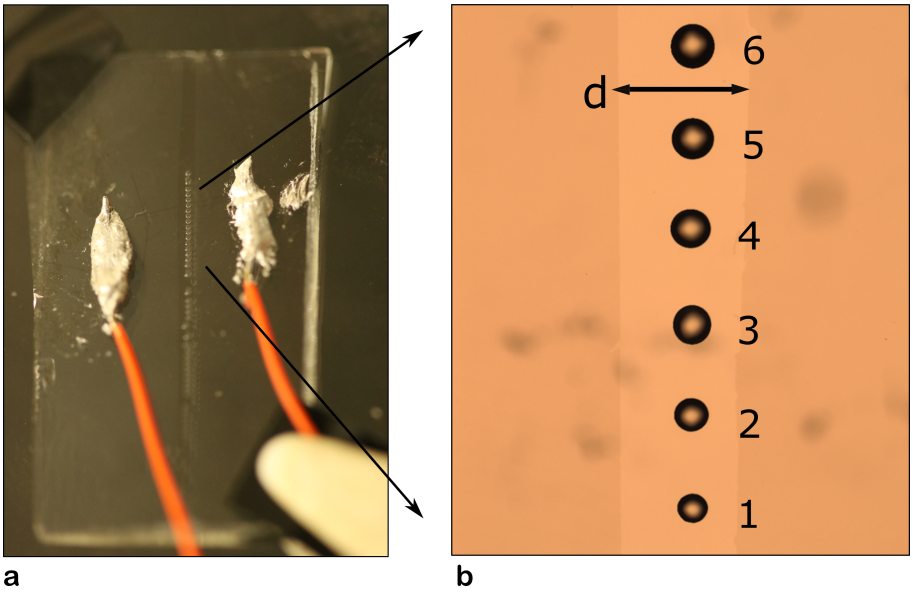

Figure 4.6: **a)** Photograph showing an array of nematic LC microlenses printed on an in-plane electrode substrate. **b)** Polarising optical microscope image (uncrossed polarizers) of microlenses with different droplet diameters. The numbers indicate the number of drops deposited at each location. The double-headed black arrow in (b) shows the separation of the electrodes (500 µm). The nematic LC used was E7, which was printed at a temperature of 60 °C using a printhead nozzle with a diameter of 80 µm. During printing, the substrate temperature was held at room temperature of 25 °C.

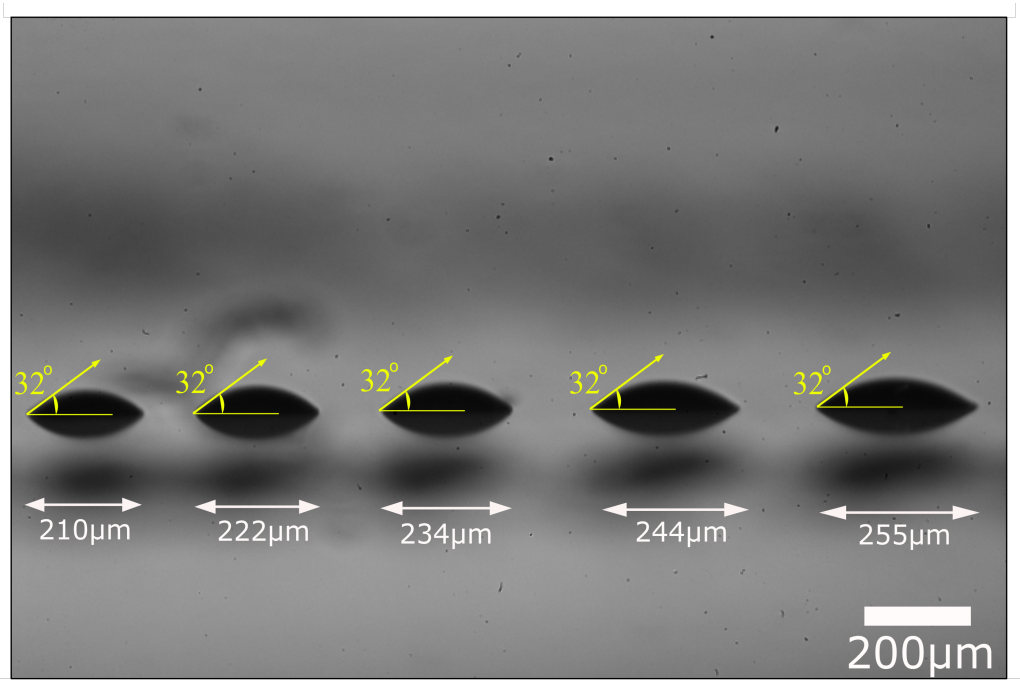

Figure 4.7: Shadowgraphy image of five nematic LC microlenses with different diameters but with the same contact angle. The same behaviour was also observed for the smaller lens diameters considered in this study. The printing process was performed at 60 °C temperature with a 80 µm nozzle. During printing, the substrate was held at room temperature of 25 °C. The image is a side view of printed microlenses, everything below the yellow line corresponds to mirror image.

The relationship between the number of drops and the resulting lens diameter can be seen in Figure 4.8(a), which indicates that the lens diameter is indeed governed by the drop volume and is in good agreement with the modelled drop diameter for a 32° contact angle spherical cap. The values with the green error bars represent the measured drop diameter and the black solid line represents the modelled drop diameter. The model was built by increasing the volume being deposited to form perfectly spherical capped plano-convex lenses of varying size and a contact angle of 32°. Similarly Figure 4.8(b) shows the change radius of curvature due to the change in number of drops deposited to form a lens(with the change in radius of curvature we can pre-select the focal length of a lens.).

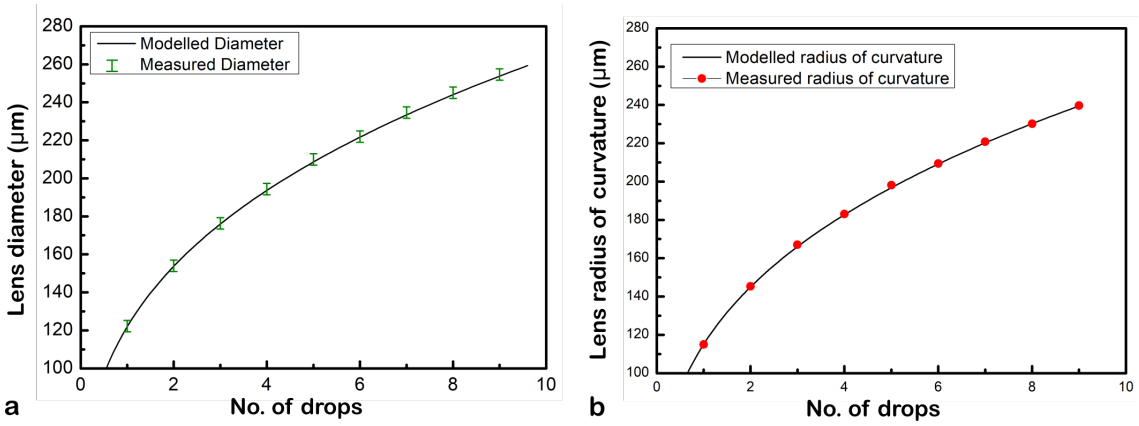

Figure 4.8: Microlens diameter as a function of the number of drops dispensed by the DoD inkjet printer. The values with green error bars correspond to measured drop diameter and the solid black line corresponds to modelled diameter. **b)** Microlens radius of curvature as a function of the number of drops dispensed by the DoD inkjet printer. The values with red correspond to measured radius of curvature and the solid black line corresponds to modelled radius of curvature. The printing process was performed at 60 °C temperature with a 80 µm nozzle. During printing, the substrate was held at room temperature of 25 °C.

4.3.3 Liquid Crystal Director Alignment

In this work, the LC microlenses have been printed on a lecithin-coated substrate to promote homeotropic alignment of the LC director. This type of alignment was preferred because the LC director configuration inside the droplets will be dictated by the homeotropic boundary conditions at the air/LC and the substrate/LC interfaces. [18,21] In addition, an advantageous property of homeotropically-aligned LC droplets is that they will possess largely polarisation independent optical properties for collimated incident light due to the symmetry in the LC director in the voltage-off state.

Figure 4.9 shows a crossed polarised optical microscope image of an array of printed LC microlenses. The microlenses have uniform circular boundary with a lens diameter of 120 µm. The centre of the dark cross in each lens indicates the homeotropic alignment of the LC director. The four bright regions result from birefringence that arises due to the slight tilt in the LC director that is induced by the curvature of the droplet. Without temperature gradient, the director shows a cylindrical symmetrical alignment that results in the Maltese cross pattern observed under the crossed polariser. This type of pattern has been discussed in the literature. [91] Our COMSOL LC director model of the droplet verifies this phenomenon and the corresponding results are presented in the following section.

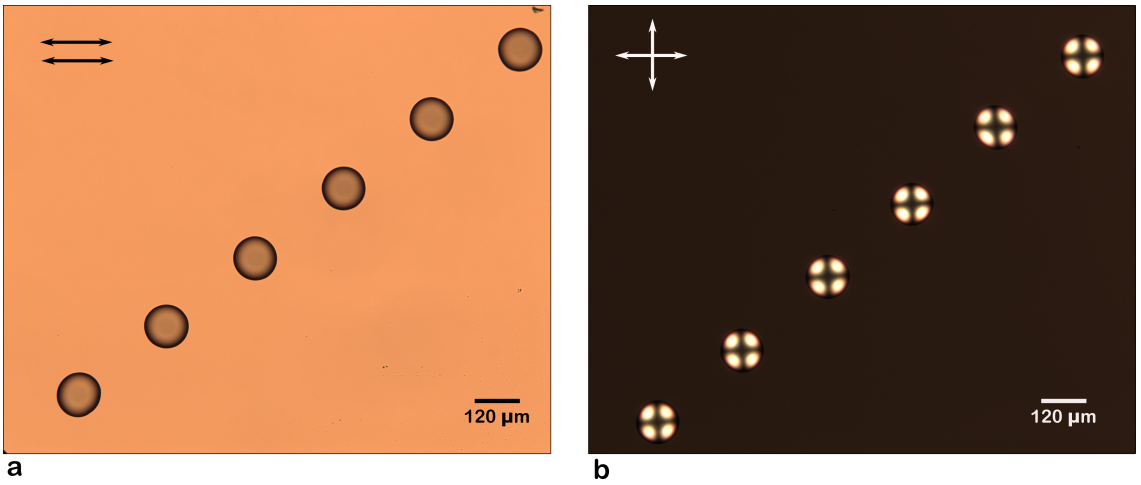

Figure 4.9: Polarising optical microscope images for, **a)** uncrossed polarisers, and **b)** crossed polarisers of an array of nematic LC microlenses printed onto a lecithin coated glass substrate. The size of individual droplets is 120 µm. The nematic LC used was E7, which was printed at a temperature of 60 °C using a 80 µm diameter MicroFab nozzle. During printing, the substrate temperature was held at 25 °C.

4.3.4 Modelling of the Liquid Crystal Director Alignment

Through observations of the LC microlenses with polarised optical microscope images, we have seen that the LC director appears to align in the droplets in a near homeotropic configuration. However, to gain a better physical understanding of the expected LC director configuration in these printed nematic LC droplets simulations have been performed based upon continuum theory. Here the objective is to establish a model that links LC continuum theory and Jones calculus in order to simulate the appearance of the LC microlenses when viewed on a polarising optical microscope. This approach is also em-

ployed to understand how the LC director behaves when the microlenses are subjected to an electric field. There are two distinct components of the model: (i) LC director modelling (with and without an electric field) and (ii) a MATLAB-based Jones matrix routine, which is used to simulate the appearance of the the microlenses when viewed on a polarising optical microscope.

The COMSOL Multiphysics® software was used to model the LC director. The COMSOL software enables modelling in 2D and 3D and has various physics modules that can aid the simulation process. However, COMSOL does not have a module that can directly perform simulations of the LC director. To model the LC director, the module termed as 'coefficient form PDE' was adapted and tailored in order to achieve a stable LC director configuration by minimising the total free energy of the system. Section 2.7 of Chapter 2 explains the theory behind the equations in the form of PDEs.

The first step in the COMSOL simulation process was to create a model geometry. A 3D model geometry of the microlens was constructed by using the parametric surface tool that controlled the lens diameter, contact angle and radius of curvature. The individual components of the lens geometry (top curved and bottom flat surfaces) were united and then converted to a single solid body by using the convert to solid command tool.

After defining the lens geometry and governing equations, the next step was to define the boundary conditions. A Dirichlet boundary Condition was used to define strong anchoring of the LC director both at the top air/LC interface and the bottom LC/substrate interface. This was an appropriate choice because both the LC/air interface and the LC/lecithin coating interface are considered to provide reasonably strong anchoring with anchoring strengths of 10^{-4} Jm^{-2} and 4.6×10^{-4} Jm^{-2}, respectively. [18, 21]

The final step before running the solver was to define a mesh to subdivide a large system into smaller domains, termed finite elements. In practice, the accuracy of the solver's solution depends upon mesh size. However, this increases computation time. In this simulation, a physics-controlled mesh with a finer element size was selected which

was found to result in reasonably good agreement between the simulation results with experiments. Figure 4.10 shows the top view of the lens geometry that is covered by a tetragonal mesh.

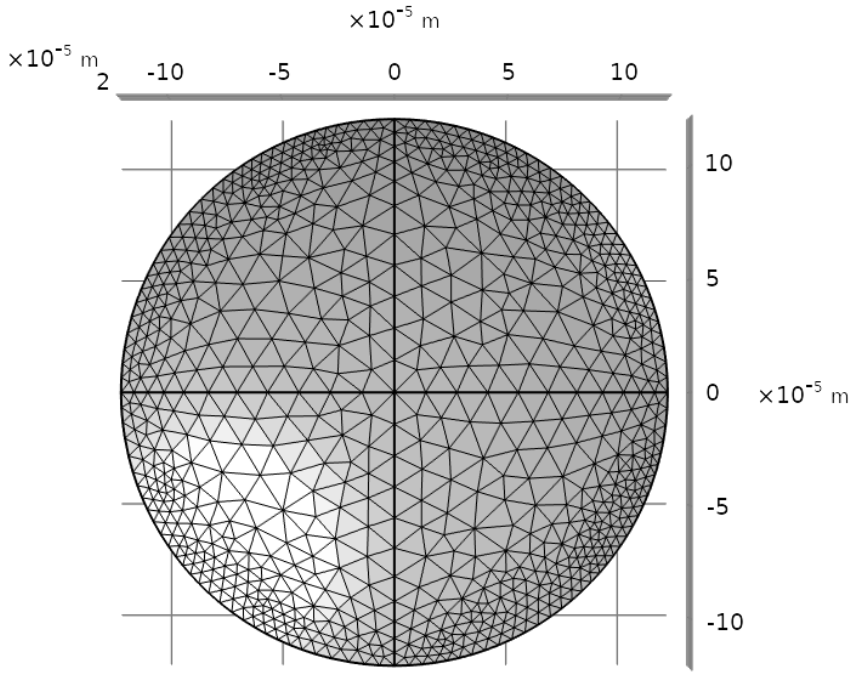

Figure 4.10: A 255 µm diameter microlens geometry produced in the COMSOL Multiphysics software. The elemental structure over the surface of the microlens corresponds to the mesh type used.

After defining the mesh type, the solver was run to simulate the LC director configuration and display the results. There are different ways to visualise the results. However, the arrow surface plots were found to be the most convenient way to demonstrate movement of the LC director. In addition, the arrow surface plots provide the opportunity to extract the orientation of the director in terms of the n_x, n_y, and n_z components of the director, which was subsequently used to model light transmission as discussed in the following section.

To simulate the propagation of light through a microlens, a MATLAB code based on Jones calculus was used (see Appendix C). The code was written with Prof Steve Elston. The MATLAB code imports pre-processed LC director orientation data (n_x, n_y, and n_z

components) in a comma separated file format (CSV) from COMSOL and arranges the data in the form of a grid in the x, y and z directions. The raw CSV file imported from COMSOL contains the director orientation information inside the lens only and it ignores the data points around the lens geometry. In this case it reads the outer region of the lens as 'NaNs' for all n_x, n_y, and n_z components. To model the propagation of light through this region, we have to specify a refractive index. This was accomplished by instructing the MATLAB code to replace 'NaNs' with $n_x = 0$, $n_y = 0$, $n_z = 1$ at those points. Doing this, it is now possible that the incoming light will see a spatially varying effective refractive index inside the lens geometry and a constant refractive index of n_o outside the area of the lens.

Figure 4.11 shows LC director simulation results from the top and side views. The arrows indicate the alignment of the LC molecules and the net director orientation ($\boldsymbol{n}$). From the model, it can be observed that the LC director assumes a homeotropic alignment at the top surface of the lens. The homeotropic alignment is obvious at different regions of the lens surface however, the curvature of the lens results in a slight tilting of the LC director.

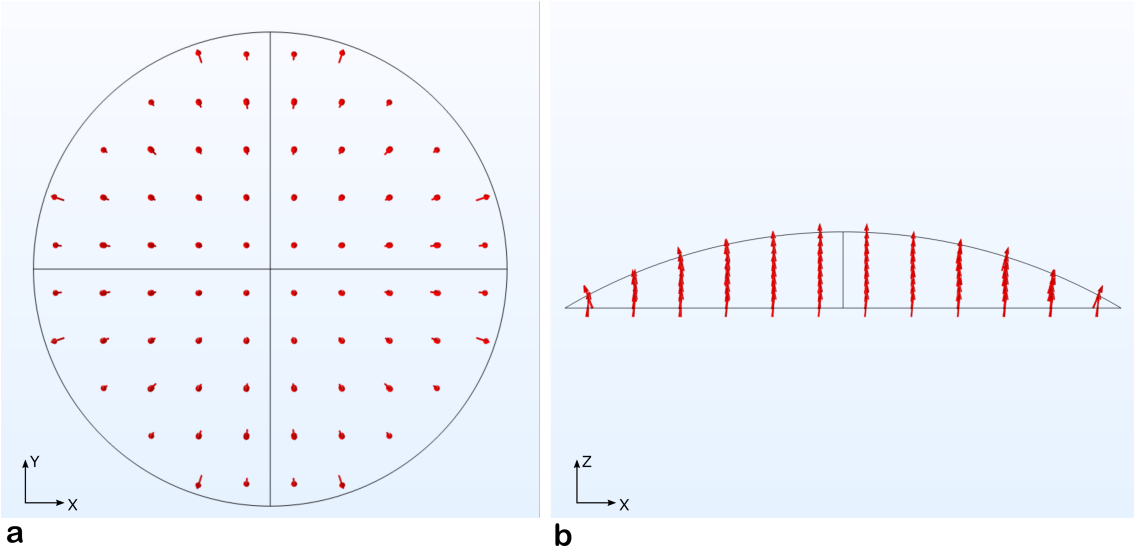

Figure 4.11: LC director model for a printed sessile droplet when viewed from **a)** the top and **b)** the side. The orientation of the LC director is illustrated by the direction of the red arrows.

Figure 4.12 shows the results of an example simulation of the appearance of a ne-

matic LC droplet printed onto a substrate with a homeotropic alignment layer when viewed on a polarising optical microscope with crossed polarisers. To create this simulated image the transmission was averaged over the visible spectrum, but as this is a qualitative comparison with a microscope image the LC dispersion was not included. From these results it is obvious that the four bright regions appear due to birefringence, which arises due to a slight tilt in the LC director across the lens profile, as shown in the COMSOL lens model in Figure 4.11. These simulation results are in good agreement with the experimental results, which have been shown earlier in Section 4.3.3.

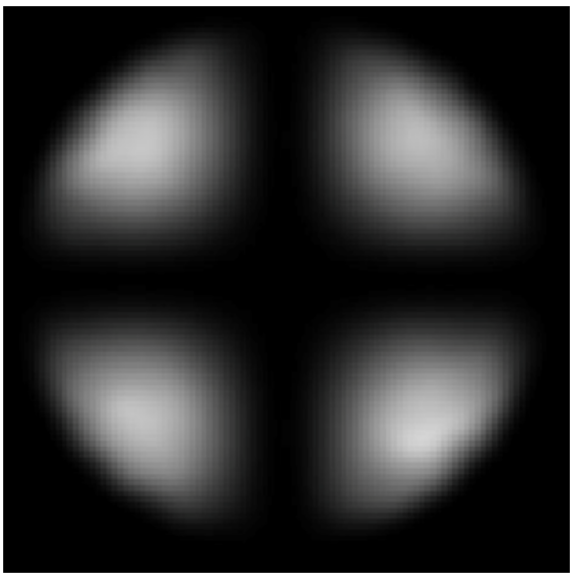

Figure 4.12: Simulation of the appearance of a nematic LC droplet printed onto a substrate with a homeotropic alignment layer when viewed on a polarising optical microscope with crossed polarisers. These results were obtained by feeding the LC director profile obtained from the COMSOL model (Figure 4.11 into Jones matrices calculated MATLAB. In the model a broadband (400 – 700 nm) light source was assumed.

4.3.5 Relationship between Lens diameter and Focal length

The focal length of a simple plano-convex lens can be estimated from the Lensmaker's equation:

$$f = \frac{R}{(n-1)} \tag{4.1}$$

which predicts that the focal length, f, depends only on the radius of curvature, R, and the refractive index, n, of the lens. [31]

From equation 4.1 it can be understood that the focal length of a LC microlens can be pre-selected in terms of radius of curvature which depends upon lens volume and contact angle. Using the DoD inkjet printing technique, it is possible that we can vary the drop volume and lens diameter to vary the radius of curvature and subsequently the focal length. The method for increasing the drop volume and the resulting lens diameter has already been discussed in Section 4.3.2 of this chapter.

Equation 4.1 assumes a homogeneous refractive throughout the volume of the lens. For LC microlenses this condition would imply that LC director should possess a perfect homeotropic alignment so that the incident light would only interact with the ordinary component, n_o, of the refractive index. The LC director simulation and POM images confirm that the LC microlenses possess a near uniform homeotropic alignment (see previous section). It can then reasonably be assumed that the ordinary refractive index, n_o, of the nematic LC (E7) at 20°C and $633\,\mathrm{nm}$ is the same for each microlens.

The method we have used to characterize the focal length of the LC microlenses follows a method described previously in the literature. [7, 80, 92] A schematic of the measurement system is shown in Figure 4.13(a). To measure the focal length of the lenses, a continuous wave He-Ne laser ($\lambda = 632.8\,\mathrm{nm}$) was used to illuminate individual lenses in an array of microlenses. A neutral density filter was employed to adjust the input intensity of the laser, and a half-wave plate ($632.8\,\mathrm{nm}$) was used to control the orientation of the input polarisation. Samples were mounted on a computer-controlled linear translation stage (LNR 50S, Thorlabs) and an imaging lens of focal length 75 mm was then translated in such a way that a clear image of the focal plane of each LC lens was formed at the CCD as shown as an inset image in bottom right corner of Figure 4.13(b). The motorised stage was then translated in 5 µm steps towards the laser source and a series of images were taken until the sharpest focal spot of the LC microlens was formed as shown as an inset image in top right corner of Figure 4.13(b). The graph in Figure 4.13(b) shows the light intensity profile of the focused spot of a 255 µm diameter microlens.

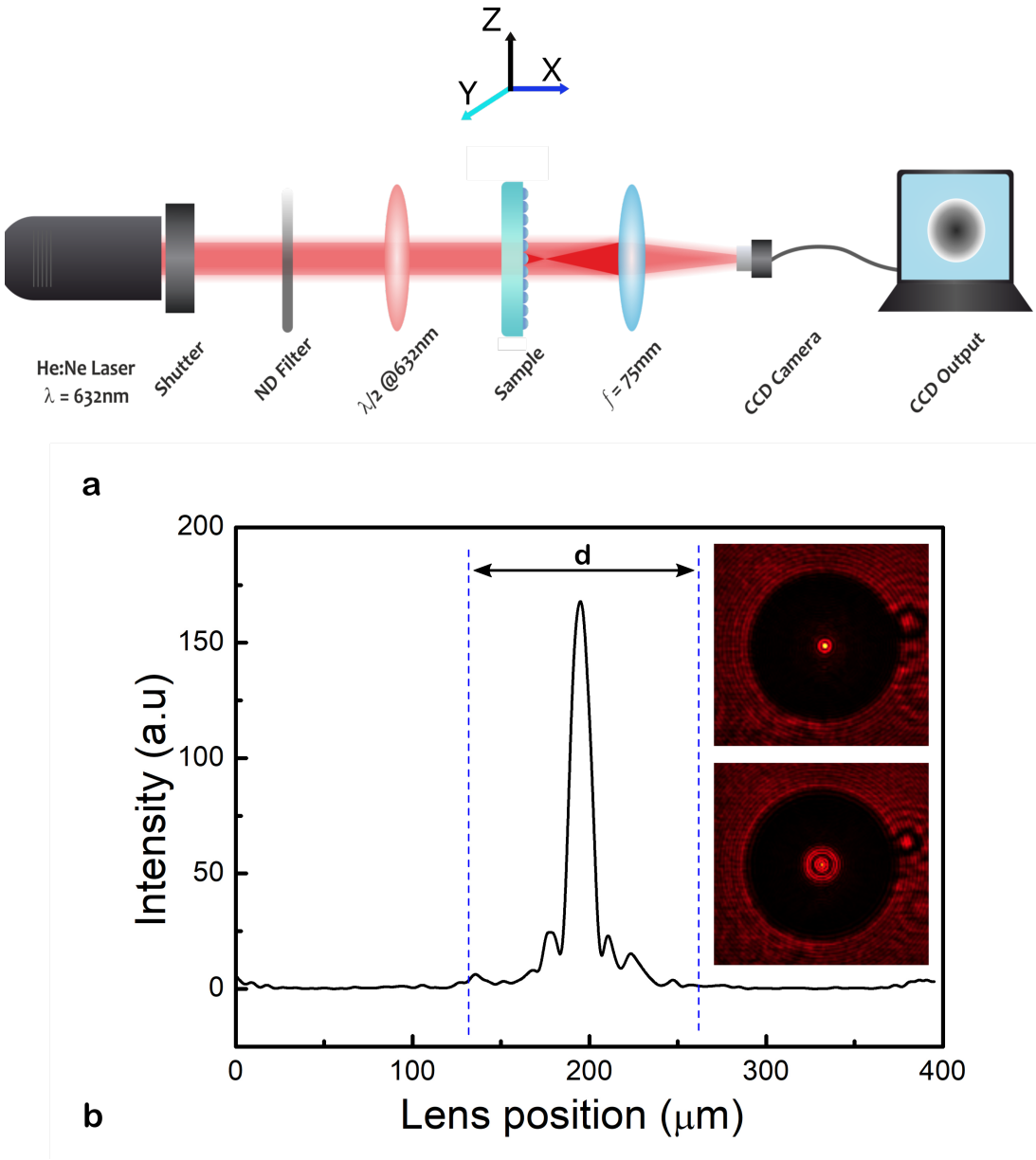

Figure 4.13: **a)** Schematic diagram of the optical setup used to determine the focal length of printed nematic LC microlenses. **b)** intensity cross-section of a 255 µm diameter lens at the image plane, along with the CCD images for the in-focus (top) and out-of-focus (bottom) lens positions (insets). The 255 µm diameter lens was formed by landing 9 LC E7 droplets at the same location using a 80 µm diameter MicroFab nozzle at 60 °C printhead temperature while the substrate was held at room temperature of 25 °C.

The method described in the above section (illustrated in Figure 4.13) was employed to investigate the focal lengths of different diameter microlenses. The results presented in Figure 4.14 shows that the focal length for the microlenses with different diameters depend only on the radius of curvature which is controlled by the drop diameter. The experimental focal length was also compared with the modelled focal length of a perfectly spherical capped plano-convex lens with the same physical dimensions and a single uni-

form refractive index that is equivalent to the ordinary refractive index for the nematic LC, E7 determined at $632.8\,\mathrm{nm}$ (n_o = 1.52). As shown in Figure 4.14, the experimental focal length is in good agreement with the modelled focal length. Moreover, the correlation between predictions and experimental results suggests that the small tilt in the LC director due to the curvature of the lens (see Figure 4.11) does not significantly affect the focusing properties of the microlenses. This is reasonable because we estimate that the small LC director tilts within the lenses (predominantly near the lens edge) would lead to an elongation in the focal spot of around 15 µm, which is within our measurement accuracy.

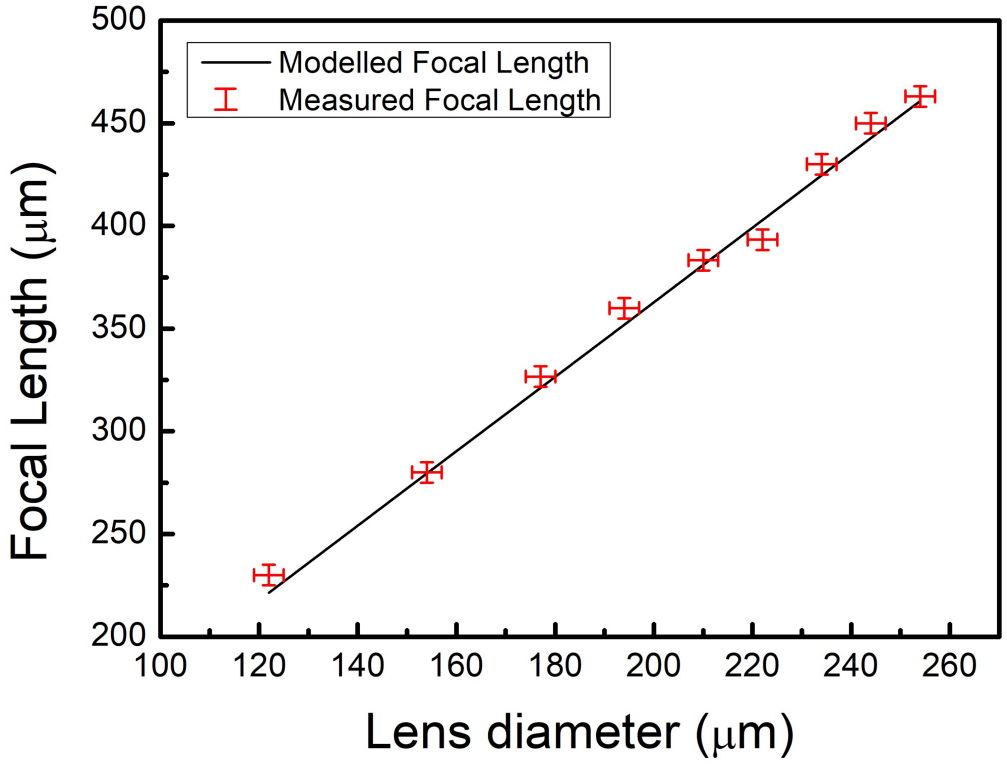

Figure 4.14: Focal length as a function of the microlens diameter. The black line represents the results for a plano-convex lens modelled to have a constant refractive index, n, of 1.52.

4.3.6 Tuning the Microlenses

To evaluate the tunability of the lenses focal lengths in the presence of an applied electric field, the microlenses were first observed on an optical polarising microscope to view the change in the orientation of the LC director. Figure 4.15 presents, as an example, results for a 255 µm diameter microlens, which was chosen due to its low driving voltage as

compared to the smaller diameter microlenses (the balance between surface anchoring and bulk elasticity leads to smaller threshold voltages for larger microlenses), at different applied voltages for a 1 kHz frequency square wave. From 0 V_{pp} to 100 V_{pp} no change in the alignment of the LC director was observed. However, as can be be seen in image sequence, as the applied voltage exceeded a value of 100 V_{pp} (threshold, V_{th}), a uniformly aligned region started to appear in the centre of the microlens which expanded concomitantly with an increase in the applied voltage. By 200 V_{pp}, the uniformly aligned region was found to cover the entirety of the microlens from the centre to the periphery of the droplet.

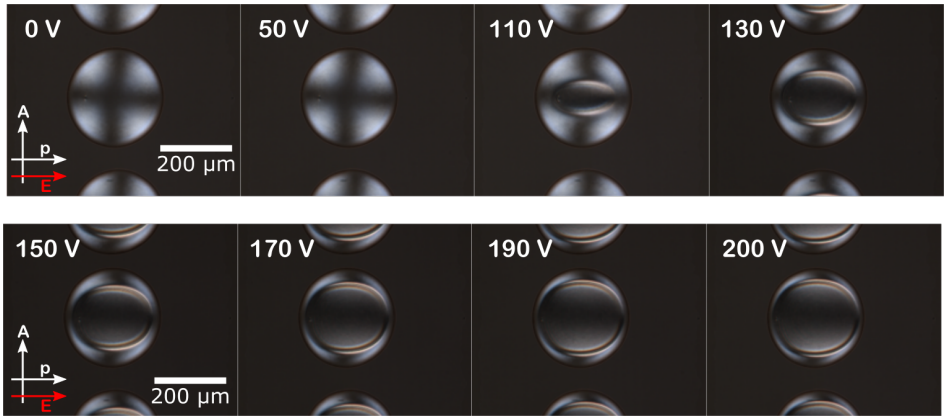

Figure 4.15: Optical polarizing microscopy images (crossed polarisers) of a 255 µm diameter nematic LC E7 microlens at different applied voltages. Numbers in the top left indicate the peak-to-peak voltage while the red arrow shows the direction of the applied in-plane electric field. The white arrows show the orientation of the transmission axes of the polarizers. The lens was formed by landing 9 LC E7 droplets at the same location using a 80 µm diameter MicroFab nozzle at 60 °C printhead temperature while the substrate was held at room temperature of 25 °C.

The simulation results presented in Figure 4.16 shows the LC director orientation and corresponding light transmission simulation results. Figure 4.16(a) shows how the LC director started to orient in the direction of the electric field when a time-dependent field was applied. If the field is increased slowly in the COMSOL model (ramped up slowly) then provided there is a small pre-tilt the tilt (to break the degeneracy) the inversion wall moves off to one side of the lens (i.e. The LC director alignment initially changes at the centre of the microlens and expands consistently across the lens profile) and the director profile behaviour leads to transmission results as shown in Figure 4.16(b). As seen in Figure 4.16(b), the corresponding light transmission results are in good agreement with the experimental results, which confirms that the realignment of the LC director due to

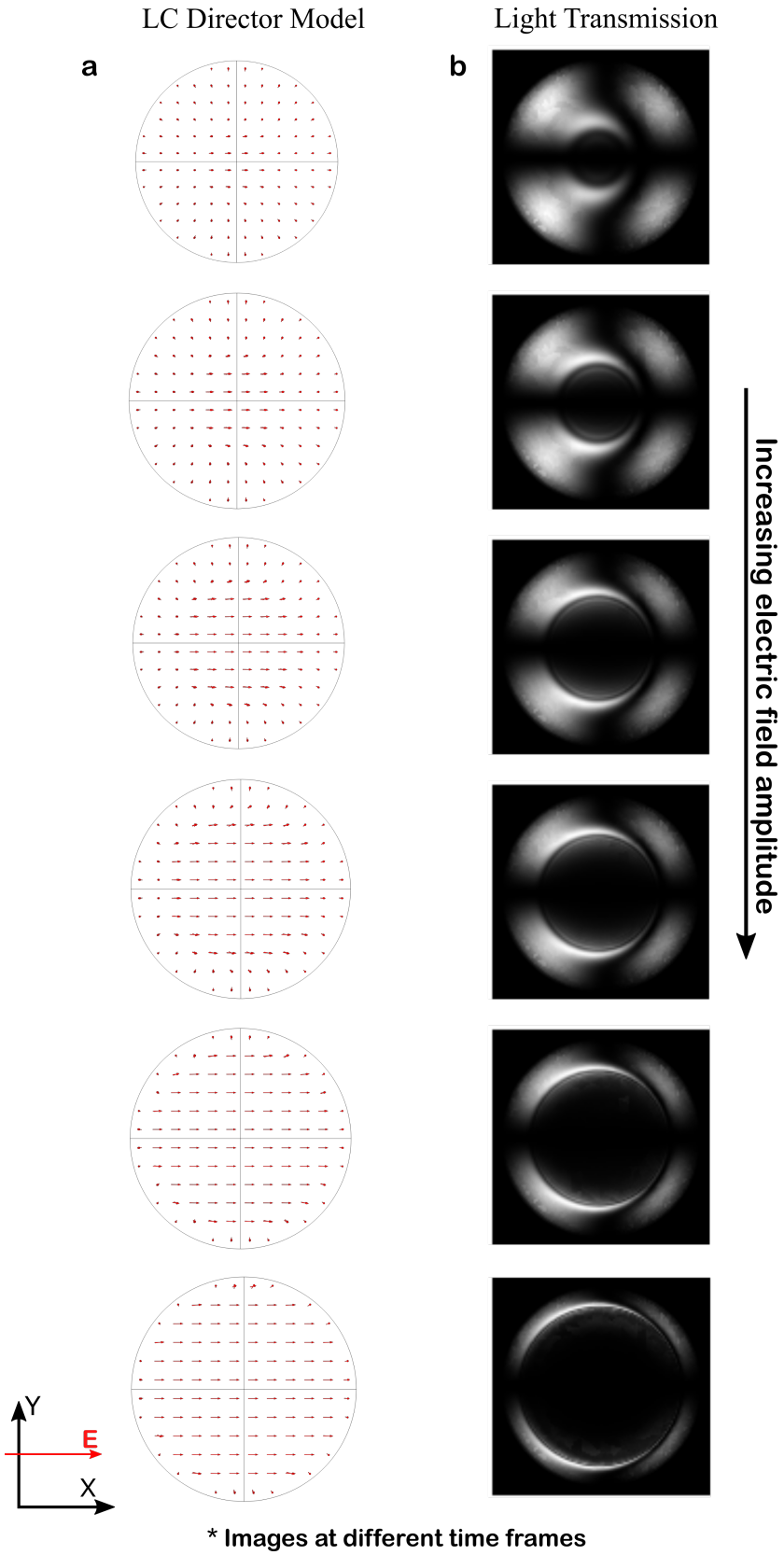

Figure 4.16: **a)** Simulation of the LC director (indicated by the red arrows) inside a microlens when the electric field was applied along the x direction. **b)** Corresponding results from simulations of light transmitted through the LC microlens when sandwiched between crossed polarisers. These results were obtained using Jones matrices and the LC refractive index properties that result from the director configuration shown in (a). The images were taken at different times when a time-varying (ramped up slowly) electric field was applied in the COMSOL model.

the electric field is along the transmission axis of the polariser in this case. This appears as a black region when viewed between crossed polarisers.

The lens transmission behaviour was also investigated for the case when the electric field was applied at a 45° angle with respect to the transmission axis of the polariser. Figure 4.17(a) presents a series of microscope image that show the evolution in the LC director alignment of a 222 µm diameter lens as the electric field amplitude was increased. The appearance of the yellow region suggests that the orientation of the LC director changes. The results presented in the POM images are found to be in good agreement with the results from simulations that are presented in Figure 4.17(c).

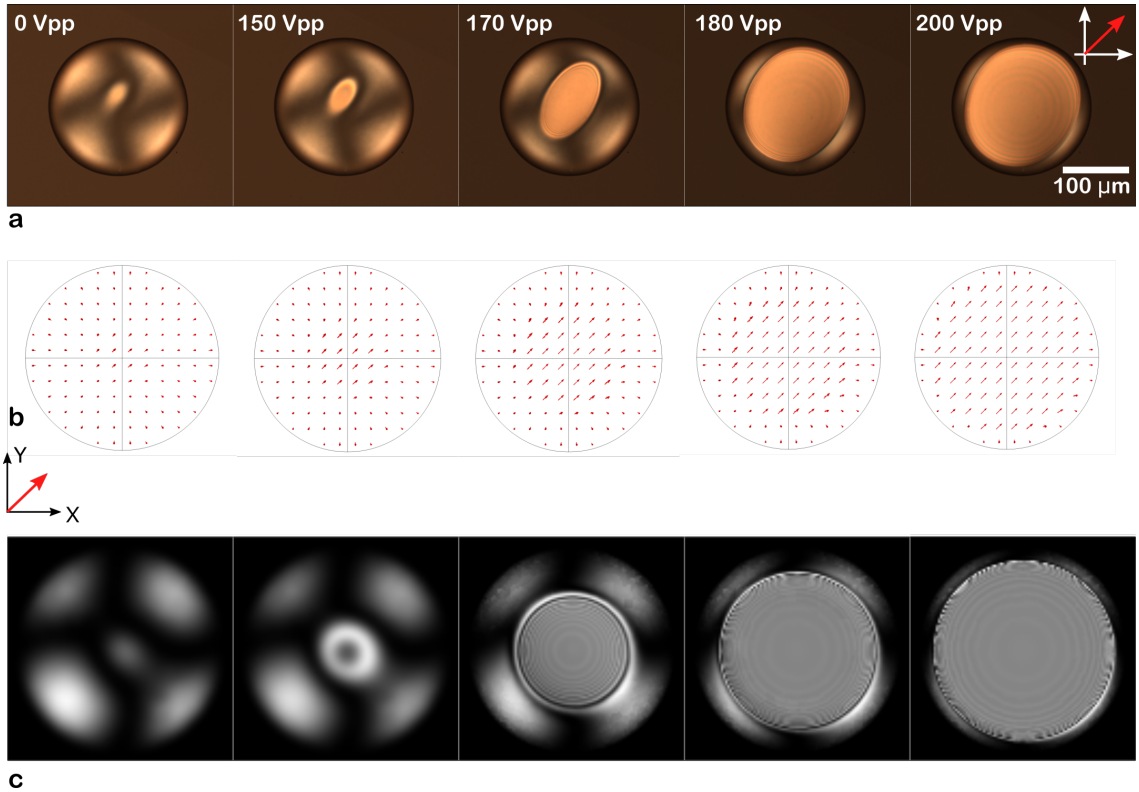

Figure 4.17: a) A series of polarising optical microscopy images for a 222 µm diameter nematic LC microlens at different applied voltages. The numbers in the top left indicate the peak-to-peak voltage while the red arrow shows the direction of the applied in-plane electric field. The white arrows show the orientation of the transmission axes of the polarisers and analyser. **b)** results from simulations of the LC director when the electric field was applied at 45° relative to the transmission axis of the polariser. **c)** Corresponding results of simulations for light transmitted through the microlens between crossed polarisers using Jones matrices and the refractive index properties inferred from the director profiles shown in (b). The images in (b) and (c) correspond to the same voltages shown in (a).

The imaging capability of the microlenses was examined by using an optical polarising microscope. A 255 µm diameter LC microlens was first examined by using a 25 µm grid as an object that was firmly attached to the substrate of the LC microlens. The distance between the grid and the LC lens plane (p) was equivalent to the thickness of the glass substrate, which was 1.1 mm. The distance between the lens plane and the image is defined by either q_1 or q_2, which represent the distances from the images to the lens planes when the applied voltage was 0 V and 200 V, respectively. Images were formed on a CCD camera via the aid of an objective lens. By using the formula, $n_g/p + 1/q = 1/f$, the focal length of the LC lens can be estimated (f). Here n_g represents the refractive index of the glass substrate, which was 1.52. Figure 4.18 shows an illustration of the process and the concept of the two image planes.

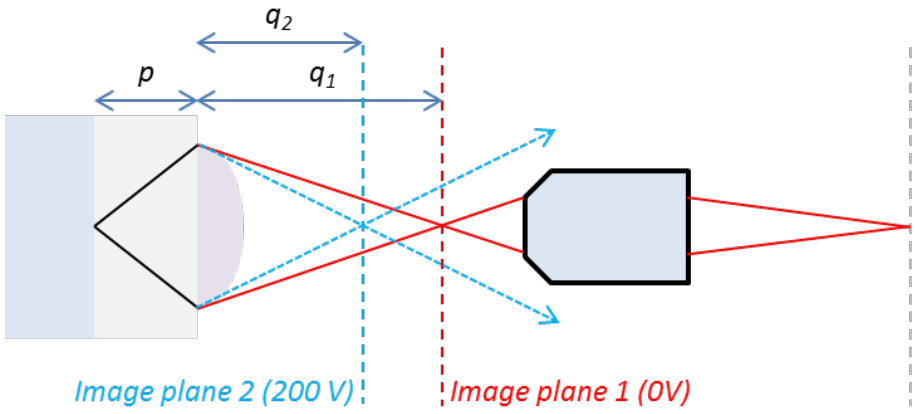

Figure 4.18: Illustration of the process for using a microscope to visually inspect the image plane of the LC microlenses. The object was a 25 µm spaced grid etched onto a glass microscope slide.

A linear polariser was positioned just above the light source of the microscope so that the input light to the lens was linearly polarised. The transmission axis of the polariser was then adjusted so that it was parallel to the direction of applied electric field. In this configuration, for an applied voltage of 200 V_{pp}, the incoming linearly polarised light experiences the extraordinary refractive index of the nematic LC, n_e = 1.74 at 20°C and 633 nm, and therefore a reduced focal length in comparison with the voltage off state. This change in the focal length can be seen in Figure 4.19(a), which shows that when the incident polarisation and applied electric field are collinear, the image formed in image plane 1 gradually becomes out of focus (see schematic in Figure 4.18 for the definition of the image planes). In contrast, when the incident polarisation is aligned perpendicular

to the electric field direction, the incident light does not experience any change in the refractive index. Therefore, in this case, the focal length will remain the same regardless of the amplitude of the applied electric field, see Figure 4.19(b).

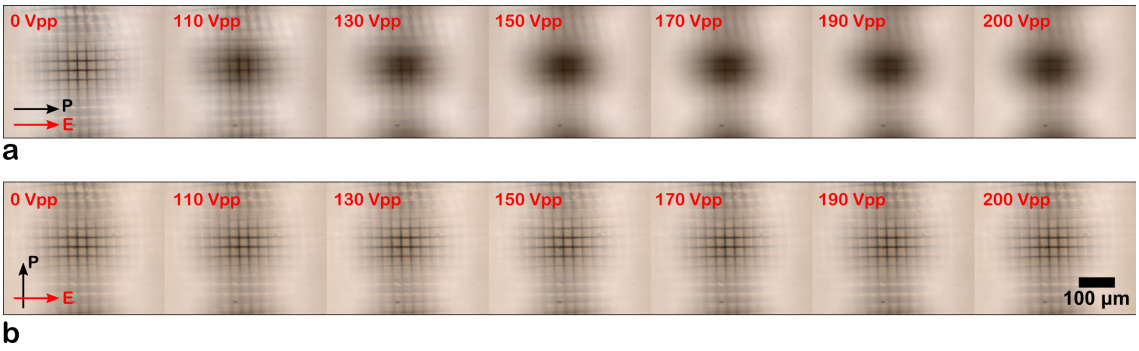

Figure 4.19: Images of the grid formed by 255 µm diameter LC E7 microlens for different applied voltages when the incident polarisation was either **a)** parallel to or **b)** perpendicular to the direction of the applied in-plane electric field. The black and red arrows represent the orientation of the transmission axis of the polariser and the direction of the applied in-plane electric field, respectively. The spacing between the lines in the grid is 25 µm.

For voltages from 0 – 100 V_{pp} the microlenses are polarisation insensitive and are in accordance with the findings in Ref [7]. However, as can be seen in Figure 4.19, above 100 V_{pp} the microlenses become polarisation sensitive, with focal lengths that differ depending upon whether the polarisation is aligned parallel or perpendicular to the direction of the applied electric field. As an example, the left-hand image in Figure 4.20 shows an in-focus image at image plane 1 without the application of an electric field (for the case of the electric field and incident polarisation being colinear) whereas the right hand image shows an in-focus image at the second image plane 2 with a voltage of 200 V_{pp}. The in-focus image at plane 2 was found to be formed at a shorter focal length with reduced magnification, consistent with the larger value of the refractive index. As noted above for the case when the polarisation is aligned orthogonal to the direction of the applied electric field there is no change in the focal length and the location of image plane, irrespective of the applied voltage.

Quantitative measurements of the focal length of the microlens at various voltages were carried out using the method shown in Figure 4.13 and the results are plotted in Figure 4.21. For what follows, the incident polarisation was aligned along the direction of the applied electric field. At 0 V_{pp} the measured focal length was found to be $463\left(\pm 10\right)$ µm.

From 0 V_{pp} to 100 V_{pp} there was no change in the intensity profile, i.e., no change in the focal length was observed.

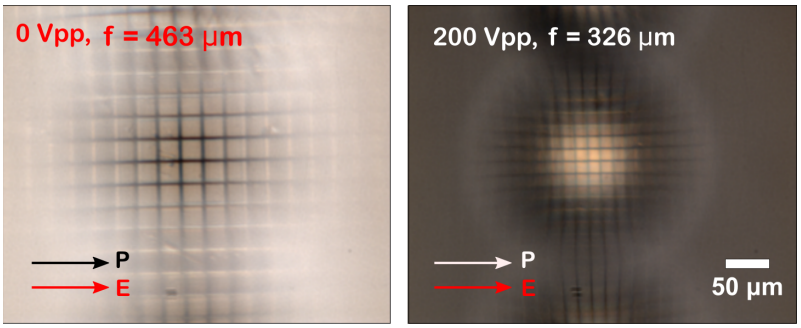

Figure 4.20: Demonstration of the bifocal tunability of the focal length of a 255 µm diameter LC E7 microlens. The image of the grid can be formed at different image planes since the focal length of the LC lens can be tuned to either 463 µm or 326 µm depending on the applied voltage.

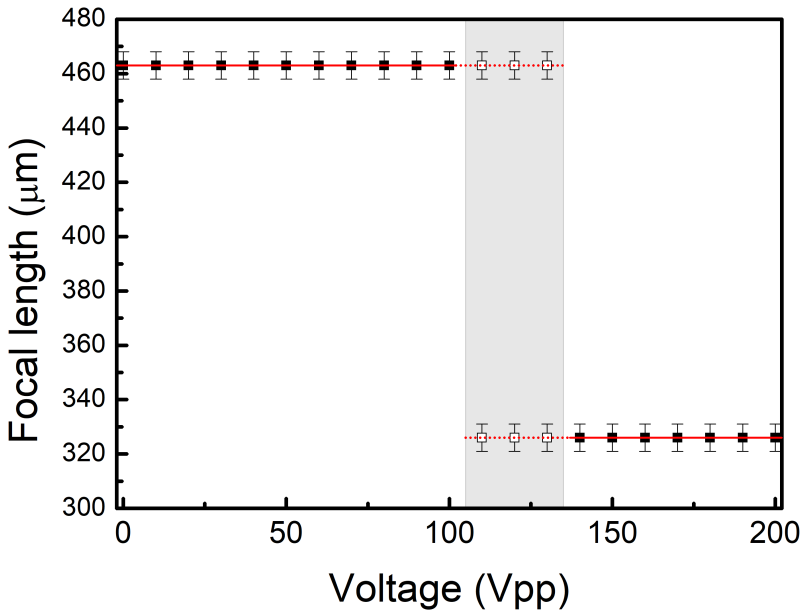

Figure 4.21: Focal length as a function of the applied voltage for the 255 µm diameter microlens. In this case the configuration is the same as that shown in Figure 4.19(a), i.e. the direction of the electric field is aligned parallel to the polarisation of the incident light.

For a range of voltages, from 110 V_{pp} to 130 V_{pp}, the LC microlens appeared to exhibit, to some degree, two focal planes. The shaded region in the graph corresponds to the range of voltages for which this behaviour was observed, which is also evident in the polarising microscopy images as shown previously in Figure 4.21. It can be seen that at these voltages the LC director only aligns with the electric field in a small central region. The transition of the LC director from the centre to the periphery results in regions with

different refractive index profiles, which focuses incident light to two separate planes, which is emphasised in Figure 4.22. The image formation of the underlying grid shows the duality of the focus.

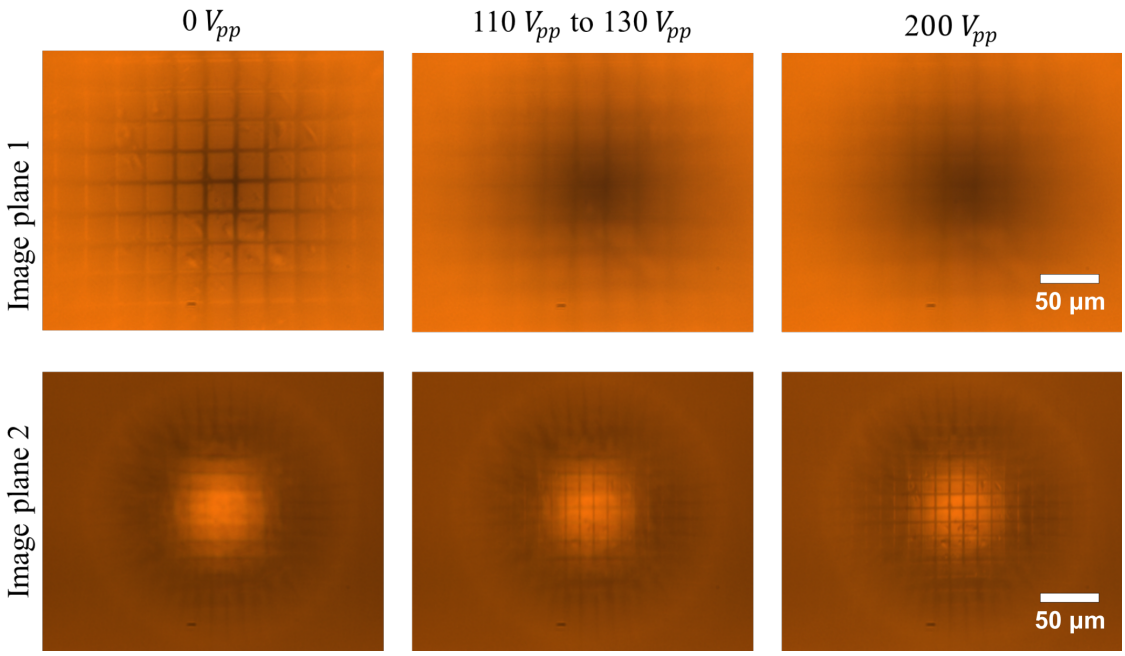

Figure 4.22: Dual focus of the 255 µm diameter microlens. The image of the underlying grid is formed at image plane 1 and 2 when the applied voltage is 0 V_{pp} and 200 V_{pp}, respectively. The behaviour of dual focus can be verified by the images formed at both image planes 1 and 2 between 110 V_{pp} to 130 V_{pp}.

The reason for the two focal planes is due to the two separate domains that form in the droplet. As can be seen in the simulation of the LC director and POM images in Figures 4.15 and 4.16, a separate domain is formed within the droplet whereby the director aligns with the electric field direction. This gives rise to a new, shorter focal length. However, between applied voltages of 110 V_{pp} and 130 V_{pp} the central domain coexists with the outer domain for which the director is aligned near orthogonal to the plane of the glass substrates, which corresponds to the smaller refractive index and the longer focal length that exists in the absence of an applied voltage.

From 130 V_{pp} to 200 V_{pp}, the focal length was reduced to a single value of 323 (± 10) µm and remained unchanged with increasing voltage. As seen in Figure 4.21, the experimentally measured focal length appears to show bifocal tuning, with only two focal lengths that are accessible using an applied voltage. The red lines show the theoretical

values of the focal length of the LC lens calculated for a plano-convex LC microlens with a refractive index of either n_o = 1.52 (0 – 110 V_{pp}) or n_e = 1.74 (130 – 200 V_{pp}).

The droplet boundary and profile was also monitored using shadowgraphy imaging to see whether there was any alteration in the shape of the microlens at the high amplitude voltages. However, no noticeable variation in the microlens profile, through electrowetting or dielectrophoresis for example, was observed, as can be seen in Figure 4.23. In Figure 4.23 (b) the red dotted line corresponds to a sphere and it can be seen that at 0 V_{pp} and at 200 V_{pp} no change/offset in the lens profile was observed. The change in the focal length is therefore considered to be due solely to a reorientation of the LC director in the presence of an applied electric field.

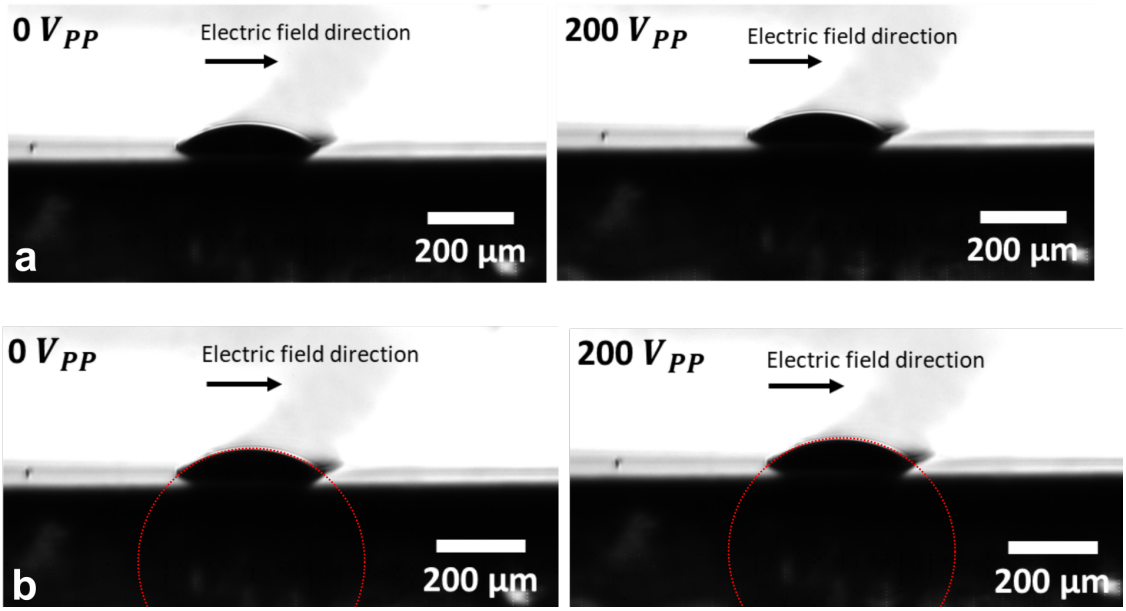

Figure 4.23: Shadowgraphy imaging of the 255 µm diameter LC E7 microlens showing the lens profile at voltages of 0 V_{pp} and 200 V_{pp}. No change in the contact angle is observed. The lens is on a homeotropic aligned glass substrate.

Table 4.1 presents data for microlenses of different diameters formed by increasing the number of droplets deposited at a given location. The focal lengths f_1 and f_2 correspond to no electric field and the case when the incident polarisation is parallel to the electric field direction, respectively. The table also shows the range of voltages for which the dual focal length region is observed. For the 120 µm and 154 µm diameter

microlenses, which are small, no switching was observed for the range of voltages considered in this study.

Table 4.1: Focal length data for a range of voltages for microlenses of different diameters that were formed by printing a number of drops at the same location on the substrate.

No of drops	Lens diameter	Threshold Voltage	Dual focal length region	f_1	f_2
	(µm)	(µm)	(µm)	(µm)	(µm)
9	255	110	110 – 130	463	323
8	244	120	120 – 140	450	310
7	234	130	130 – 150	430	302
6	222	150	150 – 170	402	286
5	210	160	160 – 170	381	271
4	194	170	180 – 190	352	250
3	177	190	190 – 200	321	228
2	154	NA	NA	279	NA
1	120	NA	NA	220	NA

4.4 Summary and Conclusion

In conclusion, this chapter has demonstrated the fabrication of electrically tunable bifocal microlenses by using drop-on-demand inkjet printing to deposit nematic LCs precisely in the 500 µm gap between in-plane electrodes. The microlenses printing procedure links back to Chapter 3 where the conditions to generate satellite free droplets of nematic LC E7 has been explained.

Droplets of nematic LC E7 were printed on a homeotropic alignment glass substrate. A number of droplets were printed to investigate the standard deviation in the printed droplet diameters. The printing substrate showed excellent uniformity of droplet profiles and provided near homeotropic alignment to the LC director inside LC droplets.

The in-plane switching substrates were produced by using a lab-made photolithography process. The IPS devices were prepared by etching the ITO to form a 500 µm gap and to promote homeotropic alignment of the LC director a surfactant solution was spun coated onto the substrate. A range of lens sizes were printed with a 80 µm MicroFab nozzle resulting in lens diameters ranging from 120 to 255 µm, depending upon the number of

drops deposited per microlens. These printed droplets were found to form plano-convex lenses after impact with the substrate.

The simple electrode arrangement on the substrate allowed understanding of the electrical tunability of the printed LC microlenses, which was found to exhibit a bifocal behaviour due to the reorientation of the LC director in the droplet in the presence of an applied voltage. The experimental LC director reorientation was compared with simulated light transmission results for the LC director which was extracted for each case from COMSOL software. The LC director model and corresponding light transmission results provided a good match with the experimental POM images and increased the understanding of LC director behaviour inside a LC droplet.

Following this, the chapter goes on to present imaging properties and focal length measurements. Without an applied voltage, the microlenses were found to be polarisation insensitive and have an inherent focal length that ranges from 220 to 463 μm depending upon the radius of curvature of the lens. However, in the presence of a high amplitude applied voltage the focal length of the 255 μm diameter microlens is found to decrease by 140 $\left(\pm 10\right)$ μm, corresponding to the larger refractive index of the LC along the director. Furthermore, it was also found that there is a range of voltages for which two focal planes are observed due to two separate domains in the LC droplet each characterised by a different refractive index profile. These findings could be of importance for 3D imaging applications where the two separate focal planes could be used to give the impression of depth perspective.

CHAPTER 5

SPATIALLY-PATTERNED PRINTED POLYMER DISPERSED LIQUID CRYSTAL DEVICES

This chapter describes the inkjet printing of polymer-dispersed liquid crystal to form spatially patterned privacy/smart windows. Following a photo-induced phase separation process, the printed droplets formed 'pixels' that have the ability to appear and disappear in the presence of an electric field. The chapter describes how drop-on-demand inkjet printing can be used to generate new privacy/smart windows with logos and images embedded that can be switched off and on with the application and removal of a voltage. Some of the results presented in this chapter formed the basis of the publication Waqas Kamal et al. 'Spatially Patterned Polymer Dispersed Liquid Crystals for Image-Integrated Smart Windows' *Advanced Optical Materials* (19, 2101748, 2022).

5.1 Introduction

Polymer dispersed liquid crystals (PDLC) are an important class of LC and polymer composite. [16, 93] In general, PDLC films are composed of micron-sized nematic LC droplets that are suspended in a polymer matrix. The alignment of the LC director inside the droplets determines the electro-optic properties of the film. For the LC droplets, the director alignment is generally either bipolar or radial. [94] However, the net orientation of the LC director in each droplet is random and this causes incident light to scatter as it passes through the film. The scattering is due to a refractive index mismatch between each of the LC droplets and the polymer binder. [95] In the presence of an electric field, the director in each droplet aligns along the direction of the applied electric field, which results in a match in the refractive index between the polymer matrix (n_p) and each LC droplet (specifically the ordinary component of the refractive index, n_o). [96, 97] This phenomenon allows light to pass through unscattered, and the PDLC film becomes transparent. Figure 5.1 illustrates both light scattering (voltage off) and transmission (voltage on) states.

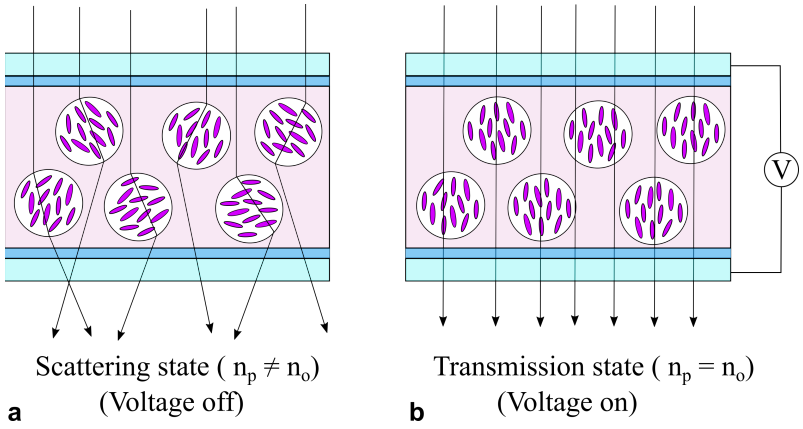

Figure 5.1: A schematic of a PDLC film **a)** with no applied voltage in a light scattering state. The LC director is randomly oriented within the droplets. **b)** with an applied voltage that orients the LC director inside the LC droplets so that the ordinary refractive index of the droplets and the polymer binder are matched. This results in switching the device to a transparent state.

The most common process employed to manufacture PDLC films involves the phase separation of a homogeneous mixture of LC and pre-polymer. The three commonly used phase separation processes, namely, photopolymerisation induced phase separation (PIPS), temperature-induced phase separation (TIPS), and solvent-induced phase separation (SIPS), have been demonstrated previously. [98] Each method produces PDLC

films with different LC droplet morphologies, which ultimately determines the resulting electro-optic properties of the PDLC device. [95] The PIPS technique provides a wide degree of control over droplet size and shape when compared to emulsification or TIPS/SIPS techniques. [10,99,100] For this reason PIPS can be used to form large area PDLCs films.

Spatially patterned PDLCs have been of interest in recent years. To produce PDLC films with spatially varying properties, the photo-polymerisation process has been performed with the aid of a photomask or hologram to create patterns or spatial variations in the film morphology. These method enables curing light with a spatially varying intensity to be applied to the PDLC films to form separate polymer-rich and LC-rich domains. [95, 101–105] Other methods reported for producing a patterned PDLC film include the use of high-power LEDs, chemically patterned substrates and using mechanical stamping processes. [106, 107] Such methods show a high degree of accuracy at the micro/nanoscale, although these techniques often require multiple additional processing steps and are not widely compatible with the production of large-area PDLC films, particularly those that have spatially varying properties.

As discussed in Chapter 3, advanced manufacturing techniques such as drop-on-demand (DoD) inkjet printing have rapidly emerged as scalable techniques that allow functional inks to be delivered to a substrate at high speeds and with a high degree of accuracy. This digital fabrication process offers new ways to manufacture large area PDLC films in the form of intricate patterns or logos as compared to conventional photo-polymerisation based techniques.

This chapter describes how DoD printing can be used to create patterned PDLC films and presents results that demonstrate the satellite-free printing of an LC-prepolymer ink without secondary ligament break-up, along with the light scattering properties of the individual printed PDLC droplets.

5.1.1 Smart windows

Windows are an essential component of any building as they perform various important functions such as providing occupants with a view to the external environment, optimum ambient illumination levels, air ventilation, and passive solar gain. Conventional glass windows become less energy efficient due to the substantial amount of thermal losses in both hot and cold climates. [108] This has led to the pursuit of so-called smart window technology. The term 'smart window' refers to panels or adhesive films that have energy-saving functionality by controlling the light that is transmitted into and out of buildings. The application of such windows has the potential to lead towards a drastic reduction of energy consumption by decreasing cooling loads, heating loads and the demand for electric lighting.

A report published in 2017 estimated that the global market for smart windows was worth up to $2.6 billion in 2016 and is forecast to reach up to $8 billion by 2022. [100,109] To date, various techniques to develop new smart windows have been proposed that include PDLC films, suspended particle devices, electrochromic (EC), thermochromic, photochromic, gasochromic, and nanocrystal devices. [110–115] In contrast to PDLC technology, these alternative devices are typically complex and consist of several functional layers, making it difficult to manufacture with spatially varying properties. [108]

The future direction of smart windows is to enable the development of energy-efficient buildings. However, modern architecture also requires aesthetically pleasing features such as windows that can enhance the internal décor and transform the workplace into a comfortable and pleasant environment. This chapter demonstrates the fabrication of smart windows with printed emblems and logos. This type of smart window is particularly suited to modern architecture as it offers an electrically-switchable alternative to conventional blinds or curtains as the printed emblem/logo can be switched between an opaque and transparent state with the application of a voltage.

5.2 Manufacturing PDLC pixels using Inkjet Printing

The PDLC droplets, termed as 'pixels' in this work, were printed by employing an inkjet printing technique as explained in Section 3.3.2, chapter 3, and a prepolymer ink formulation composed of nematic LC, E7, and Norland glue, NOA65. The nematic LC E7 was chosen because its material properties are well characterised and documented and, importantly, it has been shown to be compatible with DoD printing. [7, 44, 89, 116] In addition, E7 has a moderately large birefringence (Δn) which enables strong scattering in the voltage off state. [95] NOA65 was chosen because this forms a homogeneous mixture with the LC before illumination-photopolymerisation with UV light, and it has been employed previously as the polymer binder in PDLC systems. [89, 117] The ink preparation procedure and composition is described in the following subsection.

5.2.1 Ink preparation

The nematic LC mixture E7 (Synthon chemicals Ltd.) with refractive indices of n_o = 1.52 and n_e = 1.74 at λ = 633 nm and 20 °C was used as the LC component. The Norland Optical Adhesive, NOA65, (from Norland products) with a refractive index of n_p = 1.52, was used as the polymer binder. [89] The LC and glue formulation were prepared as a 1:1 composition. The 1:1 composition was chosen as it is acknowledged in literature to provide smaller LC droplets morphology and better light scattering properties. [118] Furthermore, the preliminary results of using higher concentrations of LC such as 60:40 resulted in separated regions of LC and glue after the photopolymerisation process. The LC was becoming phase-separated either in the centre or around the periphery of the droplet (see Figure in Appendix A).

The formulation was mixed over a hot-plate and stirred for 24 hours at 300 rpm at 65 °C. The temperature was chosen in order to raise the formulation above the clearing temperature of the LC, T_c = 58 °C, and to reduce the viscosity and surface tension of the mixture. Figure 5.2 shows a schematic illustration of the ink preparation process.

5.2.2 Inkjet Printing and Device Assembly

The inkjet printing of the PDLC ink formulation and the subsequent device assembly is schematically illustrated in Figure 5.3. The prepolymer PDLC ink formulation was printed onto an Indium tin oxide (ITO)-coated glass substrate. Before printing, the ITO-coated glass substrates were cleaned with isopropyl alcohol and rinsed with deionised water before being sonicated for 20 min in acetone. The substrates were then baked for 2 min to ensure that they were completely dry.

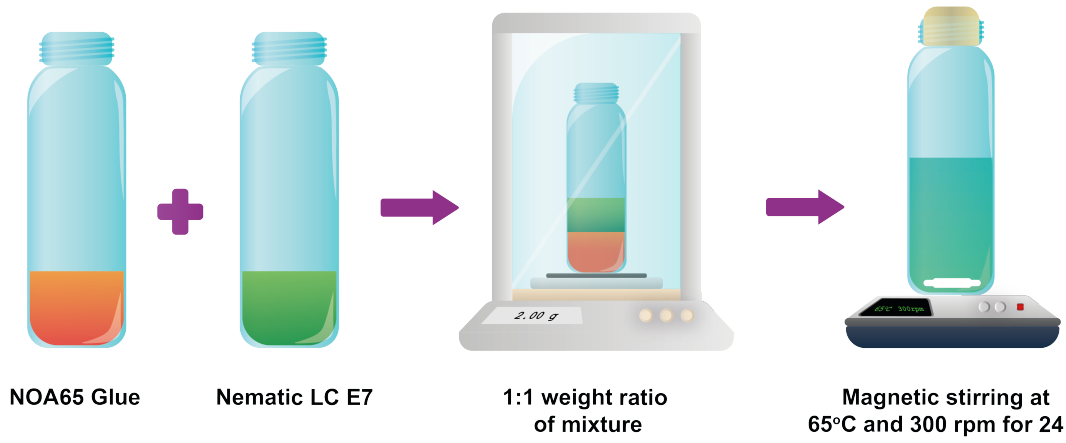

Figure 5.2: PDLC ink preparation process that involved the Norland glue, NOA65, and the nematic LC, E7, in a concentration of 1:1 by weight. The mixing was performed on a hot-stage with a magnetic stirrer.

The DoD inkjet printing results presented in this chapter were mainly obtained using the MicroFab Jetlab-II. However, the preliminary printing trials carried out to understand the conditions required to dispense the PDLC ink droplet were performed on the bespoke inkjet printing system (see Section 3.3.1, Chapter 3). As discussed previously, both printing systems incorporate printing nozzles of a similar size. Therefore, the printing parameters obtained in the form of actuation waveform and printhead temperature can reliably be implemented in both printing systems. The substrate onto which the LC formulation was printed was held at room temperature of 20 °C for all the samples presented in this study.

After printing, spacer tape (thickness around 10 µm) was attached to both edges of the printed sample and placed so as to define an approximate device thickness (Figure 5.3, step 3). A top electrode was then placed such that both ITO-coated surfaces faced each

other in order to form a complete glass cell. The substrates were clamped down using clamps to ensure that an even pressure distribution was applied across the cell (Figure 5.3, step 4). Following that, the substrates were fastened using a rapid epoxy adhesive (from Araldite) at room temperature. Finally, the device was photocured using an ultraviolet light (λ = 365 nm) source (CS2010, Thorlabs) with power density of 65 mW/cm^2 for 4 min, which was measured using a handheld power meter (PM100D, Thorlabs) attached to a photodiode (S120VC, Thorlabs) (Figure 5.3, step 5). All of the above steps, including inkjet printing, were carried out under the illumination of yellow light until the sample was fully phase separated. For the application of an electric field, wires were connected to the ITO substrates using indium shot. The step 6 in Figure 5.3 illustrates a complete stack of final device. The droplets shape after device assembly as shown in the figure is simplified as there is likely to be some distortion of the droplets with the attachment of the top substrate due to the uneven mechanical pressure and capillary effects.

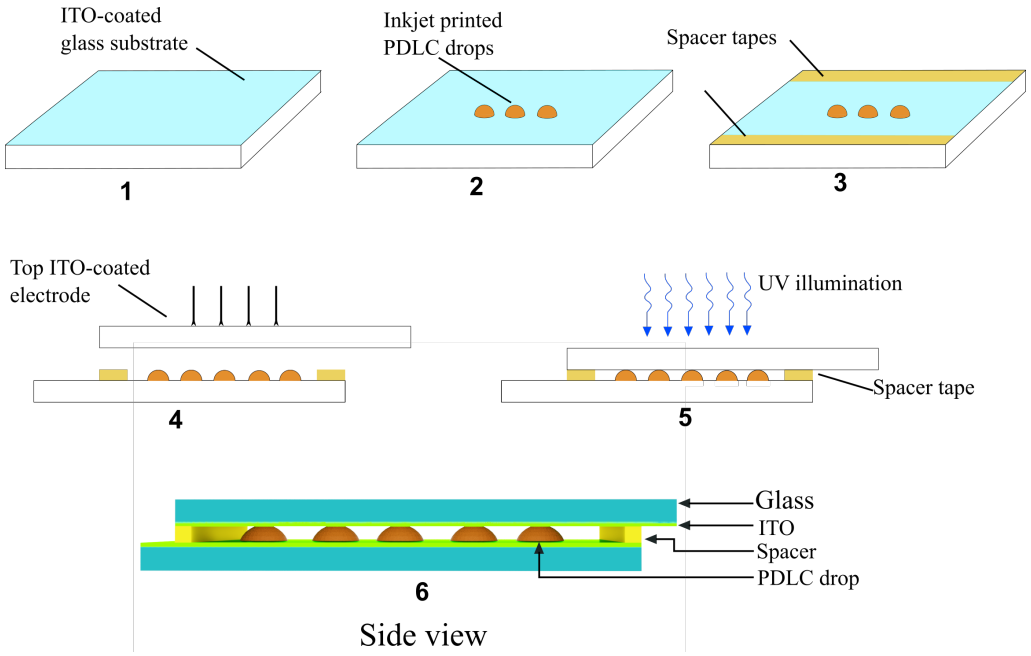

Figure 5.3: Schematic illustration showing the procedure followed for the addition of the top glass substrate and the illumination of the sample using ultraviolet light so as to form the polymer binder in each of the separate printed PDLC pixels **1):** Cleaned ITO coated glass substrate **2):** inkjet printing onto the ITO substrate. **3):** spacer tape is applied on both sides of the printed substrate. **4):** The top substrate is fastened, and the device is clamped on both sides. The top and bottom substrates were subsequently fastened with a rapid epoxy. **5):** The complete device is illuminated with UV-light. **6):** Showing a side view of the resulting device stack.

5.3 Printability and Rheological Properties of the PDLC Ink

5.3.1 Surface Tension and Viscosity

The PDLC ink, which is composed of nematic LC E7 and NOA65 glue, was characterised in terms of physical properties such as the dynamic viscosity and surface tension. The viscosity and surface tension measurements were recorded using a Physica MCR301 rheometer (from Anton Paar) and bubble tensiometer (from SITA) at different temperatures. The measurements of these properties at different temperatures are discussed below.

The plot in Figure 5.4 shows the dependence of the dynamic surface tension of the PDLC ink as a function of the bubble lifetime at three different temperatures. Here the bubble lifetime means the surface age of the bubble in milliseconds. As can be seen in the plot, different times of ageing of the bubble result in different values for the surface tension, especially when the PDLC ink was measured at 23 °C and 35 °C temperature. However, at 65 °C temperature the surface tension is largely constant with time and there is only a small variation for relatively short bubble times between 100 - 1000 ms. It should be noted that the nematic to isotropic transition temperature of the nematic LC E7 is 58 °C.

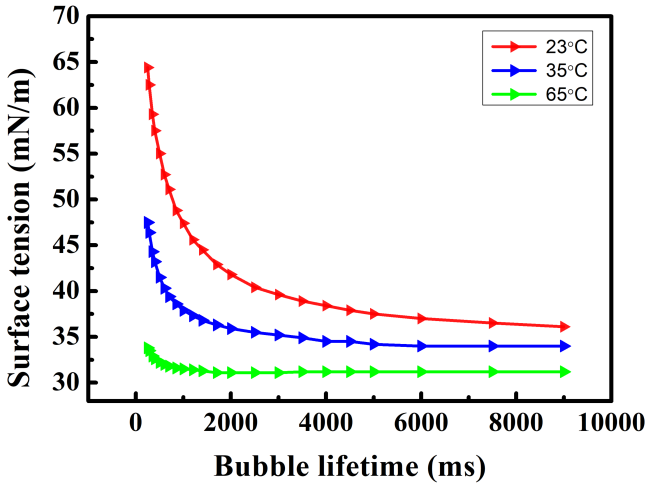

Figure 5.4: Surface tension measurement of the PDLC ink formulation. The pre-polymer ink was composed of 50 wt.% of LC E7 and 50 wt.% of NOA65 glue. The graph shows dynamic surface tension as a function of bubble lifetime at three different temperatures. The measurement was performed by using a SITA pro-line t15 bubble tensiometer.

The time dependent surface tension of a mixture of surfactants is due to the adsorption kinetics of the surfactants, which has been extensively discussed in the literature. [119, 120] Considering the literature and the results in Figure 5.4, it can be argued that the variation in surface tension is due to the LC behaving as a surfactant. In the nematic phase a large variation in surface tension was observed. However, above the clearing temperature, due to the isotropic nature of the fluid, this behaviour appears to largely disappear.

To investigate the effect of temperature on viscosity, the PDLC ink viscosity was recorded at 5 °C increments over the temperature range of 10 – 70 °C. As shown in Figure 5.5 the bulk viscosity depends strongly on the temperature. The viscosity dramatically reduces from 811.31 $\mathrm{mPa.s}$ at 10 °C to 25.4 $\mathrm{mPa.s}$ at 70 °C. At the higher temperature of 70°C, the viscosity value comes closer to the range of 3 - 25 $\mathrm{mPa.s}$, which is the viscosity range recommended by the nozzle supplier of inkjet printing system.

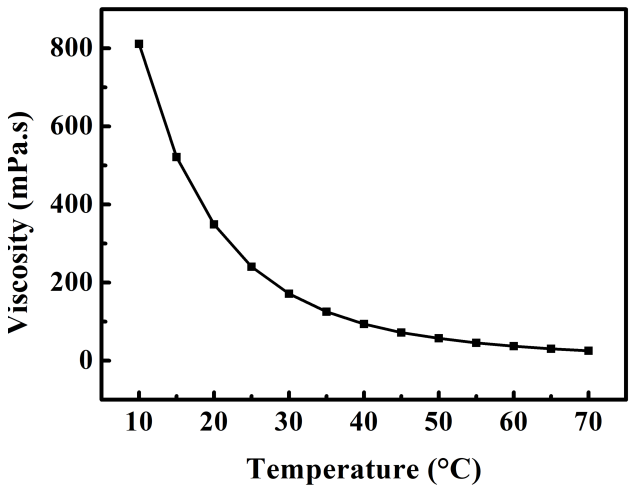

Figure 5.5: Shear viscosity measurement of the PDLC ink formulation at shear rate of 300 $1/\mathrm{s}$ as a function of temperature. The prepolymer ink was composed of 50 wt.% of LC E7 and 50 wt.% of NOA65 glue. The measurement was performed using a Physica MCR301 rheometer.

5.3.2 Conditions for Printing the PDLC Ink

The above results suggests that the addition of prepolymer has significantly increased the viscosity of the LC/polymer formulation (PDLC ink) and make it difficult to generate droplets due to large viscous forces at room temperature. Therefore, to print PDLC ink

formulation, it was essential to understand the conditions required to create a reproducible and reliable drop generation process. The experimental scheme directed in Chapter 3 was employed to determine the printing conditions in the form of range of printhead temperature and input waveform amplitude for PDLC ink.

As discussed in the previous section, the PDLC ink exhibited a temperature-dependent viscosity and surface tension. The measurement of these properties at different temperatures is presented together in Table 5.1. It can be seen that at 70°C the bulk viscosity and surface tension are found to be reduced from 811.31 $\mathrm{mPa.\,s}$ and 36.1 $\mathrm{mN \cdot m^{-1}}$ at room temperature to 25.4 $\mathrm{mPa.\,s}$ and 31.2 $\mathrm{mN \cdot m^{-1}}$, respectively. These reduced material parameters at elevated temperatures are found to be compatible with the inkjet printing process, which is discussed in the following section.

Table 5.1: Surface tension, density and viscosity of the 50 wt.% NOA65 + 50 wt.% E7 PDLC ink formulation.

Temperature	**Surface tension**	**Density**	**Viscosity**
(°C)	$(\mathrm{mN \cdot m^{-1}})$	$(\mathrm{g \cdot cm^{-3}})$	$(\mathrm{mPa \cdot s})$
20	36.1	1.08	348.7
40	34	1.08	93.8
70	31.2	1.08	25.4

The unipolar waveform which was used for a pure nematic LC (Figure 3.5, Chapter 3), was found compatible for the LC/prepolymer ink. However, waveform parameters such as voltage amplitude, rise time, fall time, dwell time, which were optimised for LC E7 were found insufficient to produce PDLC ink droplets. The waveform form was tailored for the new ink. A reliable droplet generation process was observed with 3 µs, 15 µs, and 4 µs rise, dwell and fall times, respectively. The driving voltage amplitude was 90 V, which was varied from 90 – 110 V so as to form a stable droplet at different ejection velocities. To reduce the bulk viscosity and surface tension, the print head temperature was varied between 65 - 70 °C so as to generate a satellite-free droplet. The printhead temperature was not raised above 70 °C due to its heating limit. Also, the type of printing nozzle used was not recommended to operate above 70 °C temperature. Figure 5.6 shows the in-flight motion of a single droplet which could be reliably generated during one jet-

ting cycle. The drop generation frequency was set to 500 Hz. During flight, the observed drop diameter was found to be 65 (± 5) µm and the droplet volume was 180 (± 30) pl.

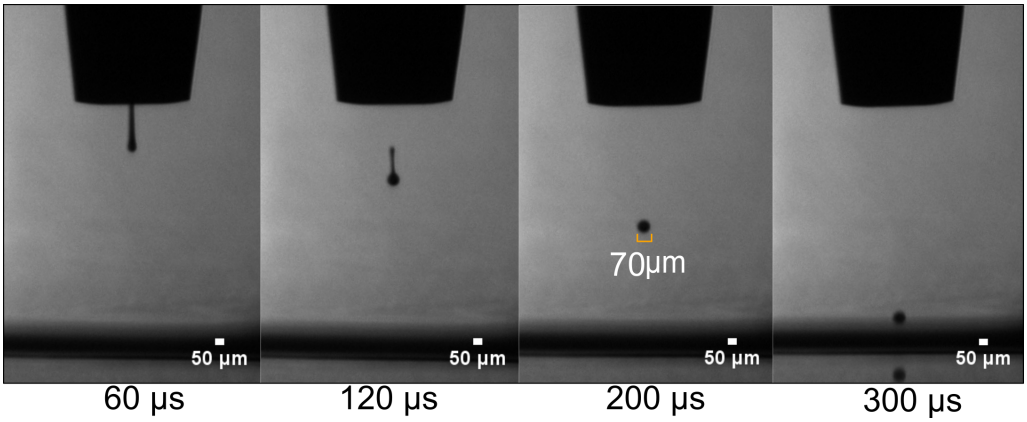

Figure 5.6: Shadowgraphy images showing the deposition of a PDLC ink formulation (50 wt.% NOA65 + 50 wt.% E7) at a temperature of 67 °C over a timescale from 60 µs (just after ejection) to 300 µs (just before impact with the substrate surface). The ink was ejected from an 80 µm diameter MicroFab nozzle.

As discussed in section 3.5.1 of chapter 3, the dimensionless number Z (Oh^{-1}) is a useful metric to define ink printability in terms of other dimensionless numbers such as Reynolds number, Re, and Weber number, We and can be expressed as

$$Z = Oh^{-1} = \frac{Re}{\sqrt{We}} = \frac{\sqrt{\eta \rho L}}{\mu} \tag{5.1}$$

where η, ρ, μ are the surface tension, density, and viscosity of the ink, respectively, and L is a characteristic length, which can be the diameter of nozzle, or drop. It is suggested that a value of $1 < Z < 10$ $(0.1 < Oh < 1)$ is typically required to eject a well-formed single drop without the formation of single or multiple satellite droplets. [42, 50, 54]

In the case of PDLC ink, with the fluid parameters enlisted in Table 5.1 and by using equation 5.1, the Oh number at 20 °C and 70 °C temperature was found to be 6.25 and 0.5, respectively. It evident that at room temperature, the Oh number is too large to perform any printing. However, at 70 °C it reduced to 0.5 which is due to a large reduction in the PDLC ink's bulk viscosity.

Referring back to Chapter 3, although the Oh number serves as useful parameter to define the printable regime however the stability of the droplet generation process depends upon the driving voltage amplitudes which in turn controls the droplet speeds, and more specifically the dimensionless numbers, Re, and We. In the case of pure LC E7, it has been shown that increasing temperature will bring large reduction in viscosity and hence Z or Oh^{-1} number. And by adjusting the printing waveform voltage amplitude and droplet speed a satellite free printing process can be initiated. For nematic LC E7, the experimental observations suggested that the satellite droplets were formed when drop Weber number, We was greater than 48.

In the case of PDLC ink, the printing setup also allowed us to vary the drop velocity by changing the voltage amplitude of the waveform between 90 – 110 V, which controlled the drop velocity to be in the range of 1.38 ms^{-1} and 4.5 ms^{-1} at 67 °C printhead temperature. However, it was found that above a drop velocity of 4.5 ms^{-1}, a spontaneous break-up of the fluid ligament was observed which resulted in the formation of satellite droplets. Therefore, the waveform conditions were adjusted such that the droplet velocity was always less than 4.5 ms^{-1} so as to avoid the formation of satellite droplets that accompany the main printed droplet.

Table 5.2 shows the PDLC ink dimensionless fluid properties in terms of Weber number, We and Reynolds number, Re when measured using the drop velocities in the range of 1.38 - 4.5 ms^{-1} and PDLC ink fluid properties enlisted in Table 5.1. By using a printability map of the form as shown in Figure 5.7, the dimensionless PDLC ink fluid properties at each drop velocity were superimposed on the plot and labelled with star symbol in four different colours. As can be seen in the plot, this corresponds to an Oh number of 0.5 (Z number of 2.04), which is within the range consistent with satellite-free printing. It should be noted that at a temperature of 20 °C the PDLC ink was very viscous, and the corresponding Oh number was found to be 6.25, which is too viscous to print. Hence, printing was performed at an elevated temperature of T = 67 °C. Furthermore, the experimental observations suggested that the satellite droplets were formed when drop weber number, We was greater than 56.

Table 5.2: Dimensionless fluid properties for the PDLC ink (50 wt.% NOA65 + 50 wt.% E7) at a temperature of 70°C. The characteristic length scale L is equal to inner nozzle diameter which is equal to 80 µm (MicroFab nozzle).

Drop velocity	Reynolds number	Weber number	Ohnesorge number	Z number
(ms^{-1})	(Re)	(We)	(Oh)	(Z)
1.38	4.7	5.2	0.5	2.04
2.5	8.5	17.3	0.5	2.04
4	13.6	44.3	0.5	2.04
4.5	15.3	56.1	0.5	2.04

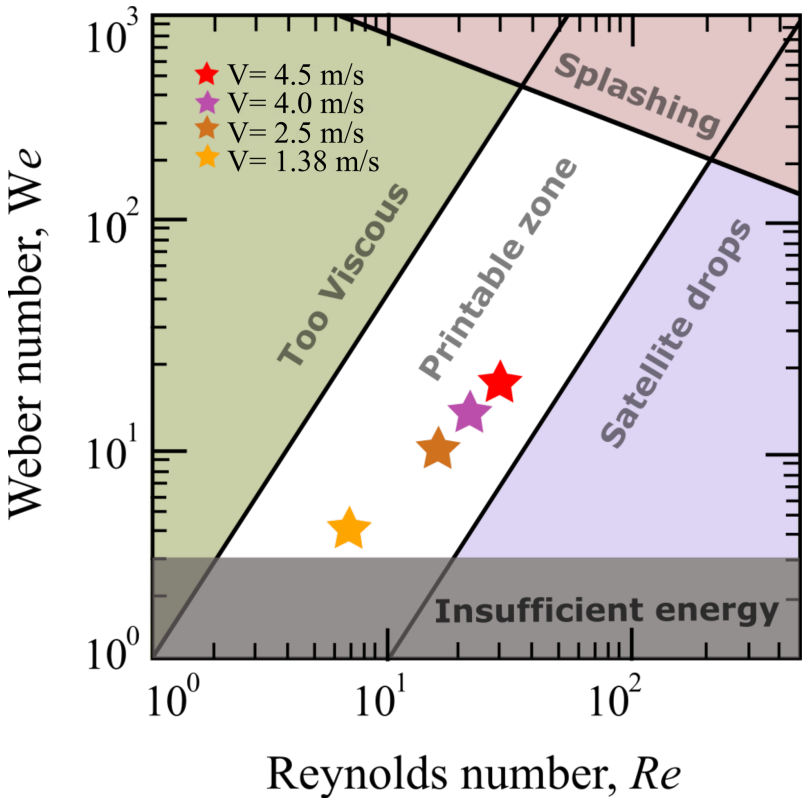

Figure 5.7: Parameter map showing the Reynolds and Weber numbers of the PDLC ink (50 wt.% NOA65 + 50 wt.% E7) at a temperature of 70°C. The figure follows the graph presented in reference, [54] but the stars correspond to the velocities at which no satellites were observed, confirming the printable regime.

5.3.3 Optimisation of Printed PDLC Droplets

After optimising the printing parameters, the PDLC droplets were first printed onto a single ITO-coated glass substrate. The printing substrate was held at a room temperature of 20 °C for all samples used in this study. In order to make small changes to the drop volume on the substrate, the actuating waveform can be adjusted. However, a sub-

tle change in the back pressure can also lead to printing instabilities. (see Section 3.5.4, Chapter 3). Moreover, an alteration to the print waveform would not be sufficient to make a pronounced variation in the drop volume on the substrate. Therefore, to circumvent the issue of potential printing instabilities, the droplet volume was increased by landing multiple drops onto the same position of the substrate. To demonstrate this, both single and multiple droplets were deposited to form PDLC 'pixels'.

The contact angle of the PDLC pixels were calculated from side profile images taken using shadowgraphy. The ImageJ software with the Drop - Analysis plugin was employed to compute the contact angles. As an example, Figures 5.8(a) presents results of the side profile of a PDLC pixel formed by landing 5 droplets of the ink onto the same location of the substrate. The pixel was found to reach an equilibrium state within a few milliseconds where it attains a spherical cap shape with a contact angle of $37^\circ \pm 2^\circ$. Further, the contact angle does not depend upon the pixel volume, as verified for 6 different variable size pixels, which were all found to be $37^\circ \pm 2^\circ$ in each case as shown in Figure 5.8(b).

The morphology of the PDLC pixels was further analysed using a polarising optical microscope (POM). Figure 5.8(c) shows subsequent optical microscope images of printed PDLC pixels that are shown as a side view in Figure 5.8(b). The images were taken soon after the printing process, and in order to prevent any unwanted polymerisation of the pre-polymer from taking place, the microscope was fitted with a filter to block UV light. The example image that was obtained (transmission axes of the polariser and analyser aligned parallel to each other) confirms that the LC and pre-polymer mixture did not appear to phase separate during or after the printing process. Phase separation was only found to take place after the UV illumination process.

5.3.4 Optimisation of Photopolymerisation Conditions

After successful deposition of the PDLC droplets, the next step was to phase separate the LC domains inside the polymer matrix of the printed droplets so that they can efficiently scatter the incident light. The phase separation process was performed by using a photo-

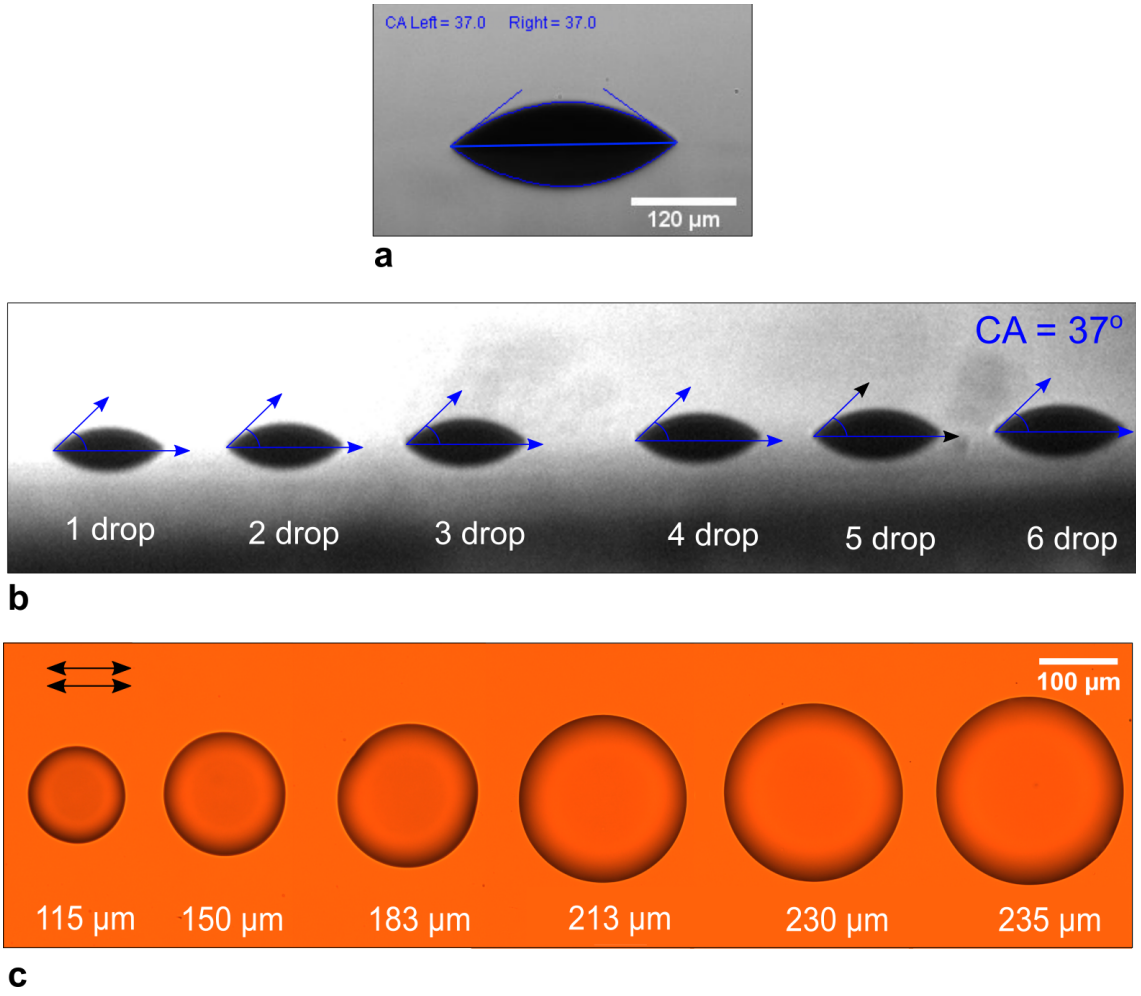

Figure 5.8: **a)** Shadowgraph image of a PDLC droplet with a 37° ± 2° contact angle that has been formed by depositing 5 droplets onto the same location of the substrate. The approximate height of the droplet was found to be 30 (± 5) µm and the droplet diameter was 230 (± 5) µm. **b)** Shadowgraphy image of six variable-size droplets with the same contact angle. The contact angle measurement error is ±2°. **c)** Optical microscope images before UV curing. The image was captured in the presence of a UV filter fitted to the microscope. The image was taken around 10 minutes after the printing process. The two black double-headed arrows on the left side correspond to the transmission axes of the analyser and polariser, which were aligned parallel to each other.

polymerisation method. For this study, the UV power density and exposure times were based initially on values presented previously in the literature. [121] Furthermore, only free-standing PDLC pixels were exposed to UV light for this brief UV curing optimisation analysis.

To begin with, a UV intensity of 30 mW/cm^2 and curing time of 4 minutes were selected. The UV curing process was carried out at a room temperature of 20 °C. Figure 5.9(a) shows the POM images of a single droplet-based PDLC pixel. As evident from

the image, the LC domains formed inside the pixel are rather large and unable to scatter the incoming light efficiently. It can also be seen that the LC has phase separated in the centre, but large regions of LC have accumulated around the droplet boundary. The optical texture for the central region suggests that the LC is aligned radially. The POM image with crossed polarisers on the right shows that the LC domain has a bipolar configuration with drop size less than 10 µm . Figure 5.9(b) shows the results of a single droplet-based PDLC pixel that was UV cured at 60 mW/cm^2 for 4 minutes. As can be seen in the POM image, for these UV curing parameters, the density of the LC domains has significantly increased, leading to a more pronounced light scattering effect. The POM image on the right side reveals that the LC domain size is approximately 5 - 6 µm.

To further enhance the scattering, the UV curing intensity was increased to 70 mW/cm^2 whilst keeping the exposure time the same, and the amount of PDLC deposited was increased by landing five consecutive droplets at the exact location. As can be seen in Figure 5.9(c), the light scattering of the PDLC pixels is much increased by increasing the drop volume and UV curing intensity. The POM images on the right show a high density of LC domains in the polymer binder of the order of 1 - 2 µm in diameter.

5.4 Electro-optic Characteristics of a Printed PDLC Droplet

To evaluate the ability of an array of PDLC droplets to switch between transparent and opaque states, the electro-optic behaviour for a single PDLC droplet was first characterized. To do this, a 230 $\left(\pm 5\right)$ µm diameter PDLC pixel was assembled into a glass device configuration with a spacing of 28 µm. The complete procedure for the device assembly is illustrated in Figure 5.3 in Section 5.2. After device assembly, the printed PDLC droplet was polymerised using UV illumination at a power density of 65 mW/cm^2 for 4 minutes.

5.4.1 Polarised Optical Microscopy

For the printed PDLC droplets to switch from a scattering (voltage OFF) state to a transparent (voltage ON) state, the LC director must re-orient under the application of an electric field. When the LC director is oriented along the direction of an applied electric

field (for the case of a positive dielectric anisotropy nematic LC), the incident light will experience only the ordinary component of the LC refractive index (n_o = 1.52). Since this is closely matched to the refractive index of the cured photopolymer (n_p = 1.52), the incident light is then not scattered by the pixel as illustrated schematically in Figure 5.10(a).

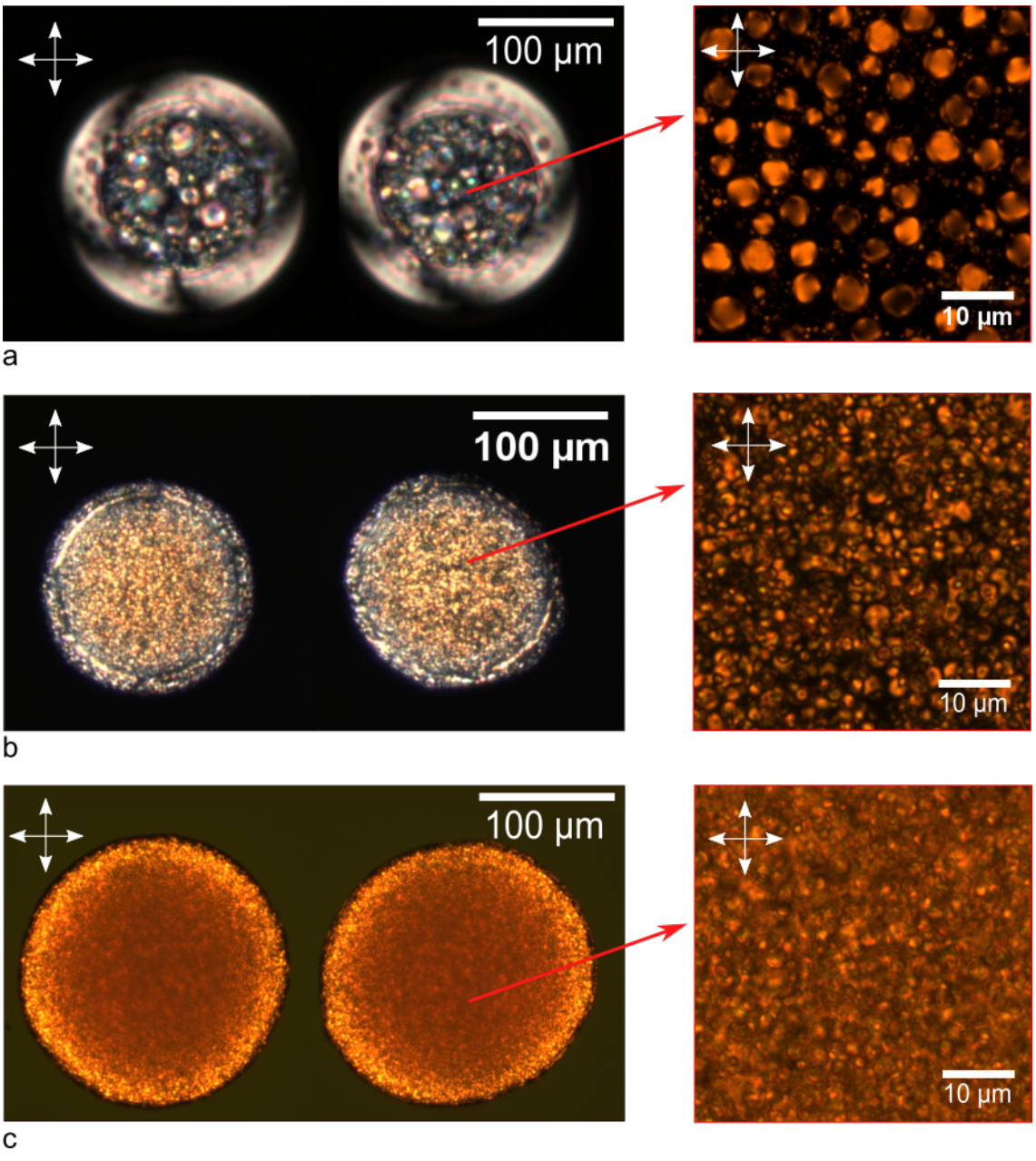

Figure 5.9: Polarised optical microscope images of printed PDLC droplets after irradiation with different UV intensities for 4 minutes. Two printed single PDLC droplets deposited onto ITO-coated glass and cured using power densities of: **a)** 30 mW/cm^2 and **b)** 60 mW/cm^2. **c)** Two printed PDLC droplets where each droplet consists of 5 droplets deposited at the same location. The droplets were UV cured with a power density of 70 mW/cm^2. All the samples were photopolymerised at a temperature of 20 °C.

The electro-optic behaviour for a single PDLC droplet was first characterised using a high numerical aperture objective lens on a POM operated in a transmission mode. Figure 5.10(b) presents results for a 230 (± 5) µm diameter PDLC droplet at a range of voltage amplitudes for a 1 kHz frequency square wave. It is obvious from the image sequence that in the OFF state (0 V_{pp}) the PDLC pixel appears opaque and strongly scatters the incoming light from the microscope lamp. However, upon the application of an electric field the director in the LC domains begins to align along the direction of the applied field, and the PDLC droplet gradually becomes transparent, as shown in the images.

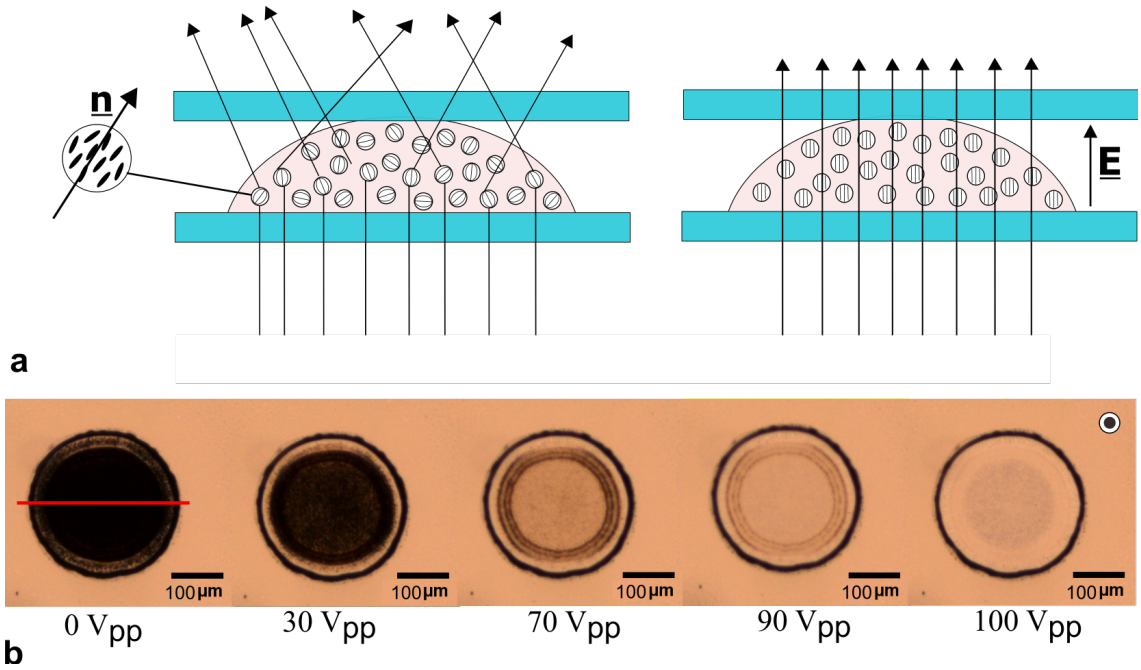

Figure 5.10: a) Schematic representation of a PDLC pixel consisting of micron-sized LC droplets. The unit vector ***n*** represents the alignment of the nematic director for an individual droplet. **b)** POM images of a 230 (± 5) µm printed PDLC droplet (50 wt.% NOA65 + 50 wt.% E7) when subjected to an electric field of different amplitudes. The white circle in the top right corresponds to the direction of the applied electric field, which is out of the plane of the device. Prior to the application of an electric field, a top electrode was fitted resulting in a device thickness of 28 µm between the top and bottom electrodes. Following this, the entire sample was irradiated with UV light (365 nm) at a power density of 65 mW/cm^2 for a duration of 4 minutes at room temperature.

It was found that there was some variation in the switching of the LC domains due to the structure of the droplet which results from the curved shape. The device thickness, however, was a constant value and found to be 28 (± 1) µm. From the line profile in Figure 5.11 and the POM images in Figure 5.10(b), it can be seen that a bright ring initially appears inside the periphery of the PDLC droplet when the voltage amplitude is

between 10 – 20 V_{pp}, and the corresponding electric field strength (E) ranges from E = 0.18 Vμm^{-1} to E = 0.36 Vμm^{-1}. A further increase in the electric field amplitude causes the LC domains at the centre of the droplet to switch before the remainder of the droplet becomes transparent. It can be seen in Figures 5.10(b) and Figure 5.11 that at 100 V_{pp} (E = 1.8 Vμm^{-1}) all of the LC domains in the centre and periphery of the droplet are switched to the ON (transparent) state, although a small degree of scattering can still be observed in the central region of the droplet.

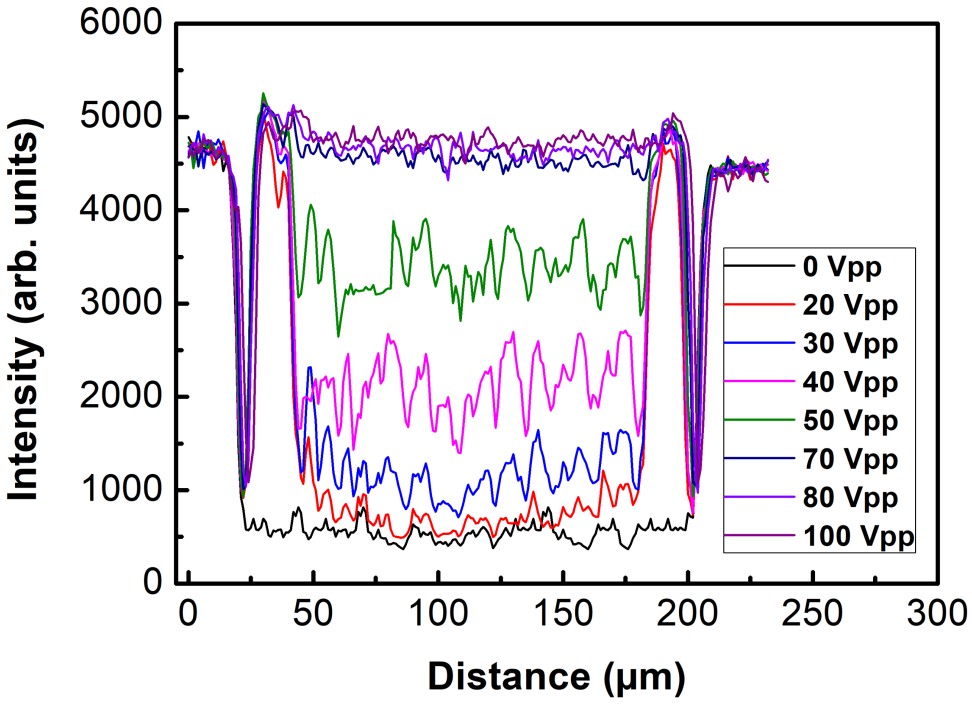

Figure 5.11: Line profile plots extracted from the POM images of the printed PDLC droplet at different voltages. The data was recorded using an Olympus BX51 microscope fitted with a 10× objective lens.

5.4.2 Transmission and Light Scattering Characteristics

The optical arrangement shown in Figure 5.12 was used to measure the optical transmission through the printed PDLC droplets. A continuous wave He-Ne laser (λ = 632.8 nm) with a 150 mm focal length lens was used to illuminate a single PDLC pixel. A neutral density filter was used to adjust the intensity of the laser. A function generator (Tektronix) coupled to a 10× voltage amplifier was used to apply an input signal to the PDLC device. Two photodiodes positioned at approximately a 100 mm distance from the sample were

used to record light transmission and scattering through the printed PDLC droplet.

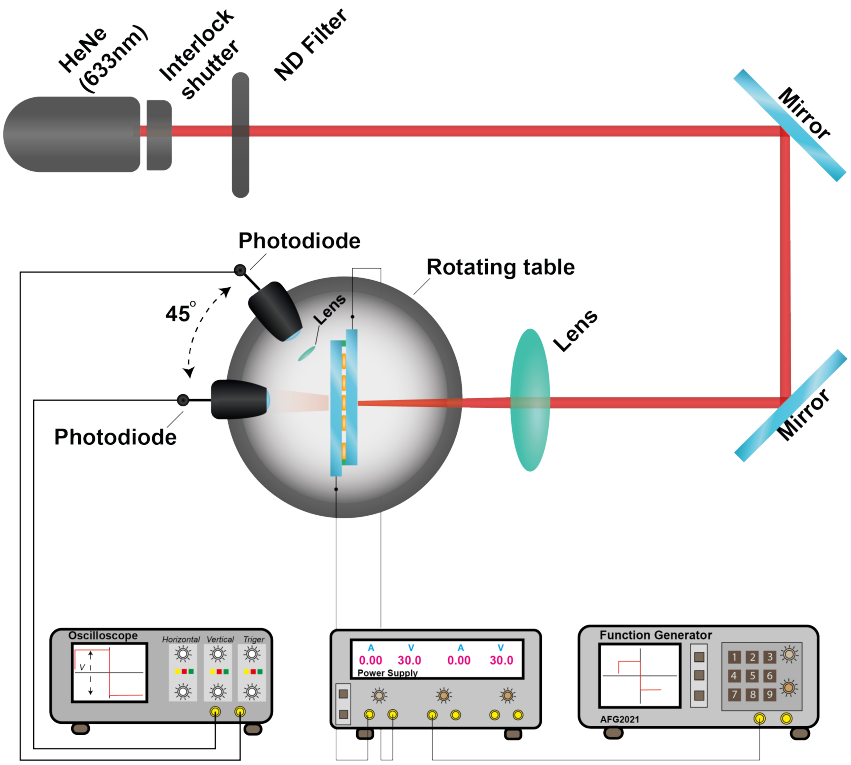

Figure 5.12: Schematic of the experiment used to determine the transmission and scattering properties from a printed PDLC droplet.

Figure 5.13 shows the resulting optical transmission through the printed PDLC droplet. For these measurements, a 1 kHz applied voltage was ramped up from 0 - 200 V_{pp} over a timescale of 6.66 seconds. The results show that the transmission started to increase with the applied voltage before reaching a maximum at 100 V_{pp} while at the same time the scattered light reduces with increasing voltage before reaching a minimum value at the same applied voltage of 100 V_{pp}. For an illumination wavelength of λ = 632.8 nm and at 0 V_{pp}, the transmission is found to be 19% which increases to 85% at 100 V_{pp}. The threshold voltage V_{th}, and saturation voltage V_{sat}, defined as the applied voltage amplitude at which 10% and 90% of the possible transmission range is achieved, respectively, were found to be V_{th} = 38 V_{pp} and V_{sat} = 64 V_{pp}. In terms of electric fields strengths, this corresponds to E_{th} = 0.7 Vμm^{-1} and E_{sat} = 1.15 Vμm^{-1}. The difference in transmission is comparable to observations reported previously on PDLC films of a similar film thickness that have been targeted for use in smart window technologies. [96, 122, 123]

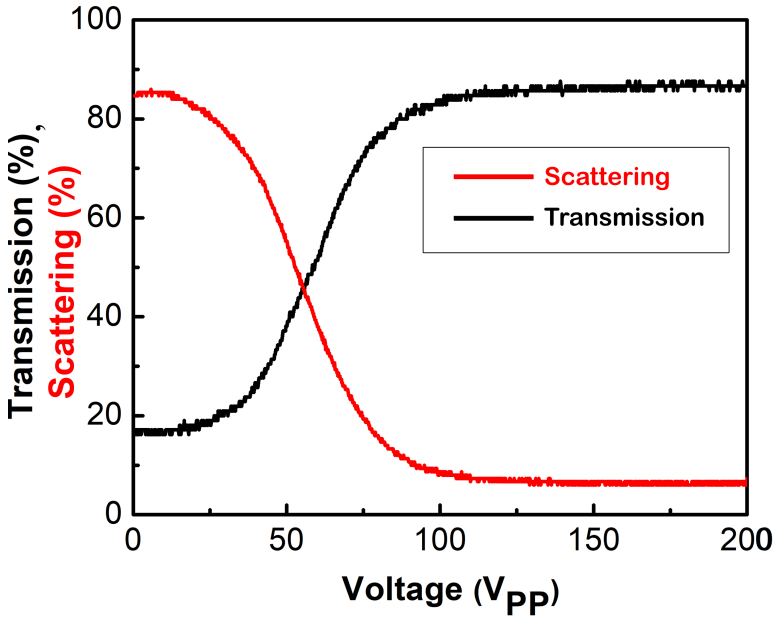

Figure 5.13: Transmission and scattering as a function of voltage of a 230 (± 5) µm diameter PDLC droplet (50 wt.% NOA65 + 50 wt.% E7) as presented in Figure 5.10(b). Prior to the application of an electric field, a top electrode was fitted resulting in a device thickness of 28 µm between the top and bottom electrodes. Following this, the entire sample was irradiated with UV light (365 nm) at a power density of 65 mW/cm^2 for a duration of 4 min at room temperature. The black and red lines in the graph represents the change in the intensity of the transmitted and scattered light, respectively.

The printed PDLC droplet was further investigated to determine the contrast ratio, which is usually characterised by the ratio of the transmittance values for the transparent and opaque states. The contrast ratio, $CR = \frac{T_{on}(\%)}{T_{off}(\%}$, is a ratio of maximum to minimum transmittance of a PDLC device, and the CR value of a printed PDLC droplet here was found to be 4.4, which is similar to conventional photo-curable polymer based PDLC film technologies. [117, 122]

At normal incidence, the scattering of light from a printed PDLC droplet was observed in order to determine the scattered light behaviour of the LC domains at a range of output angles. For this characterisation, a 25 mm focal length imaging lens and a photodiode were mounted on a rotation stage. The stage was rotated over angles ranging from -45° to +45°. The optical arrangement shown in Figure 5.14 was used for this measurement. For each angle, the scattered light received by the detector was recorded and the results are presented in Figure 5.15. The graph shows that scattered intensity is non-uniform with angle, and it tends to decrease when the photodiode collecting the scattered

light reaches the extreme angles (i.e. -45° to +45°).

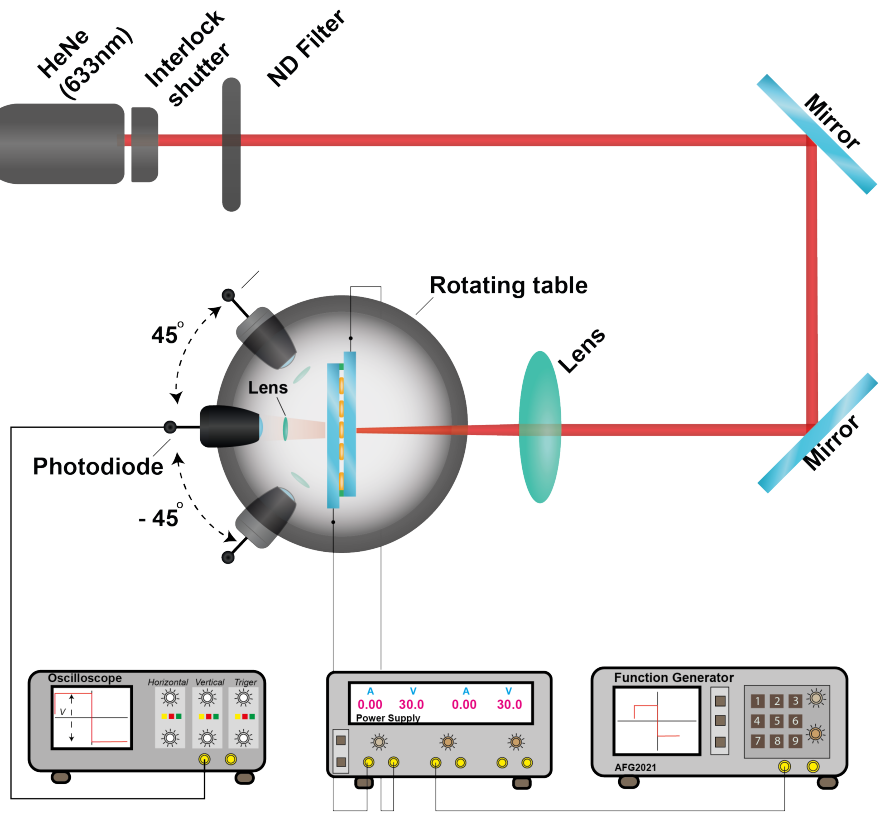

Figure 5.14: Schematic of optical setup used to determine the angular transmission properties from a printed PDLC droplet.

To characterise the PDLC pixels in terms of their dynamic response, the optical setup shown in Figure 5.12 was employed. For this, a 1 kHz square wave of 200 V_{pp} was periodically modulated to turn on and off at a frequency of 150 mHz. The results for the rise and decay times are presented in Figure 5.16(a) and Figure 5.16(b), respectively. The results show that the switching ON time, from opaque to transparent state, and the switching OFF time, from transparent to opaque state, takes around t_{rise} = 0.15 ms and t_{decay} = 77 ms, respectively. The dynamic response time measurements of the printed PDLC droplet is found to be in good agreement with the results reported previously for conventional PDLC films and represent a timescale that is expected for LC domain sizes that are of the order of 5 µm. [117, 122]

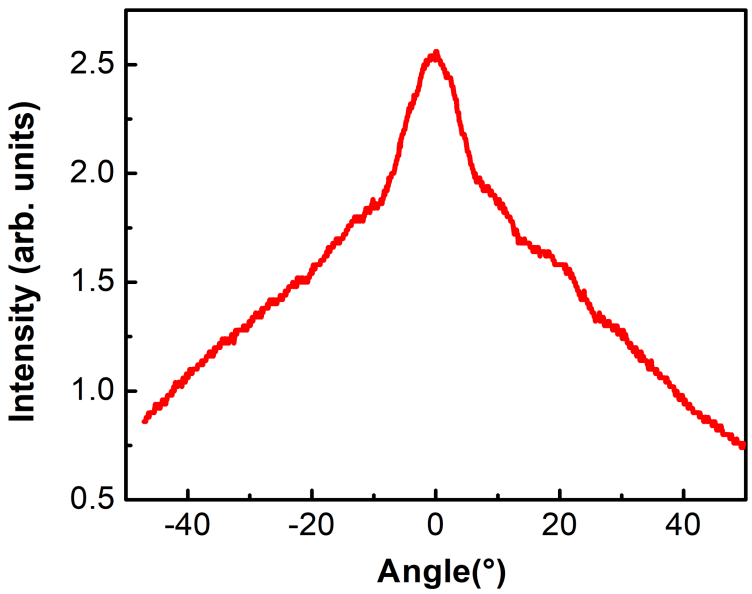

Figure 5.15: The angular dependence of the scattered light for a 230 (± 5) µm diameter PDLC droplet (50 wt.% NOA65 + 50 wt.% E7) in the voltage OFF (opaque) state. Prior to measurement, the droplet was assembled with a top electrode resulting in a device thickness of 28 µm. Following this, the entire sample was irradiated with UV light (365 nm) at a power density of 65 mW/cm^2 for a duration of 4 min at room temperature.

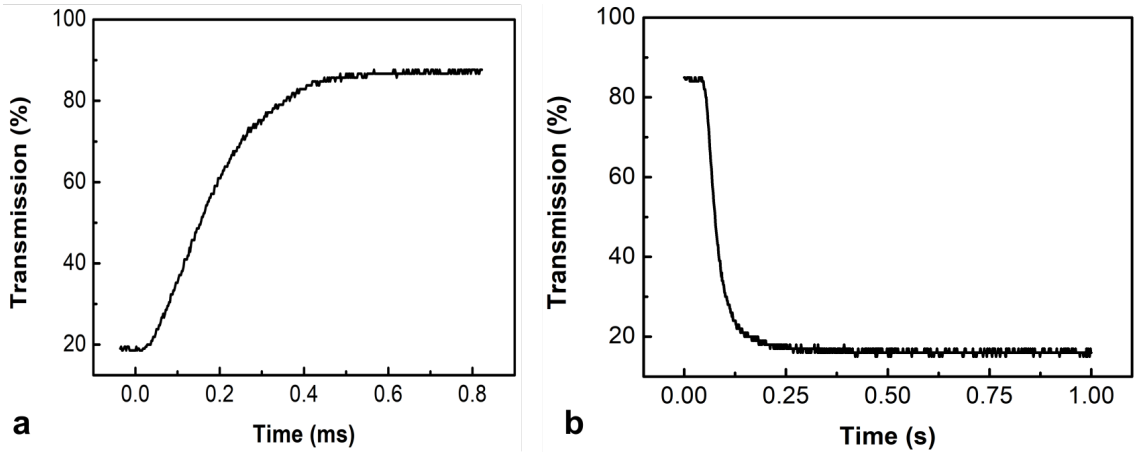

Figure 5.16: Response (rise and decay) time of a 230 (± 5) µm diameter printed PDLC droplet (50 wt.% NOA65 + 50 wt.% E7). Prior to measurement, the droplet was assembled with a top electrode resulting in a device thickness of 28 µm. The time was recorded when a 1 kHz square wave of 200 V_{pp} at 150 mHz modulation frequency is turned on and off. **a)** Rise time and **b)** decay time.

5.5 Printed PDLC arrays

So far, it has been shown that it is possible to make printed PDLC 'pixels' that can appear and disappear by applying a voltage to the device. Extending this feature, and exploiting

the flexible patterning capabilities of a MicroFab DoD inkjet printer, it is possible to print a defined density of droplets per unit length (defined as the dots per inch = dpi) which can effectively scatter the incident light. This section presents examples of POM images of PDLC pixels that can be printed close to each other so that the device in its macroscopic state scatters the incident light and the object behind it appears opaque.

For a printed PDLC technology, the scattering is an important parameter in terms of device performance and is dependent on the number of droplets deposited over a certain substrate area. For a fixed device thickness of around 14 µm, experiments were conducted to determine how closely the individual droplets could be printed before they were found to coalesce during the printing and device assembly stages. Note that in the following the device thickness has been reduced in order to decrease the voltage amplitude required to switch the PDLC 'pixels' to a transparent state.

Figure 5.17 shows POM images of the droplets with a constant volume of 180 pl that were printed with 20 µm, 40 µm, and 50 µm spacing between neighbouring droplets. The droplet volume, and consequent pixel size, is dictated by the print head nozzle size used, which had a diameter of 80 µm. Note that in order to adjust the droplet spacing the step sizes of the printer were varied. However, the minimum step size available with our system is 10 µm, corresponding to a maximum effective resolution of 250 dpi for the image (although this is of course blurred by the size of the individual printed droplets). After device assembly, the droplets were brought into direct contact with the top glass substrate, which resulted in a subtle increase in the droplet diameters. Nevertheless, each pixel remained circular in shape with a $\pm$10 µm variation in the droplet diameter. There is also a small variation in terms of the contact of the top ITO electrode with the cap of some of the droplets as can be seen in the microscope images in Figure 5.17(b) and 5.17(c). This is believed to result from the application of an uneven amount of mechanical pressure during device fabrication when the top glass substrate was attached to the printed substrate.

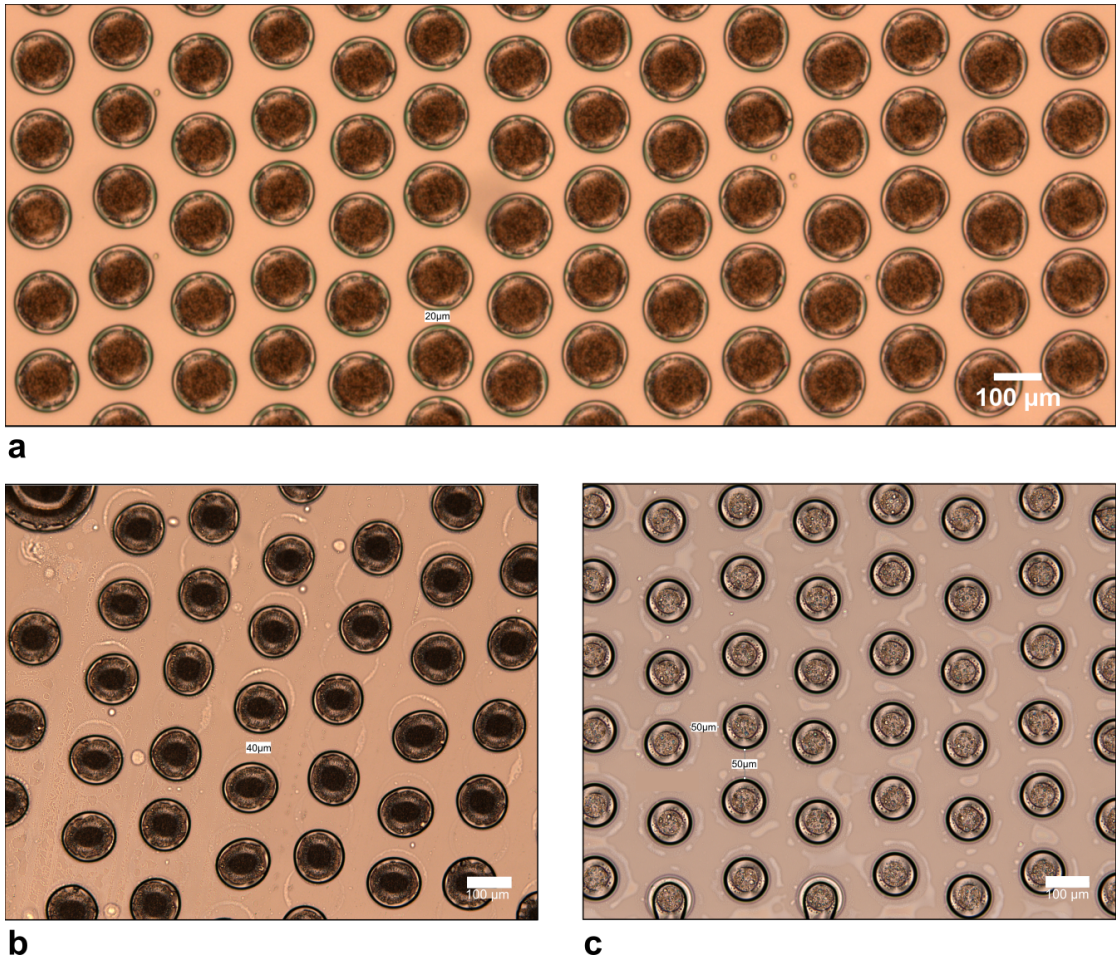

Figure 5.17: Microscope images of PDLC droplets (50 wt.% NOA65 + 50 wt.% E7) printed at: **a)** 20 µm, **b)** 40 µm and **c)** 50 µm drop spacing. The droplets are assembled in a device configuration. The individual drop diameter after device assembling is 130 (± 5) µm and the measured device thickness is 14 (± 2) µm. After device assembling, the each sample was UV cured at 65 mW/cm^2 for 4 minutes. However, 50 µm drop spacing sample as shown in figure (c) was partially cured. The UV curing intensity and time of this sample is 50 mW/cm^2, and 4 minutes, respectively.

An attempt was made to print the droplets with spacings less than 15 µm. However, for such small droplet spacings the uneven pressure applied during the application of the top glass substrate resulted in the droplets amalgamating and the printed PDLC then appeared similar in morphology to a conventional PDLC film rather than individual PDLC droplets, as shown in Figure 5.18. Therefore, with droplet spacings in the range of 2 - 15 µm the droplets were found to completely aggregate after device assembly, and with spacings of the order of 15 - 17 µm partial aggregation with each other tends to take place. A droplet spacing of 20 µm was found to be an optimal spacing to engineer coalesced-free individual droplets sandwiched between the top and bottom electrodes. For high-resolution printing, a spacing equivalent to the size of a single droplet is often

employed in the literature. [124,125] Therefore, printing with highly viscous LC polymer composites to obtain a 130 µm diameter PDLC pixel with a gap of less than one quarter of the pixel diameter (d) is considered to be a successful demonstration of high resolution inkjet printing of a PDLC ink (i.e. a centre to centre printing spacing of 1.25d).

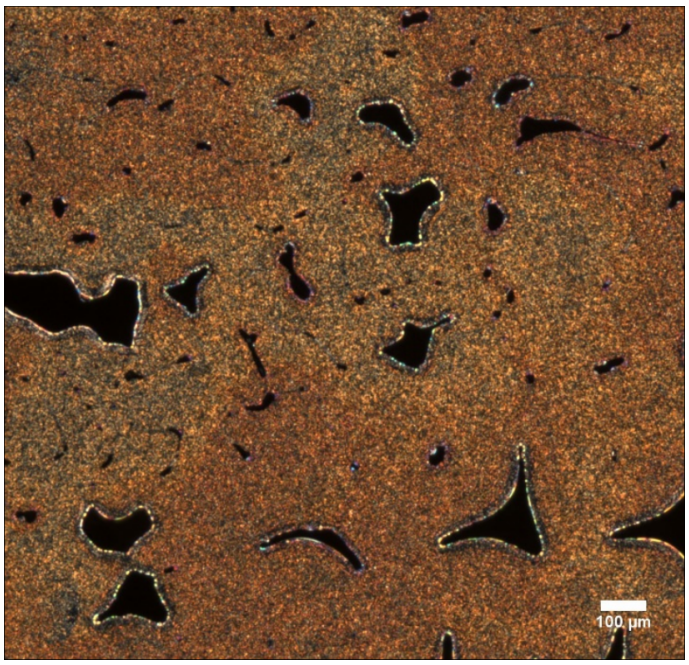

Figure 5.18: PDLC droplets printed with a spacing that was less than 15 µm after the application of top substrate the droplets coalesced into each other.

Figure 5.19 shows examples of POM images of arrays of PDLC droplets switching under the application of an external electric field, where it can be seen that the PDLC pixels switch uniformly across the device. Crossed POM images for the OFF and ON states confirm that the droplets can be switched in unison from a scattering to a transparent state. If desired, multiple ink droplets dispensed onto the same location can be used to locally enlarge the PDLC 'pixels' as can be seen in Figure 5.8(c).

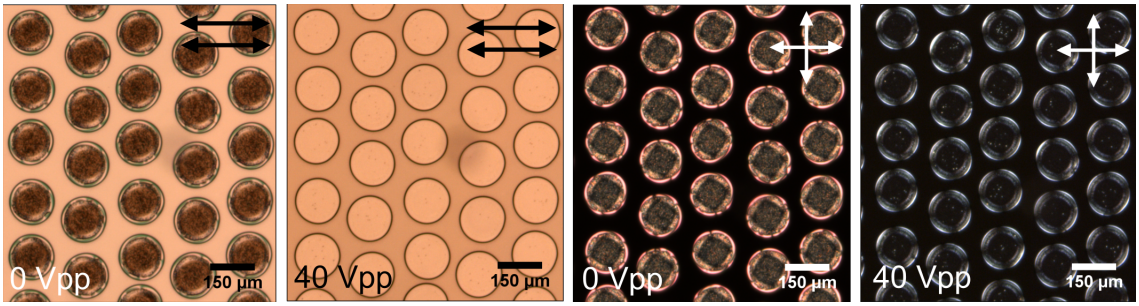

Figure 5.19: Polarised optical microscope images of printed PDLC droplets at 0 V_{pp} and 40 V_{pp}. The top right black double-headed arrows in the images indicate that the analyser and polariser axes are aligned parallel to one another. The white doubled-headed arrows that are crossed indicate that the transmission axes of the analyser and polariser are perpendicular to one another. Prior to the application of an electric field, the droplets were assembled with a top electrode. Following this, the entire sample was irradiated with UV light (365 nm) at a power density of 65 mW/cm^2 for a duration of 4 minutes at room temperature. After device assembly and photopolymerisation the individual drop diameter is 130 (± 5) µm and the measured device thickness is 14 (± 2) µm.

5.6 Printed PDLC Smart Window

The ultimate goal of this work is to demonstrate that DoD inkjet printing can be used to form intricate and sophisticated PDLC patterns so as to create pictorial representations of logos/emblems/motifs within the smart window. Figure 5.20, therefore, illustrates the proof-of-concept in which the printed image can be switched from an opaque to a transparent state in the presence of an electric field.

Figure 5.20: Graphical representation of the printed PDLC smart glass concept in which a company logo or emblem can be made to disappear with the application of an electric field.

To create a prototype of an electrically switchable PDLC smart window with embedded images, the printed PDLC 'pixels' were covered with a top glass substrate, and subjected to UV illumination to form the polymer binder and LC domains in each droplet as illustrated in Figure 5.21. While Figure 5.21(b) and Figure 5.20 demonstrate a prototype printed smart window displaying the Exeter College (Oxford) crest. The printed crest, as can be seen in Figure 5.21(b), was illuminated with a halogen light source and a series of images were recorded for a range of voltages between the OFF state and the ON (transparent) state.

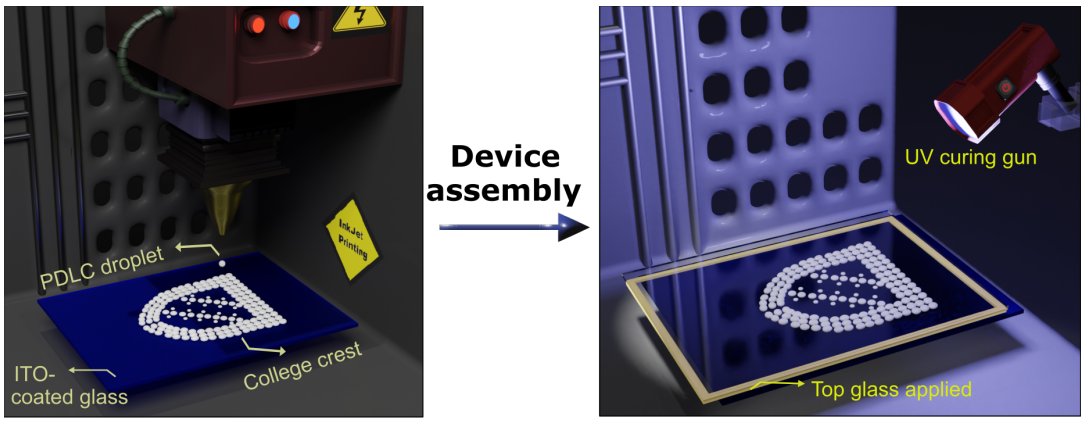

Figure 5.21: a) Schematic illustration of smart window device fabrication. The device fabrication process is similar to Figure 5.3. **b)** The crest illuminated with a halogen light source and images were recorded with a CCD camera while applying a square from 0 - 40 V_{pp} at 1 kHz frequency. To enhance the visibility of the PDLC pixels, the contrast between printed logo and dark environment was adjusted. The images look red due to the colour settings of the CCD camera and the dark environment of the room.

The time taken to print a pattern depends upon the drop ejection frequency and the substrate speed. In our pattern printing experiment, we set the print nozzle frequency to 1000 Hz and the substrate speed to 40 mm/s. For a pattern with an area of 896 mm^2, as shown in Figure 5.21, the time taken to print this pattern was then around 5 minutes.

The threshold voltage, V_{th}, and saturation voltage, V_{sat}, for this printed sample were found to be 9 V_{pp} and 32 V_{pp}, respectively. In terms of electric fields strengths, this corresponds to E_{th} = 0.3 Vμm^{-1} and E_{sat} = 1.14 Vμm^{-1}, respectively. The complete switch ON electric field strength for which the device appears transparent was found to be E = 1.4 Vμm^{-1}, which is comparable to that obtained for conventional PDLC film-based preparation techniques. [96]

Extending this principle further, Figure 5.22 demonstrates switching of the University of Oxford logo between an opaque and transparent state. This was created by depositing the PDLC ink droplets at a distance such that they coalesce with each other to form a line pattern. The example prototypes of both the Exeter College crest and the University of Oxford logo, suggests that DoD inkjet printing has the potential to form complex patterns both in the form of printed droplets/pixels and lines.

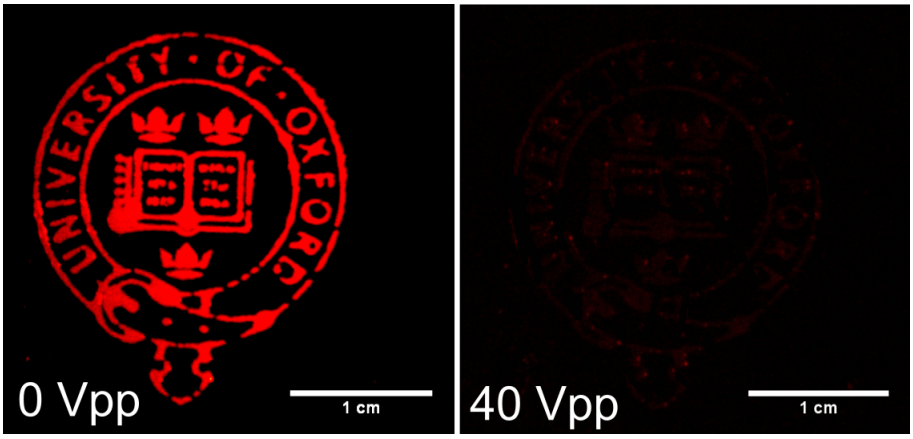

Figure 5.22: Photographs of a smart window with a printed University of Oxford logo. The scattered light is captured using a CCD camera when the device was illuminated with a halogen light source subjected to either 0 V_{pp} or 40 V_{pp} voltage amplitude. The sample was printed with 50 wt.% NOA65 + 50 wt.% E7 PDLC ink formulation. After logo printing, the device was assembled with a top electrode. Following this, the entire sample was irradiated with UV light (365 nm) at a power density of 62.5 mW/cm^2 for a duration of 10 minutes at room temperature. After device assembly, the measured device thickness is 14 (± 2) µm.

Finally, Figure 5.23 shows images captured using a digital SLR camera of the printed Exeter College crest taken when viewed from the front and at an angle to the device. As can be seen in Figure 5.23(a), the printed crest strongly scatters light when viewed both at normal (0°) and at oblique (45°) viewing angles. Similarly, when in the ON state and

viewed over the same range of angles the printed crest could not be seen as the device appears transparent, as shown in Figure 5.23(b).

To further illustrate the quality of the switching, scattering and transparency, the crest was switched ON and OFF above text printed onto white paper, as presented in Figure 5.23(c). It is evident that when the crest in the OFF state it scatters the light and the text behind the device is completely hidden. In contrast, for the ON state, the crest disappeared and the text behind the device could be read clearly. These results suggest that the density of the printed droplets was sufficient to create a printed PDLC smart window with a switchable logo. Also, the overall performance of the printed crest in terms of the light scattering, light transmittance, and contrast ratio was investigated by measuring the behaviour of individual pixels in regions within the printed pattern. It was found that the individual pixels in the printed pattern shown here have the same electro-optic properties as those presented in detail for an individual printed PDLC droplet.

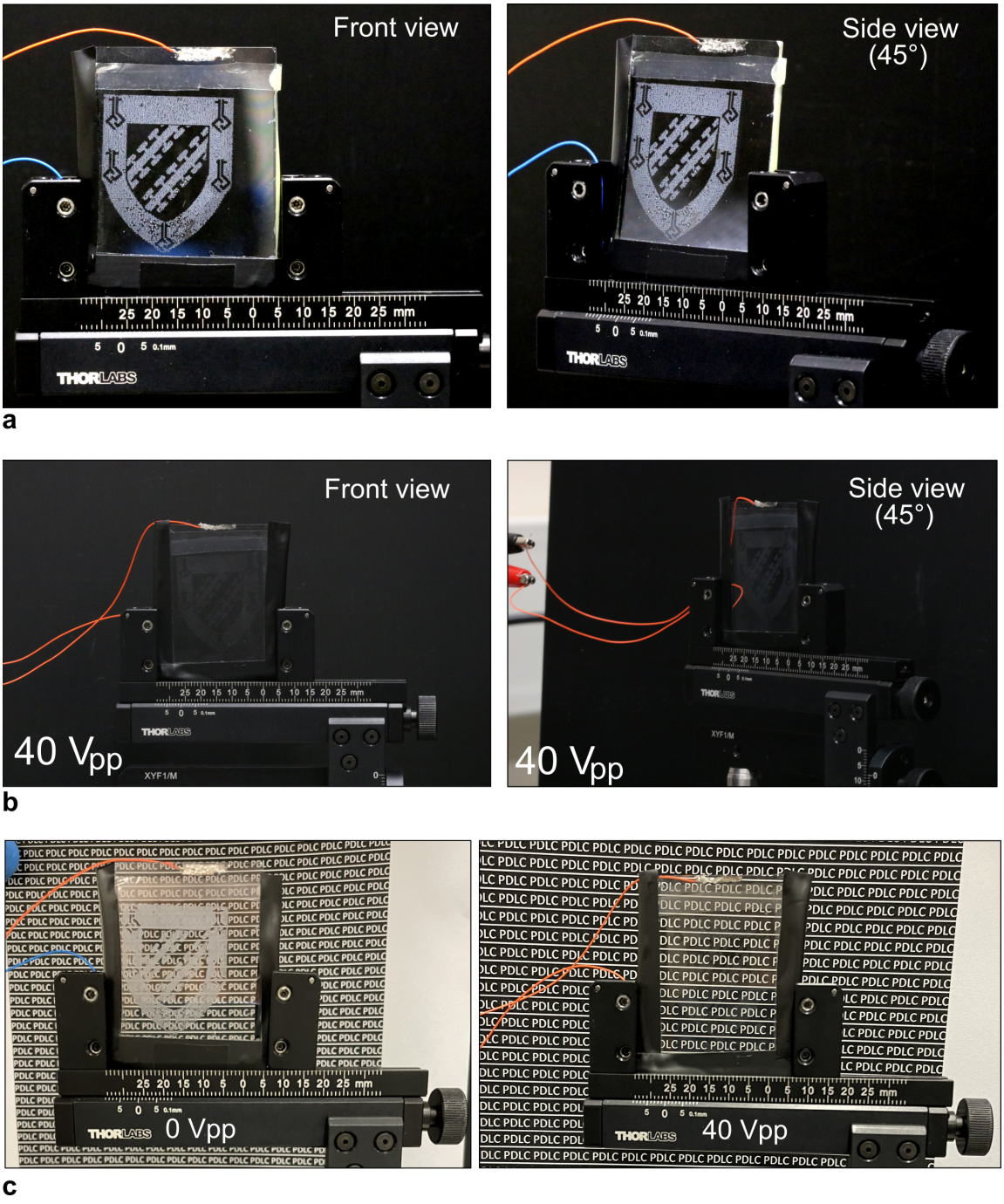

Figure 5.23: Photographs captured using a digital SLR camera from the front and side views at **a)** 0 V_{pp} and **b)** 40 V_{pp}. **c)** The crest in front of text printed onto white paper to show the scattering and transmission at 0 V_{pp} and 40 V_{pp} (E = 1.4 Vμm^{-1}), respectively, when viewed at normal incidence. The college crest was printed with 50 wt.% NOA65 + 50 wt.% E7 PDLC ink formulation. After college crest printing, the device was assembled with a top electrode. Following this, the entire sample was irradiated with UV light (365 nm) at a power density of 62.5 mW/cm^2 for a duration of 4 minutes at room temperature. After device assembly, the measured device thickness is 14 (± 2) µm.

5.7 Summary and Conclusion

In conclusion, new patterned PDLC films have been fabricated using a printing process and it has been shown that these printed materials could be used to form a smart window technology with logos and images that can be made to disappear with the application of a voltage. To begin with, the rheology and surface tension of the ink was tuned by varying the printhead temperature in order to eject uniform-sized droplets. PDLC droplets consisting of a high density of LC domains were formed upon irradiation of the sample with UV light. The photo-curing conditions were chosen such that the droplets give rise to intense scattering of light leading to high-quality arrays of PDLC 'pixels'.

The technique reported in this chapter is significant as it provides a means with which to pattern a PDLC film without the need for photomasks and would allow for different LC formulations to be used simultaneously on a substrate with the aid of a multi-printhead printing system. The approach described herein would allow for artistic designs, motifs, and additional information such as dynamic company logos or advertisements to be displayed on smart windows that could be removed with an applied voltage. Further, there is a considerable scope to enlarge the size of the printed patterns using commercial processes based on multi-nozzle printing over large area substrates. Also, the flexibility of the process would allow the expansion of the smart windows manufacturing concept to roll-to-roll inkjet manufacturing by printing and assembling PDLC ink between flexible substrates on a production line system. The future scope for the commercial exploitation of the concepts introduced here is therefore substantial.

CHAPTER 6

ELECTROHYDRODYNAMIC PRINTING OF NEMATIC LCS

This chapter demonstrates on-demand electrohydrodynamic (EHD) printing of nematic liquid crystals (LC) and presents a detailed analysis of the Taylor cone formation process in the presence of high electric field amplitudes. To generate the deposition of single well-defined LC droplets on a substrate, voltage pulses that were superimposed on a constant DC bias voltage were applied. The chapter begins with a detailed introduction of the principles of EHD printing and a brief review of the relevant literature. This is then followed by a description of the experimental procedure employed to find the optimum settings in terms of the DC bias voltage and the pulse amplitudes. Using a high-speed shadowgraph imaging technique, the effect of pulse duration and frequency on the jetting of the LC was also investigated. Results are then presented for EHD printing of micron-sized droplets on glass substrates coated with either a homeotropic or planar alignment layer as well as a micro-dripping mode using glass capillaries of different nozzle diameters. Finally, droplet properties such as droplet diameter distribution, LC director alignment, accuracy of placement on the glass substrate, and the printing of arrays of droplets and patterns are demonstrated.

6.1 Introduction

Electrohydrodynamic (EHD) printing has emerged as an electric field-driven printing technique that can be used to deposit fluids as a functional ink onto a substrate. [126, 127] It is often classed as an advanced additive manufacturing technique and the acronym "e-jet" printing is sometimes used in place of "EHD" to refer to this high quality printing technique. [128, 129] EHD printing has the ability to deposit very small volumes of fluids onto a variety of different substrates. Moreover, due to the flexibility of the system it is also possible to incorporate multiple nozzles of different configurations. Due to the low material waste and the wide range of materials that can be printed, it is also considered to be an economical manufacturing technique. [130] The unique advantage of EHD printing is that it enables the deposition of droplets that are much smaller, in diameter and volume, than is achievable using inkjet printing techniques. Depending upon the fluid and system parameters, the droplet diameters can be 2 - 15$\times$ smaller than the diameter of the printing nozzle. [127, 131, 132]

Inkjet printing is already a well-established additive manufacturing technique. The resolution of an inkjet-manufactured device is defined by the feature size and spacing that can be reliably produced using conventional printing processes. The smallest footprint diameter of a liquid that can be ejected from a piezoelectric-driven print head is typically in the range of 20 - 30 µm, depending upon the surface conditions of the printing substrate. This relatively coarse resolution results from the combined effects of nozzle size, drop placement accuracy, and the type of ink being used. [126, 131] Among these parameters, the printing nozzle dimension fundamentally limits the feature size as the in-flight drop diameters are approximately equal to the orifice size of the printing nozzle. Commercially available systems generally offer a range of inkjet nozzle sizes with nozzle orifice sizes in the range of 20 - 120 µm. [133] These nozzles function based upon a particular droplet ejection principle, which typically are thermally- or piezoelectrically-driven. This approach, however, is incompatible with very small nozzle orifice sizes due to the extremely high levels of pressure required to overcome capillary and viscous forces.

EHD printing provides a means with which to print feature sizes smaller than the size of the nozzle orifice by pulling liquids from the nozzle tip through the use of applied electric fields as compared to extrusion technologies such as piezoelectric-driven inkjet printing. This technique has been demonstrated a number of times with a range of fluids for application in the fields of printed electronics, tissue engineering, solar cells, optical components, and microfluidic devices. [134–140] The functional materials that have been considered include colloidal suspensions, heterogeneous and homogeneous solutions, nanoparticles, quantum dots, polymer composites, biomaterials, and 1D nanomaterials such as nanowires and nanotubes. The breadth of both materials and applications relating to EHD printing have been the subject of several recent review articles. [130,131,141].

Liquid crystalline materials, which have been discussed in earlier chapters, are a unique class of electro-optic material. In Chapter 3 it was shown that due to their fluid-like properties LCs can be inkjet printed to form well-defined droplets. These droplets can then be arranged on chemically-modified substrates for a range of different photonics applications such as electrically tunable microlenses, which was the subject of Chapter 4. As shown in these earlier chapters, it was observed that the inflight size of the individual LC droplets was approximately equal to the size of the nozzle orifice, and that the droplet feature size (footprint) on a lecithin-coated substrate was 120 μm when printed with an 80 μm diameter nozzle. Importantly, EHD printing has the potential to significantly improve the feature resolution so as to open up new avenues in the field of micro/nano manufacturing of LC based devices.

Electrospinning is a type of electrohydrodynamic process where a highly viscous polymer solution flows through a needle while a high amplitude voltage between the needle and collector (usually in the range of 10 - 40 kV) leads to the formation of a jet that thins and extends to form long fibres. [142–144] By improving the needle design and using a coaxial electrospinning process of two different materials, composite fibres can be fabricated to have a core and cladding. Owing to their excellent optical properties, LCs have been employed as the fluid in the cores of electrospun micro/nano fibres. [145–147].

Even though electrospinning has been demonstrated, there appears to have been no previous work on the EHD printing of LCs. As the generation of well-defined droplets is an essential aspect of printing technologies, being able to form feature sizes that extend below that accessible using traditional DoD printing processes is highly desirable. Therefore, the focus of this chapter is to demonstrate the EHD printing of a nematic LC with droplet footprints that are less than 10 microns. The chapter begins with the introduction of the EHD phenomenon by providing a detailed literature review in terms of technical understanding of the system parameters on the EHD printing. The chapter then presents the development of a suitable EHD printing setup. This is then followed by providing a description of experimental procedures used to find printing settings in terms of bias DC voltage and pulse amplitudes. The preliminary set of experiments were performed with IPA. The chapter then presents the shadowgraph images of the LC Taylor cone formation process, and optical microscope images of nematic LC droplets printed over surface coated glass substrates.

6.2 Electrohydrodynamic Printing: The Concept

Historically, the phenomenon of EHD jetting and electrospinning began in 1600 when William Gilbert reported the shape of a liquid meniscus under the influence of an electric field. Many years later, in 1882, Lord Rayleigh provided the first scientific description of liquid droplets under electrical stresses. [127] In 1969, Geoffrey Ingram Taylor described the conical meniscus observed in a charged droplet and proposed a theoretical model to explain the shape of the meniscus and the related EHD phenomena of cone jets. Today, these cones are referred to as 'Taylor cones' in recognition of this work. [148] Soon after the development of inkjet printing technologies, the EHD phenomenon was seen as a potential printing technology due to the ability to generate smaller droplets from the liquid jet. As a result, there are now a number of reports on the research and development of EHD printing and there are also a number of commercially available EHD printing systems on the market. [149–151]

There has been extensive research to fully understand the physics behind the Taylor cone formation both theoretically and experimentally. [152–155] However, the EHD

phenomenon is complex because of the dependency upon a number of parameters such as environmental conditions around the nozzle tip, the nozzle tip geometry, the voltage strength, the distance between nozzle and electrode, the fluid rheology, and the fluid's electrical/dielectric properties. Even though the fundamental process is generally understood, further investigation is still required to understand and interpret the behaviour observed for the new materials being considered for this printing process.

EHD printing involves the application of a voltage between the nozzle and an opposing conductive electrode in order to initiate the flow of a functional ink from the nozzle. Before the application of an electric field, a constant back pressure is always applied to maintain a small volume of fluid at the tip of the nozzle orifice. Generally, a back pressure is maintained either by a static back pressure or by a continuous flow of ink at a fixed flow rate from an ink reservoir. In most EHD printing applications, the nozzle is conductive, e.g., stainless steel nozzles. [156] EHD printing has also been carried out using glass nozzles that have been made conductive through the application of metallic coatings using sputtering techniques. [128] After the formation of a hemispherical meniscus, a high amplitude electric field causes the charged particles in the ink to accumulate near the surface of the ink meniscus. Coulombic repulsion between these particles deforms the meniscus into a conical shape known as a Taylor cone. [126, 127] A further increase in the electric field ruptures the Taylor cone and a very thin jet starts to emerge from the conical apex.

Figure 6.1(a) shows a graphical illustration used as an example to showcase a number of forces acting on the Taylor cone when a fluid on the tip of a capillary is subjected to an electric field. The cone formation process is governed by the balance between the following forces: electric force, surface tension, viscous force, and gravitational force. The surface deformation process involving the change from the hemispherical meniscus to a Taylor cone is triggered by small perturbations of the surface, which, in turn, enhances the local electric field through charge concentration and further increases the electrostatic pull in a cascading effect. [154, 155] Figure 6.1(b) shows the spatial distribution of the electric potential when a voltage is applied between nozzle and conductive electrode, which shows that the field strength is a maximum at the tip of the nozzle.

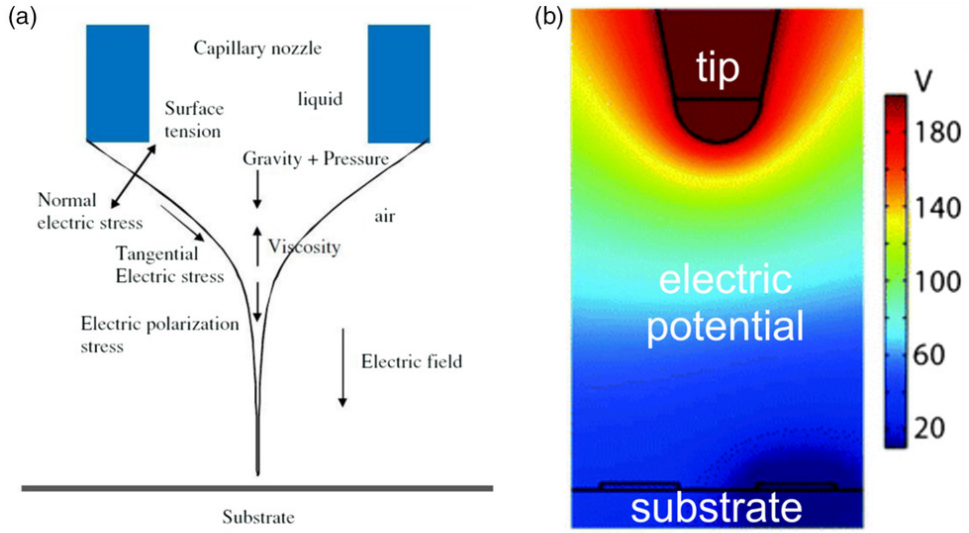

Figure 6.1: a) The forces acting at the tip of a nozzle during EHD printing. **b)** A simulation of the distribution of the electric potential around the nozzle tip and substrate. The images were taken from the literature. [131, 132]

6.2.1 EHD Printing Modes

EHD printing, as discussed in the previous sections, involves the ejection of a liquid from a nozzle, and there are a number of different drop jetting modes that can occur at the apex of the Taylor cone. These include the dripping mode, micro-dripping mode, cone-jet mode, and multi-jet modes, which are widely observed in experiments and are frequently discussed in the various review articles. [126, 130, 131] These modes arise by varying the printing conditions and fluid properties, and are generally controlled by varying the applied voltage and the flow rate of the ink. [157] The dripping mode is usually observed when the liquid flow rate is high, but the applied voltage is relatively low. It is similar to the case when a low viscous fluid drop detaches from a nozzle without any voltage. When the voltage increases and the fluid flow rate decreases, the liquid droplets begin to dispense from a conical shape meniscus. This mode is termed as the micro-dripping mode, and the droplets produced in this mode are smaller than the size of the nozzle. The cone-jet mode is formed when the voltage is further increased whilst the same fluid flow rate is maintained. In the cone-jet mode, a thin liquid jet is ejected from the apex of the cone. By increasing the voltage and ink flow rate to very high values, multiple jets are ejected from the nozzle, leading to the multi-jet mode. In the multi-jet mode, the cone shrinks and becomes flat, and the printing process is unstable and uncontrollable. [158] The micro-dripping mode and the stable cone-jet mode provide more control in terms of

the printing process. Therefore, these are the two prominent modes that have been employed for more precise DoD printing and manufacturing. [130]

EHD printing has the potential to generate a continuous stream of droplets as well as on-demand single droplets (DoD) depending upon the electric field conditions. A continuous stream of droplets is obtained by applying a constant DC voltage between the nozzle and substrate whereas for a DoD configuration droplets are produced by applying a pulsed DC voltage. In the latter case, droplets can only be triggered when the voltage pulse reaches the nozzle. [159, 160] Drop-on-demand EHD printing is advantageous when patterns of droplets are required. In addition, in DoD EHD printing the droplet separation can be increased or decreased by moving the substrate relative to the nozzle at a desired speed. If the droplet spacing is small, coalescence of the droplets is observed and a continuous print line pattern can also be achieved. [136] In this study, a pulsed voltage was employed to print isolated droplets at a predefined position on a substrate instead of using a constant DC voltage to drive a stream of droplets.

Besides flow rate and electric field strength, the environmental conditions can also affect the printing behaviour and jetting mode. For example, Hayati et al. [155] observed the EHD phenomenon with both conductive and non-conductive fluids when carried out in the presence of different gasses. In their work, they found that if a gas with a lower breakdown potential than that of the printing fluid is used, such as He/Ne, then EHD printing would not take place.

In addition to the system parameters (i.e., voltage and flow rate), ink properties such as viscosity, surface tension, dielectric constant, and conductivity have been reported as the key parameters which can influence the cone jet formation and printing process. As an example, Guo et al. [161] found that higher viscosity inks with sufficient conductivity result in a more stable Taylor cone formation and subsequent jetting behaviour. However, at $> 10^4$ $\mathrm{mPa.s}$ during the jet pinch-off process, viscoelastic forces become dominant leading to the formation of larger droplets on the substrate. Viscous inks include gels, glue, polymers additives, oils, and organic solvents such as glycerol and these materials

have been employed in EHD printing for a range of applications. [162, 163] One example is the work carried out by Su et al. [137] who have recently reported the DoD EHD printing of NOA61 and NOA68 (Norland glues) for the manufacturing of microlenses.

Surface tension is believed to be an important ink parameter in the EHD printing process. The electrical forces that convert the meniscus into a Taylor cone overcome the surface tension forces of the fluid. [131] Reports suggest that the strength of the electric field is directly related to the surface tension. If the surface tension is too high, the electrostatic force will not be sufficient to cause the jetting of the material. [131] Towards this end, Lim et al. have investigated the effect of surface tension by comparing different PEDOT: PSS solutions with different concentrations of the surfactant. In their work, they reported that a larger concentration resulted in no jetting behaviour even at high amplitudes of the electric field. [164]

The conductivity (σ) of an ink is also a very important parameter. The charge mobility on the surface of the meniscus affects both the Taylor cone formation time and the charge relaxation time. [154, 155] The charge mobility can be altered by doping ionic materials such as ionic solutions or salt. Without significantly changing the chemical properties of the ink, these dopants enable the material to be printed using the stable cone jet mode. [165]

It is believed that the EHD printing in cone-jet mode can easily be achieved with liquids having electrical conductivity (σ) in the range of 10^{-3} to 10^{-6} Sm^{-1} and a viscosity of < 150 $\mathrm{mPa.\,s}$. [166] For dielectric liquids having electrical conductivity of $\approx 10^{-13}$ Sm^{-1} such as oils, Dong et al. [152] discovered that such liquids do not produce a stable cone jet formation and they suggested that stable jetting was only observed for liquids that could be considered as 'leaky' dielectrics (i.e., weakly conducting) at a sufficient voltage amplitude. [152] In a detailed investigation, Jayasinghe et al. [167] performed a systemic analysis of dielectric liquids with conductivity of 10^{-12} Sm^{-1} and viscosity in the range of $10^2 - 10^4$ $\mathrm{mPa.\,s}$. At higher volume flow rates, they observed micro-sized thick threads detached from an elongated Taylor cone and suggested that these jets

are electrically forced jets which can be obtained from very low electrical conductivity liquids (dielectrics).

6.3 Design and Construction of EHD Printing System

In principle, a conventional EHD printer is relatively simple and composed of only a few key components. For example, a printhead consisting of a single glass capillary, a high voltage DC power supply, a conductive substrate, a backpressure to nozzle, and an imaging system are all that is needed to study the droplet ejection and drop impact process. [131] However, depending upon the drop placement accuracy and drop feature size, the external environment around the nozzle, and the droplet visualisation configuration, an EHD printing system can be made complex. Towards this end, Schneider et al. [168] used a confocal laser scanning microscope to assess the ejection process and provide in-situ visualisation of the printing by using a further set of side optics. The primary purpose of our study is to demonstrate the EHD printing of a LC material with feature sizes that are smaller than the inkjet printed droplets that have been presented in Chapter 4. Therefore, the EHD printing system was designed for the purpose of dispensing nematic LCs. A schematic diagram of the system is shown in Figure 6.2 and each component is discussed in the following section.

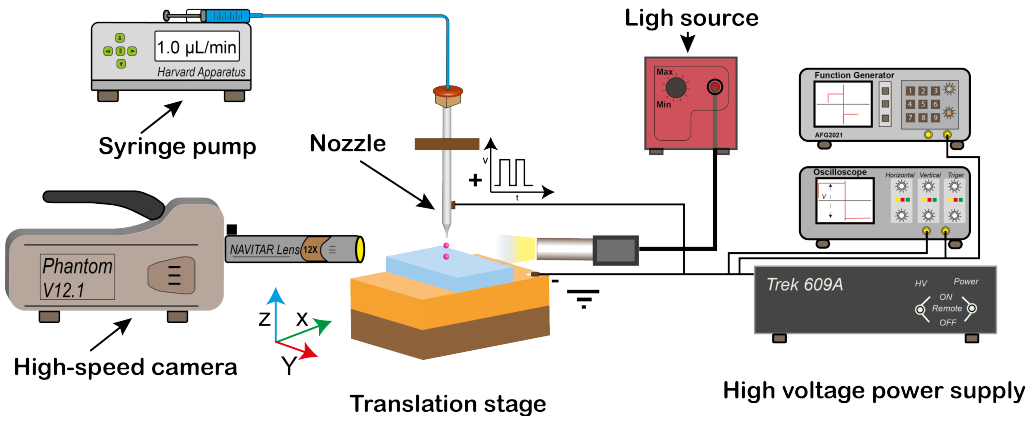

Figure 6.2: Graphical illustration of the EHD printing setup used in this work.

Commercially available glass capillaries with either 1 µm or 30 µm diameter (internal) were used for this study. However, for some of the initial trials a steel nozzle with a 150 µm internal diameter (ID) and 1586 µm outer dimeter (OD) was used. Further details

about the steel nozzles were not available from the manufacturer. Figure 6.3(a) shows camera images for these nozzles. The glass capillaries were purchased from World Precision Instruments. The ratio of the outer to inner diameters was 1.33:1, as provided by the supplier. The capillaries are made from pre-pulled borosilicate glass and fitted with a luer head fitting that facilitates the attachment of a nozzle to different types of syringe and barrel. The optical microscope image in Figure 6.3(b) and schematic diagram in Figure 6.3(c) shows the tip of the nozzle and the technical details, respectively. In order to use them for EHD printing, an electrical connection was made near the tip of the nozzle. A custom technique was used in which a copper foil tape (from 3M Science) was wrapped around the tapered end of the capillary tube. Within the layers of the copper tape a piece of wire was added. To shield the connection, a heat shrink tube was carefully added around the copper foil. The entire connection was exposed to a heat gun (BOSCH) to shrink the tube and provide a secure connection. Similarly, the other end of the wire was attached with a shrouded 'banana' plug to provide an electrical signal to the tip of the nozzle. Figure 6.3(d) shows a photograph of an assembled glass capillary. Figure 6.3(e) shows the approximate distance of the copper tape from the tip of the nozzle. The distance between the tip of the nozzle from copper tape is around 3 mm.

The LC was supplied to the glass capillary using PTFE micro bore tubing which was connected to a glass syringe and barrel that served as an ink reservoir (Hamilton). To avoid wastage of the LC material, a glass syringe with a capacity of 100 µl was used. The syringe and barrel assembly were clamped to the syringe pump (PHD-70-3009, Harvard apparatus) where the plunger of the barrel was allowed to move back and forth to push and pull the ink from the tubing and consequently from the nozzle.

Droplet positioning was achieved by translating the printing substrate, rather than the printhead. Two computer-controlled translation stages (MT1-Z8 Thorlabs) were used to perform X-axis and Y-axis movement over a range of 12 mm $\times$ 12 mm, which offered a 1.5 µm repeatability. Each axis was controlled by a standalone motion controller (KDC101 Thorlabs). The motion controller has the ability to output a signal for each step (and size) of the stage. The output signal from the motorised stage was further used as an

external input to trigger the function generator which in turn triggers the printhead.

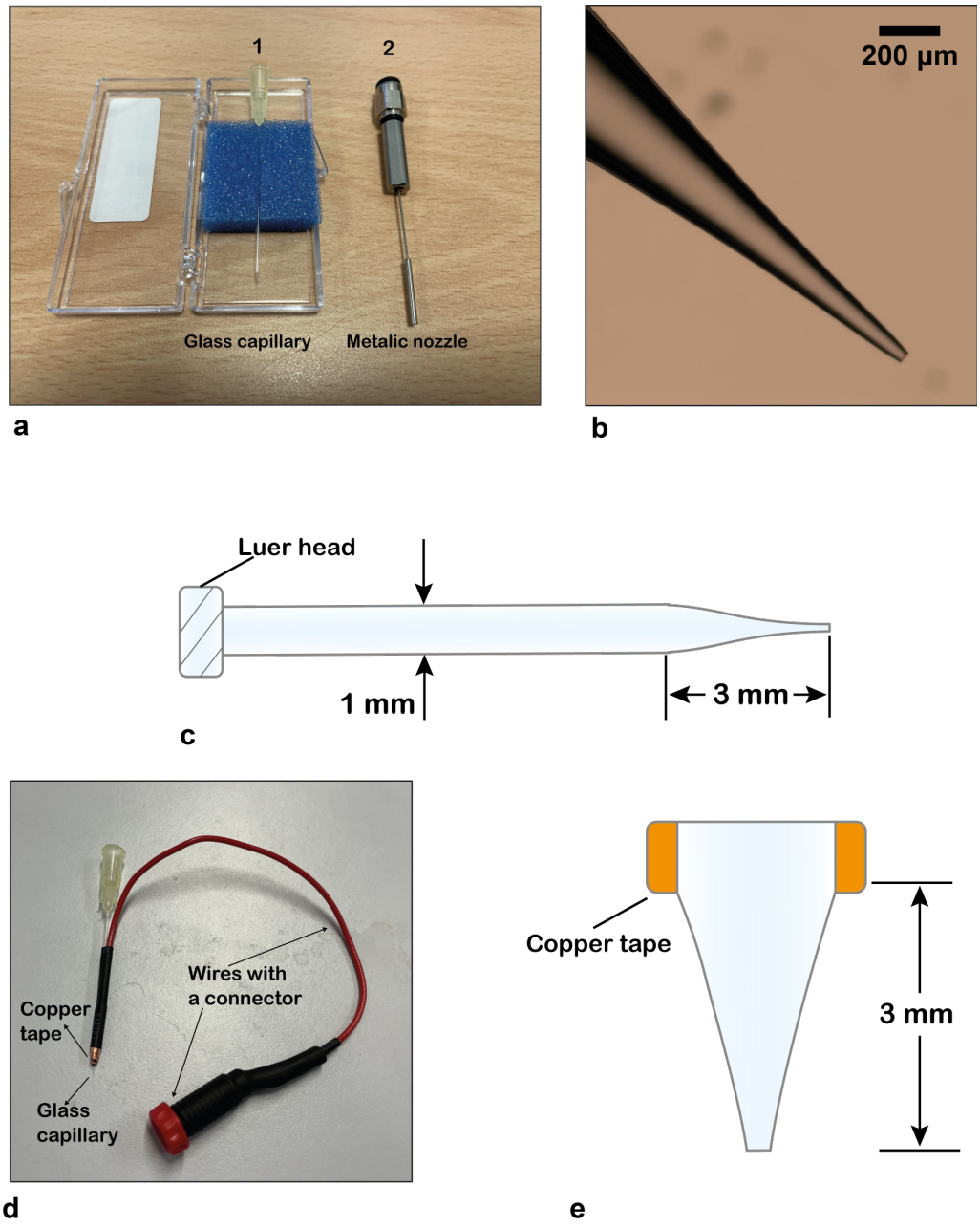

Figure 6.3: a) Photograph of the nozzles used for EHD printing. **b)** Optical microscope image of a 30 µm diameter (inner diameter) glass capillary nozzle. **c)** Graphical illustration of the design of the glass capillary nozzle. **d)** Photograph of a glass capillary nozzle after the attachment of the electrical wires. **e)** illustration of a glass capillary showing the placement of the copper tape and the distance from the tip of the nozzle to the tape.

This approach enables DoD printing and as shown later that this leads to the controlled deposition of droplets to form arbitrary patterns, discussed in the later part of this chapter. The stages were controlled using software which was provided by the hardware supplier (Thorlabs). A 61 mm $\times$ 61 mm $\times$ 61 mm silver sheet was machined and firmly attached

over a 3D printed 6 mm thick (same dimensions) plastic block which served as an insulator. The whole assembly was mounted on the translation stages. The Z-axis movement of the printhead was performed by a manual translation stage (PT1 Thorlabs). To firmly secure the capillary nozzle in place and to avoid contact with any metallic components, a printhead was 3D printed and a M6 thumbscrew was used to mechanically secure the capillary nozzle inside the 3D printed printhead.

To generate large electric field amplitudes between the nozzle and counter electrode, a high voltage amplifier was used (Trek 609A). The voltage amplifier can increase the input signal by 1000$\times$ with the output in the range of 0 - 10 kV. An arbitrary function generator (AFG 2021 Tektronix) was used to generate an input signal to the voltage amplifier and an oscilloscope (TBS 1000C Tektronix) was used to measure the amplitude and frequency prior to the high voltage amplifier. The arbitrary function generator was externally triggered by using another function generator when the Taylor cone formation was investigated at different pulse widths and voltage amplitudes. As mentioned previously, for the formation of arbitrary droplet patterns, the function generator was triggered by the output signal of the motion controller.

A high speed shadowgraphy imaging technique, discussed in section 2.9.1 of Chapter 2, was used to visualise the Taylor cone formation, jet ejection and droplet formation. Images were captured at 20,000 fps with an image resolution of 512 $\times$ 512 by manually triggering the camera.

All of the components of the printing setup were arranged on a 60 mm thick honeycomb style optical breadboard which was placed on passive-vibration isolating legs on top of a wooden laboratory bench. To avoid any potential electrical burnout, all of the individual components were placed on insulating sheets, the wires were completely insulated, plastic washers were used between screws, and the optical table was earthed. Figure 6.4 shows photographs of the EHD printing setup.

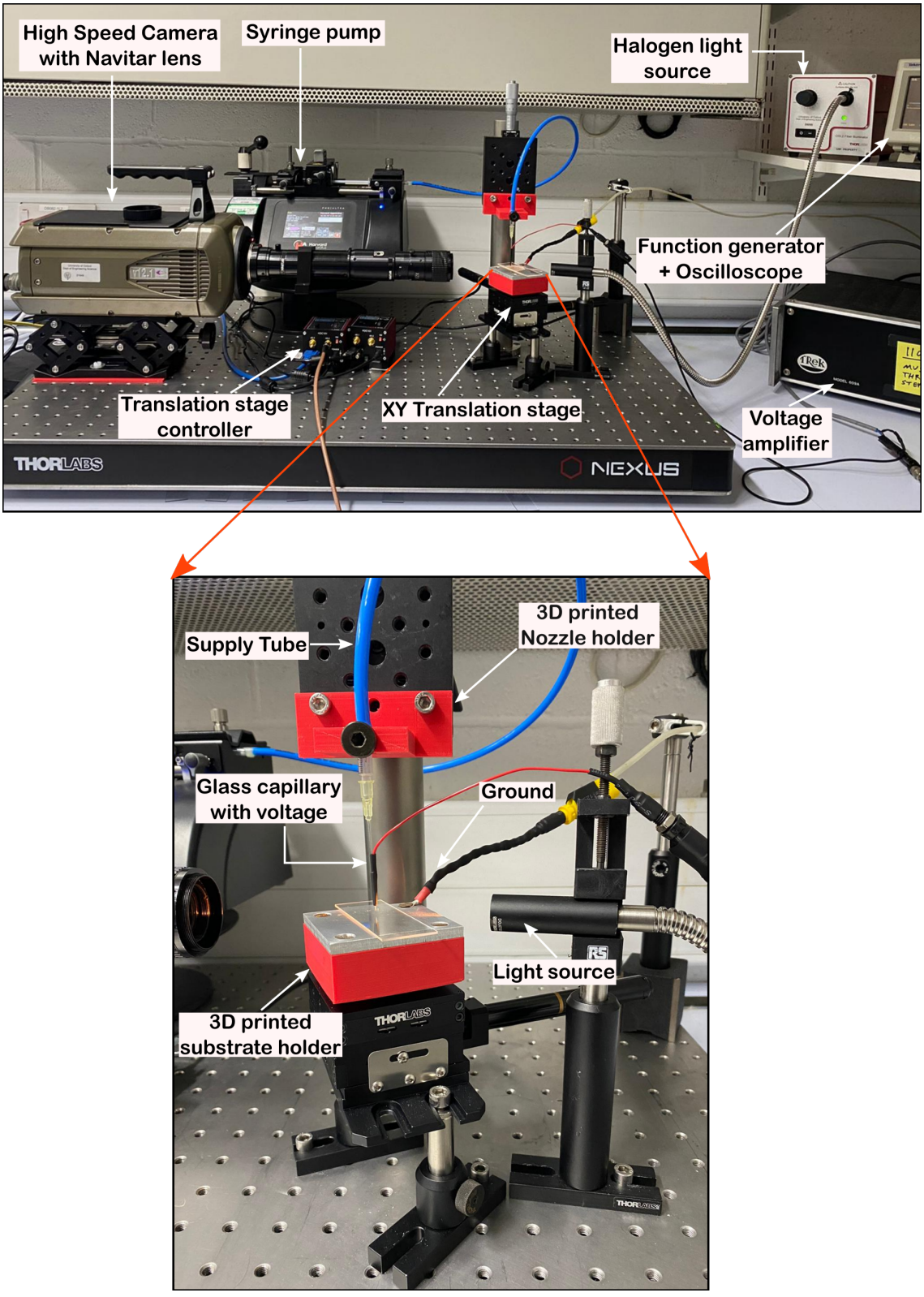

Figure 6.4: Photographs of the EHD printing system developed in this study. All of the components are labelled.

6.4 Results and discussion

To study DoD EHD printing and to achieve well-controlled and reproducible single events in terms of jet ejection, a DC unipolar pulse of the form illustrated in Figure 6.5(a) was used irrespective of the nozzle type. The input waveform consisting of rectangular voltage pulses, V_p, with pulse times t_p of the order of milliseconds, was superimposed at low frequencies (1 - 10 Hz) on a constant bias voltage. The bias voltage is particularly important as it influences the shape of the meniscus and converts it into a static cone before the arrival of the pulse voltage for the ejection of the jet. This is illustrated in Figure 6.5(b). The selection of the bias voltage is discussed in the following sections.

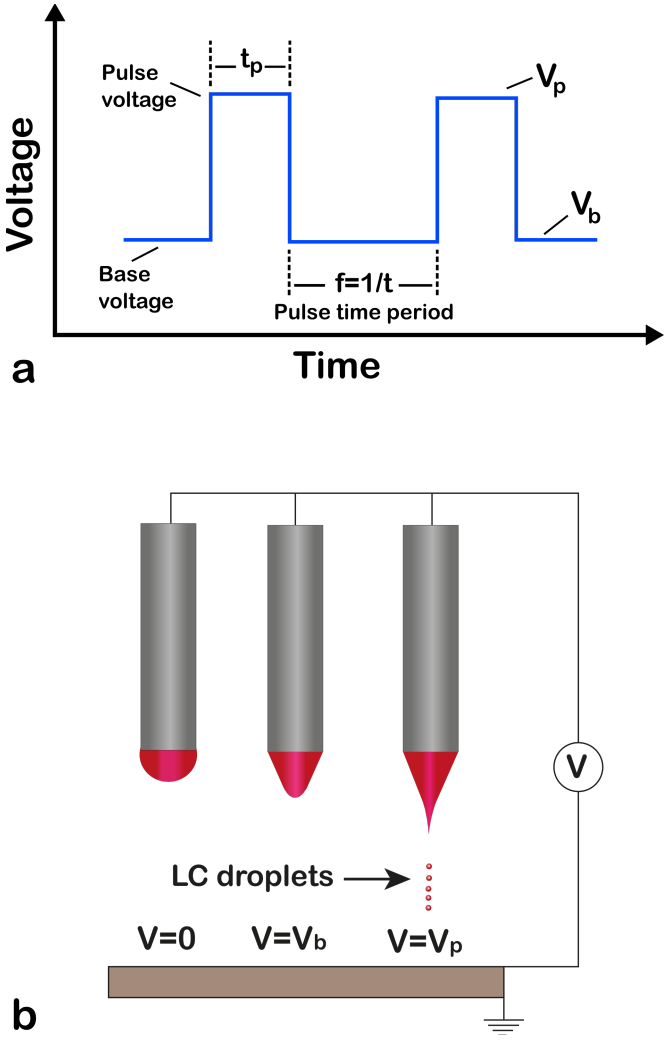

Figure 6.5: Rectangular voltage pulses were superimposed on a bias voltage (DC offset). A schematic diagram of the applied waveform is shown in **a)** which consists of a bias voltage (V_b), pulse voltage (V_p) and pulse duration (t_p). **b)** Schematic illustration of the EHD jet formation process that results from the applied waveform shown in (a).

In this work, the nematic LC mixture, BL006 (Merck), was chosen as the functional ink. This mixture has a positive dielectric anisotropy. High purity LCs are generally assumed to be non-conductive as they do not contain free charge carriers. Instead, the LC molecules possess an electric dipole moment that, in the presence of an electric field, rotates to align the LC director either parallel or perpendicular to the electric field. As discussed in Chapter 2, nematic LCs exhibit an anisotropy in the dielectric permittivity (e.g., $\varepsilon_{\parallel} > \varepsilon_{\perp}$). For voltages $> V_{th}$ a positive dielectric anisotropy LC aligns such that the director aligns with the direction of the electric field and exhibits $\varepsilon_{\parallel}$. A nematic LC layer sandwiched between two electrodes typically requires an electric field of 0.1 - 1 $\mathrm{V\mu m^{-1}}$ to completely reorient the LC director along the field direction. An EHD printing setup which is similar to this capacitive structure, typically applies high strength electric field of the order of 1 $\mathrm{kVmm^{-1}}$. [166] Therefore it can be assumed that during the EHD printing process LC molecules will be exhibiting the larger component of dielectric, $\varepsilon_{\parallel}$.

Table 6.1 displays the macroscopic physical properties of the nematic LC, BL006, at a temperature of 20 °C obtained from the literature. [169] The conductivities parallel and perpendicular to the director, as well as the conductivity anisotropy, for BL006 are unknown; however, it is believed that the properties will be comparable to that of the nematic LC eutectic mixture, E7. Therefore, it is assumed that the conductivity value of BL006 will be comparable to that of E7, which is reported to be 10^{-11} $\mathrm{Sm^{-1}}$ at a frequency of 1 kHz and a temperature of 20 °C.

Table 6.1: Macroscopic physical properties of the nematic LC, BL006. Values for the dielectric permittivity (parallel to the LC director ($\varepsilon_{\parallel}$), shear viscosity, and conductivity were obtained from the literature. [169] The surface tension is assumed to be the same as that recorded for the nematic LC E7, which was measured in Chapter 3

Dielectric constant,	**Viscosity**	**Surface tension**	**Conductivity**
($\varepsilon_{\parallel}$)	($\mathrm{mPa.\,s}$)	($\mathrm{mN \cdot m^{-1}}$)	($\mathrm{Sm^{-1}}$)
18	71	26	10^{-11}

6.4.1 Printing IPA ink

Before printing BL006, it was deemed necessary to perform preliminary experiments using a less viscous liquid to ascertain whether all components of the system functioned

correctly, and to build up a practical understanding of how the Taylor cone forms and dispenses a jet when the waveform of the type shown in Figure 6.5(a) was used. For this part of the investigation, isopropanol alcohol (IPA) was used due to its low surface tension of 20.9 mN $\cdot$ m^{-1} and weak conductivity of 6 $\times$ 10^{-6} Sm^{-1} in comparison to a nematic LC BL006. [156]

Prior to the application of a pulse voltage for DoD ejection, a DC voltage bias was applied to the IPA meniscus to investigate the range of voltages at which point the meniscus transforms into a Taylor cone without dripping droplets. In this case, IPA was delivered to the tip of the metallic nozzle which is shown in Figure 6.2(a). When a bulge meniscus was formed, the syringe pump was stopped, and an electric field was applied between the nozzle and the conductive substrate. The glass slide was always held over the counter electrode termed as substrate in all experiments unless otherwise stated.

Figure 6.6 shows an example image of the effect of the bias voltage on the meniscus evolution and the Taylor cone formation when the voltage was varied from 0 – 1100 V. The contour lines in red in Figure 6.6(a) show the corresponding change in meniscus with increasing voltage. The change in the shape of the meniscus and the increase in volume is caused by the electrical forces acting on it and due to the attraction of the charged meniscus by the counter electrode. Figure 6.6(b) shows the equilibrium shape of the meniscus in a cone shape at 1100 V. By increasing the voltage further the cone started to dispense micron-sized droplets. A further increase in the voltage amplitude resulted in the appearance of the different modes of jetting that were discussed in Section 6.2.1.

By using a bias voltage of 1000 V, pulses of different voltage amplitudes and width were then applied to obtain DoD EHD jetting. The volume flow rate from the syringe pump was varied between 10 – 100 µl/min and the pulse amplitude was varied from 300 to 500 V while keeping the pulse width fixed at 10 ms. For pulse voltages in the range of 450 - 500 V, a steady cone jet appeared and the ejection of a single jet was observed. This is referred to here as DoD ejection. Figure 6.7 shows an example image of such a case when a 500 V pulse with a pulse duration of 10 ms at a 1 kV bias voltage was applied to

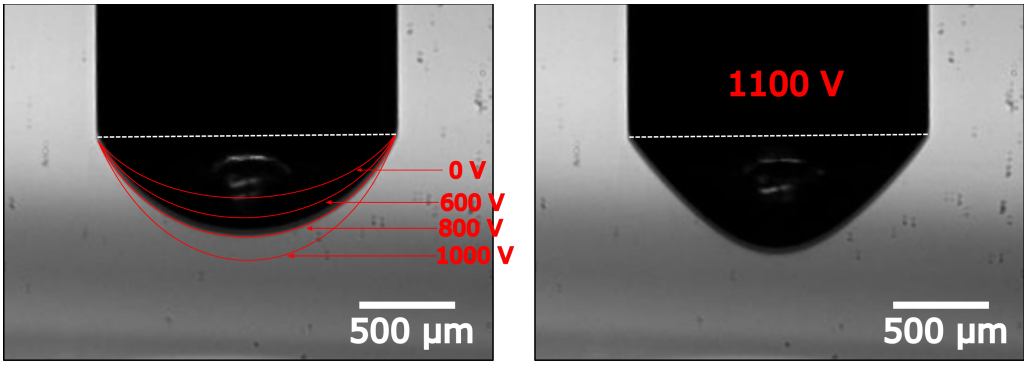

Figure 6.6: High-speed camera shadowgraph images obtained when IPA was loaded into the nozzle and then subjected to the different voltages listed in the images. The dotted white line indicates the edge of the nozzle. The distance between the nozzle and the substrate was 1.2 mm.

a steel nozzle. The images were recorded using the high speed camera. It can be observed that the meniscus, which forms a rounded cone shape, is converted to a sharp Taylor cone upon the arrival of a voltage pulse. Subsequently, a thin jet emerges from the apex of the Taylor cone. At the end of the pulse duration, the jetting stops and the meniscus forms a rounded cone. The height of the Taylor cone (from the nozzle edge to the apex of the cone) was found to be equal to the radius of the nozzle, which was 793 µm in this case (see Frame 2, Figure 6.7). The width of the jet that emerged (see Frame 4) was found to be 15 µm, which is significantly smaller than the outer diameter of the steel nozzle and is consistent with the behaviour observed for EHD printing.

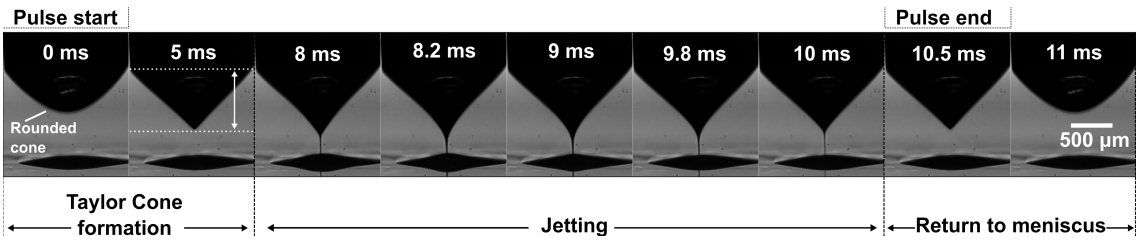

Figure 6.7: The evolution of the Taylor cone and ejection of a jet captured using high-speed shadowgraphy imaging. The images were recorded at 18,000 fps, 10 µs exposure time, and a 640 × 480 image resolution. The measurement was carried out with a bias voltage of 1 kV, a 10 ms pulse duration and a 500 V amplitude at every 500 ms. These voltage conditions were applied to the steel nozzle placed at 1.2 mm from the substrate. The experiment was performed at temperature of 20 °C.

During the experiments, a high amplitude voltage pulse without the bias voltage was also applied to see how this affected the evolution of the meniscus, the formation

of the Taylor cone and the subsequent ejection of a jet. The Taylor cone formation and jet ejection behaviour were found to be reasonably similar to that presented above except that, during the removal of the pulse, the meniscus exhibited dynamic oscillations and took 10's of milliseconds to reach a stable configuration. This effect was due to the large distortion in the material at the tip of the nozzle, which is why a bias DC voltage is needed to keep the meniscus in a stable equilibrium configuration.

6.4.2 Printing a nematic liquid crystal

Having carried out initial tests using IPA, experiments were then conducted using the nematic LC, BL006. The steel nozzle with an OD of 1586 µm was used for these experiments. The distance between the nozzle and the glass substrate was fixed at 3 mm. After filling the LC into the nozzle, a DC voltage in the range of 1 - 3 kV was applied to convert the meniscus to a cone formation. The change in the shape of the meniscus was found to occur at higher amplitudes of the DC voltage. The meniscus turned into a rounded cone at 2 kV and above this voltage long filaments of the LC began to emerge from the apex of the cone. The first frame in Figure 6.8 shows the equilibrium shape of the LC meniscus at an applied voltage of 1.9 kV.

To generate the single ejection of fluid from the Taylor cone, voltage pulses in the range of 700 - 900 V were superimposed over the bias voltage of 1.9 V, and the pulse duration was varied from 10 - 100 ms. The pulse duration was found to be an important parameter as it significantly influenced the transition from a rounded cone to the characteristic Taylor cone, and then the subsequent jet ejection process. For large diameter nozzles, pulse duration times that were less than 30 ms were found to be insufficient to transform the rounded meniscus into a Taylor cone. For pulse durations in the range of 40 - 100 ms, a Taylor cone appeared, and small droplets were found to emerge from the apex of the cone. However, in almost all of cases it was observed that during the detachment of a droplet, a thick filament of LC forms and breaks at multiple pinch of points due to viscoelastic behaviour. Figure 6.8 presents such a case where a 1.9 kV bias voltage and a 900 V pulse voltage for 50 ms duration time were applied. From the series of high-speed camera frames, it can be seen that a 60 µm thick filament extended from the Taylor cone

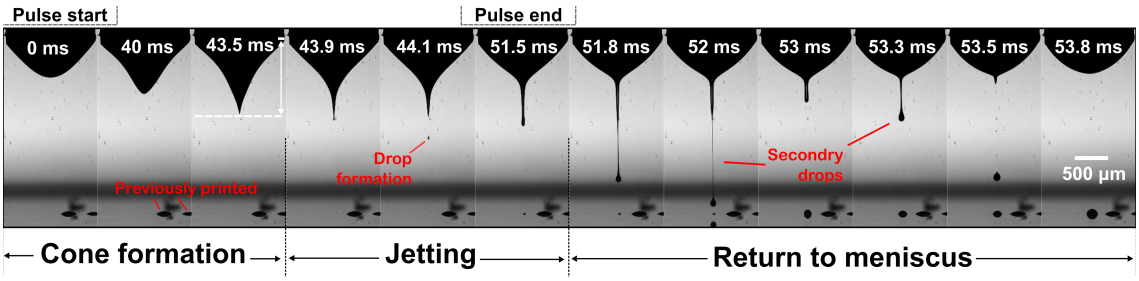

Figure 6.8: EHD printing of a nematic LC. High-speed shadowgraphy images recorded at 18,000 fps, 15 µs exposure, and a 640 × 480 image resolution. Measurements were taken when a bias voltage of 1.9 kV with a 50 ms pulse duration and a 900 V amplitude at every 1s was applied to a steel nozzle placed at 3 mm from the glass substrate. The experiment was performed at a temperature of 20 °C.

soon after the detachment of a droplet. Furthermore, it is evident that the shape of the LC Taylor cone has become elongated and its height is 1260 µm, which is almost equal to the diameter of the nozzle. This is in contrast to the results obtained for IPA, shown in Figure 6.7, whereby the Taylor cone was found to be half of the diameter of the nozzle.

From the above results, it appears that a LC material with very low conductivity and high dielectric permittivity can undergo Taylor cone formation. However, it should be noted that the time taken to form the Taylor cone was five times longer compared to when IPA was used as the ink (shown in Figure 6.7). This is because the Taylor cone formation for IPA resulted from free charge transport due to its weakly conducting, and less viscous properties. However, for the case of a nematic LC, the Taylor cone was formed due to large electrical stresses, which might have taken longer to appear due to high viscosity of LC. It is therefore reasonable to suggest that for a dielectric material such as a nematic LC, the Taylor cone is dielectrically driven, which is relatively slow, while for a conductive material, it is driven by the transfer of free charges.

6.4.3 The role of nozzle size

From the experiments carried out with the larger diameter nozzle (1586 µm) it can be observed that the size of the meniscus was dictated by the outer diameter of the nozzle. Moreover, as the nozzle is large, a high bias voltage was needed to convert the meniscus into a Taylor cone. In previous work, the size of the nozzle has proven to be an important parameter in terms of being able to print smaller feature sizes and in providing greater

stability to the Taylor cone. [128, 131] Therefore, to investigate the effect of a smaller nozzle size on the Taylor cone formation of the LC ink, a 40 µm OD glass capillary was installed in the printhead and the voltage waveform parameters (shown in Figure 6.5(a)) were varied. The experimental approach employed here was similar to that used for the optimisation of the DC bias voltage. This voltage was always below the voltage at which dripping began. A pulse signal of a certain pulse amplitude and duration superimposed on top of the DC voltage was then applied to the nozzle. The distance between the nozzle tip and substrate was set to 100 µm. It was observed that the dripping started when the bias voltage was greater than 1 kV. The DC voltage was varied between 800 - 900 V and the flow rate of the syringe pump was set to 0.5 µl/min. The optimum range of pulse voltages was found to be 300 - 400 V, and pulses of different durations were tested at 1 s and 500ms delay times (1 Hz and 2 Hz pulse frequencies).

The pulse duration and delay between two consecutive pulses are important parameters in DoD EHD printing. Briefly, these two parameters determine how quickly a meniscus of a certain conductivity can respond to the input signal and also to the minimum drop size. Therefore, an ink with optimum liquid parameters can only print at high input frequencies and for a short duration of input pulses. The pulse duration time and delay (pulse repetition in a second: frequency) thus dictates the volume of the droplet and the subsequent feature size on the printing substrate. Lee et al. [170] reported a systematic analysis of these parameters by using diethylene glycol as an ink, and pulse durations from 1 - 500 ms at 1 Hz frequency were applied which revealed that the pulse duration affected the drop sizes and overall printing quality. Similarly, An et al. [165] examined the effect of pulse frequencies on a range of liquids and they reported that the voltage pulse frequency directly related to the drop generation frequency (perfect DoD) when the voltage pulse frequency was less than 50 Hz.

Figure 6.9 shows example images when a 300 V pulse voltage and 900 V DC bias voltage was applied to the capillary nozzle and high-speed camera images were recorded at three different pulse duration times of 50 ms, 25 ms, and 10 ms. The pulse frequency was set to 1 Hz. In terms of pulse duration, when this was set to 50 ms, large and thicker

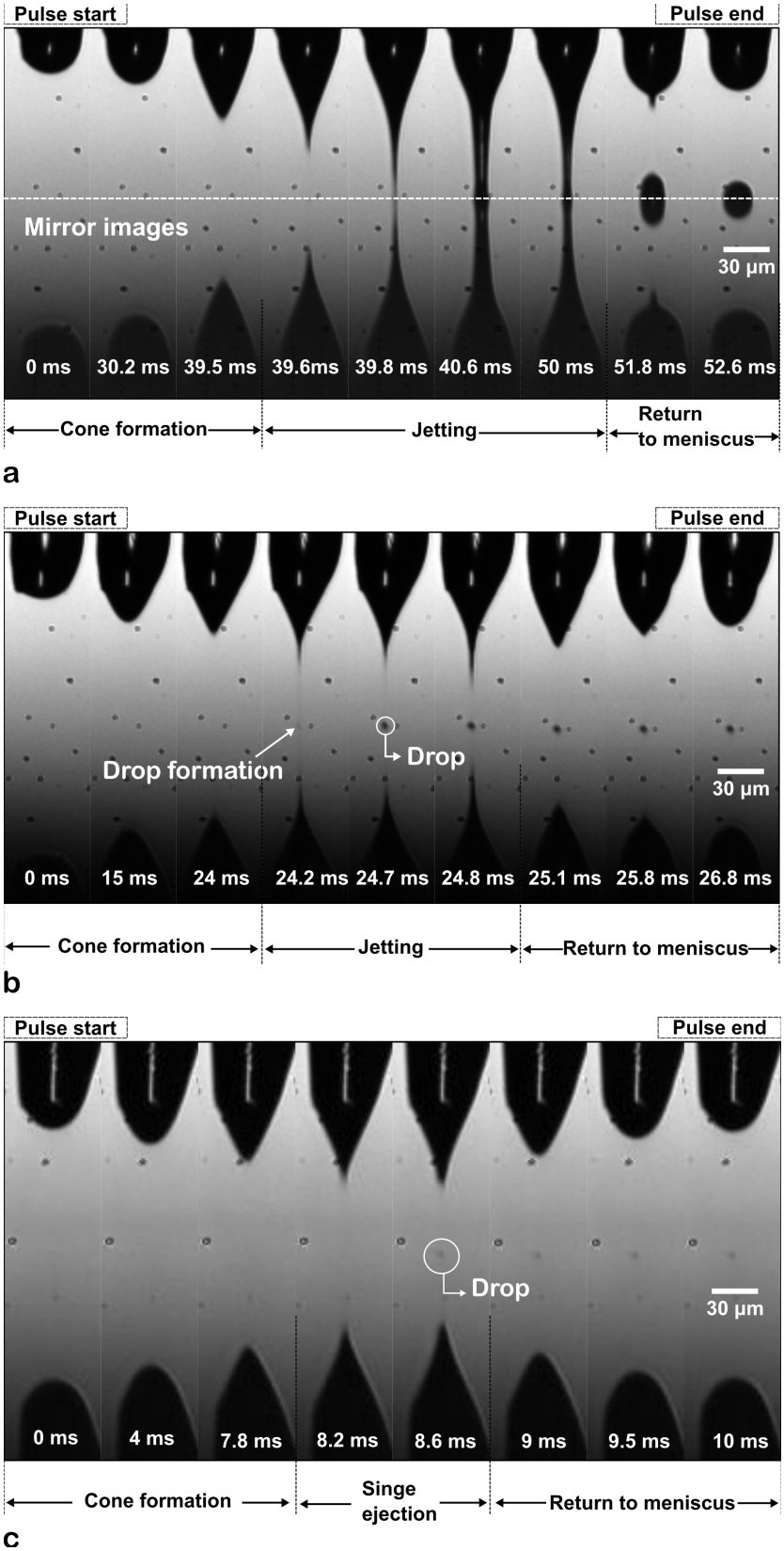

Figure 6.9: EHD printing with a smaller nozzle diameter. High-speed shadowgraphy images of the jetting of the nematic LC BL006 captured using a high speed camera (20,000 fps). The nozzle was a glass capillary with a 30 µm internal diameter and 40 µm outer diameter. The distance between the nozzle and the substrate was 100 µm. The input waveform consisted of a 900 V DC bias voltage, a pulse voltage of 300 V, and a pulse frequency of 1 Hz. The pulse duration in each case was: **a)** 50 ms, **b)** 25 ms, and **c)** 10 ms.

fluid ligaments were observed as can be seen in Figure 6.9(a). The thickness of the jet (40 ms frame, Figure 6.9(a)) was 10 µm. When the pulse duration was set to either 25 ms or 10 ms, thin fluid jets were observed with a jet thickness in the submicron range, as can be seen in Figure 6.9(b) and Figure 6.9(c), respectively. In addition, it was possible to perform jetting at 5 ms pulse duration. However, below 5 ms the meniscus did not show any movement. The jets were highly reproducible at a pulse frequency of 1 Hz. For frequencies between 2 – 4 Hz, the LC jetting was highly discontinuous and above 4 Hz no jetting was observed.

6.4.4 EHD printed nematic droplets

In order to further investigate the effect of pulse duration time on droplet sizes, the jetting process, as shown in Figure 6.9, was performed over a lecithin-coated glass substrate in order to fabricate sessile LC droplets. The substrate preparation process has already been described in Section 4.2.1 of Chapter 4. This alignment layer was chosen to provide a homeotropic surface alignment for the LC director and to enable a direct comparison between inkjet and EHD printed droplets. Figure 6.10 shows optical microscope images of different sized droplets printed at 5 ms, 10 ms, 15 ms, 25 ms, and 50 ms pulse duration times and with a 40 µm OD glass capillary. Printing was performed at 1 Hz pulse frequency, and it was observed that the drop generation rate was similar to the input pulse frequency.

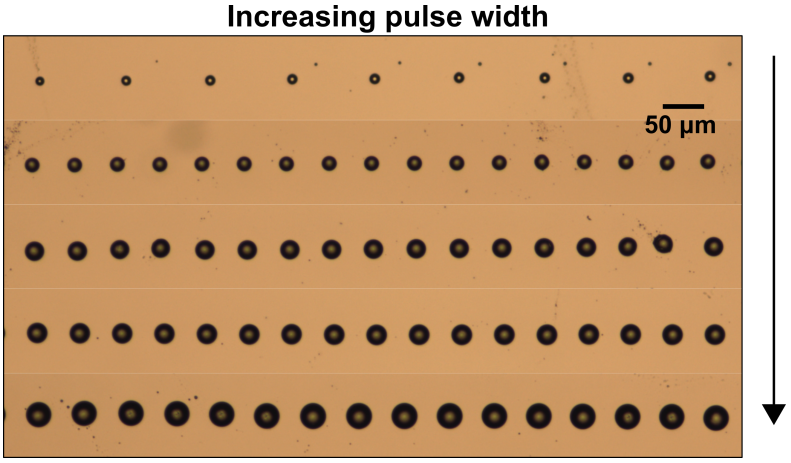

Figure 6.10: Optical microscope image of nematic LC (BL006) droplets fabricated using EHD printing onto a glass substrate with a homeotropic alignment layer. The printing was performed with a 40 µm OD nozzle. The distance between the nozzle and substrate was 100 µm. The substrate was translated at very low speeds during the printing process to form rows of droplets (less than 1 mm/s). The substrate speed is not constant for all rows of droplets.

The plot in Figure 6.11 shows the corresponding droplet diameters. It is evident that the pulse duration time greatly influenced the droplet size. The minimum droplet size with the 40 µm OD nozzle printed with a 5 ms pulse duration was found to be 8 µm whereas the maximum droplet size was recorded for a 50 ms pulse duration and was found to be 30 µm. The effect of pulse duration on droplet diameter is in accordance with the behaviour reported previously for both conductive and non-conductive inks. [137, 170, 171]

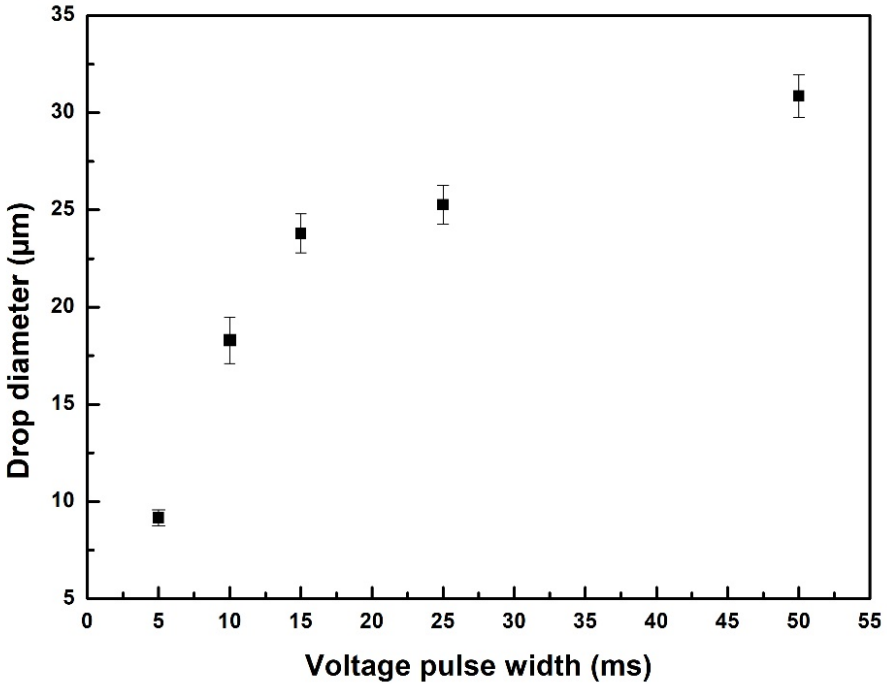

Figure 6.11: The effect of the pulse duration on the nematic LC droplet footprint diameter. The input print conditions were a DC bias voltage of 900 V, a pulse voltage of 300 V, a pulse frequency of 1 Hz, and a flow rate of 0.1 µl/min. The printing was performed with a 40 µm OD nozzle. The distance between the nozzle and substrate was 100 µm. The substrate was translated at very low speeds during the printing process to form rows of droplets (less than 1 mm/s.

Using 40 µm OD nozzle copper-wrapped glass capillaries led to EHD printing of a nematic LC with a minimum achievable droplet footprint of 8 µm. To further reduce the size of the droplet footprints, a smaller diameter tip was required. For this task, a 1 µm ID glass capillary was assembled by following the procedure described in Section 6.3 and the nozzle was then installed into the printhead. With 1 µm ID tip, it was very difficult to drive nematic LC ink to the tip of the nozzle. Any air trapped in the tip during LC loading led to air pockets which obstructed the flow of ink. To circumvent this issue, the plunger of the barrel clamped to syringe pump was deriven manually and this flushed the LC out

of the tip. When the LC reached the tip, the syringe pump was adjusted to run at the desired ink flow rates. Before printing, the nozzle and syringe pump assembly were left for a period of time to dissipate any residual back pressure that might have been produced due to an expansion of the PTFE tube.

Using a small diameter capillary enabled the generation of a much smaller meniscus of a size that was equal to the OD of the capillary nozzle. Due to the smaller nozzle size, the high-speed shadowgraphy imaging technique was not suitable for visualising the Taylor cone formation process and subsequent jetting. The high-speed camera image in Figure 6.12 shows such a case. It was possible to see the nozzle and identify some of the printed droplets (the droplets were not in-focus due to the arrangement of the glass slide on the moving substrate, see Figure 6.4 for the position of the imaging system relative to the substrate). Therefore, instead of viewing the nozzle directly, the input waveform parameters were optimised by running the printhead over the substrate and inspecting the morphology of the printed droplets on an optical microscope.

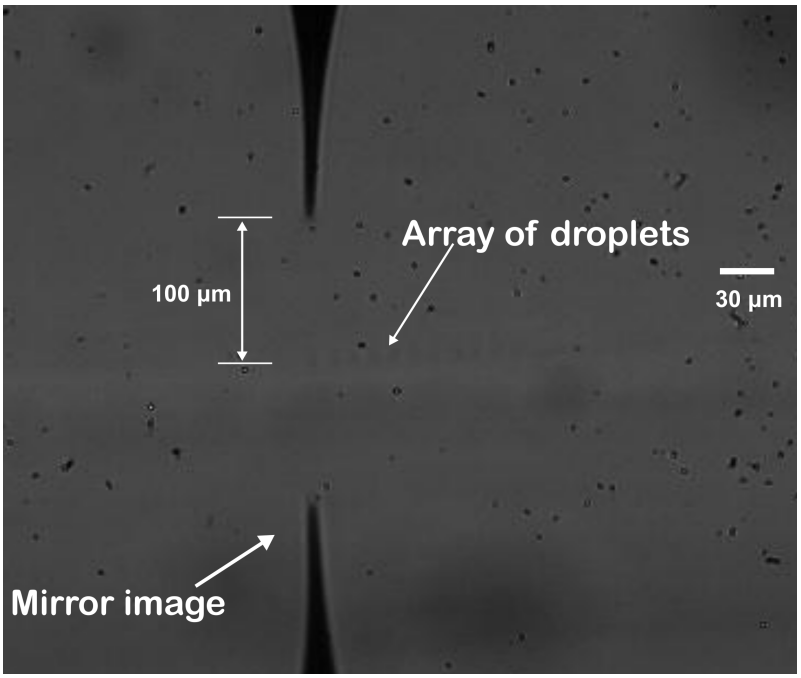

Figure 6.12: Shadowgraphy image showing the 1 µm glass capillary nozzle held at a distance of 100 µm from the substrate.

6.4.5 EHD printing-on-the-fly

While seeing a decreasing trend of DC voltage on previously used nozzles, it was assumed that a small DC voltage would be sufficient to pull the LC from the 1 µm nozzle. However, this was found not to be the case. As explained earlier, 1 µm diameter capillaries are dominated by capillary forces and for this reason a lower DC bias voltage did not result in jetting. Instead, a DC bias voltage in the range of 950 – 1000 V and a pulsed voltage in the range 300 – 400 V were applied between nozzle and substrate. The volume flow of the syringe pump was fixed to 0.1 µl/min. To perform DoD EHD printing, the pulse duration and frequency were varied between 1 - 10 ms and 1 - 10 Hz, respectively. The substrate was translated at arbitrary speeds in the range of 1 - 2 mm/s. Following this approach, LC droplets were printed using different input parameters in a *printing-on-the-fly mode*.

"Printing-on-the-fly mode" is a type of DoD printing in which the substrate moves at a constant speed and droplets are only generated during the input pulses. In this method, the drop spacing can be adjusted by varying the substrate speed and drop generation frequency. In contrast to a *'move-a-step-and-print-method'*, this method provides an efficient way to create a uniform coverage of droplets over the substrate. This form of DoD printing method has been employed previously in Chapter 5 to fabricate large area PDLC arrays that form arbitrary patterns using a MicroFab inkjet printer.

Using the 1 µm ID capillary it was observed that droplets can be generated at pulse durations less than 5 ms and frequencies greater than 4 Hz, which was not observed when the 40 µm OD nozzle was employed for EHD printing. Here, droplet footprints with 2 – 10 µm diameters were formed. However, for all of the printing trials, it was observed that the print quality was limited. The printed droplets were not uniform in terms of size, and droplets were either missed or an unexpectedly large volume of LC was deposited. Microscopy images in Figure 6.13 show representative examples for when the LC was printed using different input parameters. The limitation in the print quality is due to intermittent and unsteady jetting from the Taylor cone when printing was performed at a 10 Hz frequency. Stable Taylor cone EHD jetting was only observed at a 1 Hz frequency, which is discussed further in the subsequent section.

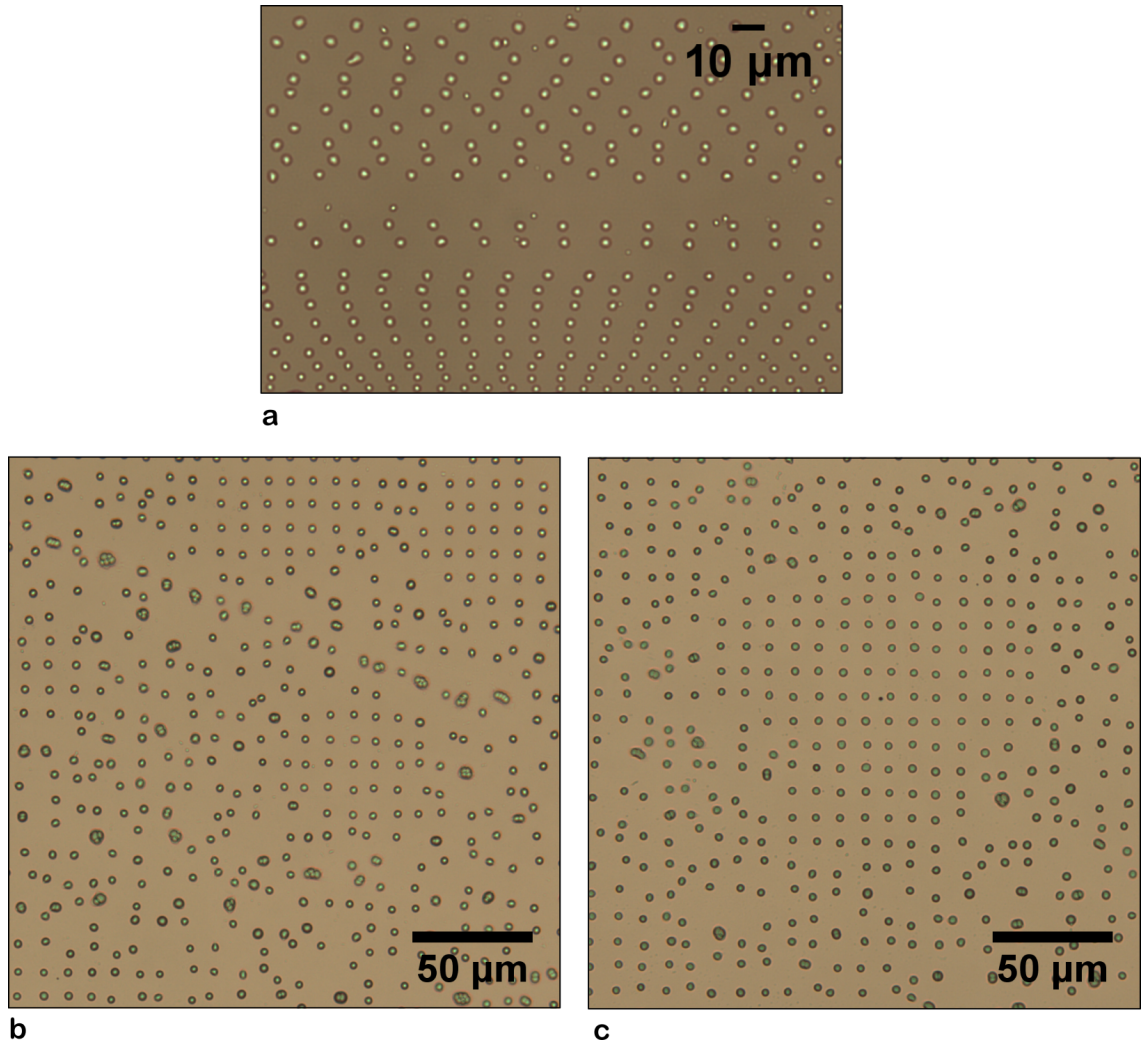

Figure 6.13: Optical microscope images of nematic LC (BL006) droplets EHD printed using the following operating conditions: 1000 V DC bias voltage, 400 V pulse voltage, and a pulse frequency of 10 Hz. The pulse durations were: **a)** 2 ms, **b)** 3 ms, and **b)** 5 ms. The substrate speed was 1 mm/s. The distance between the nozzle and the substrate was 100 µm. The printing was performed on lecithin-coated glass. The printing was performed with 1 µm glass capillary.

Figure 6.14 is an optical microscope image of a DoD EHD printed array of droplets performed using a 1 Hz frequency and 2 ms pulse duration time. The substrate was translated at a speed of 50 µm/s. It can be seen that the jet was ejected at each input pulse on the substrate forming a 4 $\times$ 6 array of droplets. The size of each droplet was around 2 µm in diameter. The patches of debris on the substrate are regions of lecithin, which appeared from an inadequately mixed solution before performing the alignment. The red dotted lines superimposed over the image are used to show the positional deviation of the printed droplets. The deviation is around $\pm$ 1.5 µm, which is very good and in accordance

with the positional accuracy of the translation stage.

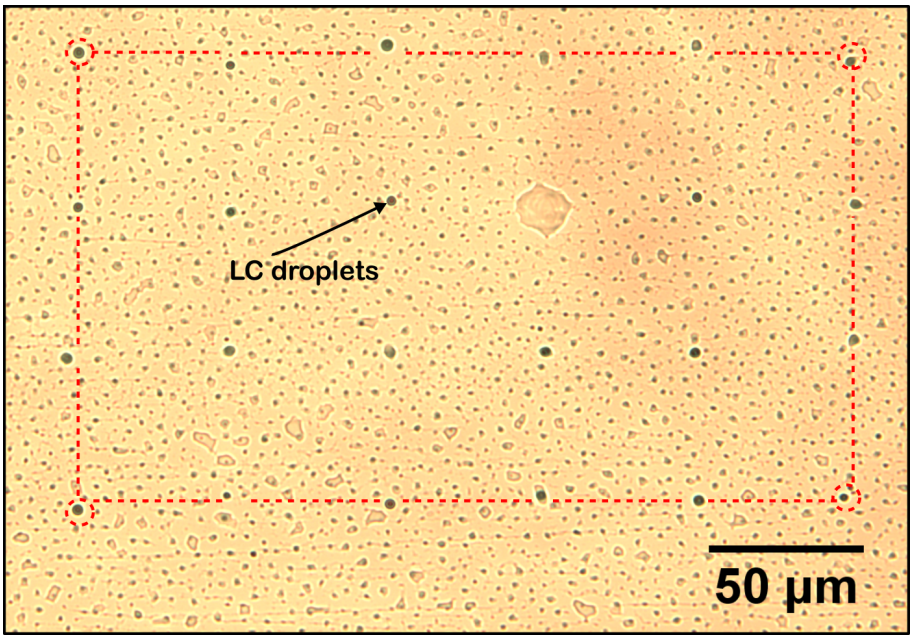

Figure 6.14: On demand EHD printing of a nematic LC (BL006). The operating conditions were 1000 V DC bias voltage, 400 V pulse voltage, a pulse frequency of 1 Hz, and a pulse duration of 2 ms. The black arrow points towards a printed LC droplet. The droplets encircled with dotted red circles and red dotted lines are used to demonstrate positional deviation of the printed droplets. The printing was performed with 1 µm glass capillary.

6.4.6 EHD Microdripping Mode

In Chapter 4 it was shown that when nematic LC E7 was printed onto a homeotropically aligned substrate (Lecithin) using DoD inkjet printing with an 80 µm inner diameter nozzle, it resulted in an average droplet footprint of 120 µm and a contact angle of 32°. (See Section 4.3, Chapter 4). In comparison, in this chapter EHD printing has shown great potential in terms of being able to print smaller LC droplets with a size that is equal to 2 µm (see previous section), which is 60 times smaller than an inkjet-printed drop.

Though it has been demonstrated that the LC can undergo EHD jetting to produce micron-sized droplets, stable cone jetting and uniform sized droplets were only observed when printing was performed at pulse frequencies that were less than 2 Hz, which is not ideal for the printing of large arrays or periodic structures as it will lead to very long fabrication times. In contrast, microdripping (introduced in Section 6.2.1) is an EHD

printing mode that has been reported to lead to a high throughput and controlled micron size droplet for a range of liquids, especially for dielectrics/poorly conductive inks that are often unable to undergo Taylor cone jetting. [156, 170, 172] The range of operating conditions for the microdripping mode largely depends upon the electric potential and volume flow rate. Generally, this mode appears before the onset of the Cone Jet mode, i.e., at comparatively low electric potential and low volume flow rate.

To enhance the uniformity and periodicity of the LC droplets, EHD printing was therefore performed in the microdripping mode. The experimental scheme illustrated in Figure 6.3 and shown in Figure 6.4 used for cone jet mode printing, was also used for microdripping mode EHD printing. The 40 µm OD glass capillary was preferred in this case because it was possible to visualise the printing dynamics at the tip of the nozzle.

For microdrip mode printing, the operating parameters optimised for the 40 µm OD (in cone jet mode) nozzle were used as a basis to identify a new set of parameters. The reduction in electric field strength was found to be the key factor in performing microdrip EHD printing. Therefore, to reduce the electric field strength the distance between the nozzle and the substrate was increased by moving the printhead along the Z direction (upwards).

Figure 6.15 shows an example image of LC microdripping from a 40 µm OD glass capillary. The high speed camera frames were recorded when the height of the nozzle was increased from 100 µm to 300 µm and the input waveform parameters were tailored to perform microdripping. For this nozzle, the Taylor cone formation and jetting process has already been presented in Figure 6.9. For the most part, the input parameters were the same as that used before; however, small variations were made to the DC bias voltage and pulse voltage amplitudes. The DC voltage was reduced to 800 V and the pulse voltage was increased to 600 V. The pulse width was 5 ms and the volume flow rate was the same, 1 µl/min. As can be seen in the fourth frame (3.5 ms), the resulting forces elongate the apex of the cone to create a liquid filament. The filament then undergoes necking and

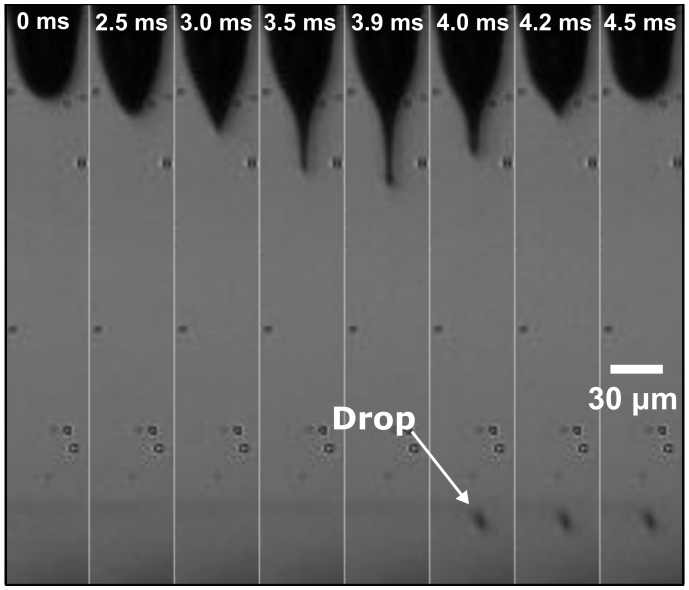

Figure 6.15: High speed shadowgraphy images showing EHD printing of a nematic LC (BL006) in the microdripping mode. The height between the nozzle and substrate was 300 µm.

detaches a micron size droplet. The remaining filament returns to the main meniscus (sixth frame, 4.3 ms). Due to the constant volume flow rate, the height of the meniscus remains unchanged, as can be seen in the first and last frames of Figure 6.15. Experiments were performed with large pulse widths >10 ms and it was observed that large fluid filaments were formed, which resulted in the formation of satellite droplets along with the main droplet. This was analogous to what has been shown previously when EHD printing was performed with the 1586 µm OD steel nozzle (Figure 6.9).

After optimising the microdripping parameters, EHD printing was performed on glass substrates that were coated with either a homeotropic or planar alignment layer. Parameters such as the droplet footprint diameter and LC director configuration were investigated using polarised optical microscope images. In addition, the distribution of the droplet diameters was used to access the homogeneity in the droplet diameter.

By using the 40 µm OD nozzle, nematic LC droplets were printed onto a glass substrate with a homeotropic alignment layer. The procedure for promoting homeotropic alignment has already been discussed in Chapter 4. The operating conditions were set to 800 V DC bias voltage, 600 V pulse amplitude, 5 ms pulse duration and 5 Hz pulse

frequency. The substrate speed was set to 0.25 mm/s. Figure 6.16 shows a microscope image where drops were printed in an array covering a size of 600 × 600 μm^2. The enlarged images show that the drops are consistent in terms of droplet shape with very little variation in the quality of droplet boundary and diameter. The wetted droplet diameter was approximately 8.5 μm with a contact angle of 32°.

The microscopy images shown in Figure 6.16 was used to determine the variation in the droplet diameter and was analysed using the ImageJ software. Figure 6.17 shows the resulting histogram of droplet diameters for 600 EHD printed droplets. The average droplet diameter was found to be 8.5 μm (mean) with a standard deviation of 0.43 μm, assuming a normal distribution. These drops are 14 times smaller than those fabricated using inkjet printing, which provides a great opportunity to fabricate printed LC devices with droplet sizes less than 10 microns.

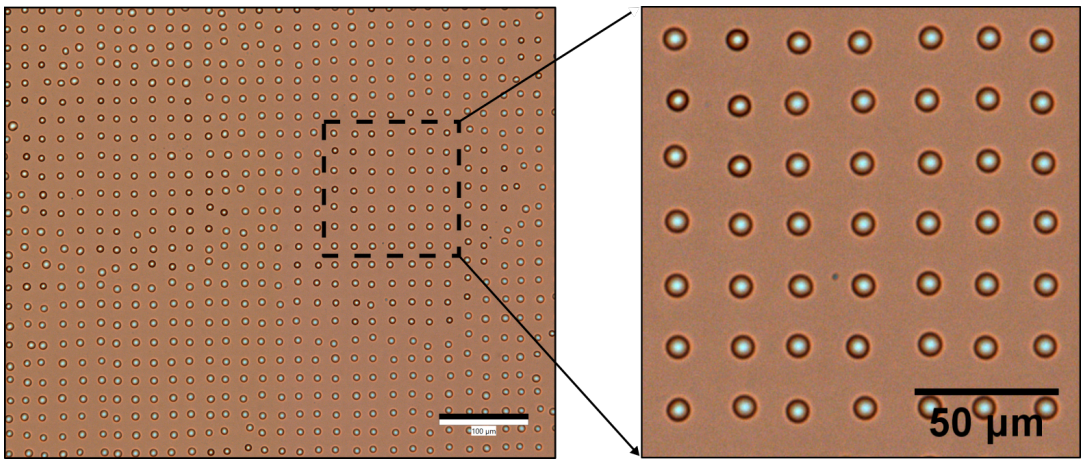

Figure 6.16: Optical microscopy images showing a two-dimensional array of EHD printed nematic (BL006) LC droplets printed onto a glass substrate with a homeotropic alignment layer. EHD printing was conducted in the microdripping mode with a 40 μm OD glass nozzle.

Figure 6.18 shows a polarised optical microscope (POM) image of a 3 × 3 array of EHD printed droplets on a glass substrate with a homeotropic alignment layer. The droplets show a degree of birefringence indicated by the four coloured quadrants in the POM image, which is in accordance with the LC director model obtained from simulations of a printed microlens using COMSOL that was presented earlier in this thesis (see Figure 4.11, Chapter 4). The POM image indicates a homeotropic alignment of the

droplets and the appearance is similar to that observed for the nematic LC (E7) droplets that were printed using inkjet printing (see Figure 4.9, Chapter 4).

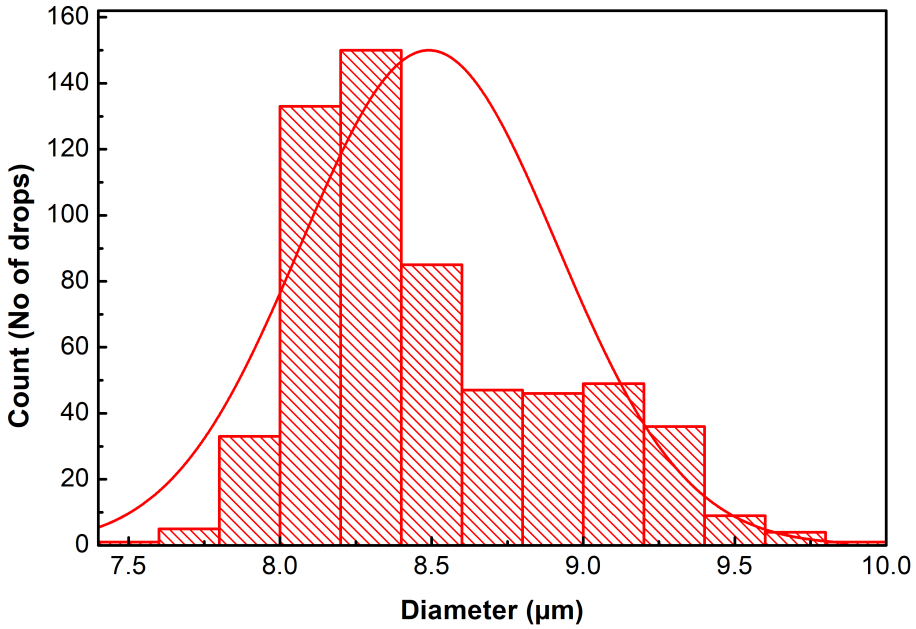

Figure 6.17: Histogram plot showing the variation in the droplet diameter of 600 EHD printed droplets when deposited onto a glass substrate with a homeotropic alignment layer. The EHD printing was performed in the microdripping mode with a 40 μm OD glass nozzle. The red curve is a normal distribution fit to the experimental data.

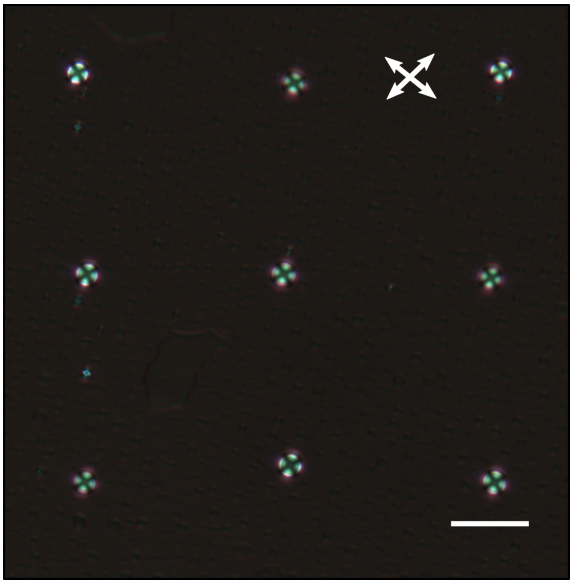

Figure 6.18: Polarised optical microscope image of 3 × 3 array of EHD printed nematic LC droplets observed through crossed polarisers (the axes of the polarisers are indicated by the double-headed white arrows). The scale bar represents a length of 20 μm. The droplets were printed on homeotropic alignment layer.

Using the same operating parameters, EHD printing was also performed on a glass substrate with a planar alignment layer. A commercially available empty LC glass cell (LC2, INSTEC) with rubbed polyimide alignment layers was carefully disassembled and one of the glass substrates was then used as the printing substrate. The spacer beads were removed by subjecting the substrate to a stream of pressurised air from a canister.

Figure 6.19(a) shows a representative POM image of a two-dimensional array of EHD printed nematic LC droplets on a glass substrate with a rubbed polyimide alignment layer. The droplets exhibited a good uniformity in terms of size and drop spacing. The average footprint diameter of the droplets was found to be 8.3 µm with a contact angle of 32°. Figure 6.19(b) shows the POM image of the array of droplets when the polarisers were crossed. Each droplet showed a disclination line running through the centre of the droplet, which is due to two different alignment conditions induced on the bottom and top surface of the LC droplet. Figure 6.19(c) schematically illustrates the nematic LC director configuration inside droplets when printed on an alignment layer.

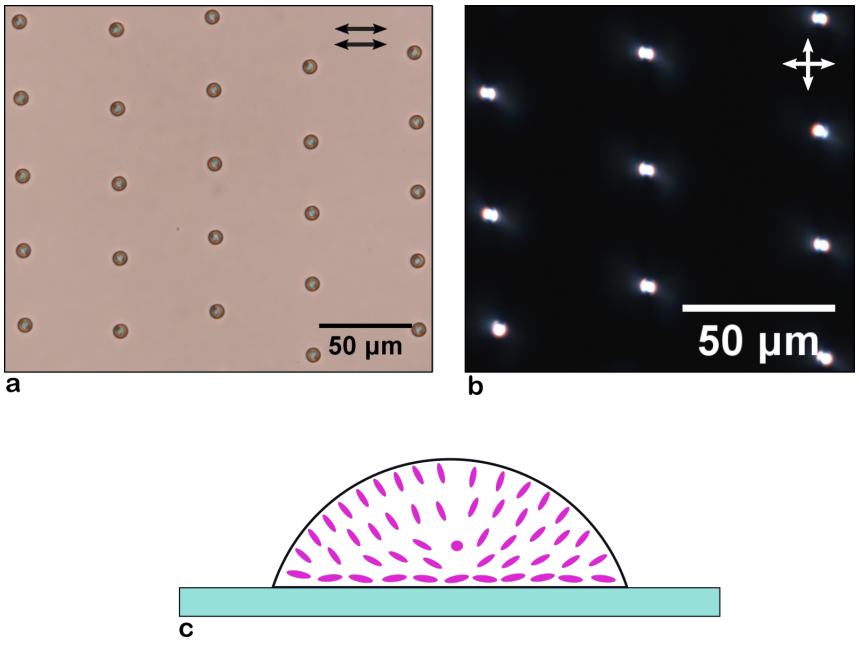

Figure 6.19: **a)** POM of EHD printed nematic LC droplets on a glass substrate with a rubbed polyimide alignment layer. The orientations of the polariser and analyser are indicated by the double-headed black arrows. **b)** POM image of the same sample when the polarisers were crossed. The double-headed white arrows show the orientations of the polariser and analyser. **c)** Schematic diagram illustrating the configuration of LC molecules alignment inside a spherical capped LC droplet when printed on a planar aligned glass substrate.

Figure 6.20 shows the distribution of droplet diameters for 87 nematic LC droplets. A small difference of 0.6 µm was observed between the maximum and minimum diameter. The average droplet diameter was found to be 8.3 µm (mean) with a standard deviation of 0.13 µm. This suggests that the droplets printed with EHD printing on a planar alignment surface also maintain good homogeneity in terms of their sizes and periodicity.

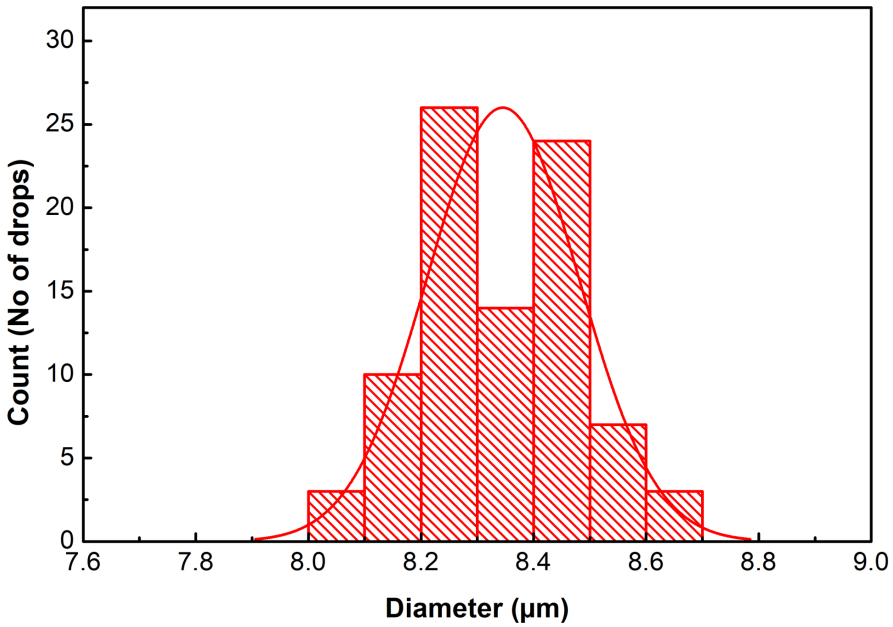

Figure 6.20: Histogram plot showing the variation in droplet diameter for 87 EHD printed nematic LC droplets deposited onto a glass substrate with a rubbed polyimide alignment layer. The printing was performed with a 40 µm OD glass nozzle in the microdipping mode. The red curve represents a normal distribution fit to the experimental data.

6.4.7 EHD Printed LC Patterns

To print droplets to form regular arrays or patterns, the function generator was arranged in such a configuration where it started to trigger with the output signal from the motion controller. The motion controller has the ability to generate a square signal of very short duration (less than 1 ms) at each step size of the translation stage. Using this experimental arrangement, EHD printing in microdripping mode was performed and droplets were assembled into arrays and patterns. Figure 6.21 shows an example optical microscopy image of a two-dimensional array of droplets printed at 50 µm step sizes using the 40 µm OD glass capillary. The average drop size was 16 µm. The drops were reasonably homogeneous both in terms of size and spacing. The accuracy of a single droplet placement is given by the accuracy of the positioning system. In this work, the translation stages that

were used provide good repeatability with ±1.5 µm error.

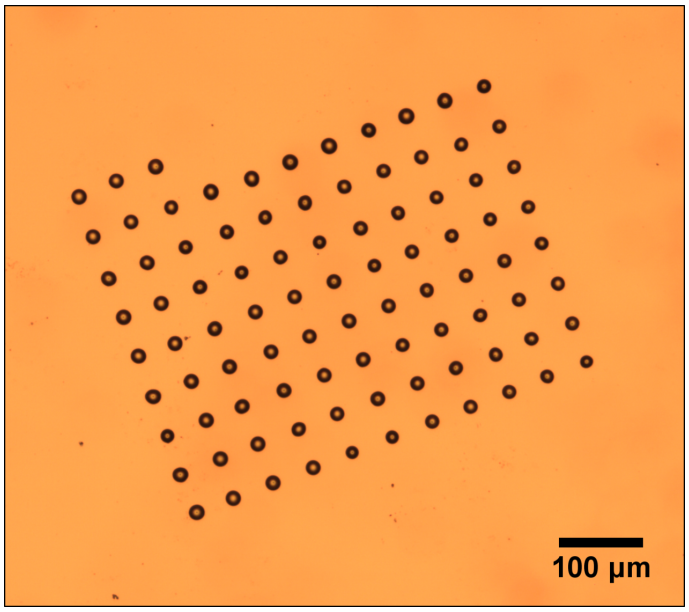

Figure 6.21: Optical microscopy image of EHD printed nematic LC droplets deposited onto glass substrates with a homeotropic alignment layer. The printing was performed in the microdripping mode with a 40 µm diameter glass capillary. The operating parameters were as follows: 600 V bias DC voltage, 400 V pulse amplitude, and a distance of 300 µm between the nozzle and the substrate. The volume flow rate was 1 µl/min.

A successful attempt was made to print alphanumeric characters with a small feature size using the 1 µm glass capillary. The optical microscopy images in Figure 6.22 show the letters 'SMP' that were printed using DoD deposition i.e., move a step and print. The EHD printing system can be used to assemble droplets to form various images/logos/-patterns by instructing the stages to move in any direction in smaller step sizes using a scripting language (as is the case for the Microfab printer). It can be seen in Figure 6.22(a) that the droplets are homogenous with an average footprint diameter of 8 µm and a distance between the droplets of 50 µm. Figure 6.22(b) shows a POM image with crossed polarisers of 90°. Every droplet shows the four colour quadrants, which indicates that even these small droplets exhibit an alignment that is similar to that shown in Chapter 4 for 120 µm diameter droplets.

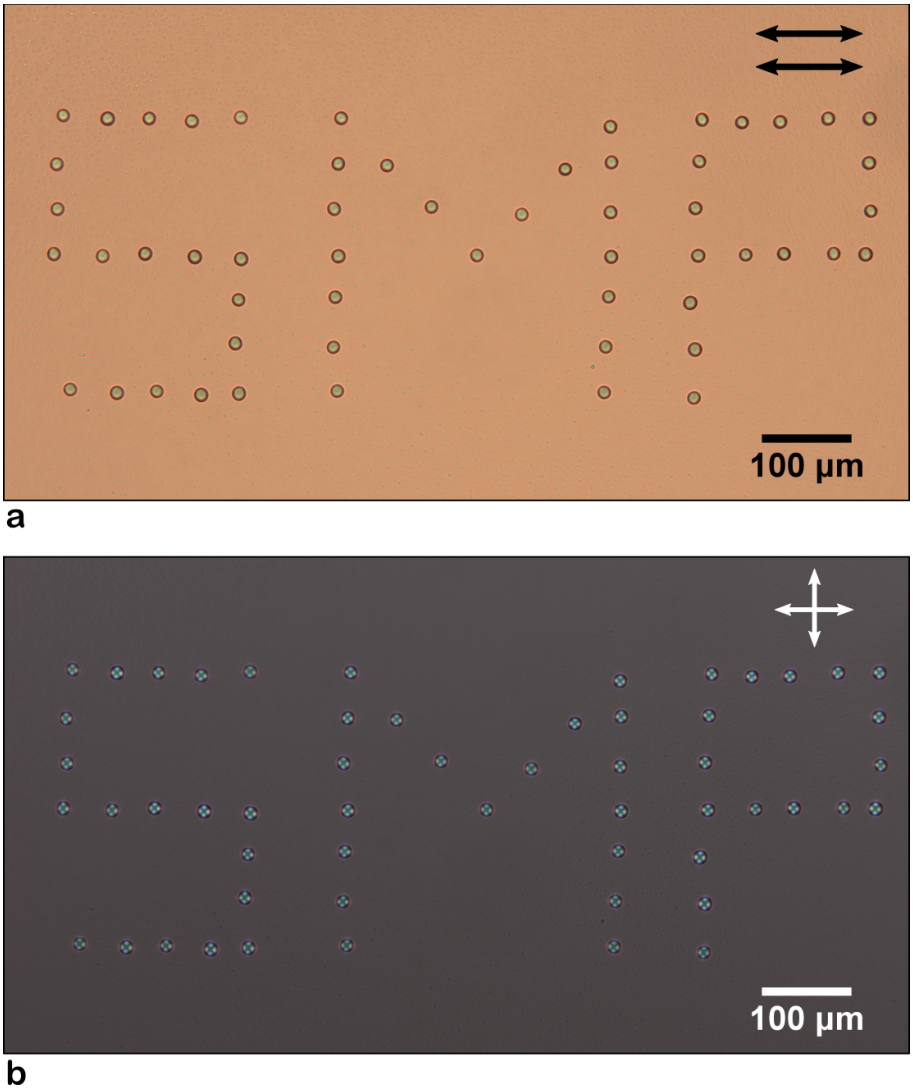

Figure 6.22: POM images of an EHD printed alphanumeric logo using a nematic LC. **a)** parallel polarisers (the orientations of the polarisers are denoted by the double-headed black arrows) and **b)** crossed polarisers (the orientations are denoted by the white double-headed arrows). The nematic LC was EHD printed with a 1 µm diameter glass capillary onto a glass substrate with a homeotropic alignment layer. The distance between nozzle and substrate and the syringe pump volume flow rate were set to 100 µm and 0.1 µl/min, respectively. The operating parameters were 475 V DC voltage, 900 V pulse amplitude and 5 ms pulse duration.

6.5 Summary and Conclusion

In summary, electrohydrodynamic (EHD) printing of a nematic LC has been demonstrated for the first time. To begin with, an EHD printing system was designed, developed, and an initial set of experiments were carried out using a large metallic nozzle to visualise the Taylor cone formation process.

To perform drop-on-demand EHD printing a unipolar pulsed waveform with a certain pulse duration time and frequency was employed. Two different glass capillaries with 40 μm and 1 μm diameter were used. The effect of pulse duration time and frequency were investigated on 40 μm glass capillary. The results obtained indicate that the volume of the dispensed fluid is directly related to the pulse duration time. It was found that a minimum of 5 ms pulse duration was required to perform EHD jetting of a nematic LC. Moreover, stable EHD jetting was only observed when the pulse frequency was in the range of 1 - 2 Hz. By reducing the size of the meniscus, it was observed that shorter pulse durations could lead to EHD jetting. As an example, a 1 μm capillary exhibited EHD jetting for a pulse time of 2 ms, but reproducible jets were only observed when the pulse frequency was set to 1 Hz.

With EHD printing in the cone jet mode, it was shown that droplet footprints with mean sizes of 2 μm and 8 μm were reliably printed with the 1 μm and 40 μm diameter glass capillaries, respectively. However, it was also observed that the LC jetting phenomenon was highly unstable and intermittent when the pulse frequency was greater than 2 Hz. This led to the formation of poor-quality printed droplets.

To overcome this problem, EHD printing of homogenous LC droplets in a microdripping mode has been demonstrated. By optimising the operating parameters, droplet sizes around 8 μm were reliably printed at higher pulse frequencies. Following this, a number of droplets of nematic LC were printed onto glass substrates with either a homeotropic or planar alignment to determine the distribution of droplet diameters.

Finally, EHD printing was performed to showcase the power of this technique to reliably produce LC droplets that were smaller than that achievable with conventional inkjet printing. This included the printing of arrays with a constant drop spacing. The drops were assembled in arrays at a density of one LC drop per 400 $\times$ 400 μm^2. The flexibility of the setup allowed us to assemble 8 μm size droplets to form alphanumeric characters. Printing droplets at such length scales could be useful in creating new LC molecular ordering that can lead towards next generation electro-optic devices or very

sensitive chemical/biological sensors, for example. Moreover, it would be very interesting to investigate the EHD printing of different pitch size cholesteric LCs in the form free standing sessile droplets at various length scales. The relationship between droplet height, diameter and chiral pitch can lead towards new applications in the area of nanostructured CLC droplets.

CHAPTER 7

CONCLUSIONS AND FUTURE WORK

This chapter summarises the key findings from the work presented in this thesis and proposes topics and experiments that could be explored in future work.

In summary, the work presented in this thesis has concerned the use of drop-on-demand (DoD) printing, in the form of inkjet and electrohydrodynamic (EHD) printing, to dispense micron-sized droplets of liquid crystalline materials for the development of new photonics components. Moreover, in this thesis, the first demonstration of EHD printing of a nematic LC has been presented. The thesis started with a detailed examination of the printing processes in the context of the Reynolds, Weber, and Ohnesorge dimensionless numbers as well as the morphology of the printed droplets. This was followed by demonstrating that DoD printing could be employed to fabricate electrically tunable microlens arrays and smart windows with switchable logos. Finally, EHD printing of a nematic LC was demonstrated experimentally. In the following sections, the key results and findings from each chapter are summarised and areas for further work are proposed.

Chapter 2

As this thesis concerns the use of a LC as a printable ink, Chapter 2 provided the relevant background on the macroscopic properties of these anisotropic materials such as the dielectric permittivity, refractive indices and elastic constants. The Chapter also described how the free-energy equation was represented in the COMSOL Multiphysics software package so that the LC director could be simulated for different electric field conditions. The latter part of Chapter 2 then described how the printed droplets were imaged in this work using both high-speed cameras in a shadowgraphy configuration and polarised optical microscopy.

Chapter 3

In the first half of Chapter 3, an introduction to inkjet printing was provided along with a review of the literature already available on printing LC materials. This was followed by an introduction and description about the inkjet printing systems that were employed in this thesis. Generating stable droplets of LCs or polymer dispersed LCs was the first hurdle to overcome. The bespoke system was therefore used to perform preliminary printing trials in order to determine the printing conditions needed for each new ink formulation. The Jetlab-II system, on the other hand, was used to print droplets for the prototype microlens array devices and PDLC devices because it was ideally suited to the

printing of more sophisticated arrays of droplets.

In the latter half of Chapter 3, a detailed analysis of the droplet generation process of a nematic LC ejected from an 80 µm diameter piezoelectric-driven nozzle was presented. The conditions needed for successful printing of a nematic LC were determined by varying the driving waveform parameters and/or the printhead temperature, and by then observing the behaviour of the ejected droplets using a high-speed camera shadowgraphy imaging technique. Dimensionless numbers such as the Ohnesorge, Reynolds, and Weber number were considered in the context of an inkjet printability map in order to understand which factors prohibited the generation of the nematic LC droplets.

The viscosity of the nematic LC E7 was considered to be a key factor that hindered the droplet formation process at room temperature. However, it was found that near to the nematic to isotropic phase transition temperature, more specifically in the range of 55 – 70 °C, stable droplet generation was observed. In this regard, the Ohnesorge number served as a useful metric for defining the nematic LC printability regime in terms of the ink rheology at these elevated temperatures. Here the Ohnesorge number was estimated to be in the range of 0.55 – 0.9, where the upper and lower limits correspond to when the printhead was set to 55 °C and 70 °C, respectively. The quality of the ejected droplets, on the other hand, was defined in terms of the drop Weber number, which was measured by estimating the droplet velocities through the capture of high-speed camera images.

By dispensing nematic LC droplets at different printhead temperatures and voltage amplitudes of the input waveform, it was observed that at each printhead temperature there existed a range of droplet velocities for which satellite-free inkjet printing was observed. The droplet velocities were altered by varying the amplitude of the driving waveform. The range of droplet velocities were reflected in the drop Weber number, which was found to be $7 < We_d < 48$ for an Ohnesorge number in the range of 0.9 – 0.55. The findings presented in this work indicate that the Ohnesorge number alone is not sufficient to define the ink printability. Instead, there exists a range of voltage amplitudes for a fixed printhead temperature that result in stable and satellite-free inkjet printing. In

other words, other dimensionless parameters such as the Weber number need to be taken into account alongside the Ohnesorge number. The systematic analysis presented in this chapter provided an important foundation for the printing of new LC/pre-polymer formulations that were employed in Chapter 5 of this thesis.

Chapter 4

After studying the process for generating nematic LC droplets, the next step was to use the printing procedure to fabricate an optical device that consisted of these printed LC droplets. Chapter 4 demonstrated the fabrication and characterisation of printed electrically tunable microlenses and arrays thereof. With the accuracy offered by the JetLab-II printing system, LC droplets were deposited between in-plane indium tin oxide electrodes that were separated by a gap of 500 µm. An alignment layer was employed that resulted in a homeotropic alignment of the nematic LC and it was shown that after impacting with the substrate the droplets formed plano-convex microlenses with lens diameters ranging from 122 µm to 255 µm, depending upon the number of droplets deposited at a single location. Correspondingly, these printed microlenses exhibited focal lengths for red light (λ = 633 nm) that ranged from 220 to 463 µm. In the presence of an electric field, these microlenses were found to exhibit a change in focal length without any change in the lens profile. Depending upon the lens diameter, the range of focal length tuning was found in the range of 228 – 323 µm. Furthermore, it was also found that there was a range of voltages for which two focal planes were observed due to the formation of two separate domains in the LC droplet, each one characterized by a different refractive index profile. These findings are of potential importance for 3D imaging applications where the two separate focal planes could be used to give the impression of depth perspective.

The microlenses presented in Chapter 4 were prone to damage whenever they were exposed to a mechanical disturbance. To make these more mechanically rugged, it is essential that a protective layer be applied that can encapsulate the LC material but that does not inhibit the tunable lens properties. An obvious direction for future work in this area would be to encapsulate the LC microlenses. A preliminary study was carried out using a mixture of LC and Reactive Mesogen (RM) which was inkjet-printed onto a glass sub-

strate with a homeotropic alignment layer. The printed droplets were then subsequently polymerised using ultraviolet light to form a polymer membrane at the top surface of the lens. To confirm the formation of membrane two quick tests were performed which are discussed in the following sections.

The degree of encapsulation and ruggedness of the microlenses was tested by exposing them to a flow of air or water. Figure 7.1 shows a series of polarisation optical microscope images when air was blown from one side of the microlens using a pressurized air canister (Thorlabs). It was found that the flexible polymer membrane did not rupture when the nematic LC was pushed towards the other side of the microlens. However, by further increasing the air pressure (by setting the canister to maximum flow) the polymer membrane was found to be damaged.

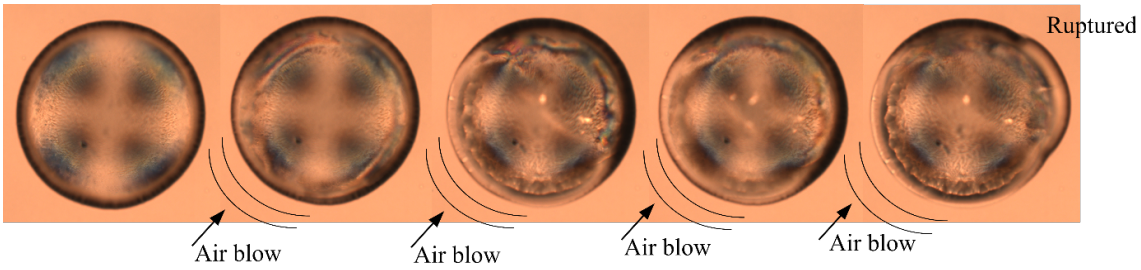

Figure 7.1: Testing the mechanical ruggedness of the printed polymer stabilised nematic LC microlenses. The images from left to right show the change in the droplet appearance for different incident air pressures. The microlenses were printed with an 80 µm diameter nozzle using and the ink formulation was composed of the nematic LC, E7, the reactive mesogen RM 257, and Irgacure photo initiator at a concentration by weight of 89.5 wt.%, 10 wt.% and 0.5 wt.%, respectively. The size of the printed lens is 250 µm. The power density and duration of UV exposure used to polymerise the microlens was 35 mW/cm^2 and 15 minutes, respectively.

Separately, a printed microlens was placed in a petri dish and exposed to a flow of water using a wash bottle. Figure 7.2 shows the polarisation optical microscope images where the first image is for the case when no water was applied. The second image, which is slightly out of focus, shows the case when water started to flow over the microlens. The third and fourth images reveal what happened when the microlens was completely immersed in water. From this test, it can be seen that the microlenses remained stable, and the polymer membrane protected the shape of the lens profile. It can also be seen that the four yellow regions, indicating an out-of-plane tilt of the director, are almost identical to

that of the microlenses that were not protected by a polymer membrane. In the future it would be interesting to investigate the image formation and focal length tuning of these encapsulated microlenses.

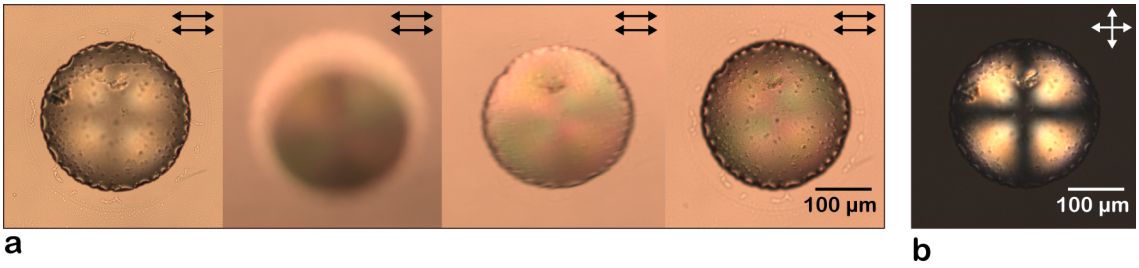

Figure 7.2: a) a series of polarisation optical microscope (POM) images (with parallel polarisers) when a printed microlens was subjected to the flow of water. The black double headed arrows indicate the orientation of the polarisers. **b)** POM image of the microlens for crossed polarisers for the case shown in the first subfigure in (a).The microlenses were printed with an 80 µm diameter nozzle using and the ink formulation was composed of the nematic LC, E7, the reactive mesogen RM 257, and Irgacure photo initiator at a concentration by weight of 89.5 wt.%, 10 wt.% and 0.5 wt.%, respectively. The size of the printed lens is 250 µm. The power density and duration of UV exposure used to polymerise the microlens was 35 mW/cm^2 and 15 minutes, respectively.

Chapter 5

The objective of Chapter 5 was to demonstrate that inkjet printing could be used to fabricate polymer dispersed liquid crystal (PDLC) smart windows that consisted of embedded logos and images. After assembling the device and initiating phase separation of the polymer from the LC host using UV illumination, the printed PDLC droplets were found to scatter the incident light when no voltage was applied but became transparent when a voltage was applied to the device. In this chapter, the UV curing conditions were chosen such that the droplets gave rise to intense scattering of light leading to high quality arrays of PDLC 'pixels'. Results were also presented on the electro-optic properties of a single printed PDLC droplet.

The flexibility of the inkjet printing system enabled the deposition of 130 µm-sized pixels with an inter-droplet spacing of 20 µm. This resulted in an array of droplets that could be switched ON/OFF with the application of a voltage across the device. In addition, to showcase the aesthetically appealing feature of creating patterned PDLC films as compared to conventionally manufactured PDLC films, a printed smart window prototype

with an embedded image was demonstrated. The image could be made to disappear with the application of a voltage.

Future work in this area could be to further investigate the device development process by performing printing of smaller feature sizes to further increase the printing resolution by allowing more droplets per square inch. This can be done by printing the PDLC ink formulation with printing technologies that can produce drop feature sizes smaller than the size of the printing nozzle. For example, EHD printing could be used to engineer new nano-PDLC devices. It would therefore be interesting to try to print the LC/pre-polymer ink formulation using the EHD printing technique and observe the single droplet scattering as well as the electro-optic behaviour of a complete printed device.

The smart windows that have been fabricated in this thesis require a two-stage process. In the first stage, the droplets were deposited using an inkjet printing technique while in the second stage a second substrate was applied to contain the droplets and to act as a top electrode. One drawback with this process was the occasional coalescence of the droplets due to the application of an uneven amount of mechanical pressure when the droplet spacing was very small (less than 10 μm). This meant that larger droplet spacings were required, which limits the deviceâs overall resolution. To mitigate this limitation, it would be interesting to print an optically matched polymer when depositing the PDLC ink formulation and performing the UV curing before/after applying the top substrate. The benefit of printing a photoresponsive material in addition to the PDLC ink pixels would be to provide more mechanical robustness to the device.

In the future, it may be possible to print a coloured PDLC ink formulation by doping the PDLC mixture with dyes/pigments. Moreover, using a multi-nozzle print process it may be possible to form colour images/motifs/logos by simultaneously printing formulations with red, green, and blue dye/pigments. Alternatively, it might be possible to print PDLCs that contain chiral nematic LCs rather than nematic LCs, whereby the pitch is chosen so that the reflection band reflects visible wavelengths (e.g., red/green/blue). This could result in aesthetically pleasing colours in an embedded image of the smart window

when viewed in the voltage OFF state.

The inkjet printing of a PDLC ink for manufacturing smart windows always resulted in device configurations where the transparent state was only possible when a voltage was applied across the device. This means that for the window to remain transparent for extended periods, a voltage needed to be continuously applied. To potentially reduce energy consumption, it would therefore be desirable to print ink formulations that can operate in either a conventional (scattering to transparent) or reverse (transparent to scattering) mode configurations.

Polymer stabilised LCs (PSLCs) and polymer stabilised chiral nematic LC (PSCLCs) are LC composites that, depending upon the material combination and photopolymerisation process, can be light scattering or transparent in the voltage off state. It is therefore interesting to consider printing PSLC/PSCLC mixtures for the manufacture of smart window technology. The benefit of using such ink formulations lies in the material's ability to operate in either a conventional or reverse mode configuration. Therefore, as a natural extension of my work on printed PDLCs, I have collaborated closely with another graduate student who has demonstrated a printed PSCLC smart window. We have shown that the PSCLC based smart window could be operated in either a conventional or reverse mode configuration. The results from this work have been submitted to a peer-reviewed journal.

Chapter 6

For Chapters 3 – 5, inkjet printing was the microfabrication technique used to generate droplets of nematic LC and nematic LC mixed with a polymer for the realisation of new printed optical components/devices. The footprint size of these droplets on a substrate with a homeotropic alignment layer, when printed using an 80 µm diameter nozzle, was typically 120 µm. The aim of Chapter 6 was to apply electrohydrodynamic (EHD) printing techniques to the printing of nematic LCs in order to obtain droplet feature sizes that were less than 10 µm. Before demonstrating EHD printing of nematic LCs, this chapter provided detailed background on EHD printing and the effect of system parameters on the droplet formation process.

A custom-built EHD printing system was developed in the lab and experiments were conducted with three different types of nozzle. EHD printing was always performed with high amplitude electric fields between the nozzle and a conductive substrate. Experiments were performed using the nematic LC, BL006, for a range of different input waveform parameters, volume flow rates and nozzle sizes. The LC BL006 due to its electro-optical and fluidic properties reasonably similar to nematic LC E7 was chosen as an ink. The effect of the control parameters on the printing process were determined via shadowgraphy imaging and polarising optical microscopy so as to observe the LC meniscus at the tip of the nozzle and the printed droplets, respectively.

In addition to achieving smaller-sized droplets, the second objective of this study was to perform DoD (single-event-ejection) printing by using a pulsed voltage signal rather than forming a continuous stream of droplets. It was observed that the volume of the LC droplets in the DoD approach was found to be related to the pulse duration and frequency. Moreover, with shorter pulse duration times, stable and reproducible droplet ejection was observed.

Compared to the size of the droplets printed with the inkjet printing technique, the footprint size for the EHD printed droplets was found to be in the range of 2 – 8 µm, which is considerably smaller than those obtained with the inkjet printing technique. The EHD printing system developed in this work enabled LC droplets to be printed to form regular arrays and patterns. The flexibility of the setup enabled the assembly of 8 µm-sized droplets to form alphanumeric characters. These results demonstrate that EHD printing of liquid crystalline materials can result in structures that are substantially smaller than those obtained with even the smallest diameter inkjet printing nozzles.

For viscous materials such as LC/LC-pre-polymer mixtures, there is still the need for further improvement to enhance the printing resolution and speed. The addition of a heating element into the printhead would enable the viscosity of the ink to be reduced by heating up the ink. This addition might help reduce the viscoelastic effects that were

observed during the droplet formation process, and it may allow the printing of droplets at higher frequencies. Furthermore, an EHD printer operating at higher electric field amplitudes can transition into an electro-spraying mode. For example, Urszula et al. have demonstrated the use of EHD printing and showed on-demand electro-spraying of ethanol. [173] A more thorough investigation of LC materials in the context of printing in an electro-spraying mode could lead towards the development of new LC thin film optics.

On demand tuning of the pitch of a Chiral Nematic LC

Throughout this thesis, nematic LCs in either a neat form or mixed with polymer have been used as the functional ink. There are, however, LC phases that can self-organise into complex macroscopic structures that exhibit unusual optical properties. Cholesteric LCs (CLC) are a liquid crystalline phase where the LC director follows a helical structure leading to optical properties that are akin to a 1D photonic crystal. In a CLC film, if the pitch of the helix is of the same order as the wavelength, then for a range of wavelengths a photonic bandgap appears whereby circularly polarised light is forbidden from propagating through the material unless it has the opposite handedness.

A nematic LC can be transformed into a CLC through the addition of chiral molecules that induce a helical arrangement of the LC director. Depending upon the concentration of these molecules, the pitch can be tuned. Inkjet printing could be employed to tune the pitch of printed CLC droplets. Specifically, this would involve preparing and inkjet printing a CLC mixture so that it aligns to form a uniform standing helix structure inside the printed droplets with a pitch that corresponds to a reflection at blue wavelengths (for example). The printed CLC droplets could then be tuned by directly printing nematic LC droplets into them, which would lead to the formation of longer pitch droplets that reflect light at longer wavelengths. Preliminary work has been carried out to demonstrate this potential idea and results are presented in the following.

A CLC mixture (mixture composition: 4.7 wt.% BDH1281 (Merck) + 95.3 wt.% E7) was inkjet-printed onto a glass substrate that had been coated with a rubbed polyimide alignment layer. Using the MicroFab inkjet printer fitted with the 80 μm nozzle,

arrays of CLC droplets were printed where each printed droplet consisted of 30 CLC droplets deposited at one single location. To dope the already printed CLC droplets with a nematic LC, the bespoke inkjet printer was employed (which had been revamped by another D.Phil student, Andrew Orr) where the landing and mixing of the nematic LC droplets could be captured in real-time using a colour high-speed camera, see Figure B.1 and Figure B.2. The deposition of a additional nematic LC was also performed with an 80 µm MicroFab nozzle. The bottom two arrays in the image in Figure 7.3(a) show colour changing of the CLC droplets when mixed with nematic LC droplets. In this case the number of additional printed nematic LC droplets was varied between 0 – 29 while Figure 7.3(b) shows the photonic bandgap of the original CLC ink composition (the base CLC droplet was always formed with the 4.7 wt.% CLC as an ink).

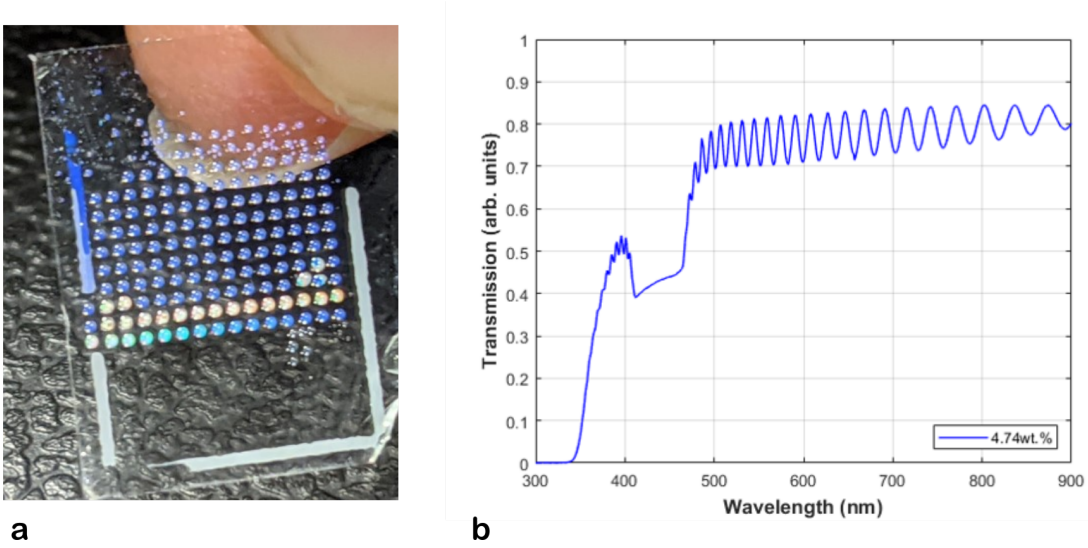

Figure 7.3: a) Tuning the pitch of chiral nematic LCs using inkjet printing. The change in the colour of the droplets on the bottom three rows correspond to the case when nematic LC (E7) droplets were dispensed into the CLC droplets. The number of Nematic LC droplets dispensed into each CLC droplet was varied from 0 to 29. **b)** The transmission spectrum for white light showing the photonic band gap of the CLC when filled in a planar aligned 5 µm-thick glass cell. The CLC mixture consisted of 4.7 wt.% BDH1281 in the nematic LC, E7. Both the nematic and chiral nematic LC printing were performed with a nozzle with an internal diameter of 80 µm. The substrates were always held at room temperature during the printing process.

Figure 7.4(a) shows a representative optical microscope image of the CLC droplets mixed with nematic LC droplets when viewed in reflection and when assembled into a glass cell by adding a second glass slide as a top substrate. The number above each droplet corresponds to the number of additional nematic LC droplets that were deposited

into the CLC droplets where each CLC droplet consisted of 30 drops. Figure 7.4(b) is the corresponding reflection spectrum recorded for each droplet that is shown in Figure 7.4(a). These results illustrate that by varying the amount of nematic LC deposited, the printed CLC droplets can be made to reflect light at different wavelengths.

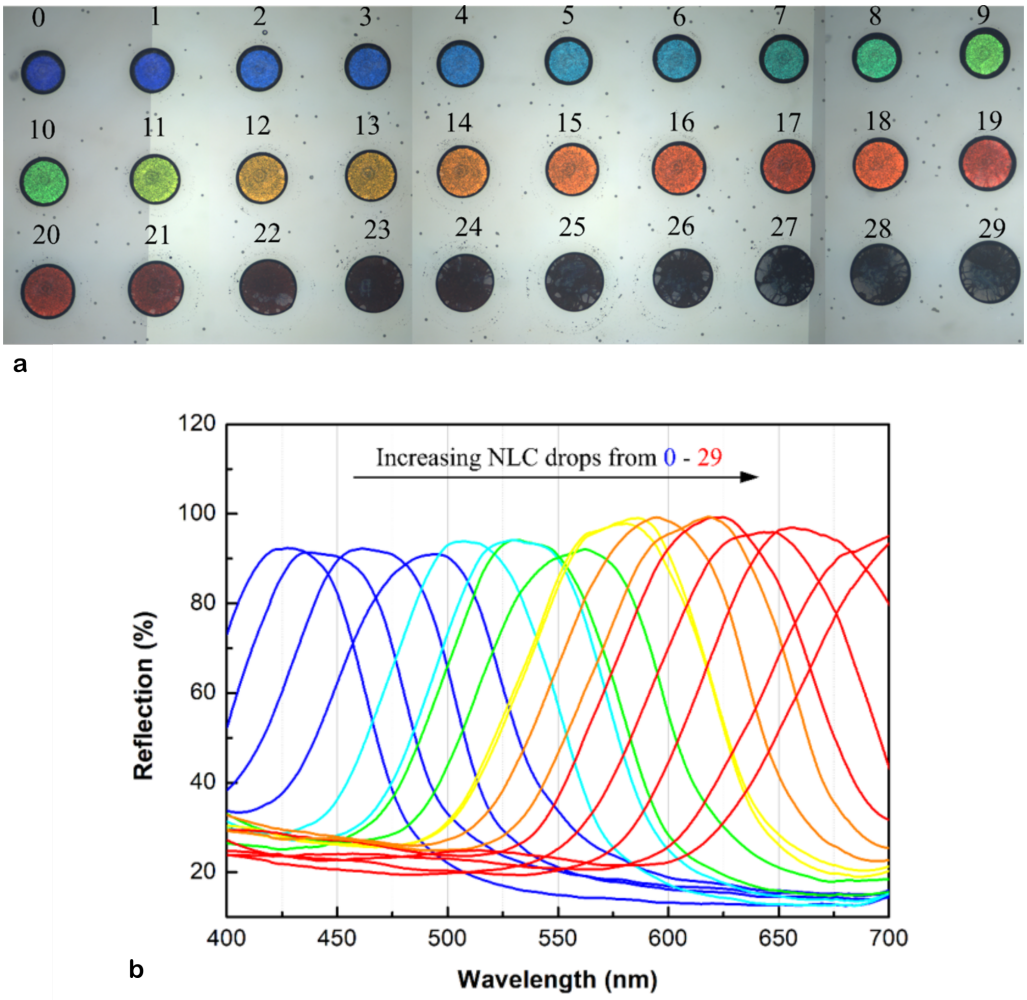

Figure 7.4: a) Three separate optical microscope images captured with a 4× objective lens in a reflection mode. The number above each droplet corresponds to the number of nematic LC droplets deposited into the CLC droplets. Each CLC droplet consisted of 30 drops of the CLC material. The nematic LC deposition was carried out with a 80 µm internal diameter nozzle performed at room temperature. **b)** Reflection spectra of the droplets shown in Figure (a).

The above results, which show a library of different colours, demonstrates that by varying the amount of nematic LC it is possible to select any colour. Figure 7.5(a) demonstrates this further by depositing nematic LC droplets onto an already printed CLC drops to form the alphanumeric abbreviation 'SMP' against a background of printed CLC droplets that reflect in the blue. Each letter appears as a different reflected colour, which

was achieved by dispensing different amounts of the additional nematic LC so as to vary the pitch. In this case, 5 (S), 8 (M), and 11 (P) droplets of nematic LC were deposited to form letters that were light blue, light green, and green, respectively. Figure 7.5(b) shows the reflection spectra of the 'SMP' droplets. These droplets could, in principle, be further tuned by applying a voltage to unwind the helix in each droplet. These preliminary results on CLC printing could be of particular interest for reflective displays and temperature sensors, chemical/gas sensors, printed lasers, anti-counterfeiting and printed security tags.

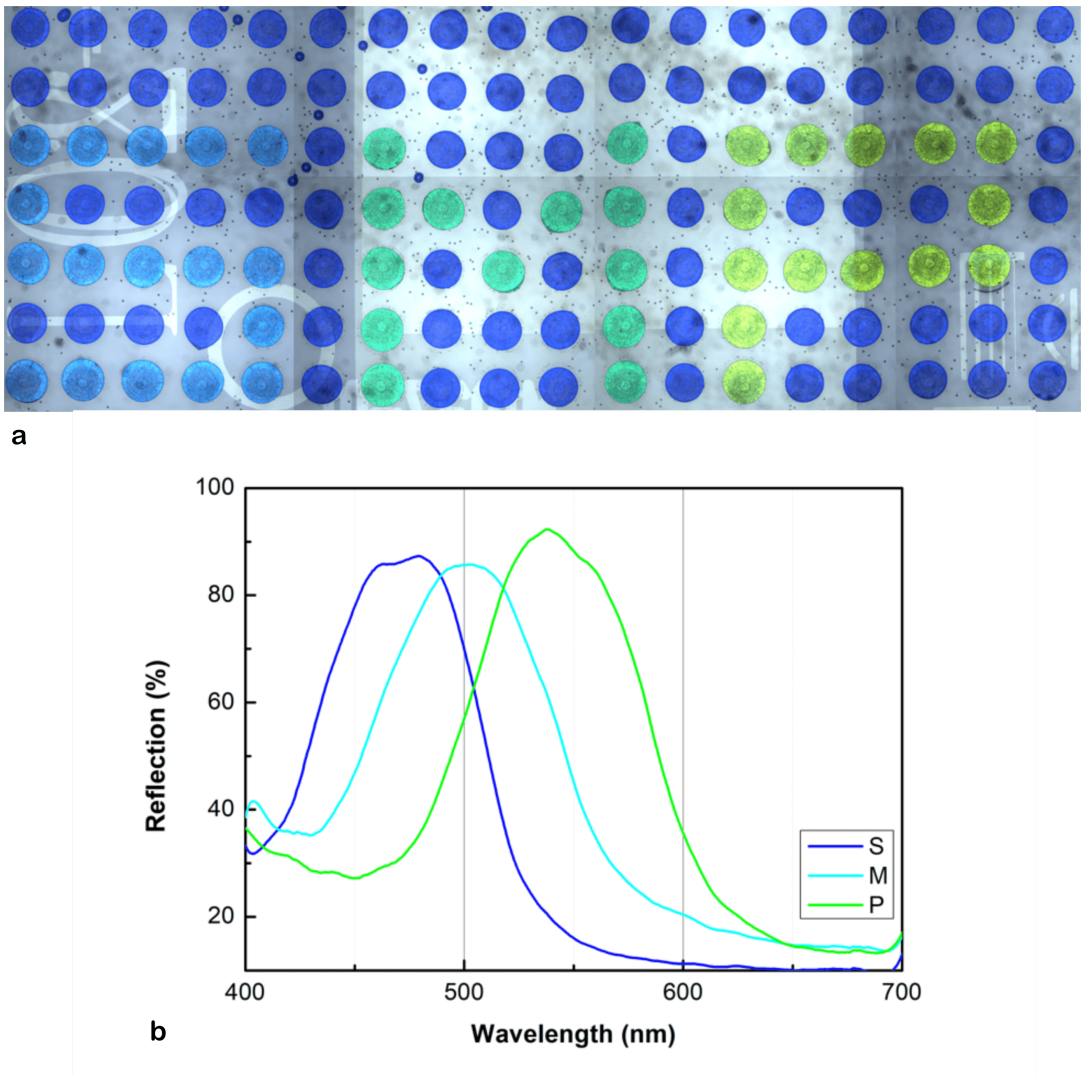

Figure 7.5: a) Nematic LC printed into CLC droplets (which reflect in the blue) to form the letters S, M, and P that reflect in the light blue, light green and green respectively. To obtain the different colours, different amounts of nematic LC were deposited into each CLC droplet. Specifically, 5, 8 and 11 droplets were deposited to form three different coloured alphanumeric characters ('SMP') on a previously printed array of CLC droplets. **b)** Reflection spectra recorded for the coloured droplets that make up the three separate letters shown in (a).

In summary, the work presented in this thesis has involved the precise deposition of liquid crystalline materials to form micron-sized droplets using on-demand inkjet and EHD printing processes. This work demonstrates strategies for fabricating printed optical components and devices by assembling droplets of LCs/PDLCs. This thesis has also reported the development of an EHD printer for LCs and studied the effects of high electric field amplitudes on the formation of an LC meniscus. This latter development is particularly exciting for new nano-optical LC components and devices. The future potential for technologies engineered using inkjet and EHD printing of LC materials is exciting.

APPENDIX A

APPENDIX

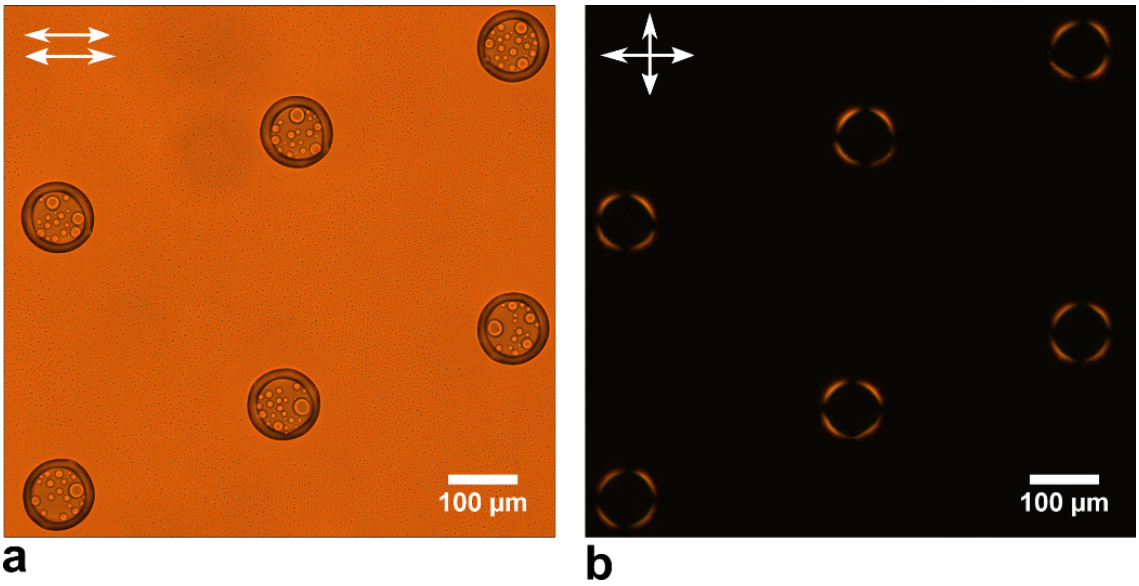

Figure A.1: a) Microscopy and **b)** polarised microscopy images of single droplets of PDLC ink composed of 60 wt.% of E7 and 40 wt.% of NOA65 glue. The ink was printed with bespoke inkjet printer using 80 µm diameter MicroFab nozzle. The droplets were UV cured at UV intensity of 65 mW/cm^2 for 5 minutes at room temperature of 20 °C.

APPENDIX B

APPENDIX

The drop-on-demand inkjet printing setup as shown in Figure B.1 used to deposit nematic LC droplets on the already printed Cholesteric LC (CLC) droplets. This system was used to deposit a nematic LC at different concentrations into printed CLC droplets.

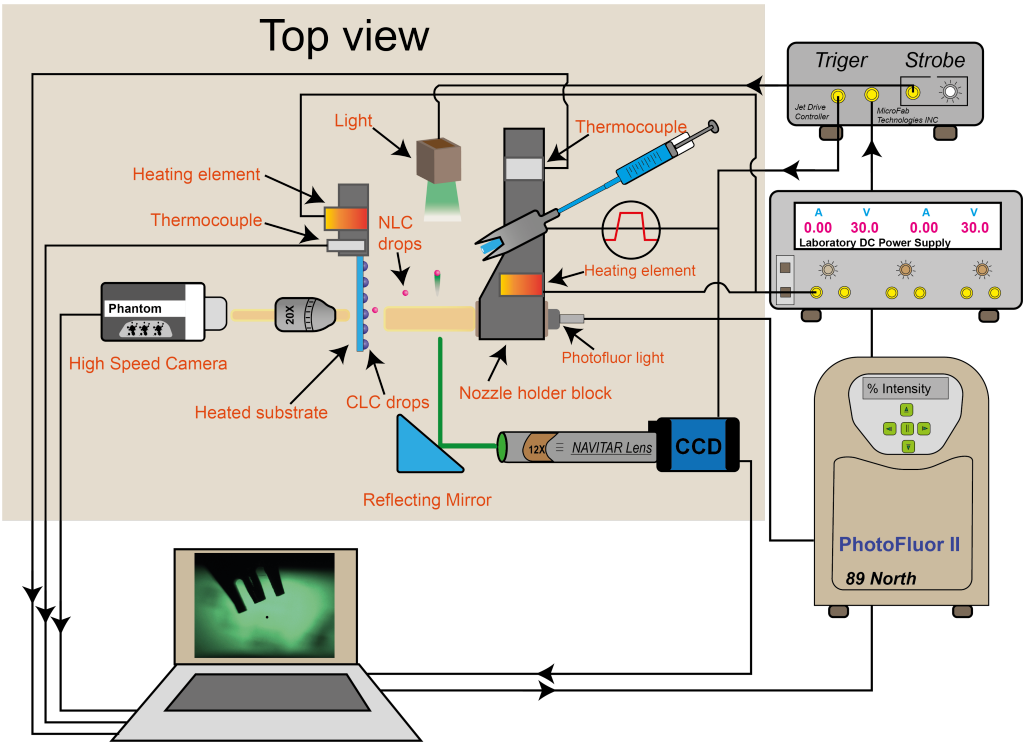

Figure B.1: Schematic diagram illustrating the arrangement of printing system used to deposit nematic LC droplets into chiral droplets. The system can image the droplet deposition process in transmission mode by using a high-speed camera installed with a 20× objective lens. The system was developed by Andrew Orr.

Figure B.2 shows a nematic LC droplet is hitting previously printed chiral LC based droplet which is composed of 30 CLC droplets.

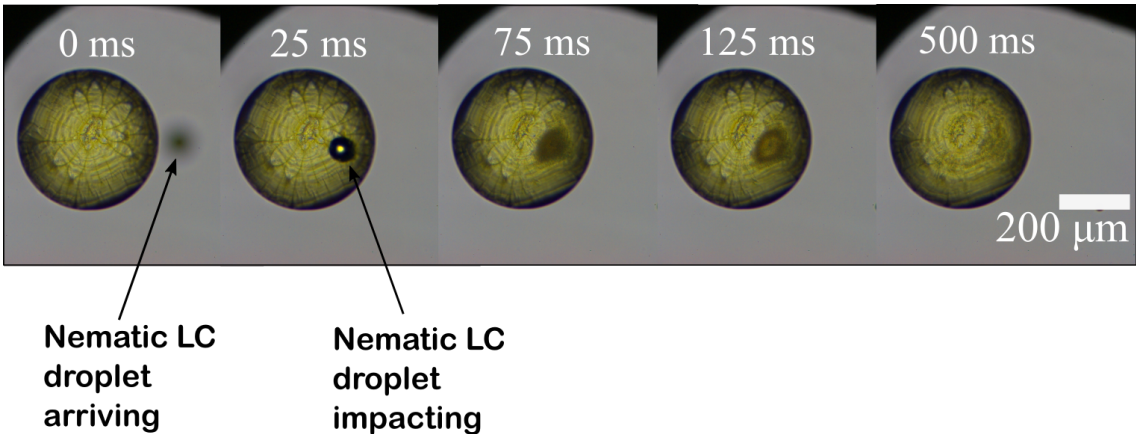

Figure B.2: Dynamic high speed camera frames showing the impact of a nematic LC droplet into a chiral droplet where the large droplet corresponds to a CLC droplet which was previously printed on a planar-aligned glass substrate using a MicroFab inkjet printer.

APPENDIX C

APPENDIX

```
clear all; % clear all variables
tic % start a programme timer
ne=1.74; % ne
no=1.52; % no
d=0.1e-6; % thickness of an individual SLICE (sub-layer) in the
    system model
%lambda=633e-9; % wavelength of light used - now this is a variable
% this sets the number of grid points in each direction - IT IS SET
    MANUALLY!!!!!!!!
Ngridsx=105;
Ngridsy=105;
Ngridsz=401;
% these lines read the pre-processed csv data format (with the title
    lines
% removed and the "NaN"s corrected to make nx=0, ny=0, nz=1 at those
    points)
%A=csvread('Zero voltage and at 5 ms copy.csv');%27,27,5
%A=csvread('Zero voltage and at 5 ms_5microns resolution copy.csv')
    ;%53,53,9
%A=csvread('Zero voltage and at 5 ms_2nd copy.csv');%261,261,5
%A=csvread('Zero voltage and at 5 ms_2.5microns resolution copy.csv')
    ;%105,105,17
%A=csvread('Zero voltage and at 5 ms_1microns Z and 2.5 microns XY
    resolution copy.csv');%105,105,41
```

```
% alternative format for direct read from COMSOL output (reads data into a
% table which automatically seems to ignore the title lines and then
% processes the data to replace the "NaN"s with nx=0, ny=0, nz=1 at those points)
%Atable = readtable('Zero voltage and at 5 ms.csv');%27,27,5
%Atable=readtable('Zero voltage and at 5 ms_1microns Z and 2.5 microns XY resolution.csv');%105,105,41
Atable=readtable('New tryV6.csv');%105,105,401
A=table2array(Atable); % convert the table into an array
Vnx=A(:,4); % load 4th column of nx values into Vnx
Vny=A(:,5); % load 5th column of ny values into Vny
Vnz=A(:,6); % load 6th column of nz values into Vnz
Vnx(isnan(Vnx))=0; % convert "nx" NaNs into zeros
Vny(isnan(Vny))=0; % convert "ny" NaNs into zeros
Vnz(isnan(Vnz))=1; % convert "nz" NaNs into ones
A(:,4)=Vnx; % load nx values back into 4th column of A
A(:,5)=Vny; % load ny values back into 5th column of A
A(:,6)=Vnz; % load nz values back into 6th column of A
nrows=size(A,1) % count the total number of rows in dataset (for later loops)
% this for-end loop "normalises" the length of |n| to make sure |n|=1 everywhere
for n=1:nrows
nlength=sqrt(A(n,4)*A(n,4)+A(n,5)*A(n,5)+A(n,6)*A(n,6));
A(n,4)=A(n,4)/nlength;
A(n,5)=A(n,5)/nlength;
A(n,6)=A(n,6)/nlength;
end
%%%%%%%%%%%%%%%%%%%%%%%%%%%%%%%%%%%%%%%%%%%%%%%%%%%%%%%%%%%%%%%%%%%%%%%%%%%%
% this is the start of the wavelength loop added on 13 August 2021.....
Tlambdaav=zeros(Ngridsx,Ngridsy); % pre-fill the Transmission "average" array with zeros
for lambda=400e-9:2e-9:700e-9 % run wavelength range from 400nm to 700nm
% this is start of lambda loop - next parts of code are identical to standard "joneslens" version.....
%%%%%%%%%%%%%%%%%%%%%%%%%%%%%%%%%%%%%%%%%%%%%%%%%%%%%%%%%%%%%%%%%%%%%%%%%%%%
```

```
B = zeros(nrows,3)+j*ones(nrows,3); % pre-define the "B" array as COMPLEX values
% this for-end loop calculates the JONES matrix elements for the director
% components in the "A" array and loads these Jones elements into the "B" array
for n=1:nrows
  deltan=ne*no/sqrt((ne*ne-no*no)*A(n,6)*A(n,6)+no*no)-no; % delta_n component in the x-y plane
  eiphi=exp(i*2*pi*deltan*d/lambda); % exp(j*phi) phase component for the sub-layer
  if(deltan>0) % if test for when delta_n=0
    lplane2=A(n,4)*A(n,4)+A(n,5)*A(n,5); % length of director component in the x-y plane
    J11=A(n,4)*A(n,4)/lplane2+eiphi*A(n,5)*A(n,5)/lplane2; % Jones "11" matrix element
    J12=(1-eiphi)*A(n,4)*A(n,5)/lplane2; % Jones "12" and "21" matrix element
    J22=A(n,5)*A(n,5)/lplane2+eiphi*A(n,4)*A(n,4)/lplane2; % Jones "22" matrix element
     B(n,1)=J11; % load "11" Jones element into "B" column 1.
     B(n,2)=J12; % load "12" Jones element into "B" column 2.
     B(n,3)=J22; % load "22" Jones element into "B" column 3.
  else % if delta_n=0 then set "B" elements for an identity Jones matrix
      B(n,1)=1+0j;
      B(n,2)=0+0j;
      B(n,3)=1+0j;
  end % end of if test for when delta_n=0
end
% now re-shape the "B" and load into "C" to make it "volumetric"
% this breaks the "B" array which has "nrows" in it with three Jones
% elements in each row into a volumetric form of shape "Ngridsx" in the
% x-direction, "Ngridsy" in the y-direction and "Ngridsz" in the
% z-direction, with three Jones elements at each of these grid points
C=reshape(B,Ngridsx,Ngridsy,Ngridsz,3);
% these nx, ny, nz loops do the Jones matrix multiplications along the z-direction
```

```
% NOTE: here nx, ny, nz are just COUNTERS - they are NOT the director components here!!!!!!!!
for nx=1:Ngridsx
    for ny=1:Ngridsy
        Ein=[1 1]; % input light vector polarisation
        for nz=1:Ngridsz % loop for light propagation direction (z)
            % do Jones matrix multiplication for this sub-layer
            Eout(1)=C(nx,ny,nz,1)*Ein(1)+C(nx,ny,nz,2)*Ein(2);
            Eout(2)=C(nx,ny,nz,2)*Ein(1)+C(nx,ny,nz,3)*Ein(2);
            % load back into Ein ready for next sub-layer
            Ein(1)=Eout(1);
            Ein(2)=Eout(2);
        end
        T(nx,ny)=abs(Ein(1)-Ein(2))^2; % change chosen final output component into an intensity
    end
end
%%%%%%%%%%%%%%%%%%%%%%%%%%%%%%%%%%%%%%%%%%%%%%%%%%%%%%%%
% this is the end of the lambda loop - next few lines were added on 13 August 2021
  if (lambda<(450e-9)) % check if wavelength is less than 450nm (i.e. in range 400-450nm)
     Tlambdaav=Tlambdaav+T*(lambda-(400e-9))/(50e-9); % taper up from 400-450nm
  elseif (lambda>(650e-9)) % check if wavelength is greater than 650 nm (i.e. in range 650-700nm)
     Tlambdaav=Tlambdaav+T*((700e-9)-lambda)/(50e-9); % taper down from 650-700nm
  else % "else" will be true for range 450nm to 650nm
     Tlambdaav=Tlambdaav+T; % just add "T" for wavelengths in 450-650 nm range
  end % this is the "end" for the if/elseif/else wavelength averaging
end % this is the end for the wavelength loop range from 400nm to 700 nm
% this is the end of the lambda average - final parts of code are very similar to the
% standard "joneslens" version, but with what was "T" now replaced with "Tlambdaav".
%%%%%%%%%%%%%%%%%%%%%%%%%%%%%%%%%%%%%%%%%%%%%%%%%%%%%%%%
```

```
M = max(Tlambdaav(:)); % get maximum intensity from "Tlambdaav".....
spare2=uint8(Tlambdaav*(255/M)); % make "Tlambdaav" into 8-bit image
    and load into "spare2"
imshow(spare2) % show this image
Iblur2 = imgaussfilt(spare2,2); % make a smoothed version of image
figure % make a new figure
imshow(Iblur2) % show the smoothed image
toc % stop programme timer and display run-time
```

BIBLIOGRAPHY

[1] Kuang Chao Fan, Jhih Yuan Chen, Ching Hua Wang, and Wen Chueh Pan. Development of a drop-on-demand droplet generator for one-drop-fill technology. *Sensors and Actuators, A: Physical*, 147(2):649–655, 2008.

[2] Ryan D. Boehm, Philip R. Miller, Justin Daniels, Shane Stafslien, and Roger J. Narayan. Inkjet printing for pharmaceutical applications. *Materials Today*, 17(5):247–252, 6 2014.

[3] Nakamura M., Kobayashi A., Takagi F., Watanabe A., Hiruma Y., Ohuchi K., Iwasaki Y., Horie M., Morita I., and Takanati S. Biocompatible Inkjet Printing Technique for Designed Seeding of Individual Living Cells. *Tissue Engineering*, 11(11/12):1658–1666, 2005.

[4] J. R. Castrejón-Pita, W. R.S. Baxter, J. Morgan, S. Temple, G. D. Martin, and I. M. Hutchings. Future, opportunities and challenges of inkjet technologies. *Atomization and Sprays*, 23(6):571–595, 2013.

[5] Pierre-Gilles de Gennes. *The Physics of Liquid Crystals*. Clarendon Press, 1993.

[6] Peter J. Collings and Michael Hird. *Introduction to Liquid Crystals Chemistry and Physics*. CRC Press, 2017.

[7] Ellis Parry, Serena Bolis, Steve J. Elston, Alfonso A. Castrejón-Pita, and Stephen M. Morris. Drop-on-Demand Inkjet Printing of Thermally Tunable Liquid Crystal Microlenses. *Advanced Engineering Materials*, 20(3):1700774, 3 2018.

[8] Chloe C Tartan, John J Sandford O'Neill, Patrick S Salter, Jure Aplinc, Martin J Booth, Miha Ravnik, Stephen M Morris, and Steve J Elston. Read on Demand Images in Laser-Written Polymerizable Liquid Crystal Devices. *Advanced Optical Materials*, 6(20):1800515, 10 2018.

[9] Amit K. Bhowmick, Afsoon Jamali, Douglas Bryant, Sandro Pintz, and Philip J. Bos. Liquid Crystal Based 5 cm Adaptive Focus Lens to Solve Accommodationâ-Convergence (AC) Mismatch Issue of AR/VR/3D Displays. *SID Symposium Digest of Technical Papers*, 52(1):410–413, 5 2021.

[10] Sergei Bronnikov, Sergei Kostromin, and Vjacheslav Zuev. Polymer-Dispersed Liquid Crystals: Progress in Preparation, Investigation, and Application. *Journal of Macromolecular Science, Part B*, 52(12):1718–1735, 12 2013.

[11] María López-Valdeolivas, Danqing Liu, Dick Jan Broer, and Carlos Sánchez-Somolinos. 4D Printed Actuators with Soft-Robotic Functions. *Macromolecular Rapid Communications*, 39(5):1700710, 3 2018.

[12] Arda Kotikian, Ryan L. Truby, John William Boley, Timothy J. White, and Jennifer A. Lewis. 3D Printing of Liquid Crystal Elastomeric Actuators with Spatially Programed Nematic Order. *Advanced Materials*, 30(10):1–6, 2018.

[13] Hongwen Ren and Shin Tson Wu. Tunable electronic lens using a gradient polymer network liquid crystal. *Applied Physics Letters*, 82(1):22–24, 2003.

[14] Harry Coles and Stephen Morris. Liquid-crystal lasers. *Nature Photonics*, 4(10):676–685, 2010.

[15] Albert P. H. J. Schenning, Gregory P. Crawford, and Dirk J. Broer. *Liquid Crystal Sensors*. CRC Press, 2017.

[16] Shin-Tson Wu and Deng-Ke Yang. *Fundamentals of Liquid Crystal Devices, 2nd Edition*. Wiley, 2014.

[17] S K Ghosh. A model for the orientational order in liquid crystals. *Il Nuovo Cimento D*, 4(3):229–244, 9 1984.

[18] Anupam Sengupta, Stephan Herminghaus, and Christian Bahr. Liquid crystal microfluidics: surface, elastic and viscous interactions at microscales. *Liquid Crystals Reviews*, 2(2):73–110, 7 2014.

[19] Dwight W Berreman. Solid Surface Shape and the Alignment of an Adjacent Nematic Liquid Crystal. *Physical Review Letters*, 28(26):1683–1686, 6 1972.

[20] Blandine Jérôme. Surface effects and anchoring in liquid crystals. *Reports on Progress in Physics*, 54:391, 1991.

[21] Fuzi Yang, Lizhen Ruan, and J. R. Sambles. Homeotropic polar anchoring energy of a nematic liquid crystal using the fully leaky waveguide technique. *Journal of Applied Physics*, 88(11):6175–6182, 12 2000.

[22] Carl V. Brown. Physical properties of nematic liquid crystals, Springer, 2012.

[23] Michael R. Fisch and Satyendra Kumar. Introduction to liquid crystals, 2001.

[24] Ilha Chirtoc, Mihai Chirtoc, and Christ Glorieux. Determination of the order parameter and its critical exponent for n CB (n = 5 - 8) liquid crystals from refractive index data. *Liquid Crystals*, 31(2):229–240, 2 2004.

[25] F C Frank. On the theory of liquid crystals. *Discussions of the Faraday Society*, 25(0):19, 1958.

[26] C W Oseen. The theory of liquid crystals. *Transactions of the Faraday Society*, 29(140):883, 1933.

[27] H Zocher. The effect of a magnetic field on the nematic state. *Transactions of the Faraday Society*, 29(140):945, 1933.

[28] O. O. Prishchepa, A. V. Shabanov, and V. Ya. Zyryanov. Director configurations in nematic droplets with inhomogeneous boundary conditions. *Phys. Rev. E*, 72:031712, Sep 2005.

[29] Axel Kilian. Computer simulations of nematic droplets. *Liquid Crystals*, 14(4):1189–1198, 1993.

[30] John J Sandford O'Neill. Two-Photon Polymerisation Direct Laser Writing for Liquid Crystal Photonics. DPhil thesis, University of Oxford, 2021.

[31] Eugene Hecht. *Optics*. Pearson, 2015.

[32] Andrea Camposeo, Luana Persano, Maria Farsari, and Dario Pisignano. Additive Manufacturing: Applications and Directions in Photonics and Optoelectronics. *Advanced Optical Materials*, 7(1):1800419, 1 2019.

[33] N. Reis and B. Derby. Ink Jet Deposition of Ceramic Suspensions: Modeling and Experiments of Droplet Formation. *MRS Proceedings*, 625(January):117, 2 2000.

[34] Mohammed G Mohammed and Rebecca Kramer. All-Printed Flexible and Stretchable Electronics. *Advanced Materials*, 29(19):1604965, 5 2017.

[35] Kyung Hyun Choi, Muhammad Zubair, and Hyun Woo Dang. Characterization of flexible temperature sensor fabricated through drop-on-demand electrohydrodynamics patterning. *Japanese Journal of Applied Physics*, 53, 5 2014.

[36] Jorge Alamán, Raquel Alicante, Jose Ignacio Peña, and Carlos Sánchez-Somolinos. Inkjet printing of functional materials for optical and photonic applications. *Materials*, 9(11), 2016.

[37] Amruth C, Marek Zdzislaw Szymański, Beata Łuszczyńska, and Jacek Ulański. Inkjet printing of super yellow: ink formulation, film optimization, OLEDs fabrication, and transient electroluminescence. *Scientific Reports*, 9(1):8493, 12 2019.

[38] Chin-Tai Chen, Kuo-Hua Wu, Chun-Fu Lu, and Fanny Shieh. An inkjet printed stripe-type color filter of liquid crystal display. *Journal of Micromechanics and Microengineering*, 20(5):055004, 5 2010.

[39] Jia Li, Fabrice Rossignol, and Joanne Macdonald. Inkjet printing for biosensor fabrication: combining chemistry and technology for advanced manufacturing. *Lab on a Chip*, 15(12):2538–2558, 2015.

[40] Ronan Daly, Tomás S. Harrington, Graham D. Martin, and Ian M. Hutchings. Inkjet printing for pharmaceutics - A review of research and manufacturing. *International journal of pharmaceutics*, 494(2):554–567, 10 2015.

[41] Stephen D. Hoath. Fundamentals of inkjet printing - The science of inkjet and droplets, wiley, 2003.

[42] A. A. Castrejón-Pita, E. S. Betton, N. Campbell, N. Jackson, J. Morgan, T. R. Tuladhar, D. C. Vadillo, and Jose Rafael Castrejon-Pita. Formulation, quality, cleaning, and other advances in inkjet printing. *Atomization and Sprays*, 31(4):57–79, 2021.

[43] Jeoung-Yeon Hwang and Liang-Chy Chien. Liquid crystal alignment on inkjet printed and air-buffed polyimide with nano-grove surface. *Journal of Physics D: Applied Physics*, 42(5):055305, 3 2009.

[44] Ellis Parry, Dong-Jin Kim, Alfonso A Castrejón-Pita, Steve J Elston, and Stephen M Morris. Formation of radial aligned and uniform nematic liquid crystal droplets via drop-on-demand inkjet printing into a partially-wet polymer layer. *Optical Materials*, 80:71–76, 6 2018.

[45] D. J. Gardiner, W. K. Hsiao, S. M. Morris, P. J.W. Hands, T. D. Wilkinson, I. M. Hutchings, and H. J. Coles. Printed photonic arrays from self-organized chiral nematic liquid crystals. *Soft Matter*, 8(39):9977–9980, 2012.

[46] Jelle E. Stumpel, Claudia Wouters, Nicole Herzer, Judith Ziegler, Dirk J. Broer, Cees W. M. Bastiaansen, and Albertus P. H. J. Schenning. An Optical Sensor for Volatile Amines Based on an Inkjet-Printed, Hydrogen-Bonded, Cholesteric Liquid Crystalline Film. *Advanced Optical Materials*, 2(5):459–464, 5 2014.

[47] Dylan J. D. Davies, Antonio R. Vaccaro, Stephen M. Morris, Nicole Herzer, Albertus P. H. J. Schenning, and Cees W. M. Bastiaansen. A Printable Optical Time-Temperature Integrator Based on Shape Memory in a Chiral Nematic Polymer Network. *Advanced Functional Materials*, 23(21):2723–2727, 6 2013.

[48] T. R. Cull, M. J. Goulding, and Mark Bradley. Liquid Crystal libraries inkjet formulation and high throughput analysis. *Advanced Materials*, 19(17):2355–2359, 9 2007.

[49] Ellis Parry. Inkjet printing of liquid crystals and polymer composites for novel thin-film optical elements. DPhil thesis, University of Oxford, 2020.

[50] Herman Wijshoff. The dynamics of the piezo inkjet printhead operation. *Physics Reports*, 491(4-5):77–177, 6 2010.

[51] Nuno Reis, Chris Ainsley, and Brian Derby. Ink-jet delivery of particle suspensions by piezoelectric droplet ejectors. *Journal of Applied Physics*, 97(9):094903, 5 2005.

[52] D. B. Bogy and F. E. Talke. Experimental and theoretical study of wave propagation phenomena in drop-on-demand ink jet devices. *IBM Journal of Research and Development*, 28(3):314–321, 5 1984.

[53] Woo Jin Shin, Young-Su Jeong, Kibong Choi, and Weon Gyu Shin. The effect of inkjet operating parameters on the size control of aerosol particles. *Aerosol Science and Technology*, 49(12):1256–1262, 12 2015.

[54] Brian Derby. Inkjet printing of functional and structural materials: Fluid property requirements, feature stability, and resolution. *Annual Review of Materials Research*, 40(1):395–414, 2010.

[55] S. D. Hoath, I. M. Hutchings, G. D. Martin, T. R. Tuladhar, M. R. Mackley, and D. Vadillo. Links between ink rheology, drop-on-demand jet formation, and printability. *Journal of Imaging Science and Technology*, 53(4):0412081–0412088, 2009.

[56] Gareth H. McKinley and Michael Renardy. Wolfgang von Ohnesorge. *Physics of Fluids*, 23(12):127101, 12 2011.

[57] J E Fromm. Numerical calculation of the fluid dynamics of drop-on-demand jets. *IBM Journal of Research and Development*, 28(3):322–333, 5 1984.

[58] Vance Bergeron, Daniel Bonn, Jean Yves Martin, and Louis Vovelle. Controlling droplet deposition with polymer additives. *Nature*, 405(6788):772–775, 6 2000.

[59] P. Calvert. Inkjet printing for materials and devices. *Chemistry of Materials*, 13(10):3299–3305, 2001.

[60] Xiaojin Peng, Jian Yuan, Shirley Shen, Mei Gao, Anthony S. R. Chesman, Hong Yin, Jinshu Cheng, Qi Zhang, and Dechan Angmo. Perovskite and organic solar cells fabricated by inkjet printing: Progress and prospects. *Advanced Functional Materials*, 27(41):1703704, 11 2017.

[61] C. Josserand and S.T. Thoroddsen. Drop impact on a solid surface. *Annual Review of Fluid Mechanics*, 48(1):365–391, 1 2016.

[62] Yuanyuan Liu and Brian Derby. Experimental study of the parameters for stable drop-on-demand inkjet performance. *Physics of Fluids*, 31(3):032004, 3 2019.

[63] M H Tsai, W S Hwang, H H Chou, and P H Hsieh. Effects of pulse voltage on inkjet printing of a silver nanopowder suspension. *Nanotechnology*, 19(33):335304, 8 2008.

[64] Elif Begum Elcioglu and S M Sohel Murshed. Drop-on-demand assessment of microdrops of dilute ZnO-water nanofluids. *Physics of Fluids*, 33(1):012013, 1 2021.

[65] Seung Hwan Kang, San Kim, Dong Kee Sohn, and Han Seo Ko. Analysis of drop-on-demand piezo inkjet performance. *Physics of Fluids*, 32(2):022007, 2 2020.

[66] B. Bahadur, R. K. Sarna, and V. G. Bhide. Refractive indices, density and order parameter of some technologically important liquid crystalline mixtures. *Molecular Crystals and Liquid Crystals*, 72(5-6):139–145, 1 1982.

[67] J Xie, K Wu, J Cheng, P Li, and J Zheng. The micro-optic photovoltaic behavior of solar cell along with microlens curved glass substrate. *Energy Conversion and Management*, 96:315–321, 2015.

[68] Akshit Peer, Rana Biswas, Joong-Mok Park, Ruth Shinar, and Joseph Shinar. Light management in perovskite solar cells and organic LEDs with microlens arrays. *Optics Express*, 25(9):10704, 5 2017.

[69] Bader Aldalali, Chenhui Li, Li Zhang, and Hongrui Jiang. Micro cameras capable of multiple viewpoint imaging utilizing photoresist microlens arrays. *Journal of Microelectromechanical Systems*, 21(4):945–952, 2012.

[70] Liang Dong, Abhishek K. Agarwal, David J. Beebe, and Hongrui Jiang. Adaptive liquid microlenses activated by stimuli-responsive hydrogels. *Nature*, 442(7102):551–554, 8 2006.

[71] Srinivas Pagidi, Ramesh Manda, Surjya Sarathi Bhattacharyya, Sung Guk Lee, Seong Min Song, Young Jin Lim, Joong Hee Lee, and Seung Hee Lee. Fast switch-

able micro-lenticular lens arrays using highly transparent nano-polymer dispersed liquid crystals. *Advanced Materials Interfaces*, 6(18):1900841, 9 2019.

[72] Xinhua Zeng, Jérome Plain, Safi Jradi, Claire Darraud, Fréderic Louradour, Renaud Bachelot, and Pascal Royer. Integration of polymer microlens array at fiber bundle extremity by photopolymerisation. *Optics Express*, 19(6):4805, 2011.

[73] Holger Becker and Claudia Gärtner. Polymer microfabrication technologies for microfluidic systems. *Analytical and Bioanalytical Chemistry*, 390(1):89–111, 1 2008.

[74] Siyu Tong, Hao Bian, Qing Yang, Feng Chen, Zefang Deng, Jinhai Si, and Xun Hou. Large-scale high quality glass microlens arrays fabricated by laser enhanced wet etching. *Optics Express*, 22(23):29283–29291, 2014.

[75] Hao Xiong and Zheyao Wang. Fabrication of ternary Ge-Se-Sb chalcogenide microlens arrays using thermal reflow. *Journal of Micromechanics and Microengineering*, 29(8):085002, 8 2019.

[76] David Daly, Roger Stevens, Micheal Hutley, and Nikolas Davies. The manufacture of microlenses by melting photoresist. *Measurement Science and Technology*, 1(8):759–766, 1990.

[77] Yongjun Zhao and Tianhong Cui. Fabrication of high-aspect-ratio polymer-based electrostatic comb drives using the hot embossing technique. *Journal of Micromechanics and Microengineering*, 13(3):430–435, 5 2003.

[78] Tianfeng Zhou, Fubin Ma, Benshuai Ruan, Jia Zhou, Payjun Liew, and Xibin Wang. Microlens array fabrication on WC mold using EDM milling with in situ electrode trimming. *The International Journal of Advanced Manufacturing Technology*, 103(5-8):3003–3011, 8 2019.

[79] Ming-Hsien Wu, Cheolmin Park, and George M Whitesides. Fabrication of Arrays of Microlenses with Controlled Profiles Using Gray-Scale Microlens Projection Photolithography. *Langmuir*, 18(24):9312–9318, 11 2002.

[80] Hongwen Ren, Yun-Hsing Fan, and Shin-Tson Wu. Liquid-crystal microlens arrays using patterned polymer networks. *Optics Letters*, 29(14):1608, 7 2004.

[81] Nikolas Chronis, Gang Liu, Ki-Hun Jeong, and Luke Lee. Tunable liquid-filled microlens array integrated with microfluidic network. *Optics Express*, 11(19):2370, 9 2003.

[82] Gui-Ping Zhu, Jia-Feng Yao, Shi-Hua Wu, and Xi-Dong Zhang. Actuation of adaptive liquid microlens droplet in microfluidic devices: A review. *Electrophoresis*, 40(8):1148–1159, 2019.

[83] Liang Dong, Abhishek K. Agarwal, David J. Beebe, and Hongrui Jiang. Adaptive liquid microlenses activated by stimuli-responsive hydrogels. *Nature*, 40(8):551–554, 2006.

[84] Se Um Kim, Jun Hee Na, Chiwoo Kim, and Sin Doo Lee. Design and fabrication of liquid crystal-based lenses. *Liquid Crystals*, 44(12-13):2121–2132, 2017.

[85] Ibrahim Halil Giden, Neslihan Eti, Behrooz Rezaei, and Hamza Kurt. Adaptive graded index photonic crystal lens design via nematic liquid crystals. *IEEE Journal of Quantum Electronics*, 52(10):1–7, 10 2016.

[86] Hung-Chun Lin, Ming-Syuan Chen, and Yi-Hsin Lin. A review of electrically tunable focusing liquid crystal lenses. *Transactions on Electrical and Electronic Materials*, 12(6):234–240, 12 2011.

[87] Jose Francisco Algorri, Virginia Urruchi del Pozo, Jose Manuel Sanchez-Pena, and Jose Manuel Oton. An autostereoscopic device for mobile applications based on a liquid crystal microlens array and an OLED display. *Journal of Display Technology*, 10(9):713–720, 9 2014.

[88] Jun-Han Han, Jaehyun Moon, Doo-Hee Cho, Jin-Wook Shin, Hye Yong Chu, Jeong-Ik Lee, Nam Sung Cho, and Jonghee Lee. Luminescence enhancement of OLED lighting panels using a microlens array film. *Journal of Information Display*, 19(4):179–184, 10 2018.

[89] Jun Li, Greg Baird, Yi-Hsin Lin, Hongwen Ren, and Shin-Tson Wu. Refractive-index matching between liquid crystals and photopolymers. *Journal of the Society for Information Display*, 13(12):1017, 2005.

[90] Pierre-Gilles de Gennes. Wetting: statics and dynamics. *Reviews of Modern Physics*, 57(3):827–863, 7 1985.

[91] Jun Yoshioka and Koji Fukao. Horizontal transportation of a maltese cross pattern in nematic liquid crystalline droplets under a temperature gradient. *Phys. Rev. E*, 99:022702, Feb 2019.

[92] Se-Um Kim, Sanghun Lee, Jun-Hee Na, and Sin-Doo Lee. Tunable liquid crystal lens array by encapsulation with a photo-reactive polymer for short focal length. *Optics Communications*, 313(February):329–332, 2 2014.

[93] Avner Friedman. Polymer-dispersed liquid crystal films for light control. pages 62–79. 1990.

[94] Gregory Philip Crawford and Slobodan Zumer. Liquid Crystals In Complex Geometries: Formed by Polymer And Porous Networks, Taylor & Francis Group, 1996.

[95] Mohsin Hassan Saeed, Shuaifeng Zhang, Yaping Cao, Le Zhou, Junmei Hu, Imran Muhammad, Jiumei Xiao, Lanying Zhang, and Huai Yang. Recent advances in the polymer dispersed liquid crystal composite and its applications. *Molecules (Basel, Switzerland)*, 25(23):5510, 11 2020.

[96] Naila Nasir, Hyeryeon Hong, Malik Abdul Rehman, Sunil Kumar, and Yongho Seo. Polymer-dispersed liquid-crystal-based switchable glazing fabricated via vacuum glass coupling. *RSC Advances*, 10(53):32225–32231, 2020.

[97] Bao-Gang Wu, John H. Erdmann, and J. William Doane. Response times and voltages for PDLC light shutters. *Liquid Crystals*, 5(5):1453–1465, 1 1989.

[98] John L West. Phase Separation of Liquid Crystals in Polymers. *Molecular Crystals and Liquid Crystals Incorporating Nonlinear Optics*, 157(1):427–441, 4 1988.

[99] H M J Boots, J G Kloosterboer, C Serbutoviez, and F J Touwslager. Polymerization-Induced Phase Separation. 1. Conversion - Phase Diagrams. 9297(96):7683–7689, 1996.

[100] H. Hakemi. Polymer dispersed liquid crystal (PDLC) "Industrial technology and development in Europe". *Molecular Crystals and Liquid Crystals*, 684(1):7–14, 5 2019.

[101] Hongwen Ren and Shin-Tson Wu. Inhomogeneous nanoscale polymer-dispersed liquid crystals with gradient refractive index. *Applied Physics Letters*, 81(19):3537–3539, 11 2002.

[102] Lalgudi V. Natarajan, Christina K. Shepherd, Donna M. Brandelik, Richard L. Sutherland, Suresh Chandra, Vincent P. Tondiglia, David Tomlin, and Timothy J. Bunning. Switchable holographic polymer-dispersed liquid crystal reflection gratings based on thiol-ene photopolymerization. *Chemistry of Materials*, 15(12):2477–2484, 6 2003.

[103] R. L. Sutherland, L. V. Natarajan, V. P. Tondiglia, and T. J. Bunning. Bragg gratings in an acrylate polymer consisting of periodic polymer-dispersed liquid-crystal planes. *Chemistry of Materials*, 5(10):1533–1538, 10 1993.

[104] Takahiro Ishinabe, Yuya Horii, Yosei Shibata, and Hideo Fujikake. Light distribution control of layer-structured PDLC fabricated by using micro lens structure and anisotropically diffused UV light. *Optics Express*, 27(9):13416–13429, 4 2019.

[105] Jun Qi and Gregory P. Crawford. Holographically formed polymer dispersed liquid crystal displays. *Displays*, 25(5):177–186, 12 2004.

[106] Jun Wang, Jianfeng Xia, Suck Won Hong, Feng Qiu, Yuliang Yang, and Zhiqun Lin. Phase separation of polymer-dispersed liquid crystals on a chemically patterned substrate. *Langmuir*, 23(14):7411–7415, 7 2007.

[107] Jianhua Zou and Jiyu Fang. Adhesive polymer-dispersed liquid crystal films. *Journal of Materials Chemistry*, 21(25):9149, 2011.

[108] Ali Bahadori-Jahromi, Abdulazeez Rotimi, Anastasia Mylona, Paulina Godfrey, and Darren Cook. Impact of window films on the overall energy consumption of existing UK hotel buildings. *Sustainability*, 9(5):731, 5 2017.

[109] H. Hakemi. Polymer-dispersed liquid crystal technology industrial evolution and current market situation. *Liquid Crystals Today*, 26(3):70–73, 7 2017.

[110] Hisham Alghamdi and A.H.M. Almawgani. Smart and efficient energy saving system using PDLC glass. In *2019 Smart City Symposium Prague (SCSP)*, pages 1–5. IEEE, 5 2019.

[111] C.G. Granqvist, M.A. Arvizu, Bayrak Pehlivan, and G.A. Niklasson. Electrochromic materials and devices for energy efficiency and human comfort in buildings: A critical review. *Electrochimica Acta*, 259:1170–1182, 1 2018.

[112] Ivan P Parkin and Troy D Manning. Intelligent thermochromic windows. *Journal of Chemical Education*, 83(3):393, 3 2006.

[113] El-Zaiat, M Medhat, Mona F Omar, and Marwa A Shirif. Effect of UV exposure on photochromic glasses doped with transition metal oxides. *Optics Communications*, 370:176–182, 7 2016.

[114] Volker Wittwer, Andreas Georg, Wolfgang Graf, and Gunther Walze. Gasochromic windows. *Solar Energy Materials and Solar Cells*, 84(1-4):305–314, 10 2004.

[115] Ruben Baetens, Bjorn Petter Jelle, and Arild Gustavsen. Properties, requirements and possibilities of smart windows for dynamic daylight and solar energy control in buildings: A state-of-the-art review. *Solar Energy Materials and Solar Cells*, 94(2):87–105, 2 2010.

[116] Vera Joanne Aliño, Kun Xiang Tay, Saif A. Khan, and Kun Lin Yang. Inkjet printing and release of monodisperse liquid crystal droplets from solid surfaces. *Langmuir*, 28(41):14540–14546, 2012.

[117] Farzana Ahmad, Muhammad Jamil, Jin Woo Lee, Seo Rok Kim, and Young Jae Jeon. The effect of UV intensities and curing time on polymer dispersed liquid crystal (PDLC) display: A detailed analysis study. *Electronic Materials Letters*, 12(5):685–692, 9 2016.

[118] Andrew J Lovinger, Karl R Amundson, and Don D Davis. Morphological investigation of UV-curable polymer-dispersed liquid-crystal (PDLC) materials. *Chemistry of Materials*, 6(10):1726–1736, 10 1994.

[119] R Miller, E.V. Aksenenko, and V.B. Fainerman. Dynamic interfacial tension of surfactant solutions. *Advances in Colloid and Interface Science*, 247:115–129, 9

2017.

[120] Karl Heinz Schweikart, Bjorn Fechner, and Hans Tobias Macholdt. Dynamic surface tension: A key parameter for excellent ink jet preparations. *International conference on digital production printing and industrial applications, DPP2005 - Final Program and Proceedings*, 2005:161–163, 2005.

[121] H. Hakemi, O. Pinshow, and D. Gal-Fuss. Evaluation of polymer dispersed liquid crystal (PDLC) for passive rear projection screen application. *Recent Progress in Materials*, 1(3):1–1, 6 2019.

[122] Yura Kim, Dayeon Jung, Seyoon Jeong, Kwangyoon Kim, Woosuk Choi, and Yongho Seo. Optical properties and optimized conditions for polymer dispersed liquid crystal containing UV curable polymer and nematic liquid crystal. *Current Applied Physics*, 15(3):292–297, 3 2015.

[123] Mujtaba Ellahi, Fang Liu, Ping Song, Yanzi Gao, Dil Faraz, Hui Cao, and Huai Yang. Characterization and morphology of polymer-dispersed liquid crystal films. *Soft Materials*, 12(3):339–345, 7 2014.

[124] Xingliang Dai, Yunzhou Deng, Xiaogang Peng, and Yizheng Jin. Quantum-Dot light emitting diodes for large area displays: Towards the dawn of commercialization. *Advanced Materials*, 29(14):1607022, 4 2017.

[125] Moon Kee Choi, Jiwoong Yang, Kwanghun Kang, Dong Chan Kim, Changsoon Choi, Chaneui Park, Seok Joo Kim, Sue In Chae, Tae-Ho Kim, Ji Hoon Kim, Taeghwan Hyeon, and Dae-Hyeong Kim. Wearable red-green-blue quantum dot light-emitting diode array using high-resolution intaglio transfer printing. *Nature Communications*, 6(1):7149, 11 2015.

[126] Serdar Onses, Erick Sutanto, Placid Ferreira, Alleyne, and John A. Rogers. Mechanisms, capabilities, and applications of high resolution electrohydrodynamic Jet Printing. *Small*, 11(34):4237–4266, 9 2015.

[127] Jack Zhou, Dajing Gao, Donggang Yao, Steven K. Leist, and Yifan Fei. Mechanisms and modeling of electrohydrodynamic phenomena. *International Journal of Bioprinting*, 5(1):166, 12 2018.

[128] Jang-Ung Park, Matt Hardy, Seong Jun Kang, Kira Barton, Kurt Adair, Deep kishore Mukhopadhyay, Chang Young Lee, Michael S Strano, Andrew G Alleyne, John G Georgiadis, Placid M Ferreira, and John A Rogers. High-resolution electrohydrodynamic jet printing. *Nature Materials*, 6(10):782–789, 10 2007.

[129] Benjamin Porter and Harish Bhaskaran. Additive nanomanufacturing – A review. *Journal of Materials Research*, 29(17):1792–1816, 9 2014.

[130] Yiwei Han and Jingyan Dong. Electrohydrodynamic printing for advanced micro/-nanomanufacturing: Current progresses, opportunities, and challenges. *Journal of Micro and Nano-Manufacturing*, 6(4), 12 2018.

[131] Nhlakanipho Mkhize and Harish Bhaskaran. Electrohydrodynamic Jet printing: Introductory concepts and considerations. *Small Science*, 2(2):2100073, 2 2022.

[132] Sang-Yoon Kim, Yong Kim, Jaehong Park, and Jungho Hwang. Design and evaluation of single nozzle with a non-conductive tip for reducing applied voltage and pattern width in electrohydrodynamic jet printing (EHDP). *Journal of Micromechanics and Microengineering*, 20(5):055009, 5 2010.

[133] Berend-Jan de Gans and Ulrich S Schubert. Inkjet printing of polymer micro-arrays and libraries: Instrumentation, requirements, and perspectives. *Macromolecular Rapid Communications*, 24(11):659–666, 7 2003.

[134] Bing Zhang, Jiankang He, Xiao Li, Fangyuan Xu, and Dichen Li. Micro/nanoscale electrohydrodynamic printing: from 2D to 3D. *Nanoscale*, 8(34):15376–15388, 2016.

[135] Jeong-Gun Lee, Hye-Jung Cho, Nam Huh, Christopher Ko, Woo-Chang Lee, Yong-Hark Jang, Beom Seok Lee, In Seok Kang, and Jeong-Woo Choi. Electrohydrodynamic (EHD) dispensing of nanoliter DNA droplets for microarrays. *Biosensors and Bioelectronics*, 21(12):2240–2247, 6 2006.

[136] Arshad Khan, Khalid Rahman, Dong Soo Kim, and Kyung Hyun Choi. Direct printing of copper conductive micro-tracks by multi-nozzle electrohydrodynamic inkjet printing process. *Journal of Materials Processing Technology*, 212(3):700–706, 3 2012.

[137] Shijie Su, Junsheng Liang, Xiaojian Li, Wenwen Xin, Li Chen, Penghe Yin, Zizhu Wang, Xushi Ye, Jianping Xiao, and Dazhi Wang. Direct microtip focused electrohydrodynamic jet printing of tailored microlens arrays on PDMS nanofilm-modified substrate. *Advanced Materials Technologies*, 6(11):2100449, 11 2021.

[138] Arshad Khan, Khalid Rahman, Shawkat Ali, Saleem Khan, Bo Wang, and Amine Bermak. Fabrication of circuits by multi-nozzle electrohydrodynamic inkjet printing for soft wearable electronics. *Journal of Materials Research*, 36(18):3568–3578, 9 2021.

[139] Qi Lei, Jiankang He, and Dichen Li. Electrohydrodynamic 3D printing of layer-specifically oriented, multiscale conductive scaffolds for cardiac tissue engineering. *Nanoscale*, 11(32):15195–15205, 2019.

[140] Sara Coppola, Giuseppe Nasti, Michele Todino, Federico Olivieri, Veronica Vespini, and Pietro Ferraro. Direct Writing of Microfluidic Footpaths by Pyro-EHD Printing. *ACS Applied Materials & Interfaces*, 9(19):16488–16494, 5 2017.

[141] Hyeok-jin Kwon, Jisu Hong, Sang Yong Nam, Hyun Ho Choi, Xinlin Li, Yong Jin Jeong, and Se Hyun Kim. Overview of recent progress in electrohydrodynamic jet printing in practical printed electronics: focus on the variety of printable materials for each component. *Materials Advances*, 2(17):5593–5615, 2021.

[142] Yiguang Wu, Qi An, Jingxiang Yin, Tao Hua, Huiming Xie, Guangtao Li, and Hong Tang. Liquid crystal fibers produced by using electrospinning technique. *Colloid and Polymer Science*, 286(8-9):897–905, 8 2008.

[143] Atilla Eren Mamuk, Ãaǵdas Koćak, and Ãiǵdem Elif Demirci Dónmez. Production and characterization of liquid crystal/polyacrylonitrile nano-fibers by electrospinning method. *Colloid and Polymer Science*, 299(7):1209–1221, 7 2021.

[144] D Li and Y Xia. Electrospinning of Nanofibers: Reinventing the Wheel? *Advanced Materials*, 16(14):1151–1170, 7 2004.

[145] Jan P F Lagerwall, Jesse T McCann, Eric Formo, Giusy Scalia, and Younan Xia. Coaxial electrospinning of microfibres with liquid crystal in the core. *Chemical Communications*, (42):5420, 2008.

[146] Dae Kyom Kim, Minsik Hwang, and Jan P F Lagerwall. Liquid crystal functionalization of electrospun polymer fibers. *Journal of Polymer Science Part B: Polymer Physics*, 51(11):855–867, 6 2013.

[147] Jia-De Lin, Che-Pei Chen, Lin-Jer Chen, Yu-Chou Chuang, Shuan-Yu Huang, and Chia-Rong Lee. Morphological appearances and photo-controllable coloration of dye-doped cholesteric liquid crystal/polymer coaxial microfibers fabricated by coaxial electrospinning technique. *Optics Express*, 24(3):3112, 2 2016.

[148] Geoffrey Ingram Taylor and M D Van Dyke. Electrically driven jets. *Proceedings of the Royal Society of London. A. Mathematical and Physical Sciences*, 313(1515):453–475, 12 1969.

[149] Erick Sutanto, Kazuyo Shigeta, Yongkwan Kim, Philip Graf, David Hoelzle, and Placid Ferreira. A multimaterial electrohydrodynamic jet (E-jet) printing system. *Journal of Micromechanics and Microengineering*, 22(4):045008, 4 2012.

[150] Kira Barton, Sandipan Mishra, K Alex Shorter, Andrew Alleyne, Placid Ferreira, and John Rogers. A desktop electrohydrodynamic jet printing system. *Mechatronics*, 20(5):611–616, 8 2010.

[151] www.enjet.co.kr.

[152] Yanqiao Pan and Liangcai Zeng. Simulation and validation of droplet generation process for revealing three design constraints in electrohydrodynamic Jet printing. *Micromachines*, 10(2):94, 1 2019.

[153] I. Hayati, Anita I. Bailey, and Th. F Tadros. Mechanism of stable jet formation in electrohydrodynamic atomization. *Nature*, 319(6048):41–43, 1986.

[154] I. Hayati, Anita I. Bailey, and Th. F Tadros. Investigations into the mechanism of electrohydrodynamic spraying of liquids. *Journal of Colloid and Interface Science*, 117(1):222–230, 5 1987.

[155] I. Hayati, Anita I. Bailey, and Th. F Tadros. Investigations into the mechanisms of electrohydrodynamic spraying of liquids. *Journal of Colloid and Interface Science*, 117(1):205–221, 5 1987.

[156] Jaehyun Bae, Jaewoong Lee, and Se Hyun Kim. Effects of polymer properties on jetting performance of electrohydrodynamic printing. *Journal of Applied Polymer Science*, 134(35):45044, 9 2017.

[157] Ayoung Lee, Howon Jin, Hyun-Woo Dang, Kyung-Hyun Choi, and Kyung Hyun Ahn. Optimization of experimental parameters to determine the jetting regimes in electrohydrodynamic printing. *Langmuir*, 29(44):13630–13639, 11 2013.

[158] Andrzej Jaworek and Andrzej Krupa. Classification of the modes of EHD spraying . *Journal of Aerosol Science*, 30(7):873–893, 8 1999.

[159] Khalid Rahman, Arshad Khan, Nauman Malik Muhammad, Jeongdai Jo, and Kyung-Hyun Choi. Fine-resolution patterning of copper nanoparticles through electrohydrodynamic jet printing. *Journal of Micromechanics and Microengineering*, 22(6):65012, 2012.

[160] Dong Soo Kim, Arshad Khan, Khalid Rahman, Saleem Khan, Hyung Chan Kim, and Kyung Hyun Choi. Drop-on-demand direct printing of colloidal copper nanoparticles by electrohydrodynamic atomization. *Materials and Manufacturing Processes*, 26(9):1196–1201, 9 2011.

[161] Lei Guo, Yongqing Duan, YongAn Huang, and Zhouping Yin. Experimental study of the influence of ink properties and process parameters on ejection volume in electrohydrodynamic jet printing. *Micromachines*, 9(10):522, 10 2018.

[162] Patrick Sammons, Sahit Bollineni, Ritika Sibal, and Kira Barton. Temperature and humidity variation effect on process behavior in electrohydrodynamic jet printing of a class of optical adhesives. *Solid Freeform Fabrication 2017: Proceedings of the 28th Annual International Solid Freeform Fabrication Symposium - An Additive Manufacturing Conference, SFF 2017*, pages 1784–1794, 2020.

[163] Thanh Huy Phung, Seora Kim, and Kye-Si Kwon. A high speed electrohydrodynamic (EHD) jet printing method for line printing. *Journal of Micromechanics and Microengineering*, 27(9):95003, 2017.

[164] Sooman Lim, So Hyun Park, Tae Kyu An, Hwa Sung Lee, and Se Hyun Kim. Electrohydrodynamic printing of poly(3,4-ethylenedioxythiophene):poly(4-

styrenesulfonate) electrodes with ratio-optimized surfactant. *RSC Advances*, 6(3):2004–2010, 2016.

[165] Seongpil An, Min Wook Lee, Na Young Kim, Changmin Lee, Salem S Al-Deyab, Scott C James, and Sam S Yoon. Effect of viscosity, electrical conductivity, and surface tension on direct-current-pulsed drop-on-demand electrohydrodynamic printing frequency. *Applied Physics Letters*, 105(21):214102, 11 2014.

[166] Zhang, Mohan J. Edirsinghe, and Suwan N. Jayasinghe. Flow behaviour of dielectric liquids in an electric field. *Journal of Fluid Mechanics*, 558:103, 7 2006.

[167] Suwan N. Jayasinghe and Mohan J. Edirisinghe. Electrically forced jets and microthreads of high viscosity dielectric liquids. *Journal of Aerosol Science*, 35(2):233–243, 3 2004.

[168] Julian Schneider. Electrohydrodynamic nanoprinting and its applications. PhD thesis, ETH Zurich, 2015.

[169] Yozo Utsumi and Toshihisa Kamei. Dielectric permittivity measurements of liquid crystal in the microwave and millimeter wave ranges. *Molecular Crystals and Liquid Crystals*, 409(1):355–370, 1 2004.

[170] Minwook Lee, Dong-kyun Kang, Na-young Kim, Hoyoung Kim, Scott C. James, and Sam Goo Yoon. A study of ejection modes for pulsed-DC electrohydrodynamic inkjet printing. *Journal of Aerosol Science*, 46:1–6, 4 2012.

[171] Shijie Su, Junsheng Liang, Zizhu Wang, Wenwen Xin, Xiaojian Li, and Dazhi Wang. Microtip focused electrohydrodynamic jet printing with nanoscale resolution. *Nanoscale*, 12(48):24450–24462, 2020.

[172] Sepehr Maktabi and Paul R Chiarot. Electrohydrodynamic printing of organic polymeric resistors on flat and uneven surfaces. *Journal of Applied Physics*, 120(8):084903, 8 2016.

[173] Urszula Stachewicz, J Frits Dijksman, Caner U Yurteri, and Jan C M Marijnissen. Experiments on single event electrospraying. *Applied Physics Letters*, 91(25):254109, 12 2007.